



DISSERTATION

Titel der Dissertation

„Crystal-plastic deformation of zircon: effects on microstructures, textures, microchemistry and the retention of radiogenic isotopes“

Verfasserin

Elizaveta Kovaleva MSc

angestrebter akademischer Grad

Doktorin der Naturwissenschaften (Dr. rer. nat.)

Wien, 2015

Studienkennzahl lt. Studienblatt: A 796 605 426

Dissertationsgebiet lt. Studienblatt: Erdwissenschaften

Betreuerin / Betreuer: Ao. Univ.-Prof. Mag. Dr. Urs Klötzli

Preface

This thesis presents the results of three-year project that has been developed in the framework of the Doctoral School “DOGMA: Deformation Of Geological MAterials: Mechanical-chemical feedback and the coupling across scales.” The thesis is focused on zircon from high-temperature shear zones, which has been affected by plastic deformation. The short introduction to the topic is given in Chapter 1. In particular, in this work I have distinguished three finite deformation patterns in deformed zircon (Chapter 2). Results of this investigation have been published in the journal *Solid Earth*. Also, I have found the genetic relationships between macroscopic kinematic frame of a shear zone, orientation of deformed zircon grains and misorientation axes in deformed zircon (Chapter 3). The results of this study are in preparation for submission to *Geology*.

I have demonstrated how trace elements and isotopic systems are affected by deformation microstructures in zircon (Chapter 4).

In paleo-seismic zones, associated with pseudotachylyte veins I have found zircon grains with planar deformation bands. These deformation features have been described in detail (Chapter 5). The results of this finding are now in press in *American Mineralogist*. Trace elements and isotopes behavior has been investigated in connection with planar deformation bands (Chapter 6).

General conclusions are given in Chapter 7. A Curriculum Vitae (CV) of the thesis’s author is attached at the end of the document (Chapter 8).

Acknowledgements

The author wishes to thank all people who supported this work:

Aaron Cavosie

Anna Rogowitz

Anne–Kathrin Schäffer

Arno Schintlmeister

Benjamin Huet

Bernhard Grasemann

Christian Auer

Claudia Beybel

Claudia Trepmann

David Grebenstein

David Mainprice

Dieter Rhede

Eugen Libowitzky

Eva Klötzli

Franz Biedermann

Franz Kiraly

Gerlinde Habler

Hugh Rice

John Eiler

John Wheeler

Jürgen Österle

Lidia Pittarello

Lutz Nasdala

Marco Lommatzsch

Markus Palzer

Matthew Huber

Nicholas Timms

Rainer Abart

Roman Schuster

Sigrid Hrabe

Steven Reddy

Thomas Griffiths

Tobias Eberlei

Yunbin Guan

And my advisor, Urs Klötzli

Thanks also go to all colleagues of the FOR741 research group for fruitful discussions, to the Geologische Bundesanstalt (GBA) of Austria for access to the SEM, to the University of Vienna (doctoral school "DOGMA", project IK 052) and the Austrian Science Foundation Fund (FWF): I471-N19, which is part of the DFG-FWF funded international research group FOR741-DACH.

Abstract

Dating of deep-crustal deformation events potentially can be achieved by using plastically-deformed accessory minerals found in high-temperature shear zones. Deformation microstructures, such as dislocations and low-angle boundaries, form due to plastic deformation in the crystal lattice and act as fluid migration pathways and trace element (e.g. Pb, Ti, U, Th, REE) diffusion pathways through so-called “pipe diffusion”. Deformation microstructures can alter the chemical and isotopic composition of certain grain parts and may lead to complete or partial isotopic resetting of certain geochronometers (e.g. U/Th/Pb, K/Ar, Rb/Sr) in the mineral domains.

This work aims to better understand the processes of crystal-plastic deformation and associated trace element redistribution and the resetting of isotopic systems in zircon. This study finds that: a) there are three general finite deformation patterns in deformed zircons; b) suggests that it is possible to reconstruct the macroscopic kinematic framework of the shear zone based on the orientation of deformed zircon grains and the operating misorientation axes; c) and demonstrates the effect of deformation microstructures on trace elements and Pb isotopes in zircon. The final goal of this project is to develop a tool for isotopic dating of high-temperature deformation events in the deep crust.

In addition to these results, zircon grains with planar deformation bands have been discovered in paleo-seismic zones; these deformation features have been described in detail and a possible mechanism of their origin and formation is suggested. The effect of planar deformation bands on trace element and isotopic behavior has also been investigated.

Zusammenfassung

Die Datierung von Deformationsereignissen in der tiefen Kruste kann über die Datierung von plastisch deformierten Akzessorien in Hochtemperatur Scherzonen bewerkstelligt werden. Deformations-Mikrostrukturen, wie Dislokationen und „low-angle boundaries“, die als Resultat plastischen Deformation eines Kristallgitters interpretiert werden, erhöhen die Wegsamkeit für Fluide und die Diffusionsraten von Elementen (sog. „pipe-diffusion“). Durch eine solcherart ermöglichte Vereinfachung von Spurenelementmobilitäten (zB. Pb, Ti, U, Th, SEEn) können einzelne Mineraldomänen in ihrer Element- und Isotopenzusammensetzung signifikant verändert werden. Dadurch kann es zu einem teilweisen oder sogar kompletten Zurücksetzen der Isotopensysteme einzelner Geochronometer (zB. U/Th/Pb, K/Ar, Rb/Sr) kommen. Damit ist die direkte Datierung von Deformationsereignissen möglich.

Die hier vorgestellten Untersuchungen zielen auf ein besseres Verständnis von plastischer Deformation in Zirkon und die damit einhergehende Element- und Isotopenumverteilung hin. Es konnten drei wesentliche Deformationsmuster von Zirkon erkannt werden. Die Orientierung deformierter Zirkone erlaubt es, die wirksame Misorientierungsachse und der makroskopische kinematische Rahmen im Umfeld der Zirkone zu rekonstruieren. Zusammen mit der Umverteilung von Spurenelementen konnte auch der Einfluss der Deformation auf die Bleisotopie nachgewiesen werden. Letztendliches Ziel ist es, ein analytisches Werkzeug zur Datierung von hochtemperierten Deformationsereignissen in der unteren Kruste zu entwickeln.

Weitere Resultate sind: in Zonen paläoseismischer Aktivität konnten Zirkone mit planaren Deformationsbahnen gefunden werden. Dieses bis anhin unbekanntes Deformationsphänomen wird detailliert beschrieben und mögliche Bildungsmechanismen werden dargestellt.

Table of contents

Preface.....	3
Acknowledgements.....	4
Abstract	6
Zusammenfassung	7
1.0. Introduction.....	13
1.1. Analytical techniques	15
1.2. Goals of the project.....	15
1.3. Importance of the project for geosciences.....	15
References	17
2.0. Finite lattice distortion patterns in plastically deformed zircon grains	19
Abstract	19
2.1. Introduction	20
2.1.1. Zircon and its significance in geosciences	20
2.1.2. Targeted material.....	21
2.1.3. Crystal-plastic deformation	22
2.1.4. Motivation and challenge	23
2.2. Geological environment	23
2.2.1. Western Tauern Window, Eastern Alps (Zillertal, Tyrol, Austria), amphibolite facies metamorphic grade.....	23
2.2.2. Ivrea-Verbanò Zone, Southern Alps (Forno, Val Strona, Northern Italy), granulite facies metamorphic grade.....	25
2.3. Analytical methods and data representation	26
2.3.1. Samples preparation.....	26
2.3.2. Scanning electron microscopy and cathodoluminescence (CL) imaging	27
2.3.3. Electron Backscatter Diffraction (EBSD) analysis and Forescattered electron (FSE) imaging	27
2.3.4. Raman spectroscopy.....	28

2.4.	Petrography and zircon content	29
2.4.1.	Shear Zone 1	29
2.4.2.	Shear Zone 2	33
2.4.3.	Shear Zone 3	35
2.5.	Microstructural and crystallographic orientation data	35
2.5.1.	CL-bright domains	36
2.5.2.	Zircon finite lattice distortion types	36
2.6.	Discussion	44
2.6.1.	Static dissolution-precipitation vs. crystal-plastic deformation	44
2.6.2.	Microstructural analysis of different lattice distortion patterns	48
2.6.3.	CL imaging and Raman spectroscopy	55
2.6.4.	What deformation conditions and host environment facilitates crystal-plastic deformation in zircon?	57
2.6.5.	What factors could influence zircon finite distortion patterns?.....	59
2.7.	Conclusions	60
	Acknowledgments.....	62
	References	65

3.0. On the relationship between deformation microstructures in zircon and the kinematic framework of the shear zone 73

	Abstract	73
3.1.	Introduction	74
3.2.	Sample material.....	74
3.2.1.	Meta-lamprophyric dyke (sample BH12-07), Tauern Window (Zillertal, Tyrol, Austria)	75
3.2.2.	STG13, Porphyritic biotite-meta-granite (sample STG13), Ötztal-Stubai Crystalline (Falbeson, Stubaital, Austria)	75
3.2.3.	Sillimanite-biotite-garnet gneiss (sample IV12-05), Ivrea-Verbano Zone (Forno, Val Strona, Northern Italy, N45°59'46.46"/E8°21'38.65").....	75
3.2.4.	Felsic mylonite (IV12-07 and IVZ02-12), Ivrea-Verbano Zone (Forno, Val Strona, Northern Italy).....	75
3.3.	Analytical method	76
3.4.	Zircon microstructures and textures	76
3.4.1.	Meta-lamprophyre	76
3.4.2.	Porphyritic biotite-meta-granite	77
3.4.3.	Sillimanite-biotite-garnet gneiss	78

3.4.4.	Felsic mylonite	79
3.5.	Discussion	79
3.5.1.	Systematics derived from natural samples	79
3.5.2.	Active slip systems.....	80
3.5.3.	Comparison of natural data with a theoretical model of zircon crystal-plastic deformation.....	81
3.5.4.	Link between zircon crystal-plastic deformation and macroscopic kinematic frame	82
3.5.5.	Implication for zircon geochronology	83
	Acknowledgements.....	84
	References	85
	Supplementary figures	88

4.0.	The effect of crystal-plastic deformation on isotopes and trace element distribution in zircon.....	96
	Abstract	96
4.1.	Introduction	97
4.2.	Geological settings and petrography	99
4.2.1.	Ivrea-Verbano Zone (IVZ), Southern Alps (Forno, Val Strona, Northern Italy)	99
4.2.2.	Western Tauern Window, Eastern Alps (Zillertal, Tyrol, Austria)	101
4.3.	Analytical methods	101
4.3.1.	Sample preparation and scanning electron microscopy (SEM).....	101
4.3.2.	Forward scattered electrons (FSE) imaging and electron backscatter diffraction (EBSD) mapping	102
4.3.3.	Field emission gun electron microprobe analyzer (FEG-EMPA)	103
4.3.4.	Nano-scale secondary ion mass spectrometry (NanoSIMS).....	103
4.4.	Results	104
4.4.1.	Orientation, chemical and isotope mapping of plastically-deformed zircon grains	104
4.4.2.	High-resolution profiles across plastically-deformed zircon grains	109
4.5.	Discussion	119
4.5.1.	Efficiency of applied imaging techniques.....	119
4.5.2.	Efficiency of chemical profiling	120
4.5.3.	Trace elements behavior.....	121
4.5.4.	Relative $^{207}\text{Pb}/^{206}\text{Pb}$ age	126
4.5.5.	Comparing with existing data	129
4.6.	Conclusions	131
	Acknowledgments.....	132

References	133
5.0. Planar microstructures in zircon from paleo-seismic zones	139
Abstract	139
5.1. Introduction	141
5.1.1. Pseudotachylytes in mylonites	141
5.1.2. Planar microstructures in zircon	142
5.1.3. Motivation and challenge	144
5.2. Geological and field settings	145
5.3. Analytical methods and data representation	146
5.3.1. Sample preparation	146
5.3.2. Scanning electron microscopy and cathodoluminescence (CL) imaging	147
5.3.3. Forward scattered electron (FSE) imaging and electron backscatter diffraction (EBSD) analysis.....	148
5.4. Petrography.....	149
5.5. Microstructural and crystallographic zircon data.....	152
5.5.1. Planar deformation bands.....	152
5.5.2. Planar fractures	154
5.5.3. Curvilinear fractures	155
5.5.4. Cataclastic deformation structures in zircon.....	155
5.5.5. Crystal-plastic deformation structures	156
5.6. Discussion	165
5.6.1. Characterization of planar deformation bands	165
5.6.2. Interrelation of PDBs with formation of other deformation structures (cataclastic and crystal-plastic)	173
5.6.3. Implications for the evolution of the IVZ	176
5.7. Implications.....	176
Acknowledgments.....	177
References	178
6.0. NanoSIMS study of planar deformation bands in zircon	185
Abstract	185
6.1. Introduction	186
6.1.1. Planar microstructures in zircon	186

6.1.2.	Trace element and isotopes distribution caused by planar microstructures in zircon	187
6.2.	Sampling locality and samples	188
6.3.	Analytical methods and data representation	188
6.3.1.	Sample preparation and scanning electron microscopy (SEM)	188
6.3.2.	Electron backscatter diffraction (EBSD)	189
6.3.3.	Nano-scale secondary ion mass spectrometry (NanoSIMS).....	189
6.4.	Results	190
6.4.1.	NanoSIMS mapping	190
6.4.2.	NanoSIMS profiling	194
6.5.	Discussion	195
6.5.1.	Mapping and profiling	197
6.5.2.	$^{207}\text{Pb}/^{206}\text{Pb}$ relative ages.....	198
6.6.	Conclusions	198
	Acknowledgments.....	199
	References	200
7.0.	Conclusions	204
7.1.	Future research directions	205
8.0.	CURRICULUM VITAE	206

1.0. Introduction

Mineral dating of low-temperature deformation events, such as metasomatism and fluid-induced recrystallization, is already widely used. For example, one of the most popular minerals for dating of low-temperature deformation is white mica (e.g. Freeman et al., 1997; Glodny et al., 2008; Schneider et al., 2013). Among accessory minerals, zircon and monazite have also been analyzed in order to establish an age of low-temperature deformation (e.g. Geisler et al., 2002; Kusiak et al., 2009; Wawrzenitz et al., 2012). However, dating of deep-crustal deformation events remains enigmatic. Such dating could be achieved using plastically-deformed accessory minerals found in high-temperature shear zones. Edge and screw dislocations are introduced to the crystal lattice of individual mineral grains during crystal-plastic deformation and can form subgrain boundaries by gathering together in arrays (Poirier, 1985). It is known that deformation microstructures, such as dislocations and low-angle boundaries (Fig. 1.1) that formed due to plastic deformation in the crystal lattice, act as fluid migration paths and element diffusion pathways through so-called “pipe diffusion” (Ruoff, 1967). Facilitating trace element mobility in the crystalline mineral grains, low-angle boundaries can alter the chemical and isotopic composition of certain grain parts (e.g. Reddy and Timms, 2010; Timms et al., 2006, 2011). Even more importantly, deformation microstructures may lead to complete or partial isotopic resetting in the mineral domains. This implies that accessory minerals potentially allow dating of high-temperature deformation. Also, since the isotopic age of the different domains in the single crystal can vary, it should be possible to recognize and interpret this variation and distinguish the timing of different events.

The most suitable mineral for such dating is zircon that is widely used for terrestrial and lunar geochronology (e.g. Maas et al., 1992; Nemchin et al., 2009). It has the important property to

incorporate and preserve uranium, thorium and rare earth elements (REE) and apart for its importance for isotopic dating is also used for the geochemical characterization of its formation environment, and for the estimation of (re)crystallization temperature (e.g. Watson et al., 2006). Thus, it is very important to learn how zircon behaves under differential stresses and high temperatures during deep-crustal deformation events. It is beneficial to work with zircon, because it is comparatively robust. For example, zircon can preserve low-angle boundaries and associated age disturbance under lower-crust temperatures for billions of years (Moser et al., 2009).

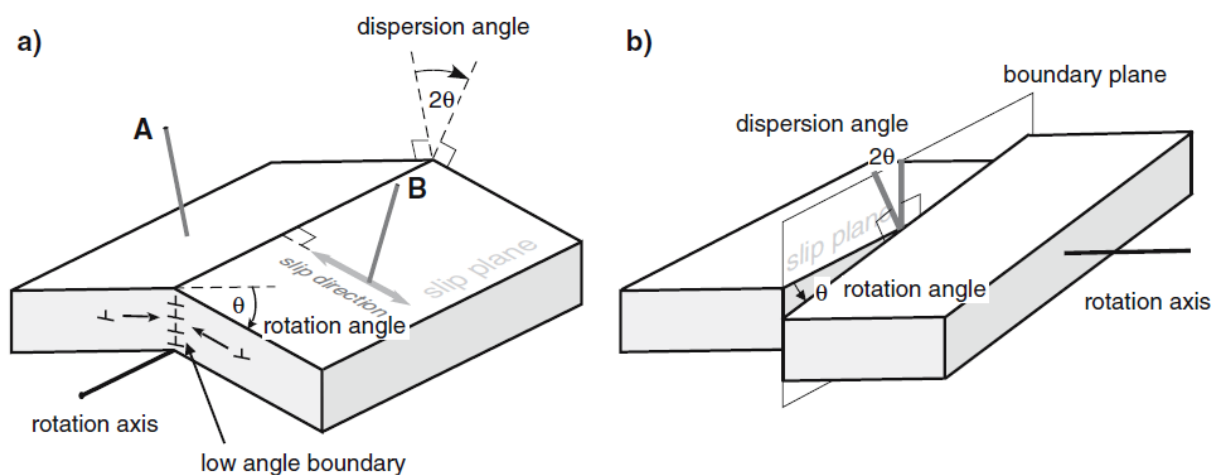


Figure 1.1. Schematic image of low angle boundaries and their components: **(a)** tilt boundary, **(b)** twist boundary. After Reddy et. al. (2007).

This work aims to better understand the processes of crystal-plastic deformation and associated trace elements re-distribution and isotopic systems resetting in zircon.

The current project is both promising and challenging. The final aim is to develop a tool for isotopic dating of high-temperature deformation events in the deep crust. As an additional result, the project aims for dating deep earthquakes. Based on the spectacular results achieved so far, future advancement of research on these topics is open and also promising.

1.1. Analytical techniques

Among analytical facilities required for this project were various scanning electron microscope techniques (SEM): secondary electron (SE), backscatter electron (BSE), electron-backscatter diffraction (EBSD) and forward scatter electron (FSE) imaging; cathodoluminescence (CL) imaging, Raman spectroscopy, several electron microprobes and nano-scale secondary ion mass spectrometry (NanoSIMS).

1.2. Goals of the project

As potential results of this work I expect to:

- Learn more about the deformation mechanisms in accessory minerals regarding temperature, the amount and direction of differential stress, host phases, and the initial properties of minerals.
- Gain better understanding of the effect of deformation microstructures on local trace element compositions.
- Gain better understanding of the effect of crystal-plastic deformation on the isotopic systems in and measured isotopic ages in accessory minerals.

1.3. Importance of the project for geosciences

The potential impact of the proposed research on geochronology and geochemistry is enormous. I try to understand the behavior of trace elements and isotopic systems in plastically-deformed individual grains and the effect of plastic deformation on mineral isotopic age and physical properties. **I believe that accurate treatment of plastically-deformed minerals, such as zircon, that were affected by rock deformation events, can open the possibility of direct dating of high-temperature deformation events** (e.g. Reddy and Timms, 2010; Timms et al., 2011). We can also

describe the effect of trace element and isotopic alteration of individual minerals on the host rock and fluid composition, which can result in mineral-fluid and mineral-host rock chemical exchange. However, we are still very far from achieving the goals and this work is still in active progress. Our understanding of trace elements and isotopic behavior in deformed mineral grains is only at the early stage and needs to be developed by further research of various samples by various methods, by collecting of a larger database from different metamorphic complexes of the world.

References

- Freeman, S.R., Inger, S., Butler, R.W.H., Cliff, R.A., 1997. Dating deformation using Rb-Sr in white mica: Greenschist facies deformation ages from the Entrelor shear zone, Italian Alps. *Tectonics*, 16, 57-76.
- Geisler, T., Pidgeon, R.T., Bronswijk, W., Kurtz, R., 2002. Transport of uranium, thorium, and lead in metamict zircon under low-temperature hydrothermal conditions. *Chemical Geology*, 19, 141–154.
- Glodny, J., Kühn, A., Austrheim, H., 2008. Diffusion versus recrystallization processes in Rb–Sr geochronology: Isotopic relics in eclogite facies rocks, Western Gneiss Region, Norway. *Geochimica et Cosmochimica Acta*, 72, 506–525.
- Kusiak, M.A., Dunkley, D.J., Słaby, E., Martin H., Budzyń, B., 2009. Sensitive high-resolution ion microprobe analysis of zircon reequilibrated by late magmatic fluids in a hybridized pluton. *Geology*, 37, 1063-1066.
- Maas, R., Kinny, P.D., Williams, I.S., Froude, D.O., Compston, W., 1992. The Earth's oldest known crust: A geochronological and geochemical study of 3900–4200 Ma old detrital zircons from Mt. Narryer and Jack Hills, Western Australia. *Geochimica et Cosmochimica Acta*, 56, 1281–1300.
- Moser, D.E., Davis, W.J., Reddy, S.M., Flemming, R.L., Hart, R.J., 2009. Zircon U–Pb strain chronometry reveals deep impact-triggered flow. *Earth and Planetary Science Letters* 277, 73–79.
- Nemchin, A., Timms, N. E., Pidgeon, R., Geisler, T., Reddy, S. M., Meyer, C., 2009. Timing of crystallization of the lunar magma ocean constrained by the oldest zircon, *Nat. Geosci.*, 2, 133-136.
- Poirier, J. P., 1985. *Creep of Crystals: High-Temperature Deformation Processes in Metals, Ceramics and Minerals*, Cambridge Earth science series, Cook, A.H., Harland, W.B., Hughes, N.F., Putnis, A., Sclater, J.G., Thomson, M.R.A., eds., Cambridge University Press, Leipzig, 260 pp..

- Reddy, S.M., Timms, N.E., Pantleon, W., Trimby, P., 2007. Quantitative characterization of plastic deformation of zircon and geological implications. *Contributions to Mineralogy and Petrology* 153, 625–645.
- Reddy, S. M., Timms, N. E., 2010. Deformation of zircon and implications for geochemistry and geochronology. *Source Abstracts with Programs - Geological Society of America* 42 (5), 634.
- Ruoff, A.L., 1967. Enhanced diffusion during plastic deformation by mechanical diffusion. *Journal of Applied Physics*, 38, 3999-4003.
- Schneider, S., Hammerschmidt, K., Rosenberg, C.L., 2013. Dating the longevity of ductile shear zones: Insight from $^{40}\text{Ar}/^{39}\text{Ar}$ in situ analyses. *Earth and Planetary Science Letters*, 369-370, 43–58.
- Timms, N.E., Kinny, P., Reddy, S.M., 2006. Enhanced diffusion of uranium and thorium linked to crystal plasticity in zircon. *Geochemical Transactions* 7, 10.
- Timms, N.E., Kinny, P., Reddy, S.M., Evans K., Clark C., Healy D., 2011. Relationship among titanium, rare earth elements, U–Pb ages and deformation microstructures in zircon: Implications for Ti-in-zircon thermometry. *Chemical Geology* 280, 33–46.
- Watson, E. B., Wark, D. A., Thomas, J. B., 2006. Crystallization thermometers for zircon and rutile. *Contributions to Mineralogy and Petrology*, 151, 413–433.
- Wawrzenitz, N., Krohe, N., Rhede, D., and Romer, R.L., 2012. Dating rock deformation with monazite: The impact of dissolution precipitation creep. *Lithos*, 134–135, 52–74.

2.0. Finite lattice distortion patterns in plastically deformed zircon grains

E. Kovaleva^{1*}, U. Klötzli¹, G. Habler¹ and E. Libowitzky²

¹ *Department of Lithospheric Research, Faculty of Earth Sciences, Geography and Astronomy, University of Vienna, Althanstrasse 14, A-1090 Vienna, Austria*

² *Department of Mineralogy and Crystallography, Faculty of Earth Sciences, Geography and Astronomy, University of Vienna, Althanstrasse 14, A-1090 Vienna, Austria*

**Corresponding author. Tel.: +43-1-4277-53462; E-mail: elizaveta.kovaleva@univie.ac.at*

Solid Earth, 5, 1099-1122, 2014.

Abstract

This study examines finite deformation patterns of zircon grains from high-temperature natural shear zones. Various zircon-bearing rocks were collected in the Western Tauern Window, Eastern Alps, where they were deformed under amphibolite facies conditions, and in the Ivrea-Verbano Zone (IVZ), Southern Alps, where deformation is related with granulite-facies metamorphism. Among the sampled rocks are: granitic orthogneisses, meta-lamprophyres and paragneisses, all of which are strongly deformed.

The investigated zircon grains ranging from 10 to 50 μm were studied in situ using a combination of scanning electron microscope (SEM) techniques, backscattered electron (BSE), forward scattered electron (FSE), cathodoluminescence (CL) imaging, and crystallographic orientation mapping by electron backscatter diffraction (EBSD), as well as micro-Raman spectroscopy. Energy-dispersive X-ray spectrometry (EDS) was applied to host phases.

Microstructural analysis of crystal-plastically deformed zircon grains was based on high-resolution EBSD maps. Three general types of finite lattice distortion patterns were detected: Type (I) is defined by gradual bending of the zircon lattice with orientation changes of about 0.6° to 1.4° per μm without subgrain boundary formation. Cumulative grain-internal orientation variations range from 7° to 25° within single grains. Type (II) represents local gradual bending of the crystal lattice accompanied by the formation of subgrain boundaries that have concentric semicircular shapes in 2D sections. Cumulative grain-internal orientation variations range from 15° to 40° within single grains.

Type (III) is characterized by formation of subgrains separated by a well-defined subgrain boundary network, where subgrain boundaries show a characteristic angular closed contour. The cumulative orientation variation within a single grain ranges from 3° to 10°. Types (I) and (II) predominate in granulite facies rocks, whereas type (III) is restricted to the amphibolite facies rocks. The difference in distortion patterns is controlled by strain rate and by ratio between dislocation formation and dislocation motion rates, conditioned by the amount of differential stress.

Investigated microstructures demonstrate that misorientation axes are usually parallel to the <001> and <100> crystallographic directions; dominant slip are <010>{001}, <010>{100} and <001>{010}, whereas in some grains cross-slip takes place. This study demonstrates that activation of energetically preferable slip systems is facilitated if zircon grain is decoupled with the host matrix or/and hosted by a soft phase.

Keywords: crystal-plastic deformation, electron backscatter diffraction (EBSD), misorientation axis, slip system, subgrain boundary, zircon.

2.1. Introduction

2.1.1. Zircon and its significance in geosciences

Zircon is one of the most stable, and abundant accessory phases in many rock types. Due to its chemical stability and ability to incorporate and preserve radioactive uranium and rare earth elements (REE) zircon is widely used for isotopic mineral dating (e.g. Davis et al., 2003; Klötzli et al., 2014), for the geochemical characterization of its forming environment (e.g. Hofmann et al., 2009; Nemchin et al., 2009; Erdmann et al., 2013), as well as for the estimations of (re)crystallization temperature (Watson et al., 2006). Volume diffusion of Pb and Ti cations in a pristine zircon crystal is usually insignificant through-out the geological history, which allows us to estimate the timing and temperature of mineral formation. For example, at 850 °C, a volume diffusion length of 5 µm would require about 10 million years for Pb, 1 billion years for Dy, and tens of billions of years for Ti (Cherniak and Watson, 2003). However, at lower temperatures, other mechanisms of enhanced diffusion have been documented in natural samples, especially so-called “Pb loss”, which is not consistent with experimental predictions for volume diffusion (e.g. Geisler et al., 2002). In the past, the common explanation for low-temperature diffusion in zircon was the effect of self-irradiation that causes metamictization and thus induces/enhances volume diffusion (Cherniak et al., 1991;

Cherniak and Watson, 2003). Recently, a number of authors have found evidences for increased trace element diffusion in zircon due to crystal-plastic deformation (Erickson et al., 2013a, 2013b; Flowers et al., 2010; Grange et al., 2013; Kaczmarek et al., 2011; MacDonald et al., 2013; Moser et al., 2009, 2011; Nemchin et al., 2009; Piazzolo et al., 2012; Reddy et al., 2006, 2007, 2009; Reddy and Timms, 2010; Schwartz et al., 2010; Timms and Reddy, 2009; Timms et al., 2006, 2011, 2012a, 2012b). These authors have shown that crystal-plastic deformation can dramatically affect the content of trace elements in zircon domains and, therefore, can cause isotopic system resetting. Deformation microstructures such as, for example, subgrain boundaries, formed by dislocation creep and recovery, may act as fluid migration and fast element-diffusion pathways that cause local variations in the chemical and isotopic compositions of grains (Timms et al., 2006, 2011). So far there were only a few documentations of these phenomena presented in the literature mentioned above, but it has already been clearly demonstrated that crystal-plastic deformation of zircon affects the interpretation of radiometric age data (e.g. Reddy et al., 2007; Timms et al., 2011; 2012a; Grange et al., 2013). Therefore it is crucial to decipher the controlling mechanisms and general features of zircon lattice distortion that may cause enhanced material transport through the crystal. The current study aims to classify and characterize different finite crystal-plastic deformation patterns of zircon found in natural rocks by comparing samples from different metamorphic environments and from various associations of host phases.

2.1.2. Targeted material

Many of the previous detailed microstructural analyses on crystal-plastic deformation of zircon crystals have focused on comparatively large zircons, from 2 hundreds of micrometers up to few millimeters in length, some of them from uncommon occurrences like impact basin (Moser et al., 2009, 2011); zircon-rich vein within meta-anorthositic body (Piazzolo et al., 2012); olivine gabbro derived from the ocean ridge (Reddy et al., 2006, 2007; Timms and Reddy, 2009); or xenolith from kimberlitic pipe (Timms et al., 2011). Other studies were focused on more widespread rock types and smaller zircons grains, less than 100 μm in length (Flowers et al., 2010; Kaczmarek et al., 2011; MacDonald et al., 2013; Reddy and Timms 2010; Schwartz et al., 2010; Timms et al., 2012b). In addition, some of the studies examined embedded zircon grains that were extracted from the sample by heavy mineral separation (e.g. Kaczmarek et al., 2011; Moser et al., 2011; Reddy et al., 2009; Schwartz et al., 2010; Timms and Reddy, 2009; Timms et al., 2006). During the conventional procedure of extracting larger grains by classical mineral separation techniques the context of host minerals and the immediate environment is lost, which restricts interpretations and conclusions.

Furthermore, deformed grains may be selectively destroyed during sample crushing and sieving. However, for the last years there is a growing number of works appeared that also study crystal-plastically deformed zircons in situ (e.g. Kaczmarek et al., 2011; McDonald et al., 2013; Piazzolo et al., 2012; Timms et al., 2011). Following this trend, the current work presents new microstructural data from crystal-plastically deformed zircon grains from common lithologies, where zircon grain-sizes range from 10 to 50 micron in length. As this is a very common grain-size of zircon in natural rocks (Silver and Deutsch 1963; Corfu et al., 2003; MacDonald et al., 2013), the data and resulting systematics are expected to be representative for the majority of zircons from various geological environments. All presented analyses were derived from thin sections of rock samples, allowing microstructural interpretations in host mineral context. The crystallographic orientation of mineral grains or grain domains was analyzed by electron backscatter diffraction (EBSD). This technique provides data at sub-micron scale spatial resolution and allows in-situ examination of a few to tens of micrometers sized grains.

2.1.3. Crystal-plastic deformation

A single crystal exposed to shear stresses deforms elastically at the initial deformation stage, but if the applied shear stresses exceed the elastic limit, geometrically necessary dislocations (GNDs) are generated in the lattice in order to accommodate the strain (Nye, 1953; Wheeler et al., 2008; Dahlberg et al., 2014). Crystal-plastic deformation of individual crystals is assumed to be a consequence of formation and motion of dislocations (lattice line-defects) caused by differential stress (Drury and Urai, 1990; Poirier, 1985; Timms et al., 2011). Migration of dislocations by climb is a thermally activated process; migration by glide is a stress-induced process; at tectonic conditions that allow dislocations to move through the crystal lattice, the crystal deforms plastically by slip along a densely packed crystallographic plane. Slip direction $[uvw]$ and slip plane (hkl) are described by Miller indices and define a slip system $[uvw](hkl)$ (Poirier, 1985). During recovery dislocations migrate and accumulate within so-called “dislocation walls” or “subgrain boundaries” or “low-angle boundaries” (e.g. Jenkins and Mellor, 1935; McLean, 1952; Sellars, 1978; Urai et al., 1986). Arrays of edge dislocations with the same Burgers vector form tilt walls, whereas arrays of screw dislocations form twist walls. All symmetrically equivalent crystallographic directions and planes which are orthogonal may represent valid glide systems (Roters et al., 2010). For zircon that has tetragonal symmetry, considering two equivalent directions $[100]$ and $[010]$, two relevant orthogonal active glide systems are $[100](010)$ and $[010](100)$ (e.g. Leroux et al., 1999; Reddy et al., 2007; Kaczmarek et al., 2011;). These two relevant glide systems could be labeled as one slip system $\langle 100 \rangle \{010\}$.

2.1.4. Motivation and challenge

This study contributes to basic issues of crystal-plastic deformation mechanisms in zircon. Based on microstructural observations of deformed zircon grains in association with the rock matrix of meta-igneous and meta-sedimentary rocks the following questions were addressed: Is crystal-plastic deformation of zircon related to dissolution-precipitation in fluid presence? Are there differences in zircon behavior in various rock types and at differing metamorphic grade? How do the specific shape and internal heterogeneities of a zircon grain influence its deformation behavior? Which misorientation axes and active slip systems are most common in deforming zircon grains? Does the orientation of the zircon lattice with respect to the external stress field influence the crystal-plastic deformation pattern? How does the nature and microstructure of the local environment (surrounding host phases and adjacent matrix phases) affect the finite deformation pattern of zircon? Which parameters define whether deformed zircon develops a low-angle boundary network or not?

Based on our observations we have classified finite deformation patterns of crystal-plastically deformed zircons, have discussed local conditions that facilitate crystal-plastic deformation, and possible reasons that define the variety of distortion patterns.

2.2. Geological environment

General information about samples and presented zircon grains is given in Table 2.1. Samples were collected from shear zones in two study areas: (1) western Tauern Window, Eastern Alps (amphibolite facies metamorphic grade), and (2) Ivrea-Verbano Zone, Southern Alps (granulite facies metamorphic grade).

2.2.1. Western Tauern Window, Eastern Alps (Zillertal, Tyrol, Austria), amphibolite facies metamorphic grade

In the Tauern Window (Eastern Alps), continental and oceanic rocks of the Penninic and sub-Penninic nappe sequences are exposed, which represent the footwall of the Austroalpine nappe

stack. Nappe stacking and predominant metamorphism are related to the closure of the Alpine Neotethys and subsequent continental collision in late Cretaceous-Tertiary (Miller et al., 2007). Samples for the present research were collected from the “Zillertaler Kern” lobe of the “Zentralgneis” formation (see Selverstone et al., 1991 and reference therein).

The magmatic protholiths of the "Zentralgneis" formation are uppermost Devonian to lower Permian in age. Three magmatic “pulses” of potassium-rich and calc-alkaline granites, felsic and intermediate volcanites and tonalitic/granodioritic plutonites can be distinguished (Veselá et al., 2011). The granitoids intruded into pre-Carboniferous, partly poly-metamorphic basement rocks consisting of various schists, para- and orthogneisses, amphibolites and meta-ophiolites. In the Zillertal section Variscan amphibolite facies regional metamorphism has been overprinted at amphibolite-facies metamorphic conditions of 0.5-0.7 GPa and 550-600 °C at ca. 30 Ma with subsequent greenschist-facies metamorphism (Selverstone, 1985; Pennacchioni and Mancktelow, 2007). Metamorphic (re)crystallization was accompanied by the formation of ductile shear zones (Pennacchioni and Mancktelow, 2007). The sampled shear zones 1 and 2 (see description below) found to the east of Berliner Hütte, presumably formed during this latter tectono-metamorphic event.

Shear zone 1 (47°01'39.308"N latitude, 11°50' 3.669"E longitude to 47°01'39.987"N latitude, 11°50'6.311"E longitude). The ~50 m thick ductile shear zone is exposed on the NE slope of the Zemmbach side valley (Sturm and Steyrer, 2003). The shear zone represents strongly foliated quartz-biotite orthogneiss (samples BH12-01-I and BH12-02) containing mylonitic layers (sample BH12-01-II) that are leucocratic and depleted in mafic minerals compared to the gneiss. The strongly foliated gneiss is enriched in biotite and white mica (Fig. 2.1a). The host rock of granitic composition is weakly foliated (sample BH12-04) and crosscut by leucocratic veins.

Shear zone 2 (47°01'18.129"N latitude, 11°50'26.709"E longitude). A strongly foliated quartz-biotite orthogneiss (sample BH12-06-I and -II) hosts two adjacent deformed dykes, a leucocratic aplitic dyke (sample BH12-08) and a melanocratic, presumably metalamprophyric dyke (sample BH12-07), as it is shown in the Figure 2.1b. The leucocratic dyke (sample BH12-08) shows thickness variations from 20 cm to 1.5 m and locally presents a cusate-lobate structure along the lithological contact 1 (Fig. 2.1b, arrow). Within aplitic dyke at hand specimen scale garnets, large green K-feldspar clasts, quartz veins and mica-rich thin layers are distinguishable. On the lower contact (contact 2, Fig. 2.1b) with the leucocratic dyke, gneiss is intruded by the mafic dyke (sample BH12-07). Mafic dyke is strongly foliated and folded and apparently accommodate the highest strain intensity representing the weakest lithology in the sequence. Quartz-biotite gneiss in contact with

the mafic dyke (contact 3, Fig. 2.1b) is also strongly foliated (BH12-06-l). The high-strain zone in gneiss adjacent to contact 3 is about 1 meter thick, whereas next to the contact 1 with the aplitic dyke, the gneiss is less foliated (sample BH12-05) and the shear zone is narrower (~10 cm).

2.2.2. Ivrea-Verbano Zone, Southern Alps (Forno, Val Strona, Northern Italy), granulite facies metamorphic grade

The Ivrea-Verbano Zone (IVZ) consists of a NE-SW trending, steeply dipping sequence of meta-sedimentary and meta-igneous basic rocks, ultrabasic mantle tectonites and a large underplated igneous complex. The sequence consists of predominant metasedimentary rocks in the SE and prevailing metabasic rocks and strongly depleted metapelites in the NW. Metamorphism increases progressively from amphibolite facies in the SE to granulite facies in the NW. The Ivrea-Verbano Zone is supposed to represent a section through the lower continental crust that experienced regional metamorphism during the uppermost Palaeozoic (Rutter et al., 2007; Quick et al., 2009) and then exhumed towards the upper crust.

Within the Ivrea-Verbano Zone a network of high-temperature shear zones, which are subparallel to the NE-SW elongation direction of the IVZ are observed. The shear zone network extends from Anzola (Val d'Ossola) to Forno (Val Strona) and can be traced for more than 20 km in length (Brodie et al., 1992). Single shear zones range in width from a few centimeters to more than 10 meters, and are rarely as much as 200 meters thick. Mylonites in the northern part of the Ivrea-Verbano zone completely (re-)equilibrated under granulite-facies conditions prevailing during crustal attenuation/extension and contemporaneous magmatic underplating (Rutter et al., 2007) between 315 Ma and 270 Ma (Rutter et al., 2007, Quick et al., 2009, Sinigoi et al., 2011). In the Val d'Ossola section at Cuzzago peak P-T estimates are 0.6-1.0 GPa and > 800 °C, based on the peak P-T estimates from the neighboring Val Strona di Omegna (Redler et al., 2012).

Shear zone 3 (45°59'45.64"N latitude, 8°21'38.75"E longitude): The sampling locality near the village of Cuzzago (Val d'Ossola) shows non-foliated metasedimentary granulite-facies rocks, locally known as stronalites (sample IV12-06C). Stronalites are crosscut by discordant layer of sillimanite-biotite-garnet gneiss, that is considered to be a restitic material from partial melting of metapelite (Barboza et al., 1999). Sample material was taken from a several meters thick non-foliated metasediments (Fig. 2.1c). At the outcrop scale this rock locally has a compositional layering, which is folded.

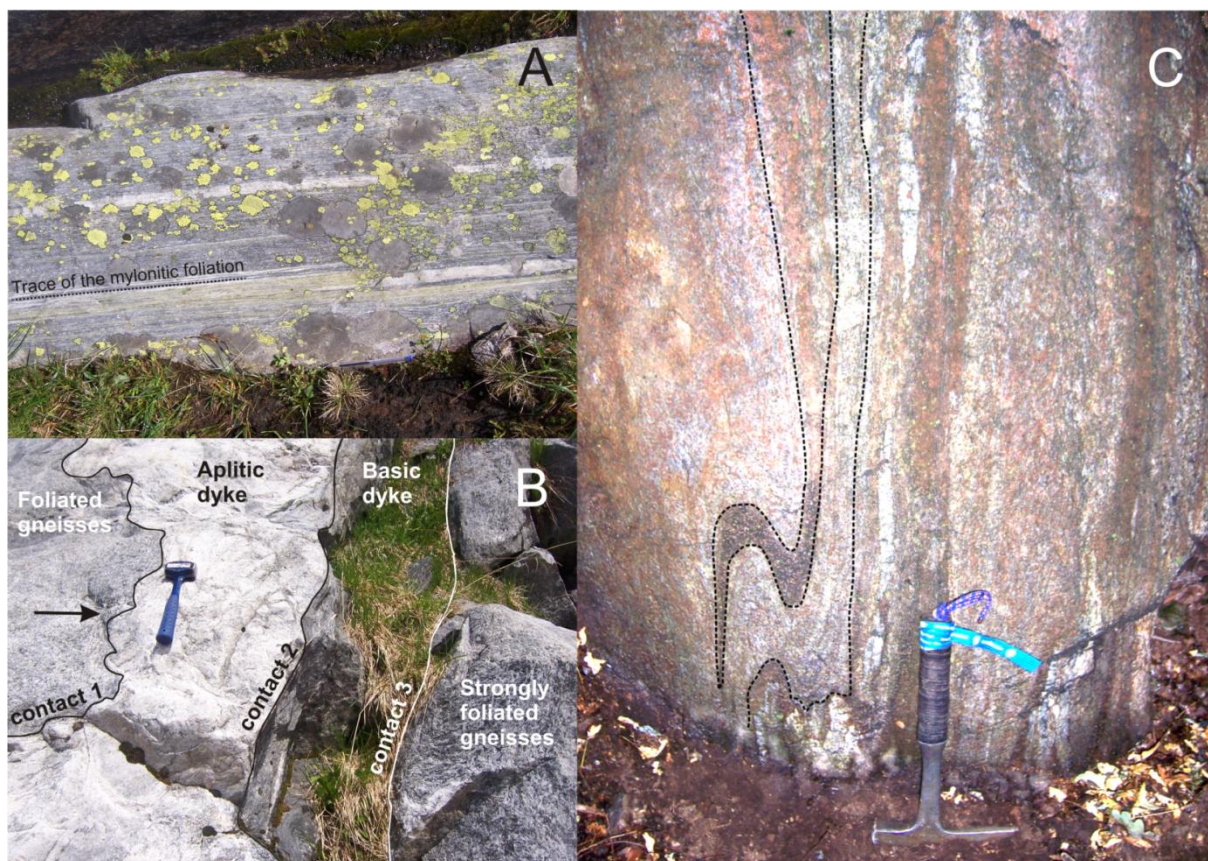


Figure 2.1. Outcrop photographs. **(a)** Shear zone 1 in orthogneiss with strong mylonitic foliation. **(b)** Shear zone 2 with two dykes hosted by granitic gneiss. Contact 1 shows a cuscate-lobate structure (black arrow). **(c)** Shear zone 3, hosting strongly-deformed and folded stromalite. Folds of compositional layering are highlighted by the dashed black lines.

2.3. Analytical methods and data representation

2.3.1. Samples preparation

Zircons were examined in-situ using polished thin sections, mechanically prepared with 0.25 μm diamond paste and subsequently chemically polished with alkaline colloidal silica solution (Köstrosol 3530; pH 9.2-10) on an active rotary head polishing machine for 4 hours. Samples were cleaned in ethanol and distilled water before carbon coating (2 carbon-threads for SEM- BSE and CL imaging, 1 carbon thread for FSE and EBSD analysis) to establish electrical conductivity.

Thin sections were cut parallel to x-z plane (normal to foliation and parallel to lineation), however, it is not always exactly so, for example, for the sample BH12-07 stretching lineation is oblique at about 45-50° to the thin section cut.

2.3.2. Scanning electron microscopy and cathodoluminescence (CL) imaging

All zircons were identified and characterized by backscattered-electron (BSE) and cathodoluminescence (CL) imaging in order to identify the internal microstructures, select areas for FSE imaging, EBSD and Raman analysis and to investigate the host mineral phases, using an FEI Inspect S scanning electron microscope equipped with a Gatan MonoCL system. Imaging conditions were at 10 kV accelerating voltage, CL-image resolution of 1500*1500 to 2500*2500 pixels using a dwell time of 80.0-150.0 ms and probe current/spot size 4.5-5.0.

2.3.3. Electron Backscatter Diffraction (EBSD) analysis and Forescattered electron (FSE) imaging

Zircon grains were examined for potential crystal-plastic deformation structures using orientation contrast images (Trimby and Prior, 1999; Prior et al., 1999). These were taken using a forescattered-electron detector (FSD) mounted on the EBSD-tube of an FEI Quanta 3D FEG instrument (Center of Earth Sciences, University of Vienna, Austria), which is equipped with a Schottky field emission electron source. Electron beam conditions were 15 kV accelerating voltage, 2.5-4 nA probe current using the analytic mode. Stage settings were at 70° tilt and 14-16 mm working distance. After identification of the potentially deformed grains, EBSD orientation mapping was applied to selected zircon grains. The FEI Quanta 3D FEG instrument is equipped with an EDAX Pegasus Apex 4 system consisting of a Digiview IV EBSD camera and an Apollo XV silicon drift detector for EDX analysis. EDX intensities and EBSD data were collected contemporaneously using the OIM data collection software v6.21. Orientation maps were obtained from beam scanning in hexagonal grid mode at step sizes of 0.1 – 0.16 micrometer.

The raw indexing for the entire EBSD maps, including zircon and host phases varies from 70% to 99,7%, depending on the host phase; raw indexing for zircon grains is more than 99,99%. In some cases, after EBSD data collecting the maps were recalculated based on chemical composition of phases with the OIM v6.21 software.

The EBSD data are represented in the sample reference frame and presented in two mapping modes. The first mapping mode is false color-coded misorientation maps, with colors showing the relative angular misorientation of each data point with respect to a user-selected single reference point within the grain (indicated by a red marker); the second mode is local misorientation maps, where each pixel is colored according to the mean misorientation of the respective data point relative to the neighboring points. The orientations of the crystallographic axes are plotted as lower hemisphere equal area projections and are color-coded according to the corresponding EBSD map of the first mapping mode. The data is usually shown for the whole mapped area of zircon grain, if subareas of interest are not specifically indicated. The first mode of maps and pole figures were produced using the EDAX OIM Analysis software v6.2.1, whereas the second mode of misorientation maps (local misorientation maps) were generated with the MTEX toolbox for MATLAB (Bachmann et al., 2010; Bachman et al., 2011; Mainprice et al., 2011). We used MTEX toolbox for plotting histograms of misorientation angles between datapoints as well as for visualizing the misorientation axis orientation and density contours in inverse pole figures.

The (sub)grain boundaries are visible in 2D sections as lines, and their traces are characterized by 200-500 nm wide linear features displayed as low-contrast EBSD pattern data points in the image quality map. We consider misorientation angles between neighboring subgrains ranging from 1 to 10° to form low-angle boundaries, and higher than 10° to be high-angle boundaries, as in Piazzolo et al. (2012).

2.3.4. Raman spectroscopy

Raman spectra were acquired on a confocal edge filter-based Renishaw RM1000 micro-Raman system equipped with a 50 mW multimode Ar⁺-laser (using the 488 nm emission at ~ 20 mW), a 1200 lines/mm grating, and a thermo-electrically cooled CCD detector. Raman intensities were collected with a Leica DMLM microscope with 50x/0.75 or 100x/0.90 objectives. These settings resulted in a spectral resolution of ~ 4 cm⁻¹ and a spatial resolution of better than ~ 3 μm. Spectra were recorded for 30 s in the range from -50 cm⁻¹ (to get also the Rayleigh line at 0 cm⁻¹ for internal calibration) to 1580 cm⁻¹. Instrument control and basic data processing was done with Grams32 software (Galactic Industries Corp., 1996). Exact peak positions and peak widths (FWHM = full width at half maximum) were extracted (after shift correction according to the Rayleigh line) with the software PeakFit 4.12 (SeaSolve Software Inc., 1999-2003).

Raman analyses were used to compare the degree of crystallinity in various zircon grain domains. For this goal a color-coding scale, based on the range of degree of crystallinity of all analyzed spots was created. The data points are superimposed as colored dots on CL images.

2.4. Petrography and zircon content

The accessory minerals in lithological descriptions are listed in order from least to most abundant. Microstructural data of zircons from the Tauern Window are shown in Figures 2.2-2.9 and 1.13, from the Ivrea-Verbano zone in Figures 2.10-2.12 and 2.13. The zircon grain numbers with general information about the sample and shear zone number is presented in Table 2.1.

2.4.1. Shear Zone 1

Data on zircons from shear zone 1 are presented in Figures 2.2, 2.6-2.8.

Sample BH12-01-II was collected from an ultramylonitic layer that represents the core of the shear zone and has a sharp contact with the host gneiss even at thin section scale. The ultramylonitic layer is composed of a fine grained, recrystallized plagioclase-quartz matrix (grain size: 70-300 μm in diameter, > 95 vol. % of the layer), with minor modal content of biotite, white mica and epidote (<5 % in total), which form a weak foliation. Along plagioclase phase boundaries K-feldspar veins a few micrometers thick occur. Zircon, apatite, and titanite are common accessory minerals. Zircon forms small (5-20 μm in diameter) rectangular grains, with aspect ratios from 1:1 to 1:3. The zircon crystals are characterized by a dark CL-signal in the core and a bright thin outer rim (Fig. 2.6b), where core has relatively low degree of crystallinity, according to Raman spectroscopy. Two grains from this zone have been analyzed by EBSD, and one grain exhibits finite crystal-plastic deformation.

The gneiss from shear zone 1 contains plagioclase, quartz, a large amount of biotite and white mica, as well as K-feldspar veinlets. Biotite is locally replaced by association of titanite, chlorite, quartz and epidote. The even or sigmoidal foliation is represented by leucocratic layers of plagioclase-quartz and layers consisting of plagioclase, quartz, biotite, white mica and epidote. In some domains the foliation is defined by pure mica bands. Zircons in this sequence have 2 to 50 μm grain size and are hosted by plagioclase or biotite grains, sometimes associated with epidote and apatite. The smaller non-deformed grains show oscillatory and sector zoning which is truncated by recrystallization zones or marginal overgrowths, which both appear bright in CL-images (Fig. 2.2b).

The largest grains fragmented with rotation of fragments and sometimes fragments are dispersed in the matrix (Fig. 2.8).

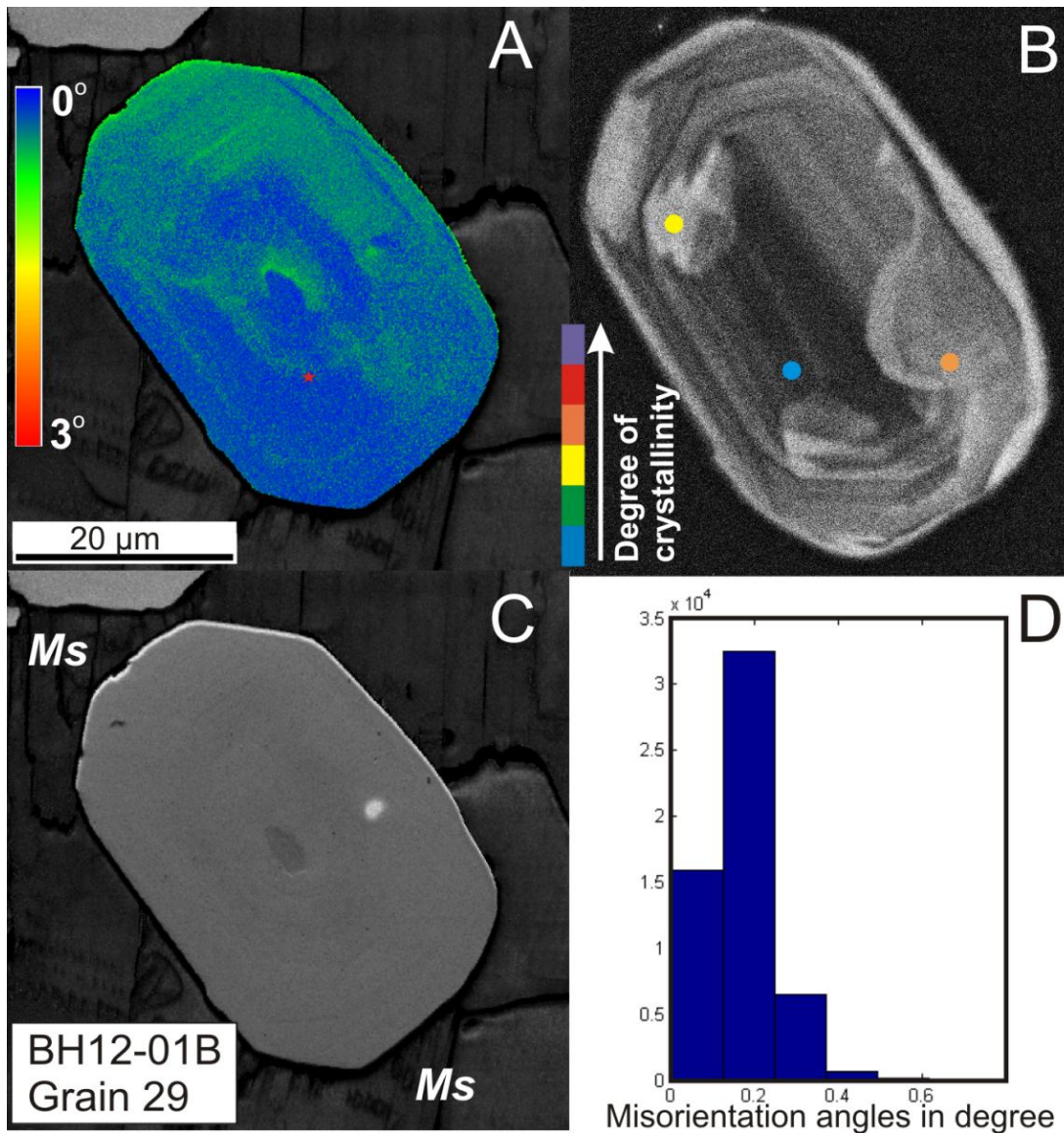


Figure 2.2. Grain BH12-01B_29, no deformation-related lattice distortion observed. **(a)** EBSD map color coded for zircon misorientation (blue – red = 0 – 3 degrees) of each pixel relative to a reference point (red star marker). **(b)** CL image with colored points representing relative degrees of crystallinity, measured by Raman spectroscopy. **(c)** EBSD pattern quality map, *Ms* = muscovite. **(d)** Histogram of the distribution of misorientation angles between neighboring data points.

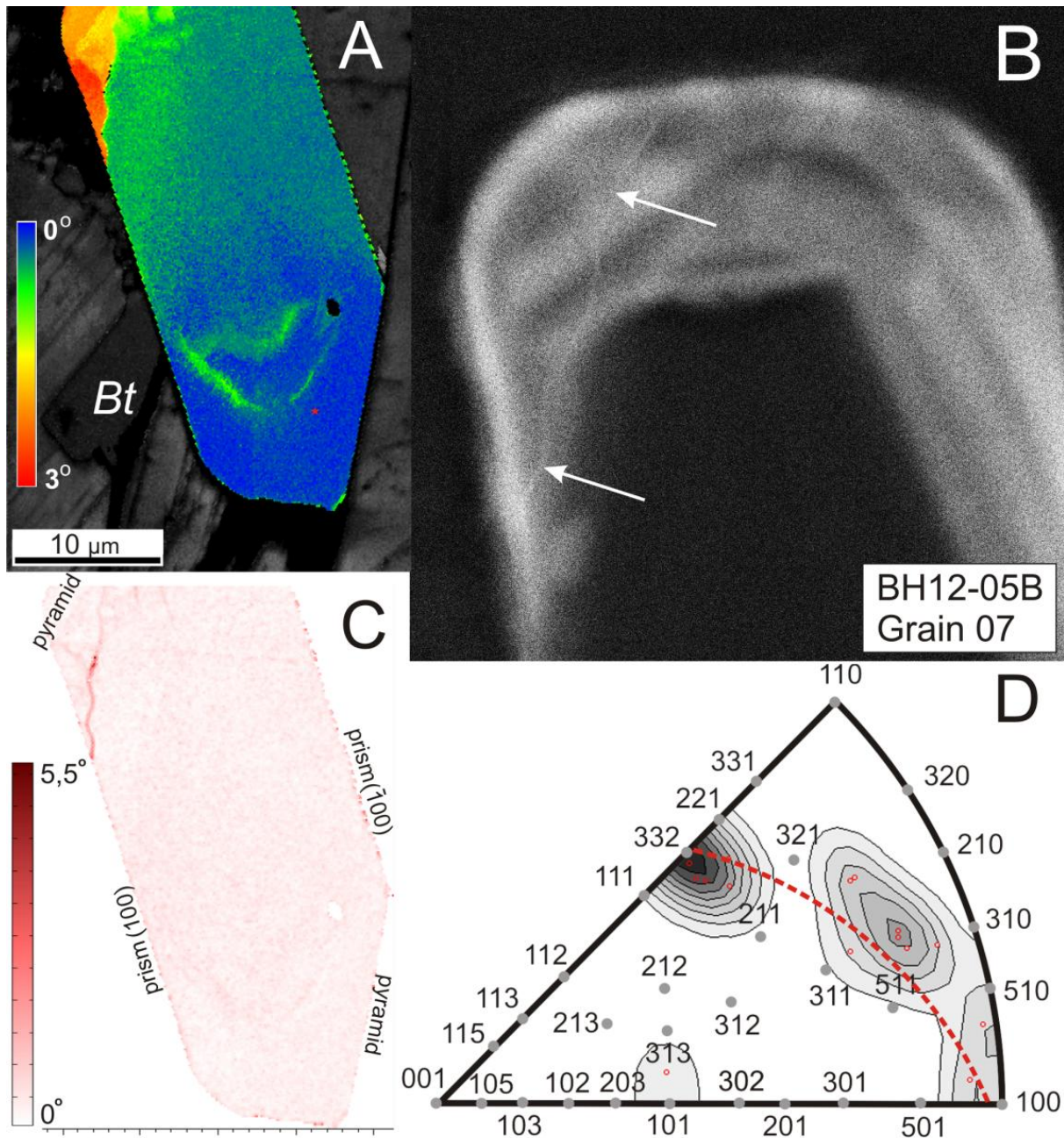


Figure 2.3. Grain BH12-05B_07, lattice distortion type (III) case 1. **(a)** EBSD map color coded for zircon misorientation with respect to a reference point (red star marker), *Bt* = biotite; **(b)** Detailed CL image of the upper part of the grain, bright trace (marked by white arrows) corresponds to subgrain boundary; **(c)** EBSD map of zircon that shows the orientation changes between neighboring data points (“local misorientation”), labels indicate families of crystallographic faces; **(d)** Inverse pole figure plot of the misorientation axes distribution density comprising the positions of misorientation axes (small red circles), crystallographic directions (gray dots) and the great circle formed by the misorientation axes (dashed red line).

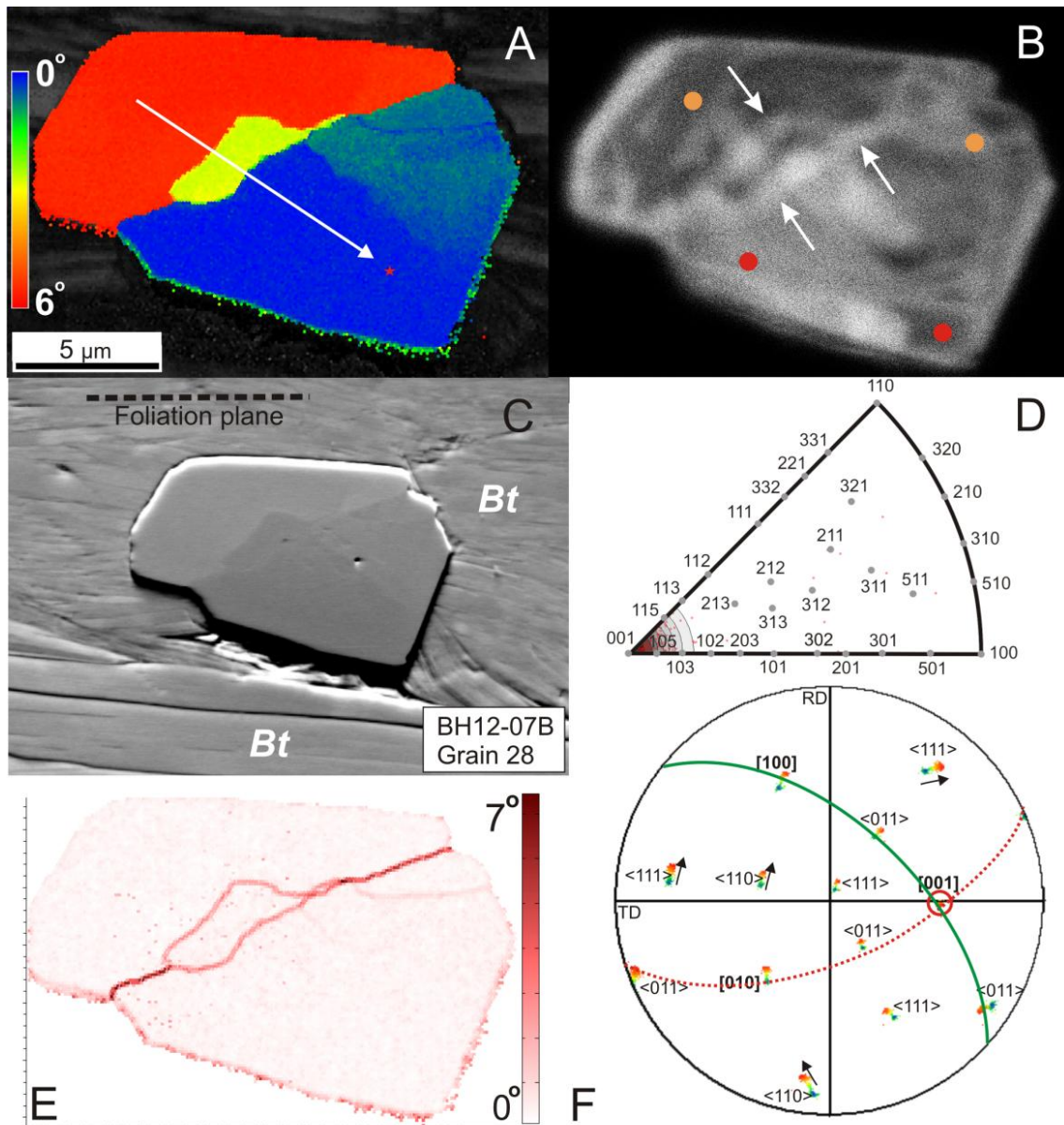


Figure 2.4. Grain BH12-07B_28, lattice distortion type (III) case 2. **(a)** EBSD map color coded for zircon misorientation with respect to a reference point (red star marker). The white arrow corresponds to the misorientation profile shown in Fig. 2.13c; **(b)** CL image, the bright lines (marked by white arrows) correspond to the subgrain boundaries, colored points represent relative degree of crystallinity, color coding is as in Fig. 2.2b; **(c)** Forescatter electron (FSE) image, *Bt* = biotite. **(d)** Inverse pole figure plot with the distribution density of misorientation axes shows concentration around zircon [001]. **(e)** EBSD map of zircon showing the misorientation between neighboring data points; **(f)** Pole figure plot showing zircon crystal directions (lower hemisphere equal area projection) color coded as in a. Labels indicate the crystallographic directions. Black arrows show scattering of axes due to rotation about zircon [001] (red circle). The dashed red line shows the orientation of the subgrain boundary, the solid green line indicates the slip plane orientation.

Samples BH12-01-I and BH12-02 – 04 are granitic gneisses with varying degrees of deformation. Sample BH12-01-I was taken adjacent to ultramylonitic strongly foliated muscovite-biotite gneiss. Sample BH12-02 exhibits lower deformation intensity than the BH12-01 series. Sigmoidal clasts of plagioclase and quartz in the mylonitic gneiss of sample BH12-02 show top to WSW sense of shear. Samples BH12-03 and BH12-04, collected from the host rock of shear zone 1, are weakly deformed, non-foliated or weakly-foliated granitic orthogneisses. A schematic histogram of shear zone 1 showing statistics on cataclastically and plastically deformed grains is presented in Fig. 2.14a.

2.4.2. Shear Zone 2

Data on zircons from the shear zone 2 are presented in Figures 2.3-2.5, 2.9 and 2.13.

Sample BH12-05 has no clear foliation and contains large, up to 1 cm sized irregular-shaped clusters of biotite grains without shape preferred orientation. The sample contains several, variably oriented small-scale paired shear zones (Pennacchioni and Mancktelow, 2007) adjacent to epidote veins. Samples BH12-05 – 06 are biotite gneisses, compositionally close to samples BH12-01 – 04. Sample BH12-06-I is a strongly foliated gneiss whereas BH12-06-II represents a biotite gneiss with sigmoidal foliation. Zircon grain size in these lithologies varies from 10 to 100 μm , with most grains having euhedral shape and oscillatory and sector zoning (Fig. 2.3b). Some of them represent the fragments of larger preexisting grains.

Sample BH12-07 was collected from a mafic dyke. As the softest lithology in the overall inhomogeneous sequence, the mafic dyke accommodated the highest strain. The sample is chlorite-rich (>50% modal content) due to intense retrogression of biotite. The sample is composed of mafic layers consisting of chlorite, biotite and titanite, with an average thickness of 1-6 mm. Mafic layers alternate with fine grained plagioclase-quartz layers of the same thickness range. The compositional layering is isoclinally folded. The accessory minerals are calcite, pyrite, zircon, rutile and titanite. Zircon is present as small (10-30 μm) euhedral grains with degraded CL-zonation. Small xenocrystic cores and oscillatory-zoned rims are sometimes distinguishable in the CL images (Fig. 2.5b).

Sample BH12-08 is taken from the aplitic dyke. The rock is almost non-foliated and contains only a small fraction of crystal-plastically deformed zircon grains (8%), none of those are presented in this paper.

A schematic histogram of shear zone 2 showing statistics on cataclastically and plastically deformed grains is presented in Fig. 2.14c.

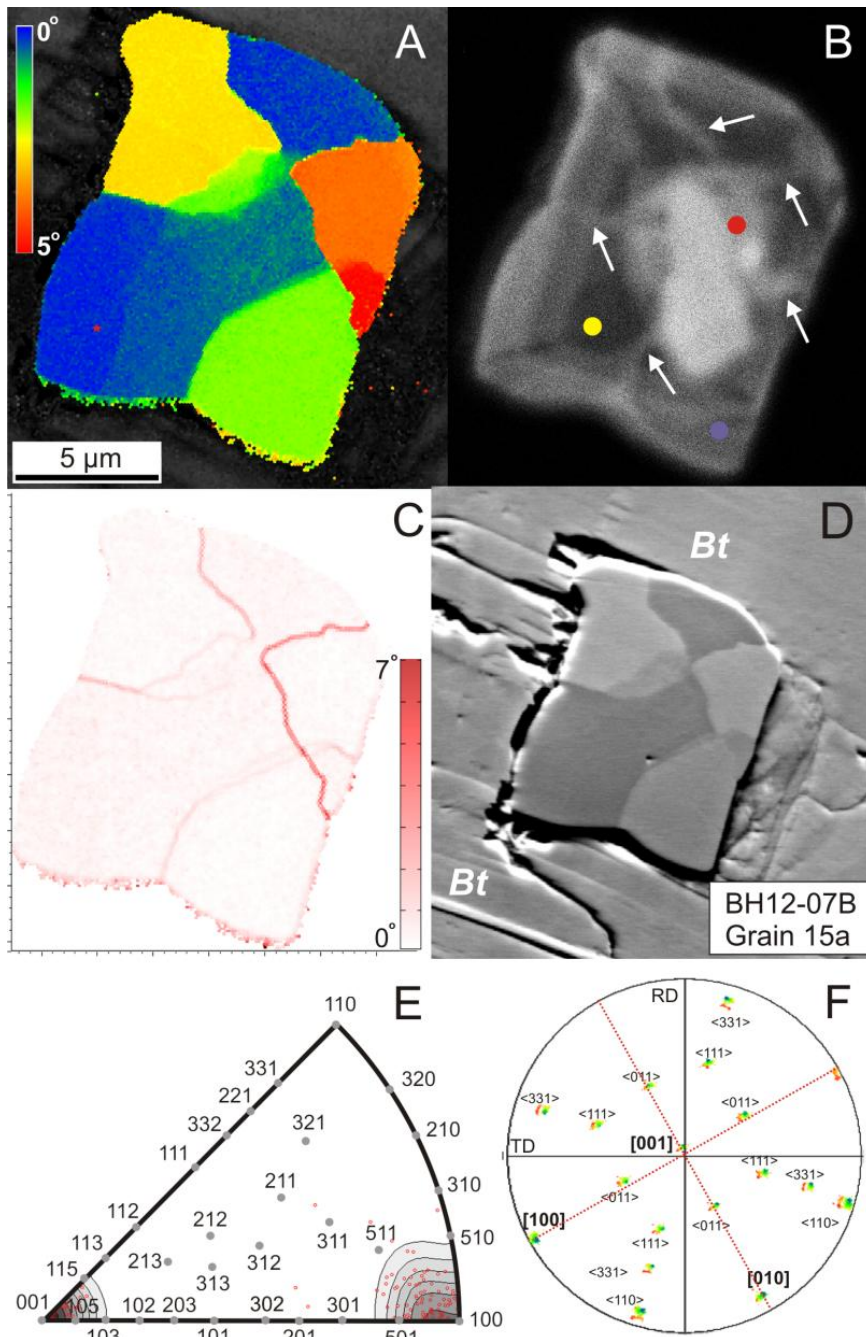


Figure 2.5. Grain BH12-07B_15a, lattice distortion type (III) case 2. **(a)** EBSD map color coded for zircon misorientation with respect to a reference point (red star marker); **(b)** CL image; bright traces (marked by white arrows) correspond to subgrain boundaries, colored dots represent the relative degree of crystallinity, color coding as in Fig. 2.2b; **(c)** EBSD map of zircon showing the misorientation between neighboring data points; **(d)** orientation contrast image (FSE), *Bt* = biotite. **(e)** Inverse pole figure plot of the distribution density of misorientation axes shows concentrations around $\langle 001 \rangle$ and $\langle 100 \rangle$. **(f)** Pole figure plot showing zircon crystal directions (lower hemisphere equal area projection) colored as in a. Labels indicate the crystallographic directions. Dashed red lines show the subgrain boundary orientations.

Within shear zones 1 and 2, the initial amphibolite-facies paragenesis is locally replaced by mineral phases that are characteristic for greenschist-facies metamorphic conditions. The association of plagioclase + quartz + biotite is decomposing to K-feldspar + albite + epidote + Al-titanite \pm calcite \pm rutile. Local chlorite-pseudomorphs after biotite supposedly represent a retrograde greenschist-facies stage of metamorphism. K-feldspar-, calcite- and epidote-rich veins as well as some dissolved zircon surfaces and healed fractures decorated by inclusion trails, are evidence of intense fluid infiltration.

2.4.3. Shear Zone 3

Data on zircons from the shear zone 3 are presented in Figures 2.10-2.13. A schematic histogram with statistics on shear zone 3 is presented in Fig. 2.14b.

Sample IV12-06C is representative of shear zone 3 from the Ivrea-Verbano zone. It is a massive rock, consisting of large garnet grains (0.5-5 mm in diameter) that are fractured and have an irregular shape. Locally garnet forms aggregates of smaller grains sized from 40 to 80 μm that form a foliation pattern. The space between the garnet clasts is filled with Mg-rich biotite (phlogopite), quartz and plagioclase. These phases occur in two grain sizes: 100-250 μm and below 10 μm . Plagioclase and biotite sometimes form thin symplectic intergrowths. The zircons range from 20 to 50 μm in diameter and mostly have a roundish shape. Zircon grains form inclusions within garnet but more often occur in the plagioclase-quartz matrix. In CL images they contain a dark core and a thick bright homogeneous rim (Fig. 2.10b). Around 13% of grains, investigated for orientation contrast, appeared crystal-plastically deformed, and 32 % appeared to be deformed cataclastically. Only irregularly-shaped grains display crystal-plastic deformation (Figs. 2.10, 2.12), and they are found in the domains with large-grained garnet.

2.5. Microstructural and crystallographic orientation data

In respect to the rheological properties of zircon and its host phases, and to characterize the difference in viscosity between them, we will try to avoid ambiguous terms and will refer to minerals that have low viscosity, and are rheologically weaker than zircon (like biotite and chlorite) as “soft” phases, and to the phases that have higher viscosity and are rheologically stronger than zircon or relevant to it (like garnet and plagioclase), as “strong” phases.

2.5.1. CL-bright domains

Grains with CL-bright domains that truncate oscillatory zoning were investigated with orientation mapping in order to establish the relationships between dissolution – reprecipitation and crystal-plastic deformation in zircon.

The characteristic feature of zircon grains in granitic gneisses from shear zones 1 and 2 is that CL-bright domains truncate initial oscillatory zoning. CL-bright domains are often forming several mutually crosscutting generations within a single grain. *Grain 29* (Fig. 2.2a-c) from sample BH12-01-I shows semi-circular CL-bright intragranular domains with smooth or ragged domain-boundaries (Fig. 2.2b). They lack significant misorientation with respect to the remaining grain, showing orientation variations of less than 0.5° (Fig. 2.2a, d). Raman spectroscopy documented an increased degree of crystallinity of the CL-bright domains (Fig. 2.2b).

2.5.2. Zircon finite lattice distortion types

Crystallographic orientation maps show intragranular orientation variations within some of the zircon grains. Three main types of lattice distortion patterns were distinguished in plastically-deformed zircon grains (see Table 2.2), based on the absence (type I) or presence (type II and III) of well-developed subgrain boundaries in strained zircon grains. Distortion pattern type (I) is characterized by gradual lattice rotation without any subgrain boundaries formation. Type II contains half-circular shaped subgrain boundary traces with high misorientation (more than 10°) whereas type III shows continuous low-angle boundary networks (less than 10° misorientation). Our classification of lattice distortion patterns is consistent with that suggested by Piazzolo et al. (2012), however, is more generalized.

Type (I) and (II) patterns are predominant in granulite-facies rocks, whereas type (III) is more common in the amphibolite-facies rocks (Fig. 2.14a-c). Below there are examples of each distortion type presented.

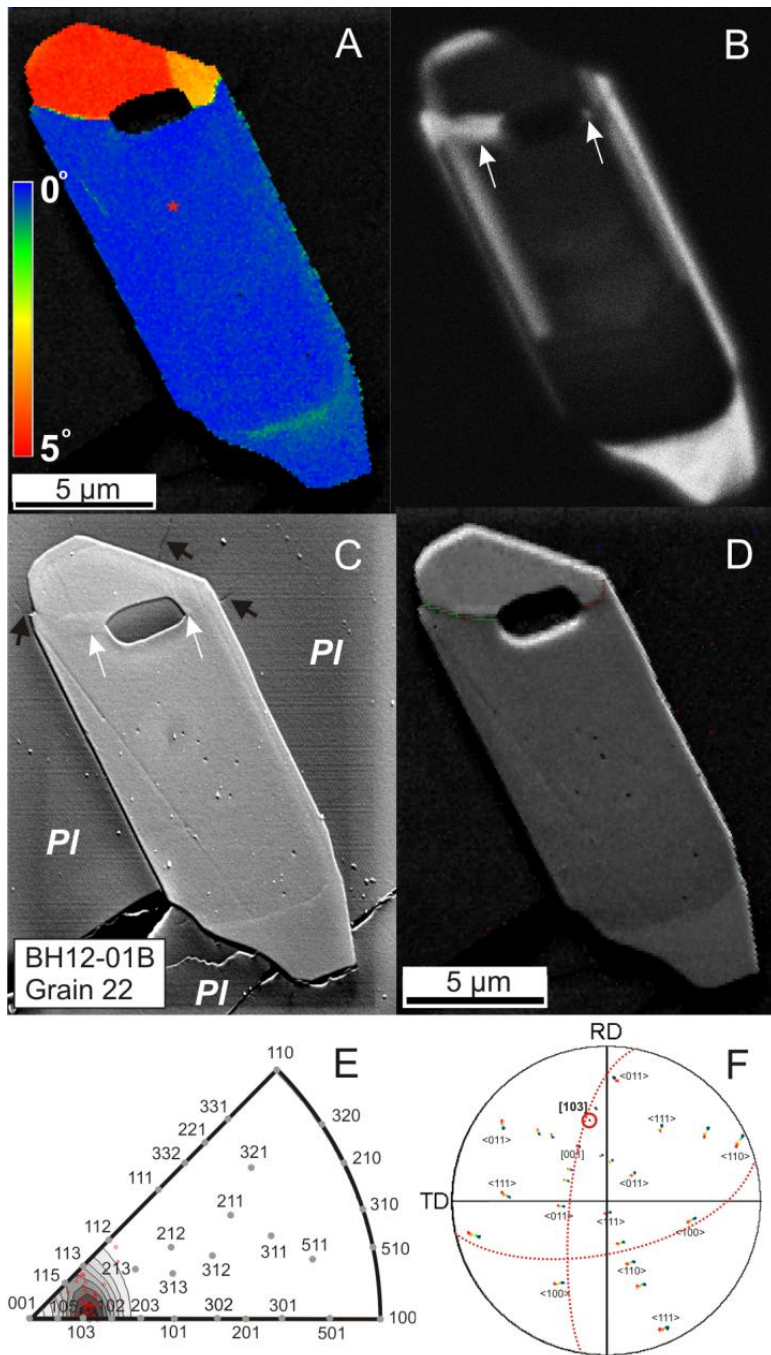


Figure 2.6. Grain BH12-01B_22 lattice distortion type (III) case 3. **(a)** EBSD map color coded for misorientation with respect to a reference point (red star marker); **(b)** CL image with bright recrystallization zones (shown by white arrows); **(c)** SE image showing subtle fractures (black arrows) in host plagioclase, and recrystallization zones as in b (shown by white arrows), *PI* = plagioclase; **(d)** EBSD pattern quality map showing subgrain boundaries colored for misorientation angles between subgrains (red lines = 2 – 3°, green lines = 3 – 5°). **(e)** Inverse pole figure plot of the misorientation axes distribution density showing concentration around zircon [103]. **(f)** Pole figure plot showing zircon crystal directions (lower hemisphere equal area projection) colored as in a. Labels indicate the crystallographic directions. Orientation scattering corresponds to rotations around [103] (red circle). Dashed red lines show boundary wall orientations.

Distortion pattern type I

Grain IV12-06C_16 is hosted by a polycrystalline plagioclase aggregate. The grain is elongated normal to its c-axis and has an anhedral shape with a smoothly curved boundary trace (Fig. 2.12). It shows a high grain-internal deformation that amounts to 25° intragranular orientation variation, but forms no (sub)grain boundaries (Fig. 2.12a, c). The EBSD mapping of host polycrystalline plagioclase reveals gradual lattice rotation that reaches the misorientation up to 20° with respect to the reference point (Fig. 2.12a, inset). The orientation of zircon gradually changes by about 0.6° to 1.4° per μm (Fig. 2.13a), so that the misorientation between single points within the grain does not reveal any distinguishable features (Fig. 2.12c). The orientation contrast image displays an undulatory pattern (Fig. 2.12d). The CL image has a uniformly bright signal without strong zoning or mantle-core structure, and the degree of crystallinity does not change significantly across the crystal (Fig. 2.12b). Misorientation data demonstrate a scattered distribution of the misorientation axis with a higher density close to zircon [001], however, the pole figure shows clear lattice rotation around zircon [001] (Fig. 2.12e, f).

Distortion pattern type II

Domain IV12-06C_05 is situated at the phase boundary between a polycrystalline plagioclase aggregate and a single garnet grain (Fig. 2.10e). The zircon aggregate has irregular shape with curved boundaries and shows significantly higher intragranular orientation variations than grains with type (III) structures, reaching 35° (Fig. 2.10a). However, the misorientation is almost indistinct in the FSE orientation contrast image (Fig. 2.10e). Unlike the lattice distortion type (I), type (II) demonstrates (sub)grain boundary formation developed within distorted zircon rims. (Sub)grain boundaries have a half-circular open shape with the convex side facing towards the undistorted grain domains (Fig. 2.10d). Subgrain boundaries occur locally, terminating within the grain, and are coupled with a gradual bending of the rim (Fig. 2.13b). The point-to-origin misorientation profile of deformed grains shows gradual distortion between subgrain boundaries and sharp steps when crossing them (Fig. 2.13b). A few grain boundaries are presented (Fig. 2.10d, green and blue contours), indicating formation of the new zircon grains next to the garnet-zircon boundary. The CL image (Fig. 2.10b) yields a dark core and bright rim. The degree of crystallinity is decreased in the strained domain with respect to the rest of the grain (Fig. 2.10b, colored dots) consistent with an increase of local misorientation angles (Fig. 2.10b). The pole figure shows a complex rotation pattern of the crystallographic axes. The rotation trend splits into two major parts (Fig. 2.10f, black arrows). Lattice rotation along a profile normal to the zircon/garnet boundary yields misorientation axes clustered

around zircon [331], whereas lattice portion parallel to the phase boundary yields a misorientation axis around the zircon [100] (Fig. 2.11b, c). This is consistent with the misorientation axes distribution density plot that demonstrates two density peaks for misorientation axes that are at a mutual angle of about 45° clustering around [331] and close to [100] (Fig. 2.11a).

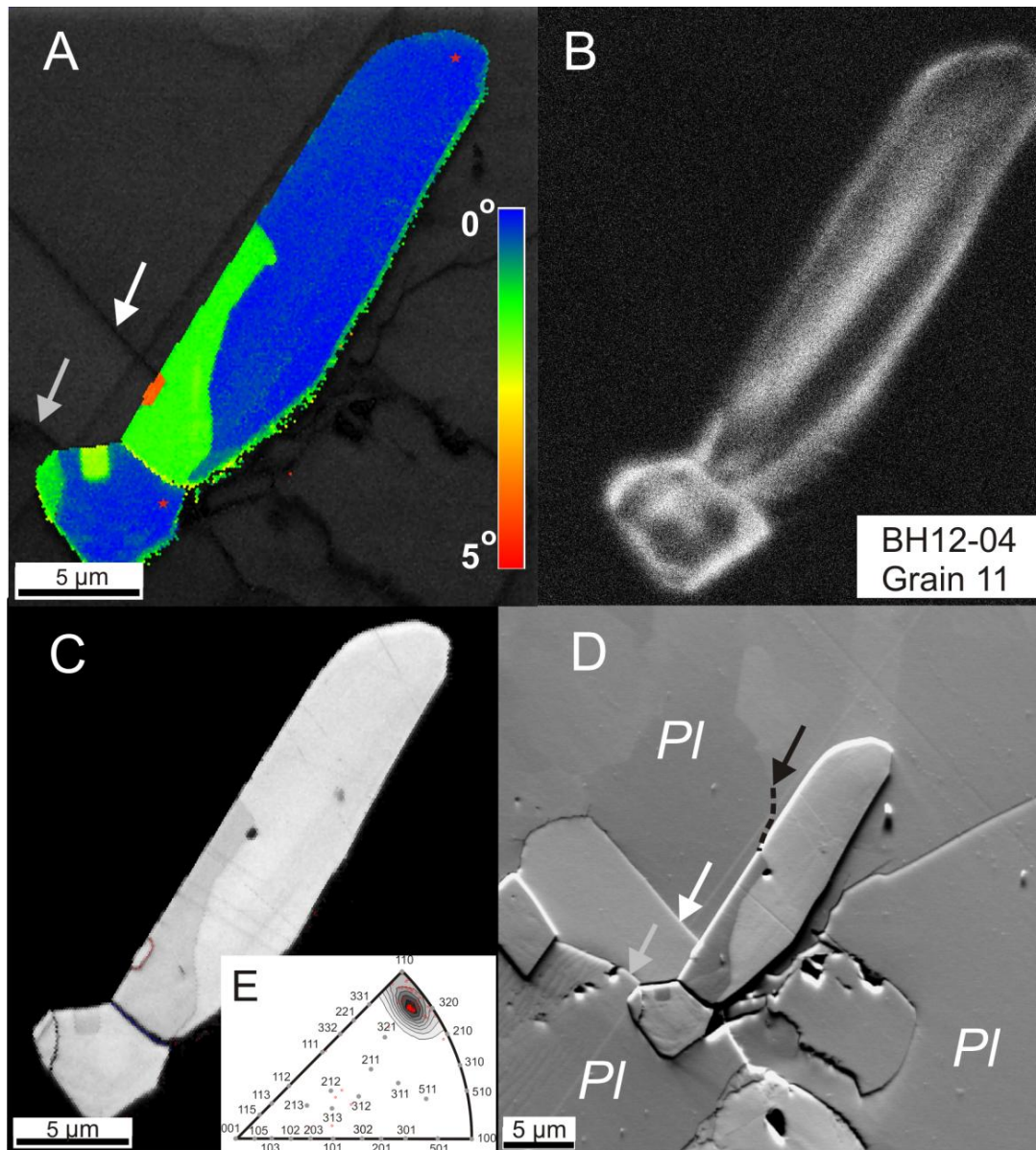


Figure 2.7. Grain BH12-04_11, lattice distortion type (III) case 4. **(a)** EBSD map color coded for zircon misorientation with respect to a reference point (red star marker). Arrows mark plagioclase grain boundary segments; **(b)** CL image; **(c)** EBSD pattern quality map with subgrain boundaries colored for misorientation angles between subgrains (red line = 2 – 5°); **(d)** FSE image, black arrow and dashed line mark plagioclase subgrain boundary, white and grey arrows as in a, *PI* = plagioclase; **(e)** Inverse pole figure plot of the misorientation axes distribution density shows maxima close to zircon [320].

Distortion pattern type III

The large variety of grains with distortion pattern type (III) has been found in amphibolite-facies shear zones. Several deformed grains are described in this study; their lattice distortion pattern was conditioned by local environment.

Grain BH12-05B_07 (Fig. 2.3) is hosted by a biotite aggregate. Zircon grain has an elongated idiomorphic, almost elliptical shape and shows lattice distortion on its upper left portion, reaching a maximum intragranular misorientation of about 3°. The subgrain boundary appears in the CL image (Fig. 2.3b) as a thin bright linear feature truncating the oscillatory zoning, and also forms curved traces in the EBSD map (Fig. 2.3a, c). The misorientation axes are arranged along a great circle in the inverse pole figure plot (dashed line in Fig. 2.3d). The curved trace of a subgrain boundary (Fig. 2.3a-c) and the distribution of misorientation axes along the great circle (dashed line in Fig. 2.3d) are the features of cross slip (Poirier 1985; Reddy et al., 2007), which in this case results from the activity of different slip planes, e.g. zircon (332), (321), (510) and (100) (Fig. 2.3d).

Grain BH12-07B_28 (Fig. 2.4) is hosted by biotite and has a short-prismatic euhedral shape (Fig. 2.4c). Zircon grain is decoupled from the host biotite, what could be concluded from normal and reverse drag of the surrounding biotite and by the void parallel to the lower face of the grain (Fig. 2.4c). Grain shows maximum intragranular orientation variations of 6° (Fig. 2.4a, e). Misorientation profile shows sharp peaks for point-to-point misorientation and steps for misorientation with respect to a single reference point when crossing traces of subgrain boundaries (Fig. 2.13c). The subgrain boundaries stretch from lower left to upper right (Fig. 2.4a-c, e), and their traces extend in C' geometry with respect to the mylonitic foliation. Subgrain boundaries appear bright in the CL image (Fig. 2.4b, white arrows). The degree of crystallinity does not vary significantly across the grain (Fig. 2.4b). Crystallographic orientation data of zircon show a clear concentration of the misorientation axes around the zircon [001] (c-axis), consistent with the crystal axes rotation along small circles around the undispersed cluster of zircon [001] direction (Fig. 2.4d, f).

Grain BH12-07B_15a (Fig. 2.5) from the same sample is also surrounded by biotite and has rectangular short-prismatic shape. Grain is decoupled from the matrix, as there is a void parallel to the left, upper and lower zircon faces, and along the right face there is recrystallized biotite aggregate. The EBSD map shows an intragranular orientation variation of 5°. The grain contains a network of approximately orthogonal subgrain boundaries (Fig. 2.5a-d). These separate distinct subgrains with clear orientation contrast (Fig. 2.5d) and appear bright in the CL image (Fig. 2.5b, white arrows). Within the grain a CL-bright xenocrystic core is observed. Some subgrain boundaries

intersect this core domain; others terminate at its boundary (Fig. 2.5b, c, upper part of the grain). Concentric growth zones show an increasing degree of crystallinity towards the rim (Fig. 2.5b). The misorientation axes inferred from misorientations of the subgrains are parallel to zircon [001] and [100] (Fig. 2.5e) whereas the crystal axes do not show complicated rotation trend (Fig. 2.5f).

Grain BH12-01B_22 (Fig. 2.6), from the ultramylonite core of shear zone 1, is located in plagioclase, has elongated euhedral shape and displays subgrain boundaries emanating from mineral inclusion (Fig. 2.6a). Subtle fractures in the host plagioclase (Fig. 2.6c, black arrows) intersect the zircon phase boundary at the positions close to those of the zircon subgrain boundary-intersects. The CL image reveals not only a dark core and a bright outer rim, but also a linear CL-bright zone that is spatially associated with a subgrain boundary (Fig. 2.6b, white arrows). The misorientation axes cluster close to zircon [103] (Fig. 2.6e) in accord with crystallographic axes that are rotated around the [103] direction (Fig. 2.6f).

Scan BH12-04_11 (Fig. 2.7) covers two idiomorphic zircon grains that are hosted by polycrystalline plagioclase (Fig. 2.7d). One of the zircon grains has elongated shape with aspect ratio 1:5 in the 2D section, whereas another is rather isometric. The elongated grain shows grain-internal orientation variations of about 5° due to the presence of subgrains, which show strong orientation contrast although subgrain boundaries do not appear in the CL image (Fig. 2.7a, b and d). Within the subgrains orientation variations are negligible. The grain boundary trace of fine-grained plagioclase at the left (Fig. 2.7a, d, white arrow) is oriented at a high angle to the trace of the zircon prismatic face. The coarser plagioclase grain covering the upper left of the map shows grain-internal orientation contrast, and a plagioclase subgrain boundary trace oblique to the zircon prismatic face (Fig. 2.7d, black arrow, dashed line). The plagioclase (sub)grain boundaries impinge on the zircon phase boundary at the same sites as the subgrain boundaries within the zircon. The misorientation axes show a maximum parallel to zircon [320] (Fig. 2.7e).

Domain BH12-02_45 (Fig. 2.8) represents a zircon aggregate hosted by plagioclase and quartz and consists of differently oriented irregularly-shaped fragments. Some fragments seem detached from the aggregate and surrounded by host plagioclase in the 2D section (Fig. 2.8c, upper right, lower left). Zircon fragments have roundish or angular shape and often form triple junctions, are separated by low- and high-angle boundaries. Misorientation angles between fragments range from 2° to more than 15° (Fig. 2.8c). The orientation of the subgrains within a cluster changes progressively as shown by false color highlighting of the misorientation with respect to a single reference point from 0° = blue (top, Fig. 2.8a) to 26° = red (bottom, Fig. 2.8a). Grain boundaries characterized by a CL-bright signal truncate oscillatory zoning (Fig. 2.8b). The distribution of misorientation axes does not show

systematics of fragments rotation (Fig. 2.8e), misorientation axes clustering is rather weak, consistent with crystallographic orientations that don't have a clear rotation trend (Fig. 2.8f). The misorientation axes are clustered around the zircon [113], [111] and [311] directions.

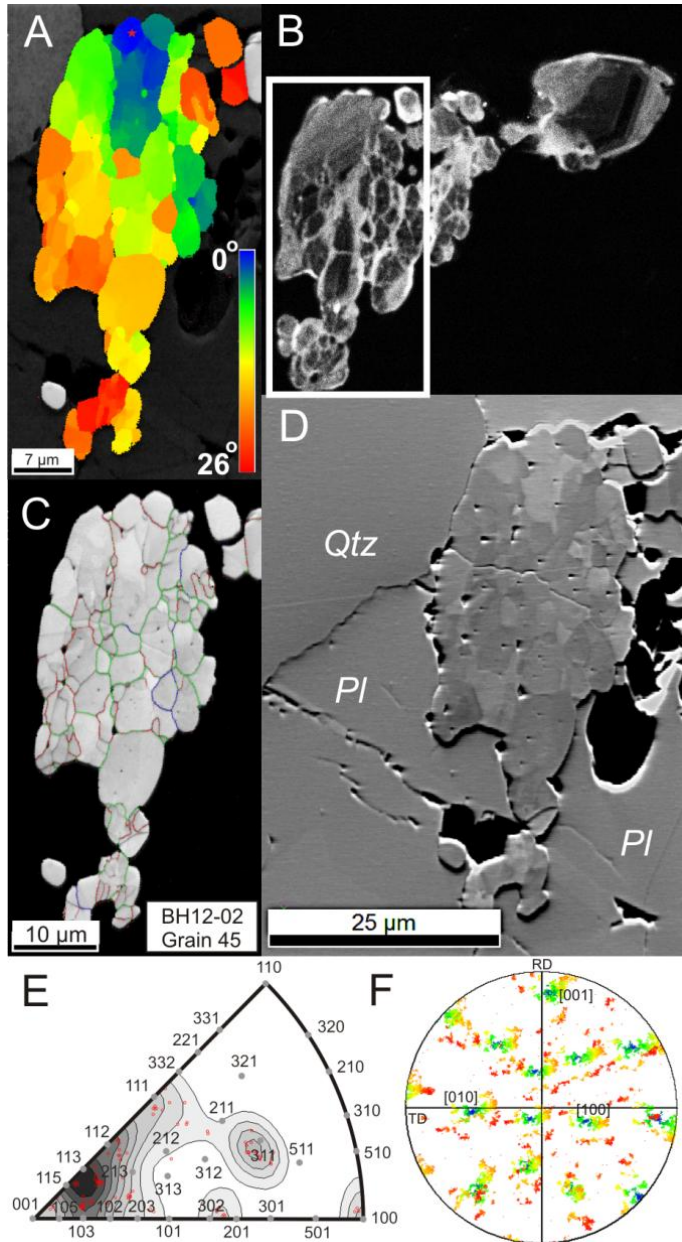


Figure 2.8. Grain BH12-02_45, lattice distortion type (III) case 5. **(a)** EBSD map color coded for zircon misorientation with respect to a reference point (red star marker); **(b)** CL image (white rectangle marks position of EBSD map); **(c)** EBSD pattern quality map with subgrain boundaries colored for misorientation angles between subgrains (red = 2° – 5°, green = 5° – 15°, blue > 15°); **(d)** FSE image, *Qtz* = quartz, *Pl* = plagioclase; **(e)** Inverse pole figure plot of the misorientation axes distribution density; **(f)** Pole figure plot showing zircon crystal directions (lower hemisphere equal area projection) colored as in a. Labels indicate the crystallographic directions.

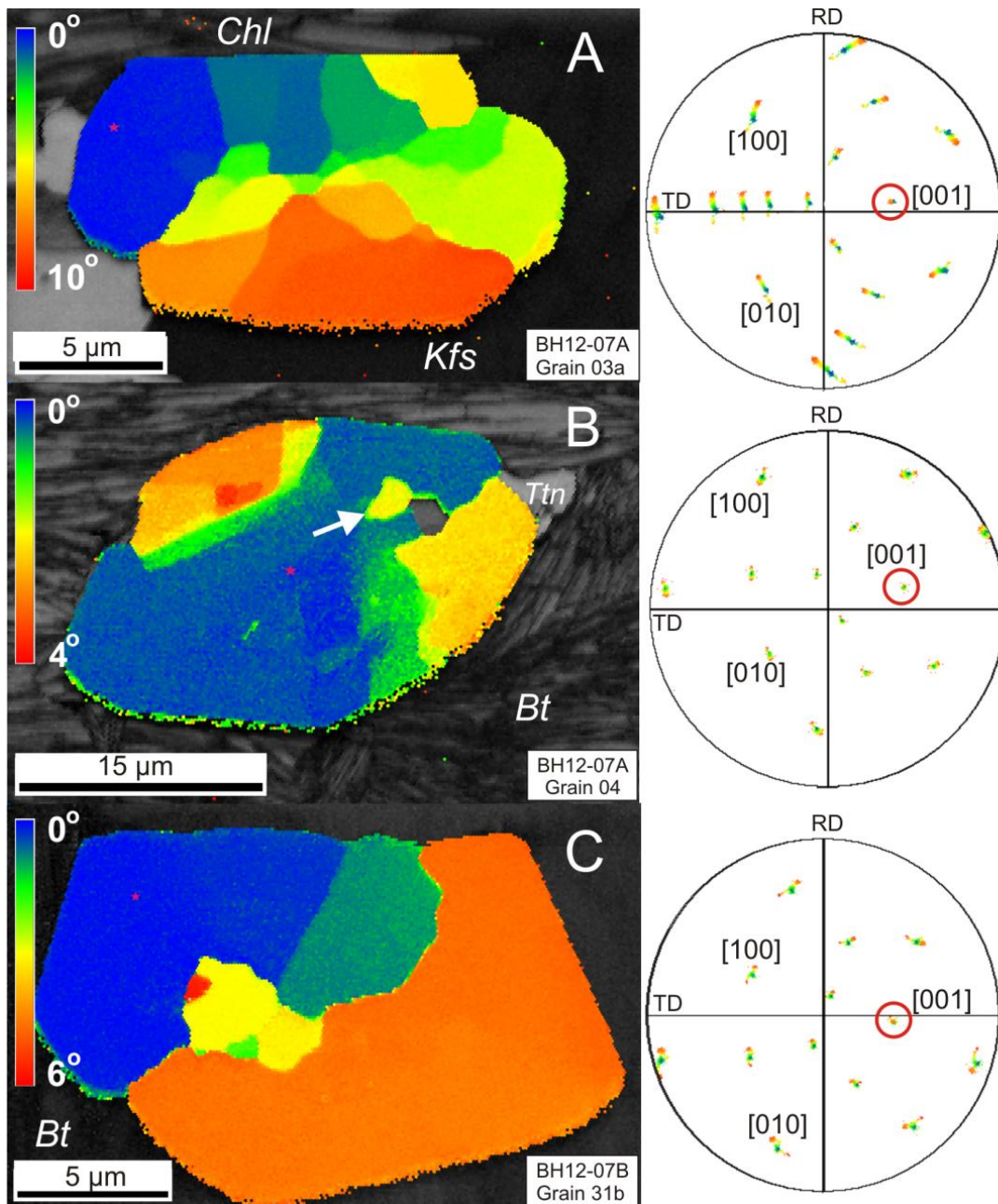


Figure 2.9. (Sub)grain shape and crystallographic orientation of zircon from sample BH12-07 (basic dyke). Left hand side – EBSD maps colored for misorientation with respect to a single reference point (red star marker), right hand side – pole figure plots showing zircon crystal directions (lower hemisphere equal area projection) colored as the corresponding EBSD map. Rotation axes parallel to zircon [001] axis are highlighted by a red circle. **(a)** Grain BH12-07A_03a, lattice distortion type (III) cases 2 and 4; **(b)** grain BH12-07A_04, lattice distortion type (III) cases 1, 2, and 3. Arrow highlights subgrain adjacent to the mineral inclusion; **(c)** grain BH12-07B_31B, lattice distortion type (III) case 2; *Bt* = biotite, *Chl* = chlorite, *Kfs* = K-feldspar, *Ttn* = titanite. NB! The thin sections were cut normal to the foliation plane and at an angle of 50° with respect to the intersection lineation, so that the zircon [001] direction coincides with the intersection lineation and the fold axis.

Grain BH12-07A_03a (Fig. 2.9a) is situated at the phase boundary between polycrystalline chlorite and potassium feldspar, whereas *grains BH12-07A_04* and *BH12-07B_31b* occur within biotite aggregates (Fig. 2.9b, c) and are decoupled with the matrix. Decoupling is identified by normal and reversed drag of adjacent biotite and also by pressure shadow filled with titanite (Fig. 2.9b). All three presented grains have sub-idiomorphic shape, are elongated with aspect ratios 2:3 – 1:2 and display subgrains with 4°-10° orientation deviation from a reference point. Grains show systematic lattice rotation about zircon [001] (right column). According to the subgrain boundary configurations active slip system in these grains is $\langle 100 \rangle \{010\}$. The [001] directions of all three grains have a similar orientation (highlighted by a red circle) coinciding with that of crystal *BH12-07B_28* (Fig. 2.4f); they are parallel with the stretching lineation of the sample.

2.6. Discussion

2.6.1. Static dissolution-precipitation vs. crystal-plastic deformation

Hydrothermally altered zircon zones resembling those in grain *BH12-01B_29* (Fig. 2.2), have been described from natural rocks (e.g. Corfu et al., 2003 and references there) and produced experimentally (Geisler et al., 2001; Geisler et al., 2003). Altered zones that crosscut the initial zoning are characterized by a sharp front with curved geometry separating altered from pristine zones within the grains. Recrystallized lattice domains are marked by increased CL intensity compared to the signal from the matrix, which is considered to be a result of dissolution-precipitation, which decreased lattice defect density (Corfu et al., 2003; Geisler et al., 2001; Geisler et al., 2003). There are at least four arrangements of CL-bright domains observed in investigated zircons: i) CL-bright domains extend into the inner parts of a grain, forming closed core zones (e.g. Fig. 2.2b, upper left part, lower right part); ii) CL-bright domains along fractures or subgrain boundaries (Figs. 2.6b, 1.8b); iii) occur as rims, framing the central part of a crystal (Fig. 2.10b), or iv) cover the entire grain (Fig. 2.12b).

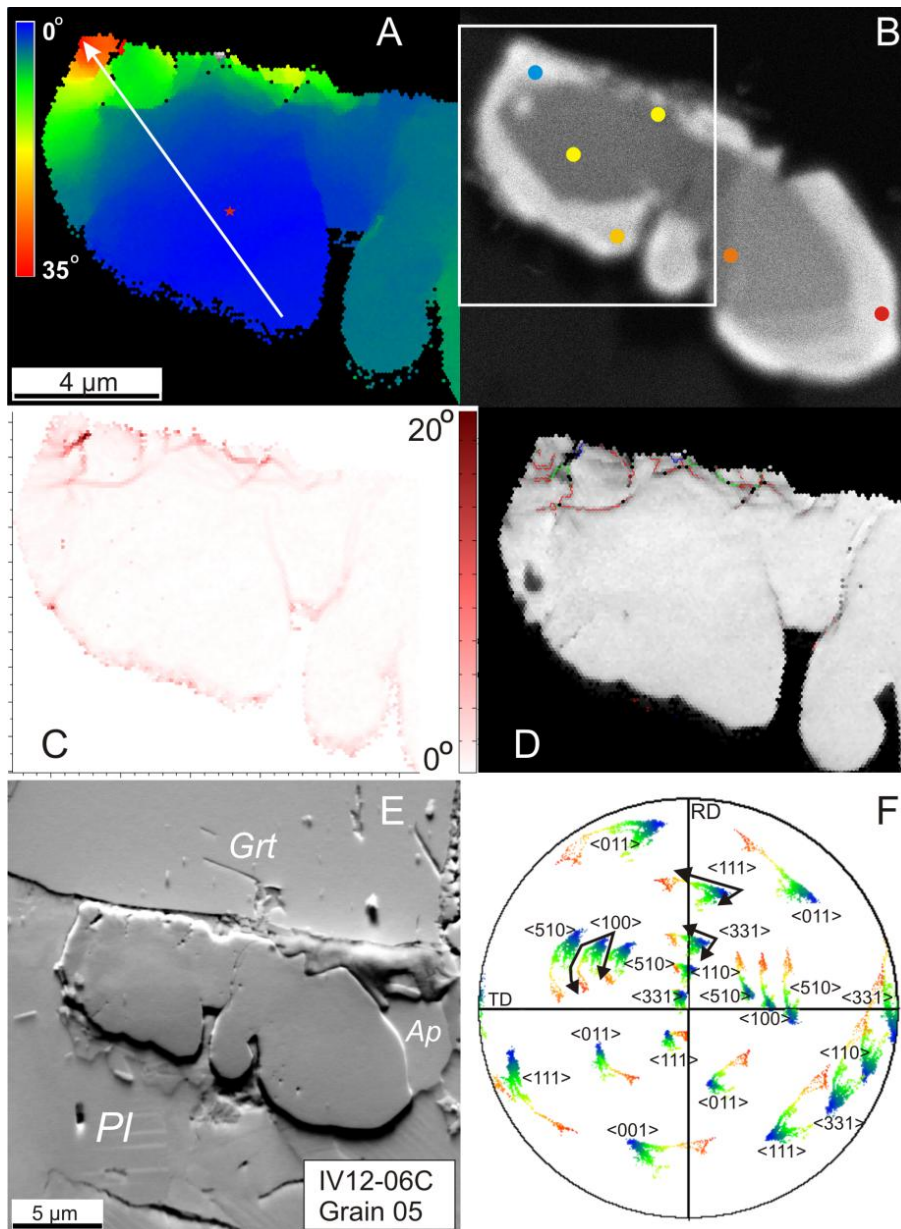


Figure 2.10. Grain IV12-06C_05, lattice distortion type (II). **(a)** EBSD map color coded for zircon misorientation with respect to a reference point (red star marker), the white arrow corresponds to the misorientation profile shown in Fig. 2.13b; **(b)** CL image, colored points represent relative degree of crystallinity, color coding as in Fig. 2.2b, the EBSD map position is marked by the white rectangle; **(c)** EBSD map of zircon showing the misorientation between neighboring data points; **(d)** EBSD pattern quality map with subgrain boundaries color-coded as in Fig. 2.8c; **(e)** FSE image, *Grt* = garnet, *Pl* = plagioclase, *Ap* = apatite; **(f)** Pole figure plot showing zircon crystal directions (lower hemisphere equal area projection) colored as in a. Labels indicate the crystallographic directions. Black arrows indicate split in the direction of axes rotation.

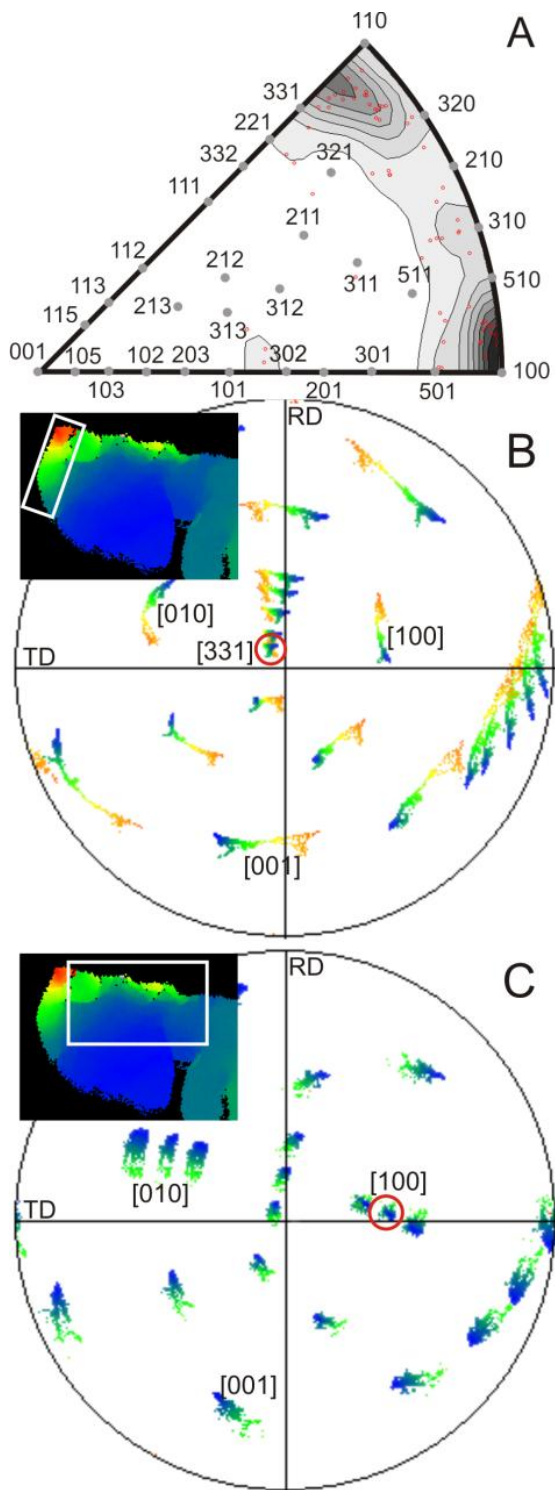


Figure 2.11. Orientation and misorientation data of grain IV12-06C_05, lattice distortion type (II). **(a)** Inverse pole figure plot of the misorientation axes distribution density, showing axes concentrated parallel to [331] and [100] axes. **(b)** and **(c)** Pole figure plot showing crystal directions (lower hemisphere equal area projection) of two deformed parts of the grain (indicated by a white rectangle in the inset), colored as in insets. Misorientation axes are highlighted by red circle.

i) Zircon grain BH12-01B_29 (Fig. 2.2, sample BH12-01-I) does not show a genetic relation of CL-bright homogeneous domains and crystal-plastic deformation. Recrystallized domains do not exhibit any significant misorientation with respect to the rest of the grain (Fig. 2.2d). Slight misorientation corresponding to intensity variations in the CL pattern can be interpreted as related with a compositional variation and the increased degree of crystallinity (Fig. 2.2a, b). Homogeneous CL-bright domains (i) forming closed zones with half-circular shape inside the crystal, frequently occur in sample BH12-01-I. Their occurrence is independent of whether grains show crystal-plastic deformation microstructures or not, leading to the conclusion that crystal-plastic deformation and recrystallization in this sample have no evident mutual effect.

ii) In contrast, grain BH12-01B_22 (sample BH12-01-II) demonstrates a genetic relation between recrystallized zones and crystal-plastic deformation microstructures. The CL-bright feature at the left of inclusion is also visible in the SE image (Fig. 2.6c, white arrows) and spatially corresponds with the trace of the subgrain boundary that accumulates the largest misorientation angle (Fig. 2.6b, white arrows; D, boundary color-coded green). However, the significant width of this CL bright zone contrasts with similar features observed in grains BH12-05B_07, BH12-07B_15a and 28. The geometric relationship between CL-signal characteristics and subgrain boundaries indicates that hydrothermal recrystallization postdated crystal-plastic deformation and exploited deformation microstructures. Subtle fractures in the hosting plagioclase (Fig. 2.6c, black arrows) are spatially associated with the crystal-plastically-deformed part of the zircon grain and might be related to the slight volume expansion of the zircon grain's tip due to recrystallization and/or, more likely, metamictization of the CL-dark core.

iii) In grain IV12-06C_05 (Figs. 2.10 and 2.11) the CL-bright recrystallized rim (iii) is locally deformed and exposed to the local grain size reduction. The degree of crystallinity is rather low where lattice distortion took place. The local distortion of the recrystallized rim shows that metamorphic recrystallization of zircon predates plastic deformation. The thickness of the recrystallized rim is reduced in the crystal-plastically-deformed zone when comparing with the average thickness of the undistorted rim in the lower portion of the grain. The bright rim almost disappears where newly formed grains are observed (Fig. 2.10b, d – domains with green and blue contours).

iv) Grain IV12-06C_16 is homogeneously bright in the CL image (Fig 2.12b), potentially reflecting complete recrystallization. Homogenization of the crystal lattice and chemical composition – if predating deformation – could explain the lack of strain localization and subgrain formation in this zircon grain. Another possibility is that the bright CL-signal is generated by dislocations, which represent evenly distributed luminescence centers in the crystal lattice. The bright CL-signal induced

by intrinsic defects in the crystal lattice including dislocations has been described for calcite, quartz, and some synthetic materials (e.g. Goetze et al., 2001; Akchurin et al., 2009).

To summarize, zircon recrystallization in the investigated samples supposedly was induced by fluid infiltration. Where observed, the temporal relationship between hydrothermal recrystallization and crystal-plastic deformation may vary: in one sample hydrothermal alteration clearly precedes crystal-plastic deformation (IV12-06C_05), in the other postdates (BH12-01B_22). Hydrothermal alteration causing dissolution-precipitation may have been operating repeatedly at different stages and in different temperature regimes during the metamorphic evolution of the rocks.

2.6.2. Microstructural analysis of different lattice distortion patterns

Based on several natural examples we have demonstrated the variety of finite deformation patterns of plastically deformed zircons. The investigated zircon grains -when deformed- show either high but coherent lattice strain without dislocation accumulation in (sub)grain boundaries (distortion type I), recrystallization by a polygonization (distortion type III), or a combination of both (type II).

Distortion type I

Type (I) finite deformation patterns are characterized by gradual intragranular lattice orientation changes affecting the entire zircon grain without any remarkable step or subgrain formation. Similar features have been described by Reddy et al. (2007), and very likely correspond to type (I) lattice distortions of the classification by Piazzolo et al. (2012). Moser et al. (2009) describe this type of lattice distortion as a result of an impact event. We suggest that this distortion pattern formed due to deformation of the host strong matrix (plagioclase). Host plagioclase is uniformly bended around zircon (Fig. 2.12a, inset), and due to high degree of coupling zircon has been deformed together with the host.

Uniform bending of the zircon lattice reaching intragranular misorientations up to 25° (Fig. 2.13a) requires the presence and even distribution of geometrically necessary dislocations (GND), which form if the lattice rotations exceed its elastic limit. However dislocations obviously are not mobile and therefore do not accumulate within (sub)grain boundaries. The degree of crystallinity and CL-intensity does not significantly change across the zircon grain, which is a result of the uniform distortion (Fig. 2.12b). Distributed strain, accommodated by dislocations that are not accumulated in

low-angle boundaries does not allow inferring active slip systems, and misorientation axes are scattered, with weak clustering around zircon [001], which is a commonly referred misorientation axis (Leroux et al., 1999; Reddy et al., 2007; Kaczmarek et al., 2011; Timms et al., 2012b). Scattering of misorientation axes is caused by subordinated deformation together with the polycrystalline host plagioclase.

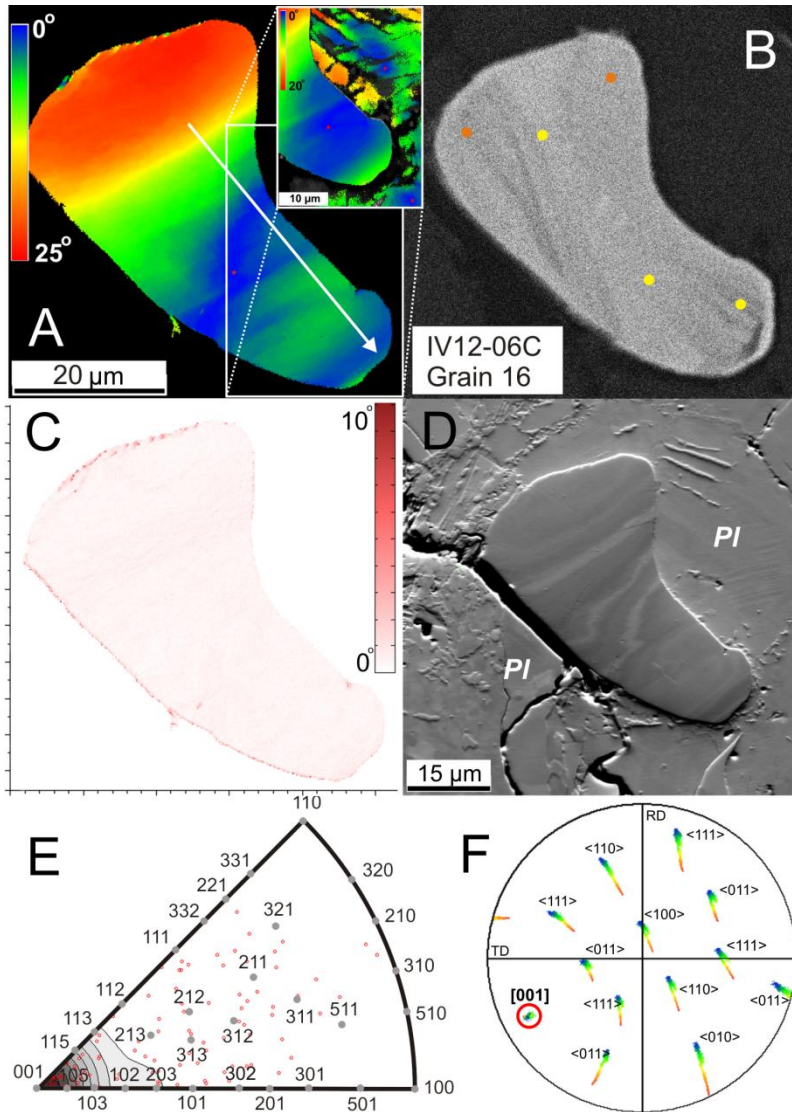


Figure 2.12. Grain IV12-06C_16, lattice distortion type (I). **(a)** EBSD map color coded for zircon misorientation with respect to a reference point (red star marker), white arrow corresponds to misorientation profile shown in Fig. 2.13a; inset – misorientation map of host plagioclase, showing lattice rotation up to 20°; **(b)** CL image, colored points represent relative degree of crystallinity, color coding as in Fig. 2.2b; **(c)** EBSD map of zircon showing the misorientation between neighboring datapoints; **(d)** FSE image, *PI* = plagioclase; **(e)** Inverse pole figure plot of the misorientation axes distribution density; **(f)** Pole figure plot showing zircon crystal directions (lower hemisphere equal area projection) colored as in a. The red circle indicates rotation axis.

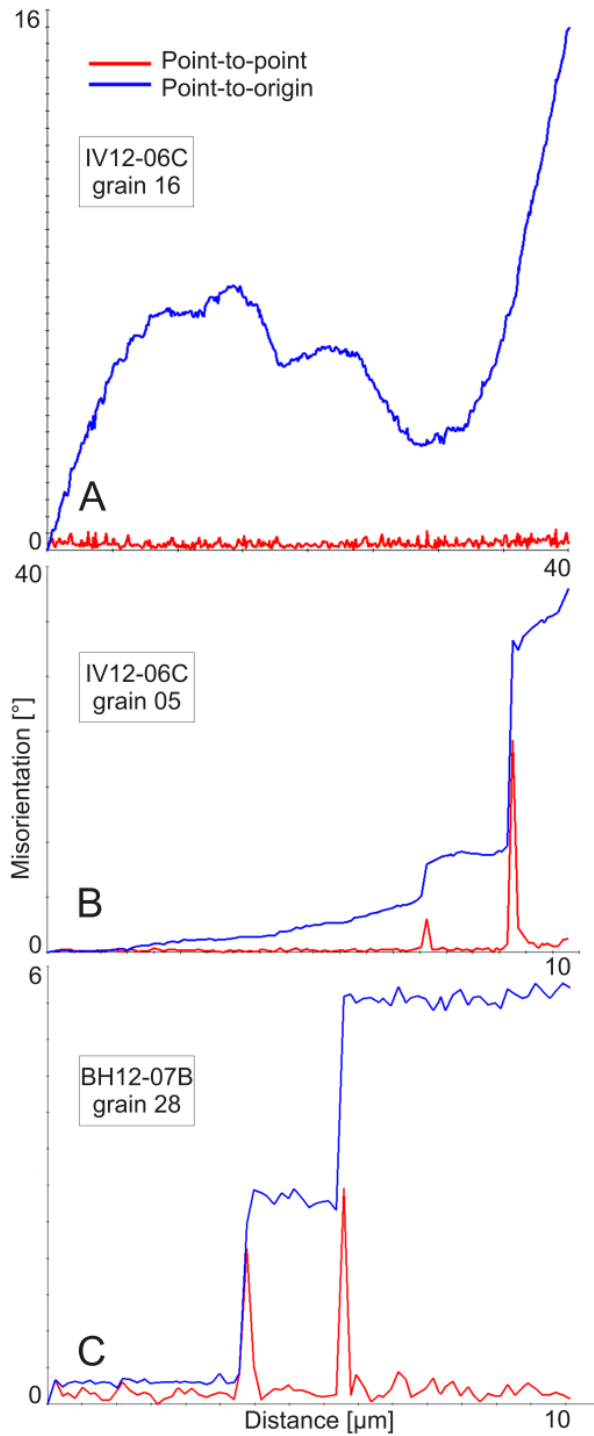


Figure 2.13. Misorientation profiles of zircon showing point-to point (red line) and point-to-origin (blue line) misorientations for **(a)** grain IV12-06C_16 displaying spatially continuous lattice rotation (for location of the profile line see Fig. 2.12a); **(b)** grain IV12-06C_05, showing subgrain boundary formation together with spatially continuous lattice distortion (for location of the profile line see Fig. 2.10a); **(c)** grain BH12-07B_28 exhibiting subgrain formation (for location of the profile line see Fig. 2.4a).

Distortion type II

This deformation pattern is accompanied by fragmentation at the margins and characterized by strong lattice distortion in local rim domains. Lattice distortion type (II) preferably develops in zircon domains adjacent to a strong phase as well as in grains hosted by polycrystalline fine-grained matrix. The load exerted by strong neighboring grain leads to high differential stress and eventually to strain in specific grain domains. The upper left part of the zircon grain IV12-06C_05 was pressed into adjacent garnet grain (Fig. 2.10) resulting in high lattice strain with relatively large angular misorientations (Fig. 2.10a). In the study of Piazzolo et al. (2012) this deformation pattern formation explained with mutual “indentation” of rheologically hard grains, when one of them have so-called “Vickers indentation” and cause locally enhanced differential stress in the neighboring grain (Ferguson et al., 1987; Lloyd, 2000; Whitney et al., 2007). The indenter interpretation is appropriate for the specific case, described in Piazzolo et al. (2012). However, as we have shown, very similar deformation pattern in zircon can also form when two strong grains with relatively straight faces (in 2D sections) are pressed into each other. Sometimes this distortion pattern forms in large zircon clasts that are hosted by fine-crystalline matrix.

Finite deformation pattern type (II) includes not only subgrain formation, but also the formation of high-angle grain boundaries and grain size reduction. Dynamic recrystallization by a subgrain rotation mechanism initially causes the formation of low-angle boundaries, whereas progressive strain accumulation induces the rotation of subgrains and an increasing dislocation density in the subgrain boundaries that develop to the high-angle boundaries. Newly forming grains are observed in the Fig. 2.10d, contoured by green and blue lines.

The crystallographic orientations in the pole figure show asterism (Fig. 2.10f), which points to several simultaneously operating slip systems with different misorientation axes that points to locally high differential stress. These are the main misorientation axes observed, but there could be several subordinate axes operating simultaneously (Fig. 2.11a).

Distortion type III

Type (III) is characterized by “polygonization” (White, 1973, 1976; Poirier and Nicolas, 1975; Gerald et al., 1983; Behrmann, 1985), due to formation of slightly misoriented subgrains which lack internal lattice strain, separated by subgrain boundaries. Subgrain boundaries form closed contours and often have a bright CL-signature (e.g. Figs. 2.3-2.5). All subgrains are clearly visible in the

orientation contrast images, more pronounced than in case of lattice distortion type (II) (Fig. 2.10e). The type (III) distortion pattern presumably results from mechanisms such as formation and migration of dislocations, thermally-controlled recovery and recrystallization by rotation of subgrains. These are the components of dislocation creep regime and lead to accumulation of dislocations within subgrain boundaries (e.g. Hobbs, 1968; White, 1973, 1976; Poirier and Nicolas, 1975; Behrmann, 1985; Drury and Urai, 1990; Poirier, 1985).

The type (III) finite deformation pattern can be conditioned by variety of factors controlling the crystal-plastic behavior of zircon. The following discussion will present several cases of the commonly observed end members that are possible for this distortion type, however, most grains of this type fall between the following end members:

Case 1 is defined by favorable shape orientation of deformed grain in the local stress field. These zircon finite deformation patterns develop only locally; distortion, for example, affects the portion of grain comprising the intersection of prism and pyramid faces in euhedral prismatic zircon grains (or similar geometry, e.g. Figs. 2.3, 2.9b; Moser et al., 2011). The observed local deformation of the grain (Figs. 2.3c, 2.9b) implies the presence of differential stress and, therefore, inhomogeneous strain distribution within the grain. This scenario can occur in case of strong elliptical inclusions in a softer matrix affected by simple shear, in case when inclusion is decoupled with the matrix (Kenkmann, 2000; Schmid and Podladchikov, 2005). The highest pressure affects those portions of matrix, which are adjacent to the clast boundary segments normal to the shortening direction (e.g. Schmid and Podladchikov, 2004; Manktelow, 2008). According to numerical modeling (Schmid and Podladchikov, 2005), portions of the clast that are exposed to relatively higher pressure, experience differential stress. However, most of the strain is accommodated within soft matrix and the resulting intragranular misorientation of zircons is subtle ($<5^\circ$). Various slip systems are active. Portions of grain, which are not affected by differential stress, remain undistorted.

This finite deformation pattern can be observed in grain BH12-05B_07 (Fig. 2.3). Grains portion adjacent to pyramid-prism conjugation is deformed. Presumably distortion in this domain formed due to differential stress, and, therefore, inhomogeneous strain distribution during shearing; and was defined by decoupling from the matrix. Another example is elliptical grain BH12-07A_04 (Fig. 2.9b) that is deformed at its opposite portions; from the distribution of distorted domains shortening direction could be reconstructed.

Case 2 is defined by favorable crystallographic orientation in the local stress field. This lattice distortion patterns are controlled by the crystallographic anisotropy of zircon, causing slip along the

dominant slip systems that are genetically connected with the main crystallographic axes $\langle 001 \rangle$ and $\langle 100 \rangle$. In order to activate dominant slip systems certain crystallographic orientation with respect to the local stress field is preferable. Grains, characterized by this deformation pattern usually perform specific shape geometry, they are rather short prismatic with the aspect ratio 1:2-1:3, or isometric; some of them have nearly rectangular shape (Figs. 2.4, 2.5). This case of lattice distortion is mostly observed in the grains hosted by soft matrix or decoupled from the matrix. We use term “decoupling” meaning that the grain is able to slide along grain-matrix interface. Decoupling from the matrix can be identified (i) by presence of coating at the interface (recrystallized biotite, for example, grain BH12-07B_15a), by (ii) opening of voids at the interface (grains BH12-07A_04 (pressure shadow, filled with titanite), BH12-07B_15a, 28), and by (iii) evidence of sliding of inclusion in matrix, when the elements of inclusion and matrix are shifting with respect to each other (e.g. Kenkman, 2000; grains BH12-07A_04, BH12-07B_28). Generally, most of the grains hosted by biotite are decoupled with it, because biotite is a soft phase and strong clasts can easily slip along the interface.

Assuming that the boundary wall is parallel to $\{100\}$ and contain misorientation axis in sample BH12-07B_28 (Fig. 2.4d, f), the resulting slip systems are $\langle 100 \rangle \{010\}$. These systems we assert as “dominant”, as more favorable for zircon crystals (e.g. Leroux et al., 1999; Kaczmarek et al., 2011; Reddy et al., 2007; Reddy et al., 2009; Timms et al., 2012b; Piazzolo et al., 2012), and the other systems, if active, “unfavorable”, as less energetically-preferable. Microstructure of grain BH12-07B_15a (Fig. 2.5) is implying the operation of at least two slip systems. Accommodating slip by edge dislocations yields either $\langle 100 \rangle \{010\}$ or $\langle 010 \rangle \{001\}$ correspondingly; a twist boundary forms in case of misorientation axis parallel to $[100]$ and subgrain boundary (100) . The observation of radial subgrain boundaries may lead to the conclusion that they are fractures, formed due to expansion of the metamictized core. In contrast, in this case the core shows a comparatively high degree of crystallinity (Fig. 2.5b, colored dots) although heterogeneities due to growth zoning certainly may influence the development of the deformation pattern.

The preferable slip along $\{100\}$ or $\{001\}$ is facilitated by the specific crystallographic orientation with respect to a local stress field. Orientation helps the resolved shear stress (CRSS) along the specific glide plane to be reached (Hobbs, 1985). Similarly orientated zircon grains in one sample have similar lattice distortion patterns (e.g. BH12-07B_28, 31b; BH12-07A_03a, 04; Figs. 2.4, 2.9): they indicate activation of the slip systems $\langle 100 \rangle \{010\}$. Grains BH12-07A_03a, BH12-07B_28 and 31b show two symmetrical “lobes” that are displaced along the subgrain boundary tracing from the lower left to the upper right corner of each grain (Figs. 2.4a, 2.9a-b).

Case 3 is characterized by subgrain formation with boundaries emanating from mineral inclusions in zircon (Fig. 2.6a).

This geometric arrangement of subgrain boundaries could be a result of pinning of dislocations by obstacles during recovery and recrystallization of the crystal lattice (Drury and Urai, 1990). However, more favorable scenario describes xenocrystic cores, inclusions, pores and fractures within a crystal as structural heterogeneities that may induce inhomogeneous stress distribution (Mancktelow, 2008; Timms et al., 2012a) and strain localization during deformation. Stress may be heterogeneously distributed in the grain around mineral inclusion or pore, what leads to local lattice distortion even within the central portions of grains during post-growth deformation (Timms et al., 2012a).

Superimposing the traces of subgrain boundaries from grain BH12-01B_22 in the pole figure gives two general families of planes, where one contains the rotation axis and the other is rather normal to it (Fig. 2.6f). From this observation we infer that the two families of subgrain boundaries represent tilt and twist walls correspondingly. Thus, glide system for the edge dislocations presumably is $\langle -103 \rangle \{30-1\}$. The activation of slip along the high Miller indices plane may be controlled by the inclusion geometry. Grain boundary sliding at the inclusion/host interface may have induced the activation of specific slip planes within the enclosing host (e.g. Raj and Ashby, 1971; Wang et al., 2014). Another grain that shows subgrain boundaries emanating from a mineral inclusion is BH12-07A_04 (Fig. 2.9b). The subgrain adjacent to the inclusion (Fig. 2.9b, marked by arrow) forms due to the presence of differential stress around the inclusion during shearing.

Case 4 shows a deformation pattern controlled by the microstructure of the host phase, i.e. phase-, grain- or subgrain boundary structure of the host. As the applied differential stress is transferred to the zircon by the host phase, there seems to be a relationship between the zircon subgrain boundary geometry and host (sub)grain boundary geometry, especially in case of strong host/coupling with host. (Sub)grain boundaries of the host grain(s) can be often traced inside the hosted zircon grain as subgrain boundaries or fractures as, for example, in grain BH12-04_11 (Fig. 2.7a, d, arrows). Subgrain boundaries in elongated zircon BH12-04_11 relate to crystal-plastic deformation by subgrain rotation, because misorientation axes density distribution demonstrates a well-defined cluster (Fig. 2.7e). Coupling of zircon with strong host mineral prevents the activation of energetically preferable slip systems in zircon and therefore causes the formation of high indexed misorientation axes.

Case 5 is characterized by zircons, where (sub)grain boundaries formed due fragmentation, fragments rotation with respect to each other, and subsequent fracture-healing, as in the sample BH12-02_45. This case of finite deformation patterns predominates in amphibolite-facies rocks, which were affected by intensive fluid circulation that induced fracture-healing by material precipitation. Formation of the new grains occurs due to progressive subgrain rotation recrystallization, or as a result of cataclastic behavior due to high strain rates at comparatively low temperatures. Similar process occurred in zircon grains was described and discussed in detail by Rimsa et al. (2007). In this case traces of former fractures and/or (sub)grain boundaries are clearly shown as bright CL-domains and are often decorated by inclusions or pores (Fig. 2.8b, d). This deformation pattern reflects the mylonitization process taking place within the high-temperature shear zones. Fine-grained zircon found in ultramylonite, characterized by a dark CL-core and a thin bright outer rim (Fig. 2.6b), possibly represents fragments of large grains, detached from a parent grain this way.

2.6.3. CL imaging and Raman spectroscopy

Subgrain boundaries resulting from deformation type (III) often demonstrate a brighter CL signal than the dislocation-free domains (Figs. 2.3b, 2.4b, 2.5b, 2.8b). A bright CL response, linked to deformation features, has been already described in the literature (Piazolo et al., 2012; Timms and Reddy, 2009). It has been shown repeatedly that ductile deformation-related microstructures in zircon associated with compositional changes often influence the CL signal (Reddy et al., 2006, 2007; Timms et al., 2006). Therefore, a bright CL-signal is attributed not only to a high dislocation density, but also to a potential trace element enrichment/depletion along the subgrain boundaries, which is supposedly capable of disturbing the isotopic system of the bulk grain (Moser et al., 2009; Timms et al., 2006, 2011).

The results of Raman spectroscopy do not indicate any ductile deformation-related metamictization of zircon grains that belongs to type (III) deformation patterns. This is an indicator of high level of recovery in these grains. In contrast, zircons from granulite facies rocks contain homogeneously distributed dislocations within specific grain domains (IV12-06C_05, type II) or within the entire grain (IV12-06C_16, type I) leading to a decreased degree of crystallinity.

2.6.4. What deformation conditions and host environment facilitates crystal-plastic deformation in zircon?

Deformation regime of minerals depends on their properties at the given environmental conditions. The following conditions facilitate zircon crystal-plastic deformation:

Temperature. Finite deformation patterns in zircon result from various combinations of temperature-dependent deformation mechanisms (diffusion of vacancies, solution-precipitation, dislocation formation and motion by glide and climb, grain boundary sliding, etc.) (e.g. Ion et al., 1982; Poirier, 1985). In our study zircon, deformed under higher temperatures (granulite facies), mostly shows finite lattice distortion pattern type (I) and (II), and deformed under lower temperatures (amphibolite facies) – mostly distortion type (III) (Fig. 2.14a-c). However, difference in distortion patterns can be influenced not by temperature of deformation, but by duration of recovery. Recovery was presumably longer for amphibolite-facies rocks, probably, due to overprinted greenschist-facies metamorphism, resulting in the formation of dislocation-free subgrains in zircon (e.g. Hobbs, 1968; White, 1973, 1976; Gerald et al., 1983).

Differential stress. Distribution, magnitude and direction of applied stress can influence the deformation behavior. GNDs form under lithostatic pressure and applied differential stress, therefore, the dislocation density in the deformed crystal is stress-dependent (Ranalli, 1995). The orientation of differential stress with respect to the lattice orientation influences the crystal-plastic behavior (Reddy and Buchan, 2005; Kaczmarek et al., 2011). If loading is applied parallel to a certain crystallographic plane and deformation conditions are achieved at that plane, in-plane slip systems can be activated (Dahlberg et al., 2014). As we have demonstrated, specific crystallographic orientation relative to the local stress field causes glide along Miller low-indices planes (Figs. 2.4, 2.9), which activates energetically preferable slip systems.

As shown by Kenkmann (2000) and Schmid and Podladchikov (2005), simple shear causes an inhomogeneous spatial distribution of pressure and differential stress within a strong clast that is decoupled from soft matrix. This, in turn, causes an inhomogeneous distribution of strain inside the clast. We have demonstrated that these agents in some cases lead to the localized lattice distortion of specific zircon domains (finite deformation types (II), (III), cases 1 and 2). In type (II) this is caused by grain pressed against stronger phase. Specific grain shape orientation in a local stress field induces applied differential stress in specific grain domains (type (III), case 1); specific crystallographic orientation in a stress field induces applied differential stress on certain crystallographic planes (type (III), case 2).

We suggest that grain BH12-07A_04 (Fig. 2.9b) represents a natural example for the 2D models of heterogeneous stress distribution within an elliptical inclusion (Schmid and Podladchikov 2005). The portions of grain BH12-07A_04 that are distorted correspond spatially to the portions of modeled clast affected by high pressure (differential stress). The growth of the titanite next to zircon boundary (Fig. 2.9b, *Ttn*) spatially corresponds to pressure shadow in the models.

Grain shape. Specific grain shape can affect the lattice distortion patterns of zircon. For example, it has been demonstrated by Reddy et al. (2009) that grains with euhedral shape that were deformed in syn-magmatic conditions soon after crystallization are distorted in a uniform way: they are mostly deformed on their flanks with rotation axis [001] and presumable slip system $\langle 100 \rangle \{010\}$. As we have demonstrated, grains from the sample BH12-07 (Figs. 2.4, 2.9) has an euhedral short-prismatic shape and its c-axis is parallel to the stretching lineation, what likely induced specific crystal-plastic deformation mechanisms with activation of the slip system $\langle 100 \rangle \{010\}$. In sample IV12-06C zircon grains with isometric roundish shape appear to be undeformed, whereas crystal plastic deformation features are restricted to irregularly-shaped grains (Figs. 2.10, 2.12). This is consistent with above mentioned inhomogeneous stress and strain distributions during deformation, caused by specific grain shape.

Host matrix. According to the figure 2.14 a-c, more deformed rocks (i. e. stronger foliated, stronger folded) contain higher ratio of deformed zircon grains than non-foliated rocks from the same sequence.

Based on the new data, we can demonstrate that degree of coupling with host matrix is an important agent controlling zircon distortion, as well as the zircon/host difference in hardness. The strength of coupling between clast and matrix influences the magnitude of differential stress within the clast (Kenkmann, 2000) and thus affects finite deformation pattern. Difference in hardness between host and inclusion define the external stress magnitude that the host phase transfers to the inclusion. Crystal-plastic deformation of zircon decoupled with host mica results in locally high differential stress and activation of dominant slip systems (type (III) case 2). Contrastingly, when a single grain is deformed being enclosed by a strong phase and/or strongly coupled with the matrix, there is no differential stress within the grain (e.g. Mancktelow, 2008). In this case active glide planes of the grain are controlled by the host phase, and unfavorable slip planes are activated in zircon, which often forms subgrain boundaries, which correlate with host mineral deformation features (type (III), case 4). When the strong host shows gradual lattice rotation, enclosed zircon also rotates gradually with scattering of misorientation axes (type I, Fig. 2.12a). According to Kenkmann (2000),

clasts that are well coupled with the matrix can show high amount of defects, concentrated at the rim as in grain IV12-06C_05 (patterns type II).

Distribution of misorientation axes statistically depends on host mineral. Based on 60 deformed grains investigated for the current study, the density distribution of the misorientation axes have been plotted, resulting in 6 distinct areas in the pole figure (Fig. 2.14d). In the most common case, misorientation axes are spread around the $\langle 001 \rangle$ direction; a large cluster of misorientation axes is located around $\langle 320 \rangle$ and orientation clusters around $\langle 100 \rangle$ and $\langle 111 \rangle$. Less common, the misorientation axes are clustered around $\langle 201 \rangle$ and $\langle 203 \rangle$. Thus, misorientation axes do not necessarily coincide with the most common rotation axes $\langle 001 \rangle$ and $\langle 100 \rangle$ (Reddy et al., 2007; Kaczmarek et al., 2011), but can be activated in different crystal directions, controlled by a number of agents that influence the mechanical behavior of the system. Grains hosted by biotite or fine-grained matrix mostly belong to areas around $\langle 001 \rangle$ and $\langle 100 \rangle$, whereas grains hosted by feldspars preferably occupy areas around $\langle 110 \rangle$, $\langle 210 \rangle$ and $\langle 311 \rangle$. This regularity demonstrates that the ratio between clast and matrix hardness may control slip inside the clast. The higher is this ratio, the less is degree of mechanical coupling, the higher is the probability of activation of the dominant or energetically-preferable slip systems in the clast.

Internal mechanical weakness. If grain contains some mechanical weakness (e.g. inclusion, crack, pore, core-mantle structure), during deformation differential stress occurs in the domain that contains mechanical weakness (Timms et al., 2012a). The sources of internal inhomogeneous stress could be, for example, fractures, growth zoning, inclusions, pores (Macktelow, 2008). Finite deformation patterns type (III) case 3 can be described as lattice distortion that follows the internal mechanical weakness in zircon crystal structure, where the sources of internal anisotropy are mineral inclusions.

2.6.5. What factors could influence zircon finite distortion patterns?

Based on empirical observations, the grains with structure types I-III accommodate approximately the same amount of strain. Internal misorientation increases from patterns type (III) (3-10°) to type (I) (7- 25°), and the highest internal misorientation accompanied by marginal fragmentation is observed for type (II) (15-40°). We assume that differential stress increases accordingly.

At moderate differential stress and strain rate GDNs are expected to form, to glide and to climb. By dislocation glide well-defined subgrain walls are formed; and by dislocation climb subgrains are recovered (e.g. Hobbs, 1986; White, 1973, 1976; Drury and Urai, 1990). At low differential stress the rate of dislocation formation is lower, or at least the same that the rate of dislocation recovery. As a result, we observe subgrain rotation recrystallization, or polygonization, which is illustrated by deformation patterns *type (III)* (e.g. Hobbs, 1968; Gleason and Tullis, 1995).

At higher stress and strain rate GDNs are produced within the grain with higher rates; if there is no recovery, GDNs density increases, and they tangle with no opportunity to move (e.g. McLaren and Retchford, 1969; Leroux et al., 1999). Thus there is no evidence of dislocation motion and, therefore, no subgrain boundaries formation. Grain is gradually bending, resulting in the deformation patterns *type (I)*.

If the stress and strain rate increase, the increasing density of GDNs may eventually result in strain hardening and brittle deformation (Poirier, 1985). Thus, brittle deformation and marginal fragmentation of the grain, coupled with gradual bending of the lattice is observed, as in distortion patterns *type (II)*. If the high stress continues to operate, we expect complete fragmentation of a grain into a fine-grain aggregate.

In more detail, ratio between the *rate of dislocations formation* and the *rate of dislocations motion* that are stress-dependent should be responsible for the variety of lattice distortion patterns that are observed. A model of zircon crystal-plastic deformation is based on comparison of zircon with various distortion patterns. The schematic diagram proposed for different finite deformation patterns, depending on stress (GND formation/GND motion rates) and strain rate, is presented in figure 2.15.

2.7. Conclusions

The detailed investigation of the deformation behavior of fine-grained zircon in association with the host phases provides important new information on the zircon crystal-plastic deformation in common metamorphic settings:

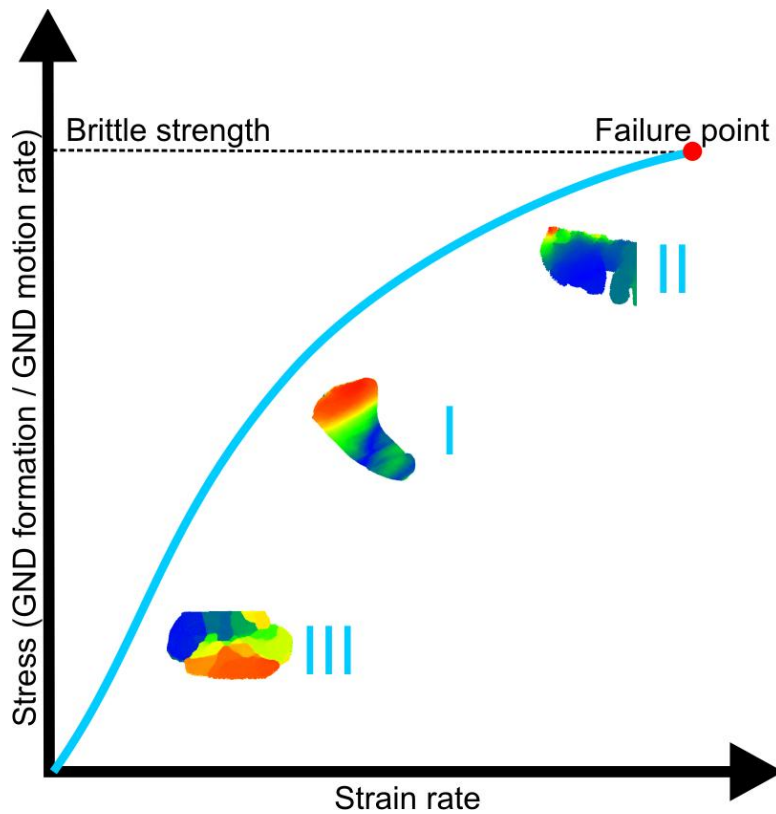


Figure 2.15. Schematic diagram for different finite crystal-plastic deformation patterns in zircon that are stress-strain rate dependent. I–III reflect deformation pattern types (I), (II) and (III), respectively. GND: geometrically necessary dislocations.

1. New microstructural and textural data describe three clearly distinguished crystal-plastic distortion patterns of zircon. Type (I) distortion patterns are characterized by comparatively large intra-granular orientation variations, subgrains and subgrain boundaries are absent. Type (II) distortion patterns are indicated by gradual bending of the crystal lattice coupled with (sub)grain boundary formation exhibiting concentric shape and significant intragranular misorientation. Distortion patterns of type (III) show the formation of well-defined low-angle boundary networks separating strain-free subgrains.

2. During deformation at amphibolite – granulite facies metamorphic conditions fine-grained zircon behaves identical to coarse-grained zircon (compared with e.g. Reddy et al., 2007; Piazzolo et al., 2012).

3. Zircon crystal-plastic deformation is facilitated by the following agents: orientation of the local stress field with respect to the zircon lattice orientation and grain shape, soft host phase(s), decoupling with the matrix and internal mechanical anisotropy.

4. Host phase(s) play the leading roles in misorientation axes distribution. In favorable cases (e.g. when the matrix is soft) the following energetically-preferable slip systems in zircon are active: $\langle 100 \rangle \{010\}$, $\langle 010 \rangle \{001\}$ and $\langle 001 \rangle \{010\}$. When the matrix is strong, and/or when the grain is

strongly coupled with its host, unfavorable slip along the high indexed crystallographic planes and unfavorable slip systems can be activated.

5. Difference in zircon finite deformation patterns I-III is considered to be dependent on the strain rate and on the ratio between dislocations formation and dislocations motion rates, which are, in turn, stress dependent.

6. Hydrothermal alteration of zircon does not obviously induce or influence crystal-plastic deformation, although in some cases a temporal and spatial relationship between those two processes can be inferred.

Acknowledgments

This study was funded by the University of Vienna (doctoral school "DOGMA", project IK 052) and the Austrian Science Foundation Fund (FWF): I471-N19, which is part of the DFG-FWF funded international research group FOR741-DACH.

The authors are grateful to Rainer Abart, Christian Auer, Claudia Beybel, Franz Biedermann, Bernhard Grasmann, Sigrid Hrabec, Matthew Huber, Hugh Rice, Claudia Trepmann, and all colleagues of the FOR741 research group for fruitful discussions and the Geologische Bundesanstalt (GBA) of Austria for access to the SEM.

Location and shear zone N	Metamorphic grade	Rock type and degree of strain	Zircon grain size range	Subgrain size range	Sample and grain N	Zircon length	Host phase(s) for zircon	Type of lattice distortion in zircon	Misorientation axes
WTW, shear zone 1	Amphibolite facies	Mylonitic strongly foliated muscovite-biotite orthogneiss	2 - 50 μm	4-15 μm	BH12-01-I, grain 29	40 μm	Muscovite	No lattice distortion	-
WTW, shear zone 1	Amphibolite facies	Ultramylonite, core of the shear zone in granitic orthogneisses	5 - 20 μm	2-5 μm	BH12-01-II, grain 22,	20 μm	Plagioclase	Type (III)	<103>
WTW, shear zone 1	Amphibolite facies	Foliated biotite orthogneiss	2 - 50 μm	2-15 μm	BH12-02, grain 45	50 μm	Plagioclase and quartz	Cataclastic deformation	<113> and <311>
WTW, shear zone 1	Amphibolite facies	Non-foliated granitic orthogneisses	2 - 50 μm	1-7 μm	BH12-04, grain 11	22 μm , 5 μm	Plagioclase	Type (III)	<110> - <320>
WTW, shear zone 2	Amphibolite facies	Weakly foliated granitic orthogneisses	10 - 100 μm	7-12 μm	BH12-05, grain 07	50 μm	Biotite	Type (III)	Cross-slip
WTW, shear zone 2	Amphibolite facies	Mafic dyke, strongly foliated	10 - 30 μm	1-10 μm	BH12-07, grains 03a, 04, 28, 31b	15-25 μm	Biotite, chlorite	Type (III)	<001>
WTW, shear zone 2	Amphibolite facies	Mafic dyke, strongly foliated	10 - 30 μm	1-10 μm	BH12-07, grain 15a	15 μm	Biotite	Type (III)	<100> and <001>
IVZ, shear zone 3	Granulite facies	Stronalite (non-foliated metasediment)	20 - 50 μm	0,5-3 μm	IV12-06C, grain 05	22 μm	Garnet and plagioclase	Type (II)	<100> and <331>
IVZ, shear zone 3	Granulite facies	Stronalite (non-foliated metasediment)	20 - 50 μm	-	IV12-06C, grain 16	53 μm	Plagioclase	Type (I)	<001>

Table 2.1. List of samples and zircon grains, discussed in this study, containing the basic information. WTW = Western Tauern Window, IVZ = Ivrea-Verbano Zone.

Type (I) gradual bending, no subgrain boundaries		Type (II) both gradual bending and subgrain boundaries		Type (III) network of low-angle boundaries		
Description and conditions	Examples	Description and conditions	Examples	Description	Cases and conditions	Examples
Free dislocation density, no subgrain/subgrain boundary formation, gradual bending of the lattice. Deformation together with bending strong matrix.	IV12-06C_16 (Fig. 2.12); “type I lattice distortions” in Piazolo et al., 2012; BP03/3 in MacDonald et al., 2013; LG-2a Grain 17 in Moser et al., 2009; area A in Reddy et al., 2007; zircon 5 from 73215,122 in Timms et al., 2012b.	Local deformation of the rim(s) due to collision of crystals/mineral grains or deformation within fine-grained matrix; presence of 2 and more misorientation axes often observed. Inhomogeneous pressure distribution required.	IV12-06C_05 (Figs. 2.10, 2.11); “type II lattice distortions” in Piazolo et al., 2012; GG09/1 in MacDonald et al., 2013; area B and C in Reddy et al., 2007; grain from GST15 (area A) in Timms et al., 2006 and Timms and Reddy, 2009; grains 5 and 8 from Jhs2PON4, Timms and Reddy, 2009.	Formation of network of well-defined subgrain boundaries that separate strain-free subgrains. Subgrains are rotated with respect to each other along subgrain boundaries.	Case 1 Deformation of specific grain domains. Favorable shape orientation in the local stress field; decoupling from the matrix.	BH12-05B_07 (Fig. 2.3) BH12-07A_04 (Fig. 2.9b); DP02/7 in MacDonald et al., 2013; V09-237 G4 in Moser et al., 2011; UX in Timms and Reddy, 2009. Possibly Reddy et al., 2009.
					Case 2 Activation of dominant slip system(s). Favorable crystallographic orientation in the local stress field and decoupling with the host phase required.	BH12-07A_03a (Fig. 2.9a), BH12-07A_04 (Fig. 2.9b), BH12-07B_15a (Fig. 2.5), BH12-07B_28 (Fig. 2.4), BH12-07B_31b (Fig. 2.9c). Type of distortion III, Piazolo et al., 2012.
					Case 3 Low-angle boundaries emanating from mineral inclusion. Internal heterogeneity required.	BH12-01B_22 (Fig. 2.6), BH12-07A_04 (Fig. 2.9b); Timms et al. (2012a).
					Case 4 Depends on the configuration of the host phase boundaries, coupling with the matrix required.	BH12-04_11 (Fig. 2.7), BH12-07A_03a (Fig. 2.9a); BP06/3 in MacDonald et al., 2013 (?).
					Case 5 Brittle deformation with rotation of fragments, followed by the fracture healing.	BH12-02_45 (Fig. 2.8); Rimsa et al., 2007.

Table 2.2. Types of finite deformation patterns with examples from the present study and from literature. Different end-member cases characterizing type (III) lattice distortion describe various mechanisms for finite deformation pattern formation observed.

References

- Akchurin, M. Sh., Zakalyukin, R. M., Kaminsky, A. A., Kuppenko I. I.: Role of Twinning in Plastic Deformation, *Crystallogr. Rep.*, 55, 621–625, 2010.
- Bachmann, F., Hielscher, R., Schaeben, H.: Texture Analysis with MTEX – Free and Open Source Software Toolbox, *Sol. St. Phen.*, 160, 63-68, 2010.
- Bachmann, F., Hielscher, R., Schaeben, H.: Grain detection from 2d and 3d EBSD data-specification of the MTEX algorithm, *Ultramicroscopy*, 111, 1720-1733, 2011.
- Barboza, S.A., Bergantz, G.W., Brown, M.: Regional granulite facies metamorphism in the Ivrea zone: is the Mafic Complex the smoking gun or a red herring? *Geology*, 27, 447–450, 1999.
- Behrmann, J.H.: Crystal plasticity and superplasticity in quartz: a natural example, *Tectonophysics*, 115, 101-129, 1985.
- Brodie, K.H., Rutter, E.H., Evans, P.: On the structure of the Ivrea-Verbano Zone (northern Italy) and its implications for present-day lower continental crust geometry, *Terra Nova*, 4, 34-39, 1992.
- Cherniak, D. J. and Watson E. B.: Diffusion in Zircon, in: *Zircon*, Hanchar, J. M., Hoskin, P. W. O., eds., Mineralogical Society of America and Geochemical Society, *Reviews in Mineralogy and Geochemistry*, Washington D.C., 53, 113-143, 2003.
- Cherniak, D.J., Lanford, W.A., Ryerson, F.J.: Lead diffusion in apatite and zircon using ion implantation and Rutherford Backscattering techniques, *Geochim. Cosmochim. Ac.*, 55, 1663-1673, 1991.
- Corfu, F., Hanchar, J. M., Hoskin P. W.O., Kinny, P.: Atlas of zircon textures, in: *Zircon*, Hanchar, J. M., Hoskin, P. W. O., eds., Mineralogical Society of America and Geochemical Society, *Reviews in Mineralogy and Geochemistry*, Washington D.C., 53, 468-500, 2003.
- Dahlberg, C.F.O., Saito, Y., Öztop, M.S., Kysar, J.W.: Geometrically necessary dislocation density measurements associated with different angles of indentations, *Int. J. Plasticity*, 54, 81–95, 2014.

- Davis, D.W., Williams, I.S., Krogh, T.E.: Historical development of zircon geochronology, in: Zircon, Hanchar, J. M., Hoskin, P. W. O., eds., Mineralogical Society of America and Geochemical Society, Reviews in Mineralogy and Geochemistry, Washington D.C., 53, 145-181, 2003.
- Drury, M.R. and Urai, J.L.: Deformation-related recrystallization processes, *Tectonophysics*, 172, 235-253, 1990.
- Erdmann, S., Wodicka, N., Jackson, S.E., Corrigan, D.: Zircon textures and composition: refractory recorders of magmatic volatile evolution? *Contrib. Mineral. Petr.*, 165, 45–71, 2013.
- Erickson, T.M., Cavosie, A. J., Moser, D.E., Barker, I.R., and Radovan, H.A.: Correlating planar microstructures in shocked zircon from the Vredefort Dome at multiple scales: Crystallographic modeling, external & internal imaging, and EBSD structural analysis, *Am. Mineral.*, 98, 53-65, 2013a.
- Erickson, T.M., Cavosie, A. J., Moser, D.E., Barker, I.R., and Radovan, H.A., Wooden, J.: Identification and provenance determination of distally transported, Vredefort-derived shocked minerals in the Vaal River, South Africa using SEM and SHRIMP-RG techniques, *Geochim. Cosmochim. Ac.*, 107, 170-188, 2013b.
- Ferguson, C.C., Lloyd, G.E., and Knipe, R.J.: Fracture mechanics and deformation processes in natural quartz: a combined Vickers indentation, SEM and TEM study, *Can. J. Earth Sci.*, 24, 544–555, 1987.
- Flowers, R.M., Schmitt, A.K., Grove, M.: Decoupling of U–Pb dates from chemical and crystallographic domains in granulite facies zircon, *Chem. Geol.*, 270, 20–30, 2010.
- Geisler, T., Ulonska, M., Schleicher, H., Pidgeon, R. T., Van Bronswijk, W.: Leaching and differential recrystallization of metamict zircon under experimental hydrothermal conditions, *Contrib. Mineral. Petr.*, 141, 53–65, 2001.
- Geisler, T., Kurtz, R., Pidgeon, R.T., van Bronswijk, W.: Transport of uranium, thorium and lead in metamict zircon under low-temperature hydrothermal conditions, *Chem. Geol.*, 191, 141-154, 2002.
- Geisler, T., Pidgeon, R. T., Kurtz, R., Bronswijk, W., Schleicher H.: Experimental hydrothermal alteration of partially metamict zircon, *Am. Mineral.*, 88, 1496-1513, 2003.

- Gerald, F.J.D., Etheridge, M.A., Vernon, R.H.: Dynamic recrystallization in a naturally deformed albite, *Texture Microstruct.*, 5, 219-237, 1983.
- Gleason, G.C. and Tullis, J.: A flow law for dislocation creep of quartz aggregates determined with the molten salt cell, *Tectonophysics*, 247, 1-23, 1995.
- Goetze, J., Ploetze, M., Habermann, D.: Origin, spectral characteristics and practical applications of the cathodoluminescence (CL) of quartz - a review, *Miner. Petrol.*, 71, 225-250, 2001.
- Grange, M.L., Pidgeon, R.T., Nemchin, A.A., Timms, N.E., Meyer, C.: Interpreting U–Pb data from primary and secondary features in lunar zircon, *Geochim. Cosmochim. Ac.*, 101, 112–132, 2013.
- Hobbs, B.E.: Recrystallization of single crystals of quartz, *Tectonophysics*, 6, 353-401, 1968.
- Hobbs, B.E.: The geological significance of microfabric analysis, in: Preferred orientation in deformed metal and rocks. An introduction to modern texture analysis, Wenk, H.R., ed., Elsevier Inc., 463-484, 1985.
- Hofmann, A.E., Valley, J.W., Watson, E.B., Cavosie, A.J., Eiler J.M.: Sub-micron scale distribution of trace elements in zircon, *Contrib. Mineral. Petr.*, 158, 317-335, 2009.
- Ion, S.E., Humphreys, F.J., White, S.H.: Dynamic recrystallization and the development of microstructure during the high temperature deformation of magnesium, *Acta Metall.*, 30, 1909-1919, 1982.
- Jenkins, C.H.M. and Mellor, G.A.: Investigation of the behaviours of metals under deformation at high temperature. I – structural changes in mild steel and commercial iron during creep, *J. Iron Steel Inst.*, 132, 179-227, 1935.
- Kaczmarek, M. A., Reddy, S. M., Timms, N. E.: Evolution of zircon deformation mechanisms in a shear zone (Lanzo massif, Western-Alps). *Lithos*, 127, 414-426, 2011.
- Kenkmann, T.: Processes controlling the shrinkage of porphyroclasts in gabbroic shear zones, *J. Struct. Geol.*, 22, 471-487, 2000.
- Klötzli, U.S., Sinigoi, S., Quick, J.E., Demarchi, G., Tassinari, C.C.G., Sato, K., Günes, Z.: Duration of igneous activity in the Sesia Magmatic System and implications for high-temperature metamorphism in the Ivrea–Verbano deep crust, *Lithos*, 206–207, 19–33, 2014.

- Lloyd, G.E.: Grain boundary contact effects during faulting of quartzite: an SEM/EBSD analysis, *J. Struct. Geol.*, 22, 1675–1693, 2000.
- MacDonald, J.M., Wheeler, J., Harley, S.L., Mariani, E., Goodenough, K.M., Crowley, Q., Tatham, D.: Lattice distortion in a zircon population and its effects on trace element mobility and U–Th–Pb isotope systematics: examples from the Lewisian Gneiss Complex, northwest Scotland, *Contrib. Mineral. Petr.*, 166, 21–41, 2013.
- Mainprice, D., Hielscher, R., Schaeben, H.: Calculating anisotropic physical properties from texture data using the MTEX open source package, in: *Deformation Mechanisms, Rheology and Tectonics: Microstructures, Mechanics and Anisotropy*, Prior, D.J., Rutter, E.H., Tatham, D. J., eds., Geological Society, London, Special Publications, 360, 175-192, 2011.
- Mancktelow, N.S.: Tectonic pressure: theoretical concepts and modelled examples, *Lithos*, 103, 149-177, 2008.
- Mancktelow, N.S.: Behaviour of an isolated rimmed elliptical inclusion in 2D slow incompressible viscous flow, *J. Struct. Geol.*, 46, 235-254, 2013.
- McLaren, A.C. and Retchford, J.A.: Transmission electron microscope study of the dislocations in plastically deformed synthetic quartz, *Phys. Status Solidi*, 33, 657, 1969.
- McLean, D.: Crystal fragmentation in aluminium during creep, *J. Inst. Metals*, 81, 287-292, 1952.
- Miller, C., Konzett, J., Tiepolo, M., Armstrong, R.A., Thöni, M.: Jadeite-gneiss from the eclogite zone, Tauern Window, Eastern Alps, Austria: metamorphic, geochemical and zircon record of a sedimentary protholith, *Lithos*, 93, 68-88, 2007.
- Moser, D.E., Davis, W.J., Reddy, S.M., Flemming, R.L., Hart, R.J.: Zircon U–Pb strain chronometry reveals deep impact-triggered flow, *Earth and Planet. Sc. Lett.*, 277, 73–79, 2009.
- Moser, D. E., Cupelli, C.L., Barker, I.R., Flowers, R.M., Bowman, J.R., Wooden, J., Hart, J.R.: New zircon shock phenomena and their use for dating and reconstruction of large impact structures revealed by electron nanobeam (EBSD, CL, EDS) and isotopic U–Pb and (U–Th)/He analysis of the Vredefort dome, *Can. J. Earth Sci.*, 48, 117–139, 2011.
- Nemchin, A., Timms, N. E., Pidgeon, R., Geisler, T., Reddy, S. M., Meyer, C.: Timing of crystallization of the lunar magma ocean constrained by the oldest zircon, *Nat. Geosci.*, 2, 133-136, 2009.

- Nye, J.F.: Some geometrical relations in dislocated crystals, *Acta Metall.*, 1, 153–162, 1953.
- Pennacchioni, G. and Mancktelow, N.S.: Nucleation and initial growth of a shear zone network within compositionally and structurally heterogeneous granitoids under amphibolite facies conditions, *J. Struct. Geol.*, 29, 1757-1780, 2007.
- Piazolo, S., Austrheim, H., Whitehouse, M.: Brittle-ductile microfabrics in naturally deformed zircon: Deformation mechanisms and consequences for U-Pb dating, *Am. Mineral.*, 97, 1544–156, 2012.
- Poirier, J. P.: *Creep of Crystals: High-Temperature Deformation Processes in Metals, Ceramics and Minerals*, Cambridge Earth science series, Cook, A.H., Harland, W.B., Hughes, N.F., Putnis, A., Sclater, J.G., Thomson, M.R.A., eds., Cambridge University Press, Leipzig, 260 pp., 1985.
- Poirier, J.P. and Nicolas, A.: Deformation-induced recrystallization by progressive misorientation of subgrain-boundaries, with special reference to mantle peridotites, *J. Geology*, 83, 707-720, 1975.
- Prior, D.J.: Problems in determining the orientation of crystal misorientation axes for small angular misorientations, using electron backscatter diffraction in the SEM, *J. Microsc.*, 195, 217-225, 1999.
- Quick, J.E., Sinigoi, S., Peressini, G., Demarchi, G., Wooden, J.L., Sbisà, A.: Magmatic plumbing of a large Permian caldera exposed to a depth of 25 km, *Geology*, 37, 603-606, 2009.
- Raj, R. and Ashby M.F.: On grain boundary sliding and diffusional creep, *Metall. Trans.*, 2, 1113-1127, 1971.
- Ranalli, G.: *Rheology of the Earth*, second edition, Chapman & Hall, London, 413 pp., 1995.
- Reddy, S.M. and Buchan, C.: Constraining kinematic rotation axes in high-strain zones: a potential microstructural method? in: *Deformation mechanisms, rheology and tectonics: from mineral to the lithosphere*, Gapais, D., Brun, J.P., Cobbold, P.R., eds., 243, Special publications, Geological society, London, pp. 1-10.
- Reddy, S.M. and Timms, N.E.: Deformation of zircon and implications for geochemistry and geochronology, *Source Abstracts with Programs, Geological Society of America*, 42, 634, 2010.

- Reddy, S.M., Timms, N.E., Trimby, P., Kinny, P.D., Buchan C., Blake K.: Crystal-plastic deformation of zircon: a defect in the assumption of chemical robustness, *Geology*, 34, 257-260, 2006.
- Reddy, S.M., Timms, N.E., Pantleon, W., Trimby, P.: Quantitative characterization of plastic deformation of zircon and geological implications, *Contrib. Mineral. Petr.*, 153, 625–645, 2007.
- Reddy, S.M., Timms, N.E., Hamilton, P.J., Smyth, H.R.: Deformation-related microstructures in magmatic zircon and implications for diffusion, *Contrib. Mineral. Petr.*, 157, 231–244, 2009.
- Redler, C., Johnson, T. E., White R. W., Kunz, B. E.: Phase equilibrium constraints on a deep crustal metamorphic field gradient: metapelitic rocks from the Ivrea Zone (NW Italy), *J. Metamorph. Geol.*, 30, 235–254, 2012.
- Rimsa, A., Whitehouse, M.J., Johansson, L., Piazzolo, S.: Brittle fracturing and fracture healing of zircon: An integrated cathodoluminescence, EBSD, U-Th-Pb, and REE study. *Am. Mineral.*, 92, 1213-1224, 2007.
- Roters, F., Eisenlohr, P., Hantcherli, L., Tjahjanto, D.D., Bieler, T.R., Raabe, D.: Overview of constitutive laws, kinematics, homogenization and multiscale methods in crystal plasticity finite-element modeling: Theory, experiments, applications, *Acta Mater.*, 58, 1152–1211, 2010.
- Rutter, E.H., Brodie, K.H., James T., Burlini, L.: Large-scale folding in the upper part of the Ivrea-Verbano zone, NW Italy, *J. Struct. Geol.*, 29, 1-17, 2007.
- Schwartz, J.J., John, B.E., Cheadle, M.J., Wooden, J.L., Mazdab, F., Swapp, S., Craig, B., Grimes, C.B.: Dissolution–reprecipitation of igneous zircon in mid-ocean ridge gabbro, Atlantis Bank, Southwest Indian Ridge, *Chem. Geol.*, 274, 68–81, 2010.
- Schmid, D.W. and Podladchikov, Y.Yu.: Are isolated stable rigid clasts in shear zones equivalent to voids? *Tectonophysics*, 384, 233–242, 2004.
- Schmid, D.W. and Podladchikov, Y.Yu.: Mantled porphyroclast gauges, *J. of Struct. Geol.*, 27, 571–585, 2005.
- Sellars, C.M.: Recrystallization of metals during hot deformation, *Phil. Trans. R. Soc. Lond.*, 135, 513-516, 1978.

- Selverstone, J.: Petrologic constraints on imbrication, metamorphism, and uplift in the SW Tauern Window, Eastern Alps, *Tectonics*, 4, 687-704, 1985.
- Selverstone, J., Morteani, G., Staude, J.-M., Fluid channelling during ductile shearing: transformation of granodiorite into aluminous schist in the Tauern Window, Eastern Alps, *J. Metamorp. Geol.*, 9, 419–431, 1991.
- Silver, L.T., Deutsch, S., Uranium-lead isotopic variations in zircons: A case study, *J. Geol.*, 71, 721-758, 1963.
- Sinigoi, S., Quick, J.E., Demarchi, G., Klötzli, U.: The role of crustal fertility in the generation of large silicic magmatic systems triggered by intrusion of mantle magma in the deep crust, *Contrib. Mineral. Petr.*, 162, 691-707, 2011.
- Sturm, R. and Steyrer, H. P.: Use of accessory zircon for the quantification of volume changes in ductile shear zones cutting plutonic rocks, *Chem. Erde-Geothem.*, 63, 31-54, 2003.
- Timms, N.E. and Reddy, S.M.: Response of cathodoluminescence to crystal-plastic deformation in zircon, *Chem. Geol.*, 261, 11–23, 2009.
- Timms, N.E., Kinny, P., Reddy, S.M.: Enhanced diffusion of uranium and thorium linked to crystal plasticity in zircon, *Geochem. T.*, 7, 10, doi: 10.1186/1467-4866-7-10, 2006.
- Timms, N.E., Kinny, P., Reddy, S.M., Evans K., Clark C., Healy D.: Relationship among titanium, rare earth elements, U–Pb ages and deformation microstructures in zircon: Implications for Ti-in-zircon thermometry, *Chem. Geol.*, 280, 33–46, 2011.
- Timms, N.E., Reddy, S.M., Gerald, F.J.D., Green, L., Muhling, J.R.: Inclusion-localised crystal-plasticity, dynamic porosity, and fast-diffusion pathway generation in zircon, *J. of Struct. Geol.*, 35, 78-89, 2012a.
- Timms, N.E., Reddy, S.M., Healy, D., Nemchin, A.A., Grange, M.L., Pidgeon, R.T., Hart, R.: Resolution of impact-related microstructures in lunar zircon: a shock-deformation mechanism map, *Meteorit. Planet. Sci.*, 47, 120–141, 2012b.
- Trimby, P.W. and Prior, D.J.: Microstructural imaging techniques: a comparison of optical and scanning electron microscopy in the study of deformed rocks, *Tectonophysics*, 303, 71–81, 1999.

- Urai, J.L., Means, W.D., Lister, G.S.: Dynamic recrystallization of minerals, in: Mineral and Rock Deformation (Laboratory Studies), Heard, H.C. ed., Geophysical Monograph of the American Geophysical Union, Washington D.C., 36, 161–200, 1986.
- Veselá, P., Söllner, F., Finger, F., Gerdes, A.: Magmato-sedimentary Carboniferous to Jurassic evolution of the western Tauern window, Eastern Alps (constraints from U-Pb zircon dating and geochemistry), *Int. J. Earth Sci.*, 100, 993–1027, 2011.
- Wang, L., Zhou, J., Zhang, S., Liu Y., Dong, S.: Effects of accommodated grain boundary sliding on triple junction nanovoid nucleation in nanocrystalline materials, *Mech. Mater.*, 71, 10–20, 2014.
- Watson, E.B., Wark, D.A., Thomas, J.B.: Crystallization thermometers for zircon and rutile, *Contrib. Mineral. Petr.*, 151, 413-433, 2006.
- Wheeler, J., Mariani, E., Piazzolo, S., Prior, D.J., Trimby, P.J., Drury, M.R.: The weighted Burgers vector: a new quantity for constraining dislocation densities and types using electron backscatter diffraction on 2D sections through crystalline materials, *J. Microsc.-Oxford*, 233, 482–494, 2008.
- White, S.: Syntectonic recrystallization and texture development in quartz, *Nature*, 244, 276-278, 1973.
- White, S.: The effects of strain and microstructure fabrics and deformation mechanisms in quartzite. *Phil. Trans. R. Soc. London*, 283, 69-86, 1976.
- Whitney, D.L., Broz, M., Cook, R.F.: Hardness, toughness, and modulus of some common metamorphic minerals, *Am. Mineral.*, 92, 281–288, 2007.

3.0. On the relationship between deformation microstructures in zircon and the kinematic framework of the shear zone

Elizaveta Kovaleva¹, Urs Klötzli¹, John Wheeler², Gerlinde Habler¹

¹Department of Lithospheric Research, Faculty of Earth Sciences, Geography and Astronomy, University of Vienna, Althanstrasse 14, A-1090 Vienna, Austria

²Department of Earth, Ocean and Ecological Sciences, School of Environmental Sciences, University of Liverpool, L69 3GP, Liverpool, United Kingdom

Article is in preparation for submission to Geology

Abstract

This study aims for describing the effect of zircon crystallographic orientation with respect to the macroscopic kinematic framework on deformation microstructures and misorientation axes in zircon.

Microstructural and textural analyses of crystal-plastically deformed zircon were obtained from a variety of strained rocks of different lithologies showing well-developed kinematic indicators. Analyses of zircon have been done in situ using crystallographic orientation mapping by electron backscatter diffraction. New data show strong geometrical relationships between orientations of: (i) $\langle c \rangle$ (c-axes) of crystal-plastically deformed zircons, (ii) misorientation axes of crystal-plastically deformed zircons and (iii) the orientation of mylonitic foliations and stretching lineations of the respective sample. Crystal-plastically deformed zircons in shear zones usually have $\langle c \rangle$ parallel to the mylonitic foliation plane; crystals that $\langle c \rangle$ oriented at high angle to the foliation are undeformed or only cataclastically deformed. Zircons with $\langle c \rangle$ aligned parallel to the foliation and parallel or normal to the stretching lineation develop misorientation and rotation axes parallel to $\langle 001 \rangle$, with activation of the $\langle 100 \rangle \{010\}$ slip system. Zircons with $\langle c \rangle$ aligned parallel to the foliation and at 45° with respect to the lineation reflect either two misorientation axes or one high-indices misorientation axis.

Consequently there is a strong geometric control of the macroscopic kinematic rotation axis on the deformation behavior of zircon. Based on the derived statistics, we can justify the initial

crystallographic orientation of zircon in kinematic framework regarding the amount of crystal-plastic deformation and orientation of misorientation axes in zircon. Relationships between zircon deformation and macroscopic kinematic frame potentially have important implications for zircon geochronology. If deformation events resulted in zircon crystal-plastic deformation and in rejuvenation of zircon isotopic system, they may be dated.

3.1. Introduction

Crystal-plastic deformation in zircon has been documented for different geological settings: syn-magmatic deformation (Reddy et al., 2009; Timms and Reddy, 2009; MacDonald et al., 2013), deformation in HT shear zones (Reddy et al., 2006, 2007; Timms et al., 2006, 2011; Timms and Reddy, 2009; Flowers et al., 2010; Kaczmarek et al., 2011; Piazzolo et al., 2012; Kovaleva et al., 2014), impact-related lattice distortion (Leroux et al., 1999; Moser et al., 2009, 2011; Nemchin et al., 2009; Timms et al., 2012; Grange et al., 2013).

Reddy and Buchan (2005) suggested the existence of a geometric control of the kinematic framework during simple shear deformation on the activity of slip systems and misorientation axes in calcite. This concept was used in the model of Kaczmarek et al. (2011) describing crystal-plastic deformation of zircon during bulk simple-shear. However, although these authors have documented the alignment of zircon long axes parallel to the stretching lineation, the misorientation axes have various orientations independent of the kinematic framework, which is explained by a later rigid body rotation of zircon grains.

In our study we present microstructures and textures of zircon from high-strained rocks and demonstrate that crystal-plastic deformation of zircon is, in fact, controlled by the zircon <c> orientation with respect to the macroscopic kinematic rotation axis. We emphasize the importance of studying individual crystals in situ, taking into account crystallographic orientation relative to the foliation, stretching lineation and host phases.

3.2. Sample material

Different rock types deformed by simple shear were sampled at four different localities:

3.2.1. Meta-lamprophyric dyke (sample BH12-07), Tauern Window (Zillertal, Tyrol, Austria)

A detailed description of sample and the hosting shear zone (Fig. 3.S1a, e) is given in Kovaleva et al. (2014).

3.2.2. STG13, Porphyritic biotite-meta-granite (sample STG13), Ötztal-Stubai Crystalline (Falbeson, Stubaital, Austria)

The polymetamorphic Upper Austroalpine Ötztal-Stubai crystalline basement complex (ÖSC) consists largely of paragneisses and micaschists with abundant intercalations of various pre-Variscan meta-igneous gneisses (Klötzli et al., 1997; Thöni and Miller, 2004). The investigated sample stems from a ca. 10-cm thick shear zone in a coarse-grained K-feldspar porphyritic biotite-meta-granite body (Fig. 3.S1b). Strongly foliated fine-grained rocks (Fig. 3.S1f) contain lenses of plagioclase and quartz, interlayered with fine-grained mica and minor amphibole. Zircon crystals are euhedral, isometric or elongated with lengths from 10 to 100 μm and aspect ratios of 1:1-1:3.

3.2.3. Sillimanite-biotite-garnet gneiss (sample IV12-05), Ivrea-Verbano Zone (Forno, Val Strona, Northern Italy, N45°59'46.46"/E8°21'38.65")

Sillimanite-biotite-garnet gneisses are interlayered with massive, non-foliated granulites (Kovaleva et al., 2014; Figs. 3.S1c, g). Elongated garnet and sillimanite crystals (90% of the sample) generate a weak foliation whereas the stretching lineation is formed by biotite. Quartz and ilmenite-rutile-quartz intergrowths crystallized in strain shadows of garnet and sillimanite. Zircons in the matrix have lengths of 30 to 100 μm ; in garnet they form euhedral roundish crystals with 1:1-1:3 aspect ratios; in cracks zircon shows irregularly serrated phase boundaries (Fig. 3.S4a-b); in sillimanite zircon grain shapes are often irregular (e.g. Fig. 3.S4d).

3.2.4. Felsic mylonite (IV12-07 and IVZ02-12), Ivrea-Verbano Zone (Forno, Val Strona, Northern Italy)

A detailed description of these samples (Fig. 3.S1d, h, i) and their sampling sites is given in Kovaleva et al. (in press). Zircon grains are hosted by a fine-grained mylonitic matrix consisting of quartz, plagioclase, biotite and ilmenite and vary in size from 30 to 100 μm representing isometric, euhedral or roundish crystals (Figs. 3.S5-3.S7).

3.3. Analytical method

Electron backscatter diffraction (EBSD) analysis and forward-scattered electron (FSE) imaging in a Field-emission gun SEM was obtained from zircons and host phases in chemically-polished thin sections. We used a FEI Quanta 3D FEG instrument equipped with a Digiview IV EBSD camera. EBSD data were collected using the OIM v6.21 software. Orientation maps were obtained from beam scanning in hexagonal grid mode at step sizes of 0.1 – 0.2 μm . Indexing of raw data for zircon was successful for 99.99% of the data points. Orientation contrast images were collected using a forward scatter detector mounted on the EBSD-tube of the instrument. The analytical settings are detailed in Kovaleva et al. (2014).

EBSD data are presented in the sample reference frame as color-coded misorientation maps, showing relative misorientation of each data point with respect to a reference point (white marker). The orientations of the crystallographic axes are plotted as lower hemisphere equal area projections using the same color-code as for the corresponding EBSD map. EBSD maps and pole figures were produced using the EDAX OIM v6.2.1 Analysis software, whereas the local misorientation map, the misorientation axes orientations and density contours in inverse pole figures were visualized with the MTEX 3.4.0 toolbox for MATLAB (Bachmann et al., 2010; Mainprice et al., 2011). Geometrically necessary dislocation densities were derived using Weighted Burgers Vector (WBV) calculations (Wheeler et al., 2009). Rectangular areas with WBV components were calculated over the EBSD maps with the MATLAB toolbox CrystalScape 1.3.

3.4. Zircon microstructures and textures

3.4.1. Meta-lamprophyre

Crystal-plastically-deformed zircons from sample BH12-07 reveal strain-free subgrains separated by low-angle boundaries (Fig. 3.52), representing lattice distortion type (III) (according to Piazzolo et al., 2012 and Kovaleva et al., 2014). $\langle C \rangle$ of deformed crystals are roughly aligned in the foliation plane (Fig. 3.1a, solid circles). Zircons with $\langle c \rangle$ oriented parallel to foliation plane have one or two misorientation axis, zircons with $\langle c \rangle$ at low angle to foliation plane have two or more misorientation axes (Fig. 3.1a, solid circles), whereas zircon 20b also shows brittle deformation. Crystals with $\langle c \rangle$ oriented at $> 15^\circ$ to the foliation plane remain undeformed (Fig. 3.1a, open circles).

Zircon with $\langle c \rangle$ oriented approximately at 90° to the lineation has misorientation axes maxima at [001] direction (Figs. 3.1a, 3.S2g; grain 24b). Grains, which $\langle c \rangle$ are close to the stretching lineation, have misorientation and rotation axes parallel to [001] (Figs. 3.1a; 3.S2a, c, h-j; grains 03a, 04, 26, 28, 31b). The weakly strained grain 03b (Fig. 3.S2b), however, represents an exception as plastic deformation affected only a small portion of the grain at rather intragranular orientation variations; and the determination of misorientation axis for low-angle misorientations can generate significant errors (Reddy and Buchan, 2005). Zircons with $\langle c \rangle$ lying parallel to the foliation plane and at an angle of about 45° with the lineation have at least two clusters of misorientation axes (Figs. 3.1a, 3.S2d-e; grains 15a, 20a).

Zircons enclosed in rheologically weaker phases (biotite, chlorite) usually reveal misorientation axes parallel to the main crystallographic directions in zircon, $\langle 001 \rangle$ and $\langle 100 \rangle$ (Fig. 3.S2a, c, d, h-j; grains 03a, 04, 15a, 26, 28, 31b). Zircons enclosed in rheologically strong phases (plagioclase, titanite) usually show a complicated misorientation axes distribution – with several clusters and high Miller indices (Fig. 3.S2e-g; grains 20a, 20b, 24b).

3.4.2. Porphyritic biotite-meta-granite

Crystallographic orientation data on crystal-plastically deformed zircon in sample STG13 are presented in figures 3.1b and 3.S3. Zircon grains show gradual lattice rotation without formation of low angle boundaries or lattice distortion type (I) (Figs. 3.S3b-c and e-f) and local deformation at margins with semi-circular subgrain boundaries (distortion type (II), Figs. 3.S3a and e).

Grains with $\langle c \rangle$ lying subparallel to the foliation plane mostly display one strong cluster of misorientation axes (Figs. 3.1b; 3.S3a-b, d; grains 18, 20, 30). Grains with $\langle c \rangle$ at an angle of $>15^\circ$ to foliation, besides of crystal-plastic deformation with at least two clusters of misorientation axes, reveal intense brittle deformation (Figs. 3.1b, 3.S2c and e; grains 25 and 33).

Zircon with $\langle c \rangle$ subparallel to foliation and at about 90° to stretching lineation reveals misorientation axes clustering close to [001], and rotation axis parallel to the [001] direction (Fig. 3.S3d; grain 30). Zircons that have $\langle c \rangle$ parallel to foliation and at about 45° to stretching lineation reveal misorientation and rotation axes parallel to [001] direction (Figs. 3.1b; 3.S3a-b; grains 18 and 20) or have 2 clusters of misorientation axes (Fig. 3.S3f; grain 36).

All crystals except of grain 33 (Fig. 3.S3e, hosted by biotite) are surrounded by phase mixtures dominated by rheologically strong feldspars.

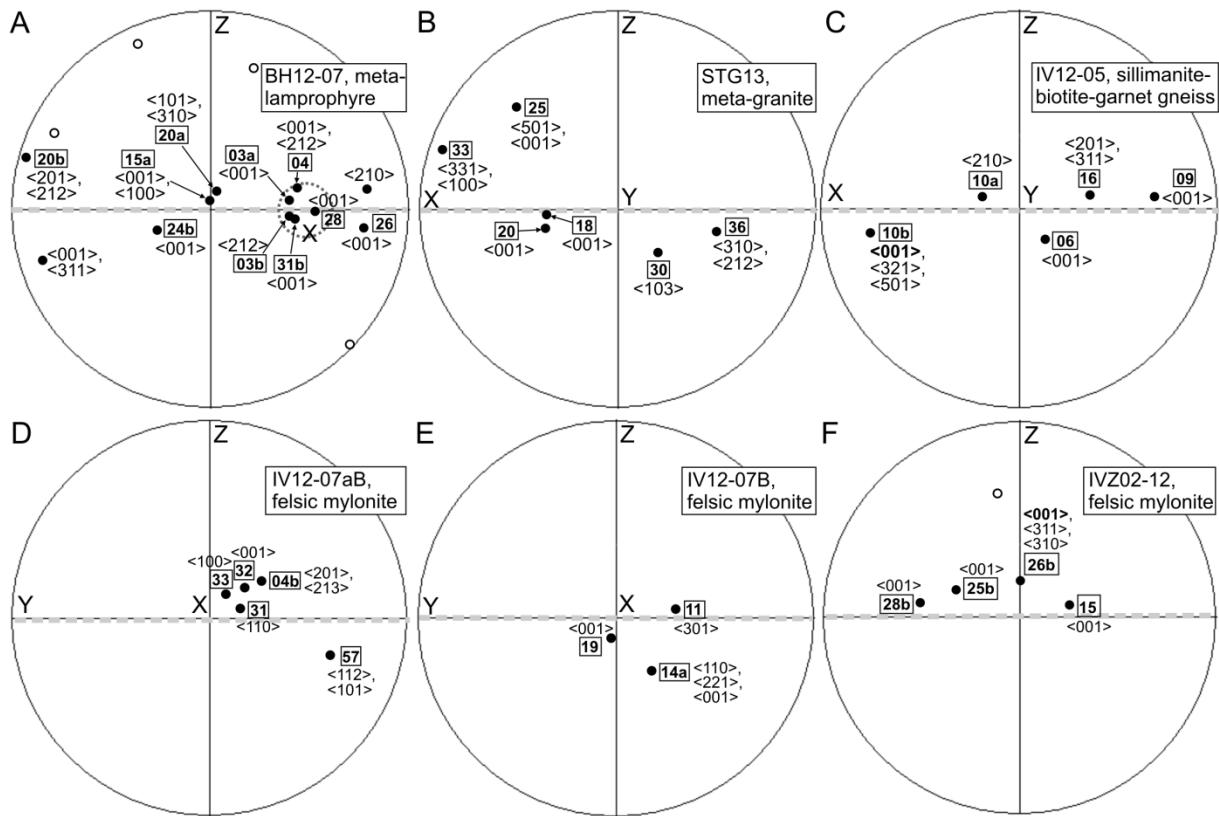


Figure 3.1. Pole figures giving $\langle c \rangle$ orientations of zircon. X, Y, and Z represent kinematic directions as shown in figure 3.3. Labels in rectangles indicate individual zircon grains, labels in angle brackets give misorientation axes for the corresponding crystals. Gray dashed lines indicate approximate trace of foliation, solid circles correspond to plastically-deformed grains, empty circles to undeformed grains. **(a)** Sample BH12-07; dashed circle indicates approximate direction of lineation; **(b)** sample STG13; **(c)** sample IV12-05; **(d)** IV12-07aB; **(e)** IV12-07B; **(f)** IVZ02-12.

3.4.3. Sillimanite-biotite-garnet gneiss

Data on plastically-deformed crystals in sample IV12-05 are presented in figures 3.1c and 3.S4. Grains reveal lattice distortion type (I) (Figs. 3.S4a, b, c, d) and, in rare cases, type (II) (Fig. 3.S4e). All grains show features of brittle deformation. $\langle C \rangle$ of all crystals are roughly aligned in the foliation plane that is horizontal in pole figures.

Most of the grains that have their $\langle c \rangle$ approximately at 90° and 0° ($\pm 10^\circ$) to stretching lineation show strong clustering of misorientation axes around [001] (Figs. 3.1c; 3.S4a-b, d; grains 06, 09, 10b). Grain with $\langle c \rangle$ oriented at about 45° to stretching lineation shows two clusters of misorientation axes around (Fig. 3.S4e; grain 16).

Zircon grains that are enclosed in rheologically softer matrix (fine-grained minerals) have one dominant cluster of misorientation axes around [001] (Fig. 3.S4a-b; grains 06 and 09). Grains that are

enclosed in rheologically strong phases (sillimanite, quartz and titanite) show either a high-indices misorientation axis or more than one cluster of misorientation axis (Figs. 3.S4c-e; grains 10a, 10b, 16).

3.4.4. Felsic mylonite

Data on plastically-deformed zircons in samples IV12-07aB, IV12-07B and IVZ02-12 are shown in figures 3.1d-f and 3.S5-3.S7. Plastically-deformed zircon crystals in sample IV12-07aB reveal lattice distortion type (III), crystals in samples IV12-07B and IVZ02-12 show lattice distortion type (II). $\langle C \rangle$ of all plastically-deformed zircons are subparallel to the mylonitic foliation (Figs. 3.1d-f).

Zircon crystals with $\langle c \rangle$ oriented subparallel to the foliation plane develop one cluster of misorientation axes; those with $\langle c \rangle$ at $>10^\circ$ to the foliation have two or more misorientation axes (Figs. 3.1d-f).

Zircons with $\langle c \rangle$ oriented roughly normal or parallel to the stretching lineation reveal misorientation axes mainly around low-indices crystallographic directions, e.g. [001], [100] or [110] (Figs. 3.S5b-d, grains 31-33; 3.S6c, grain 19). Crystals with $\langle c \rangle$ oriented at about 45° to lineation develop either two misorientation axes (Fig. 3.S5e, grain 57), or high-indices misorientation axis (Fig. 3.S6a, grain 11). Sample IVZ02-12 did not show a clear stretching lineation, but most of the grains develop one misorientation axis parallel to [001] (Figs. 3.1f; 3.S7a-b, d; grains 15, 25b, 28b).

All zircons in felsic mylonites are enclosed in fine-grained mylonitic matrix.

3.5. Discussion

3.5.1. Systematics derived from natural samples

New following regularities are derived from our new zircon data:

a. Zircon crystal-plastic deformation is restricted to grains with $\langle c \rangle$ aligned in or close to the foliation plane. Grains those $\langle c \rangle$ are a high angle to the foliation plane ($>15^\circ$) show no or only cataclastic deformation (Fig. 3.3 iii).

b. When $\langle c \rangle$ are at an angle of 10-20° to the foliation, complicated distributions of the misorientation axes with two and more clusters and complex rotation of crystallographic axes can be observed.

c. When $\langle c \rangle$ are parallel to the foliation plane and parallel or normal to the stretching lineation, misorientation and rotation axes are usually parallel to [001] (Fig. 3.3 i, ii). In this case activation of [100]{010} slip system is common (Kovaleva et al., 2014).

d. When $\langle c \rangle$ are aligned parallel to the foliation plane and at an acute angle to the stretching lineation (for example, at 45°), most frequently we observe either two misorientation axes, or one but high-indices misorientation axis.

e. Zircon enclosed in rheologically weak host (e.g. biotite, chlorite, fine-grained matrix) preferably activates misorientation axes with low Miller indices, mostly [001]. Misorientation axes then strongly cluster and coincide with the rotation axes. When the crystal is hosted by rheologically strong host (e.g. plagioclase, K-feldspar, quartz), complex rotation of crystallographic axes and complex misorientation axes distributions may occur. It has been shown by Kovaleva et al. (2014) that if crystal is enclosed in rheologically strong phases and/or coupled with the matrix, its plastic deformation is strongly controlled by the host and not by energetically-preferable slip.

Behaviors a-e are found consistently in different shear zones, rock types and for zircon crystals of different size and with different lattice distortion types.

3.5.2. Active slip systems

Geometry of low angle boundaries in deformed crystal (distortion pattern type III) gives an opportunity to determine active slip system(s) (e.g. Reddy et al., 2007; Kaczmarek et al., 2011; Timms et al., 2012; Kovaleva et al., 2014). In zircon 04 (Fig. 3.2) low angle boundary traces are parallel to (100) plane; misorientation axis is [001] and thus lies in low angle boundary plane. This geometry implies operating of the [100]{010} slip system. The conclusion is supported by Weighted Burgers Vector (WBV) calculations (Wheeler et al., 2009). This method gives the summary Burgers vector of all dislocations passing through the selected area in EBSD map (Wheeler et al. 2009). WBV is measured in [μm^{-2}] and expressed as three numbers, a , b and c , which are the components of summary Burgers vector. Lower left portion of the crystal is strain-free, so the WBV values are rather low (Fig. 3.2a, gray rectangles). In the lower right portion WBV is dominated by a component (dotted rectangles) and in the upper left portion by b component (dashed rectangles); a and b dominating

components mean dislocations with {100} Burgers vector. In the upper right part of crystal, where subgrain boundaries are emanating from inclusion, WBV show mixed components (black rectangles). Such non-homogeneous distribution of WBV values indicate that plastic deformation in zircon crystal was a post-growth process, and it caused by directed external differential stress (MacDonald et al., 2013).

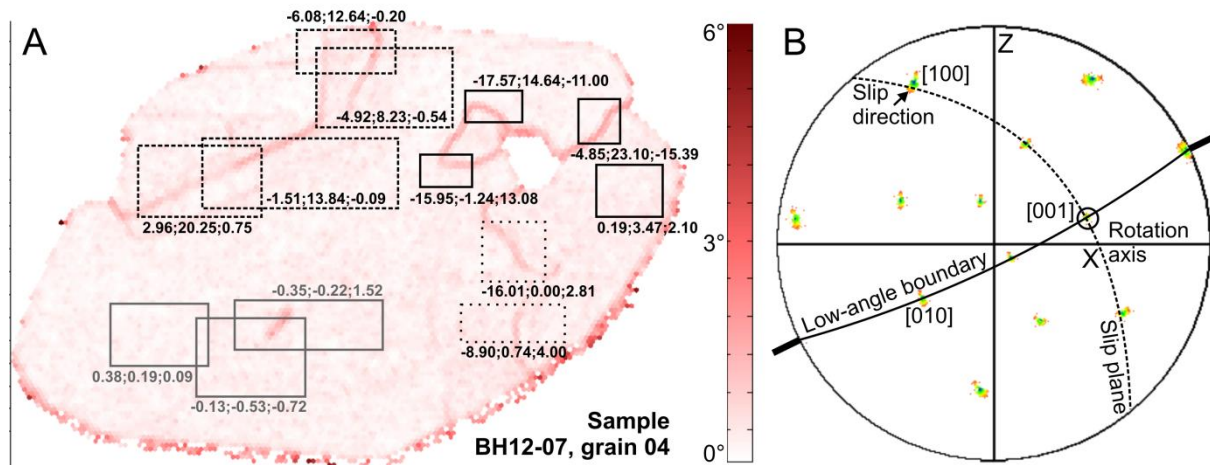


Figure 3.2. (a) Local misorientation map of the grain 04 from sample BH12-07 with Weighed Burgers Vector (WBV) components for the highlighted subareas. The a , b and c components of WBV measured in $(\mu\text{m})^{-2}$ listed for each subarea (Wheeler et al., 2009). Gray rectangles show the areas with WBV that is comparatively low; dotted and dashed rectangles show areas with WBV dominated by a or b components accordingly, black rectangles show areas with mixed WBV components. (b) Reconstruction of the slip system $\langle 100 \rangle \{010\}$ of the grain 04 in the pole figure with crystallographic axes directions. Thick lines – traces of the low angle boundary trace; solid line – reconstruction of low angle boundary plane; dashed line – reconstruction of slip plane. Circle highlights rotation axis. Color-coding as in Fig. 3.S1c.

3.5.3. Comparison of natural data with a theoretical model of zircon crystal-plastic deformation

Because we have sampled shear zones that were formed mainly by simple shear deformation we can compare our natural data with the model for zircon evolution presented in Kaczmarek et al. (2011). Our new observations on natural samples are only partially consistent with the model of Kaczmarek et al. (2011). According to the new data, zircons with $\langle c \rangle$ in the foliation plane normal to the kinematic rotation axis indicate the preferable activation of the [001] misorientation axis, and not [100] as suggested by Kaczmarek et al. (2011). New data is however supported by observations of rocks with pseudotachylytes, where plastic deformation of zircon results in planar deformation bands

(Kovaleva et al., in press). Kaczmarek et al. (2011) assumed that any orientation of $\langle c \rangle$ that is not parallel or normal to kinematic rotation axes would cause activation of multiple glide systems, which is not supported by new observations. We have shown that it is true only for grains which $\langle c \rangle$ is aligned in or close to the foliation plane (Fig. 3.1). For example, $\langle c \rangle$ in grain 15a (Fig. 3.S2d) is oriented at 45° to the stretching lineation, intermediate to (i) and (ii). Consistently this grain develops two misorientation axes and the slip systems could be $\langle 100 \rangle \{010\}$ and $\langle 001 \rangle \{010\}$, as suggested in Kaczmarek et al. (2011). However, for grains with orientation of $\langle c \rangle$ at a high angle to the foliation no crystal-plastic deformation is observed (Figs. 3.1a, f; 2 iii); or plastic and brittle deformation rarely occur (Figs. 3.S3c, e; grains 25 and 33).

Two possibilities could explain differences between natural and theoretically modeled crystals:

1. The sampled shear zones were formed by general shear with a different geometry of the kinematic rotation axis. However, in general shear the orientation-deformation relations are expected to be far more complex than observed (Reddy and Buchan, 2005).
2. Zircon behaves distinctly different from calcite, so the model of Kaczmarek et al. (2011) based on plastic deformation of calcite (Reddy and Buchan, 2005) may not be fully accurate for zircon.

Also, Kaczmarek et al. (2011) have not taken into account the importance of host phase for deformation microstructures in zircon, which is highlighted by new data.

3.5.4. Link between zircon crystal-plastic deformation and macroscopic kinematic frame

Zircon crystal-plastic deformation may be restricted to specific conditions and thus, lattice distortion patterns of zircon may represent only a snapshot of the potentially complex deformation history. Based on natural data we have demonstrated macroscopic kinematic control during simple shear on the critically resolved shear stress and geometry of the dominant slip systems in deformed minerals. Using the derived systematics it is possible to reconstruct the macroscopic tectonic frame during zircon crystal-plastic deformation. According to regularity (c) we can reconstruct the shear direction in sample IVZ02-12, which should be close to $\langle c \rangle$ direction of grains 25b and 28b or to $\langle c \rangle$ of grain 15 (Fig. 3.1f).

The schematic sketch showing character of zircon deformation in a simple shear-dominated environment is based on the observed systematics (Fig. 3.3).

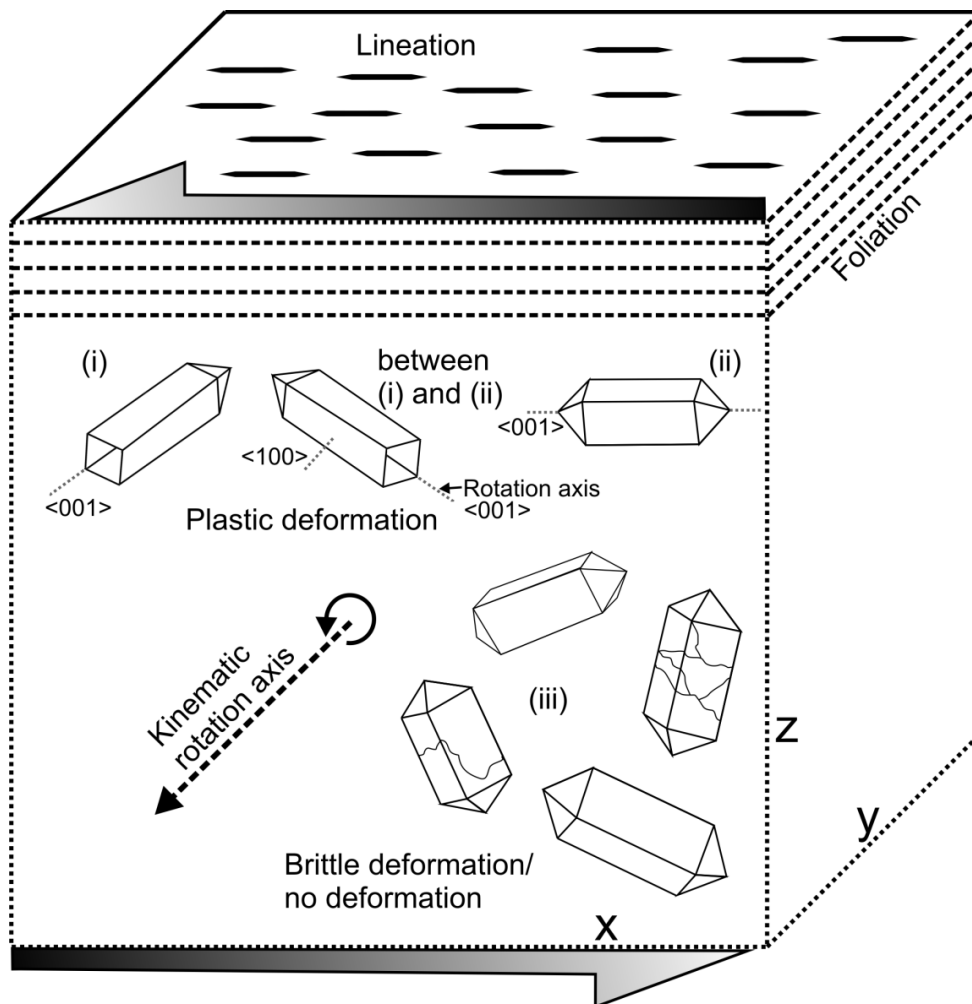


Figure 3.3. Schematic sketch showing character of zircon deformation depending on $\langle c \rangle$ orientation in a macroscopic kinematic frame. (i), (ii) and intermediate cases with $\langle c \rangle$ parallel to the foliation undergo plastic deformation: (i) $\langle c \rangle$ is parallel to macroscopic kinematic rotation axis, zircon misorientation and rotation axes are parallel to $\langle 001 \rangle$; (ii) grain with $\langle c \rangle$ normal to macroscopic kinematic rotation axis develops intragranular lattice rotation axes parallel to $\langle 001 \rangle$; intermediate case between (i) and (ii): grain with $\langle c \rangle$ at 45° to the macroscopic kinematic rotation axis develops two rotation and misorientation axes, for example, $\langle 100 \rangle$ and $\langle 001 \rangle$. (iii) – grains with $\langle c \rangle$ not aligned to foliation develop brittle deformation or do not deform.

3.5.5. Implication for zircon geochronology

Our observations have important implications for zircon geochronology. It has been shown that crystal-plastic deformation can dramatically affect the trace element budget of zircon domains and therefore can cause isotopic system disturbance or resetting (e.g. Flowers et al., 2010; MacDonald et al., 2013; Moser et al., 2009, 2011; Piaolo et al., 2012; Reddy et al., 2006, 2007, 2009; Reddy and Timms, 2010; Timms and Reddy, 2009; Timms et al., 2011, 2012). In accordance with regularity (a), crystals, aligned parallel to the foliation plane are likely to be crystal-plastically

deformed, and thus might be (partly) rejuvenated; crystals with $\langle c \rangle$ at a high angle to foliation plane are unlikely to be deformed, and thus are not rejuvenated and might preserve older ages. Such systematics may potentially help to select grains for zircon in situ dating of deformation events.

Acknowledgements

This study was funded by the University of Vienna (doctoral school “DOGMA”, project IK 052) and the Austrian Science Foundation Fund (FWF): I471-N19, which is part of the DFG-FWF funded international research group FOR741-DACH. Thanks go to the Laboratory for FE-SEM and IB applications at the Faculty of Geosciences, Geography and Astronomy (University of Vienna, Austria) for access to the EBSD facility and the Geological Survey of Austria (GBA) for access to the SEM.

References

- Bachmann, F., Hielscher, R., Schaeben, H., 2010. Texture Analysis with MTEX – Free and Open Source Software Toolbox. *Solid State Phenomena*, 160, 63-68.
- Flowers, R.M., Schmitt, A.K., Grove, M., 2010. Decoupling of U–Pb dates from chemical and crystallographic domains in granulite facies zircon. *Chemical Geology*, 270, 20–30.
- Grange, M.L., Pidgeon, R.T., Nemchin, A.A., Timms, N.E., Meyer, C., 2013. Interpreting U–Pb data from primary and secondary features in lunar zircon. *Geochimica et Cosmochimica Acta*, 101, 112–132.
- Kaczmarek, M. A., Reddy, S. M., Timms, N. E. 2011. Evolution of zircon deformation mechanisms in a shear zone (Lanzo massif, Western-Alps). *Lithos*, 127, 414-426.
- Klötzli, E., Klötzli, U., Koller, F., 1997. Lower Ordovician migmatization in the Ötztal crystalline basement (Austria): linking U/Pb and Pb-Pb dating with zircon morphology. *Schweizerische Mineralogische und Petrographische Mitteilungen*, 77, 315-324.
- Kovaleva, E., Klötzli, U., Habler, G., Libowitzky, E., 2014. Finite lattice distortion patterns in plastically deformed zircon grains. *Solid Earth*, 5, 1099-1122.
- Kovaleva, E., Klötzli, U., Habler, G., Wheeler, J., in press. Planar microstructures in zircon from paleo-seismic zones. *American Mineralogist*.
- Leroux, H., Reimold, W.U., Koeberl, C., Hornemann, U., Doukhan, J.C., 1999. Experimental shock deformation in zircon: a transmission electron microscopic study. *Earth and Planetary Science Letters*, 169, 291–301.
- MacDonald, J.M., Wheeler, J., Harley, S.L., Mariani, E., Goodenough, K.M., Crowley, Q., Tatham, D., 2013. Lattice distortion in a zircon population and its effects on trace element mobility and U–Th–Pb isotope systematics: examples from the Lewisian Gneiss Complex, northwest Scotland. *Contributions to Mineralogy and Petrology*, 166, 21–41.
- Mainprice, D., Hielscher, R., Schaeben, H., 2011. Calculating anisotropic physical properties from texture data using the MTEX open source package. In: Prior, D.J., Rutter, E.H., Tatham, D. J.

- (eds) Deformation Mechanisms, Rheology and Tectonics: Microstructures, Mechanics and Anisotropy. Geological Society, London, Special Publications, 360, 175-192.
- Moser, D.E., Davis, W.J., Reddy, S.M., Flemming, R.L., Hart, R.J., 2009. Zircon U–Pb strain chronometry reveals deep impact-triggered flow. *Earth and Planetary Science Letters* 277, 73–79.
- Moser, D. E., Cupelli, C.L., Barker, I.R., Flowers, R.M., Bowman, J.R., Wooden, J., Hart, J.R., 2011. New zircon shock phenomena and their use for dating and reconstruction of large impact structures revealed by electron nanobeam (EBSD, CL, EDS) and isotopic U–Pb and (U–Th)/He analysis of the Vredefort dome. *Canadian Journal of Earth Sciences*, 48, 117–139.
- Nemchin A., Timms N. E., Pidgeon R., Geisler T., Reddy S. M., Meyer C. 2009. Timing of crystallization of the lunar magma ocean constrained by the oldest zircon. *Nature Geoscience*, 2, 133-136.
- Piazolo, S., Austrheim, H., Whitehouse, M., 2012. Brittle-ductile microfabrics in naturally deformed zircon: Deformation mechanisms and consequences for U–Pb dating. *American Mineralogist*, 97, 1544–156.
- Reddy, S.M. and Buchan, C., 2005. Constraining kinematic rotation axes in high-strain zones: a potential microstructural method? In: Gapais, D., Brun, J.P., Cobbold, P.R. (Eds.), *Deformation mechanisms, rheology and tectonics: from mineral to the lithosphere*, 243. Special Publications. Geological Society, London, pp. 1–10.
- Reddy, S.M. and Timms, N.E., 2010. Deformation of zircon and implications for geochemistry and geochronology. *Source Abstracts with Programs - Geological Society of America* 42, 634.
- Reddy, S.M., Timms, N.E., Trimby, P., Kinny, P.D., Buchan C., Blake K., 2006. Crystal-plastic deformation of zircon: a defect in the assumption of chemical robustness. *Geology*, 34, 257-260.
- Reddy, S.M., Timms, N.E., Pantleon, W., Trimby, P., 2007. Quantitative characterization of plastic deformation of zircon and geological implications. *Contributions to Mineralogy and Petrology* 153, 625–645.
- Reddy, S.M., Timms, N.E., Hamilton, P.J., Smyth, H.R., 2009. Deformation-related microstructures in magmatic zircon and implications for diffusion. *Contributions to Mineralogy and Petrology* 157 (2), 231–244.

- Thöni, M., Miller, Ch., 2004. Ordovician meta-pegmatite garnet (N-W Ötztal basement, Tyrol, Eastern Alps): preservation of magmatic garnet chemistry and Sm–Nd age during mylonitization. *Chemical Geology*, 209, 1 – 26.
- Timms, N.E. and Reddy, S.M., 2009. Response of cathodoluminescence to crystal-plastic deformation in zircon. *Chemical Geology* 261, 11–23.
- Timms, N.E., Kinny, P., Reddy, S.M., 2006. Enhanced diffusion of uranium and thorium linked to crystal plasticity in zircon. *Geochemical Transactions* 7, 10.
- Timms, N.E., Kinny, P., Reddy, S.M., Evans K., Clark C., Healy D., 2011. Relationship among titanium, rare earth elements, U–Pb ages and deformation microstructures in zircon: Implications for Ti-in-zircon thermometry. *Chemical Geology* 280, 33–46.
- Timms, N.E., Reddy, S.M., Healy, D., Nemchin, A.A., Grange, M.L., Pidgeon, R.T., Hart, R., 2012. Resolution of impact-related microstructures in lunar zircon: a shock-deformation mechanism map. *Meteoritics & Planetary Science*, 47, 120–141.
- Wheeler, J., Mariani, E., Piazzolo, S., Prior, D. J., Trimby, P., Drury, M. R. 2009. The Weighted Burgers Vector: a new quantity for constraining dislocation densities and types using Electron Backscatter Diffraction on 2D sections through crystalline materials. *Journal of Microscopy*, 233, 482-494.

Supplementary figures

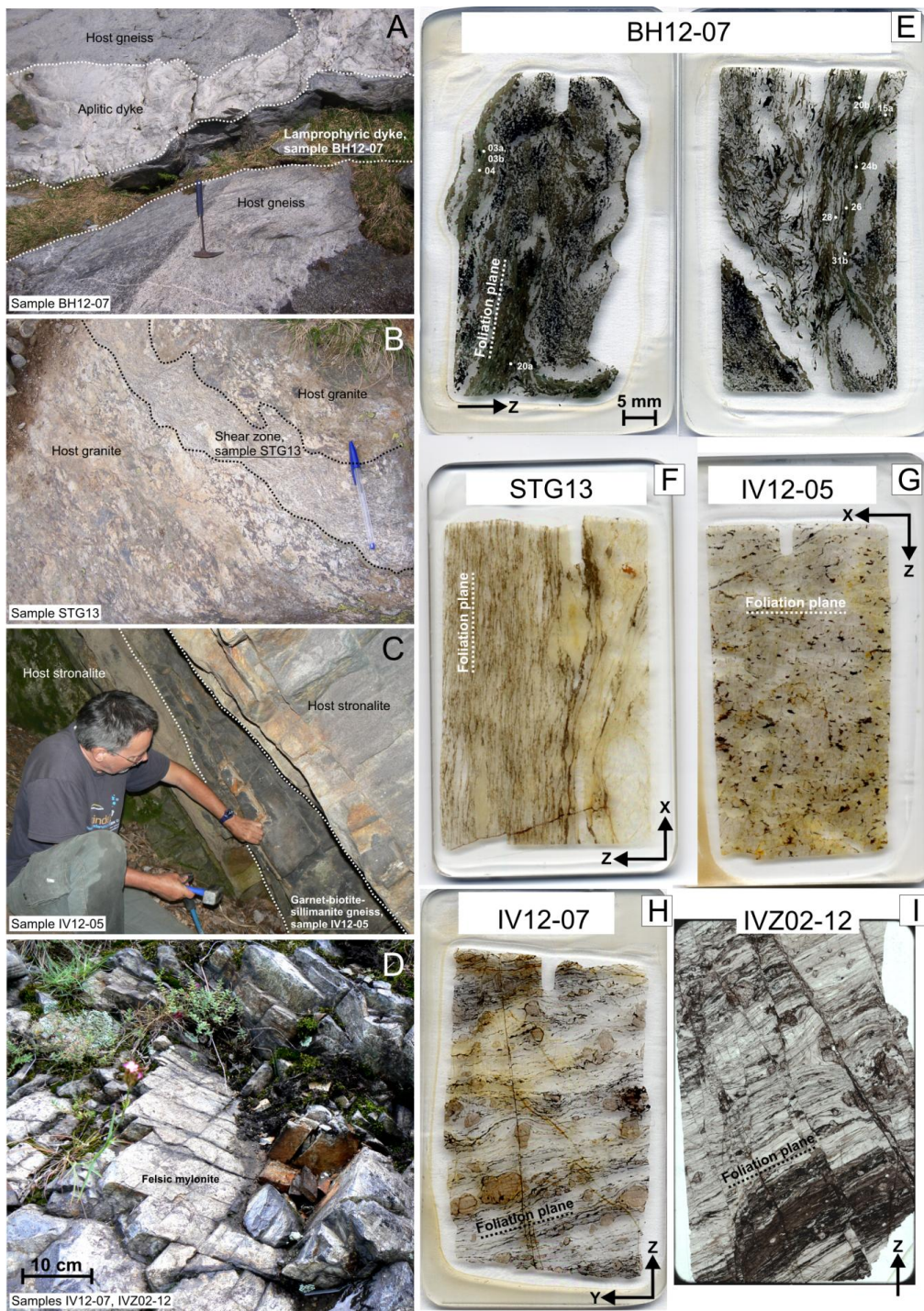
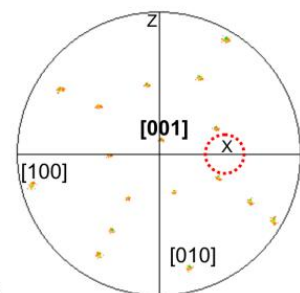
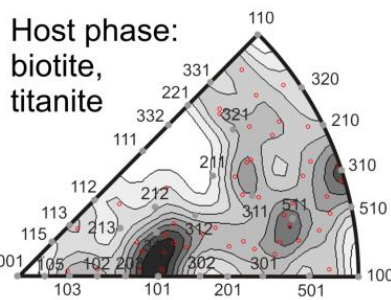
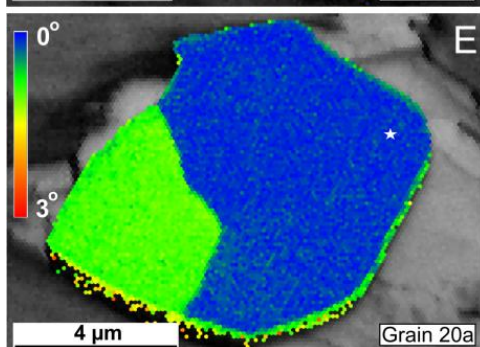
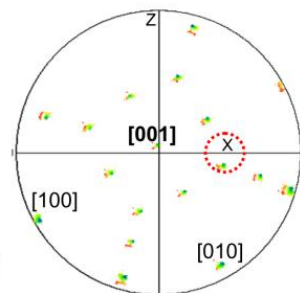
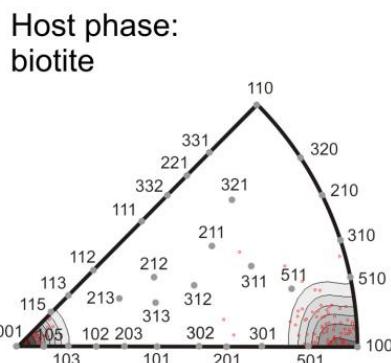
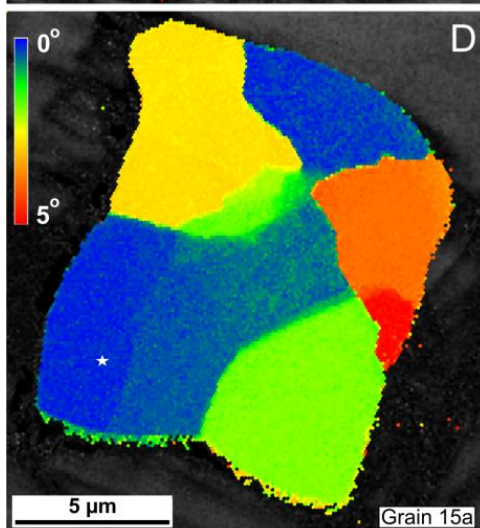
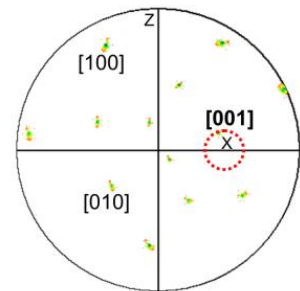
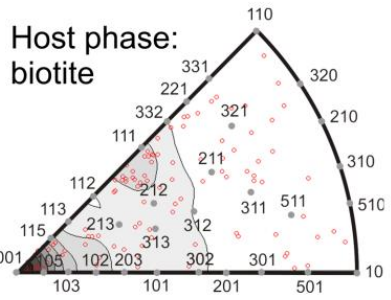
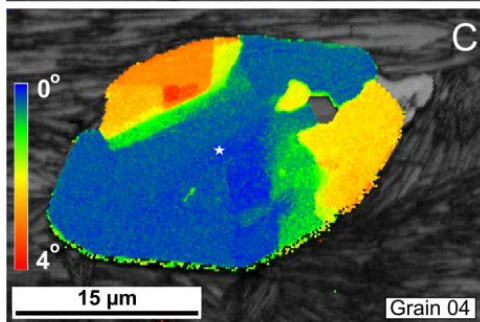
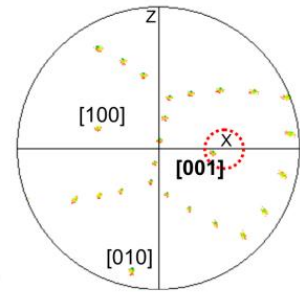
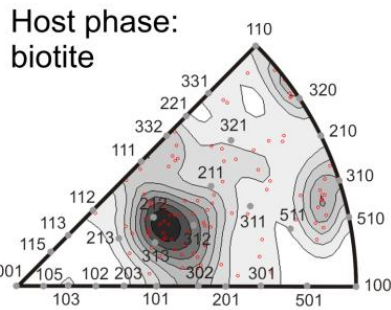
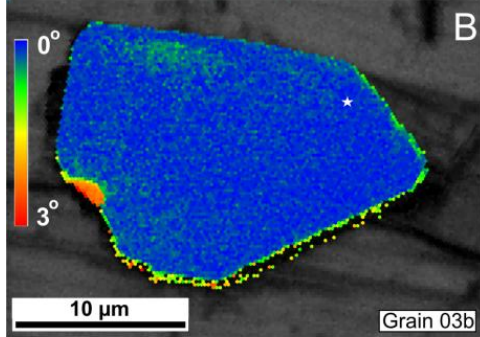
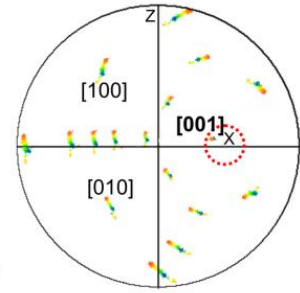
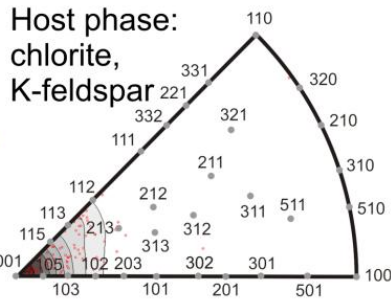
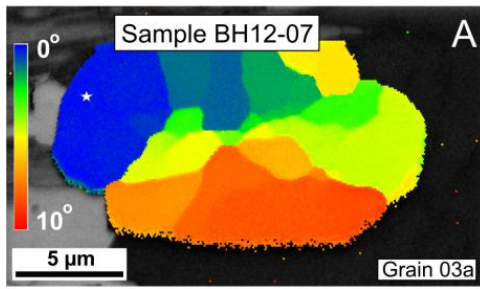


Figure 3.S1. (a)-(d) field photographs of the sampled shear zones. (a) Shear zone in Western Tauern Window, meta-lamprophyric dyke, sample BH12-07. (b) Shear zone in Ötztal-Stubai crystalline complex, porphyritic biotite-meta-granite, sample STG13. (c) Ivrea-Verbano zone, sillimanite-biotite-garnet gneiss, sample IV12-05. (d) Ivrea-Verbano zone, shear zone in felsic mylonite, samples IV12-07 and IVZ02-12. (e)-(i) thin section photographs, axes are the orientation with respect to the kinematic indicators. (e) Sample BH12-07, labels are positions of analyzed zircon crystals, white rectangles frame areas with the same crystallographic orientation of zircon grains. (f) Sample STG13; (g) sample IV12-05; (h) sample IV12-07; (i) sample IVZ02-12.



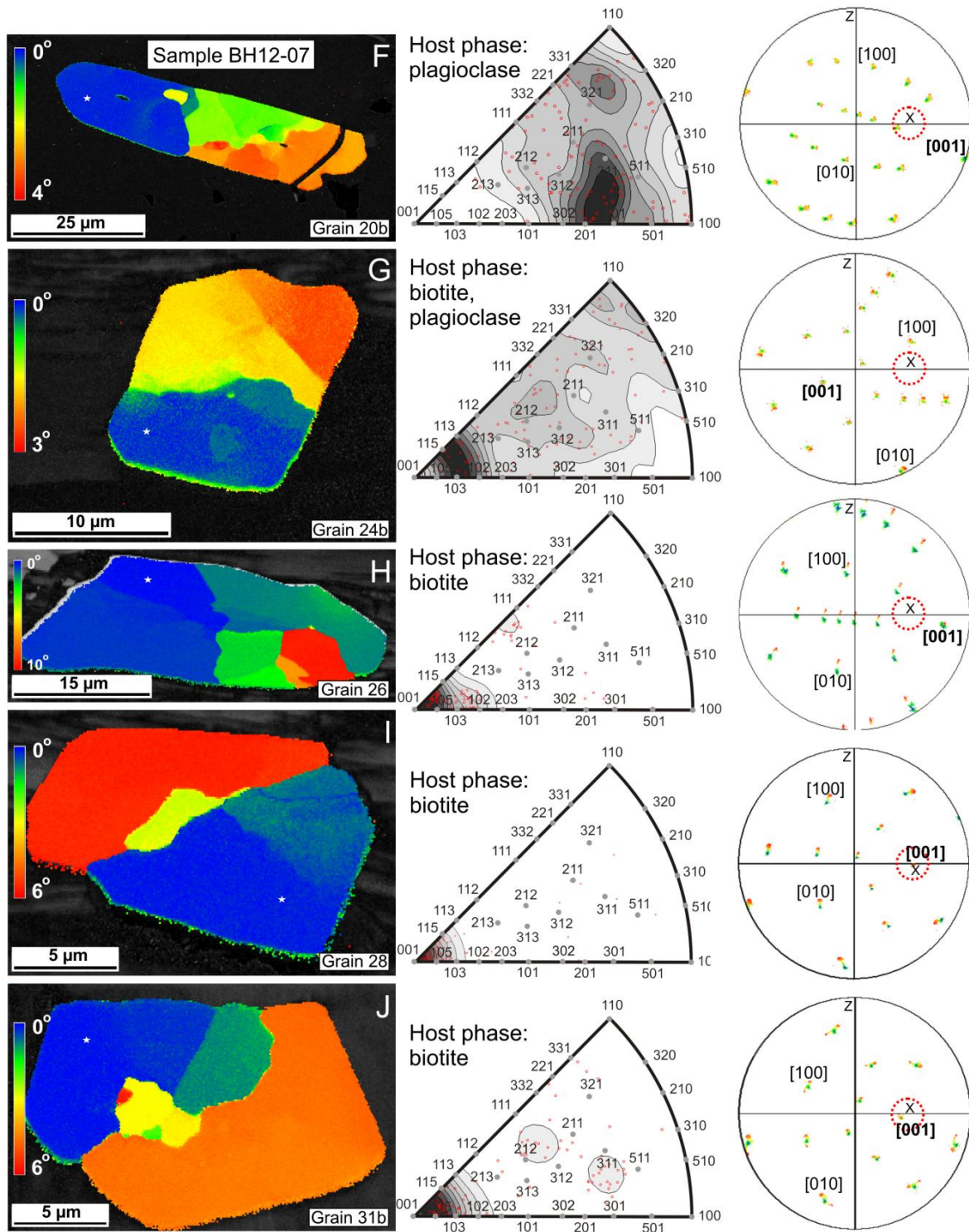


Figure 3.S2. Orientation and misorientation data of plastically-deformed zircon crystals from sample BH12-07. Left column: EBSD maps, color-coded for misorientation with respect to a user-selected reference point (white star marker in each map). Central column: Inverse pole figure showing misorientation axes orientations and their contoured density distribution. Red open circles are misorientation axes, gray filled circles and labels are crystallographic directions. Right column – pole figures with crystallographic orientations of zircon grain to the left, main crystallographic axes are labeled. Red dotted open circle indicates orientation of stretching lineation in thin section cut.

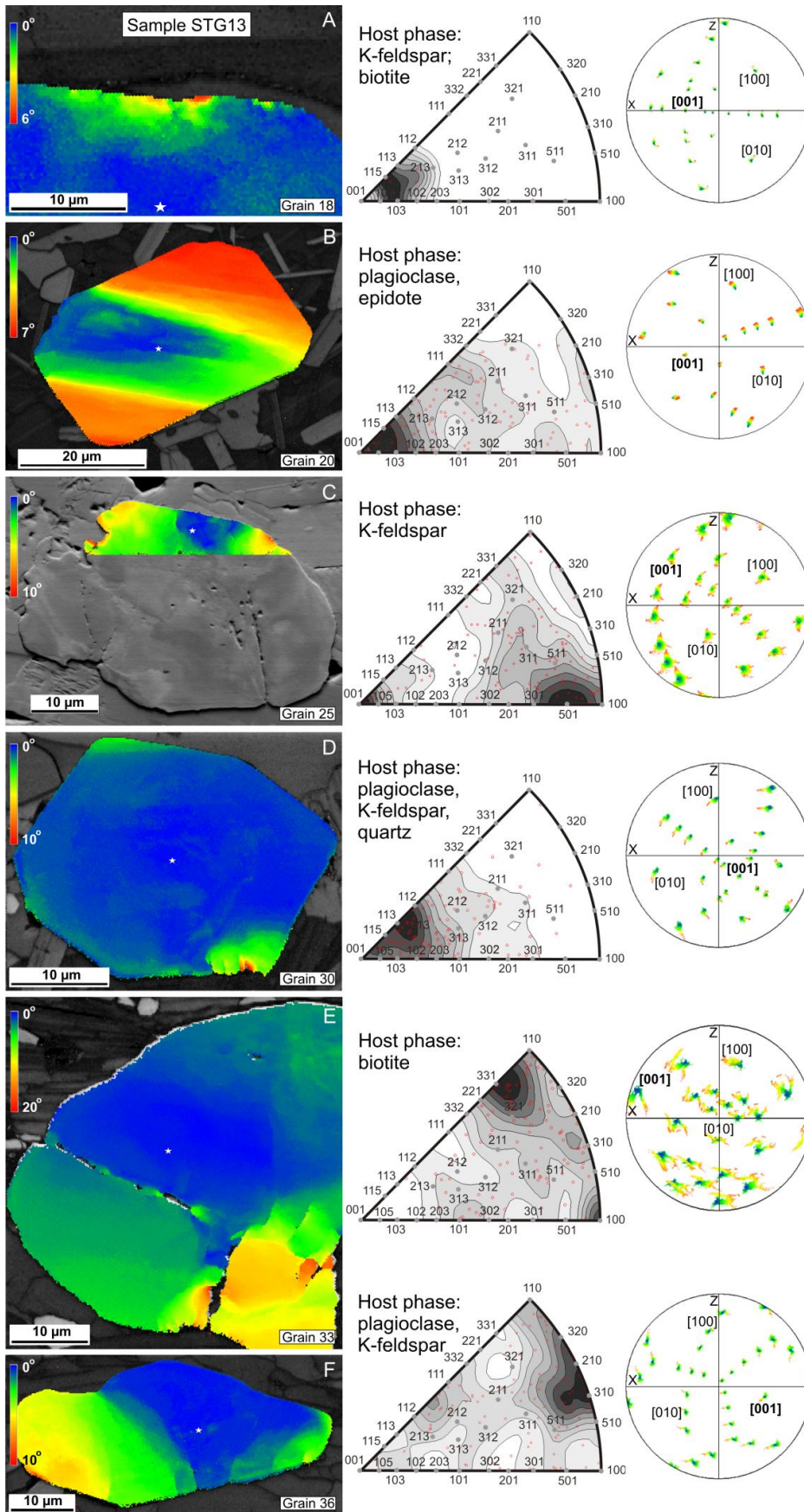


Figure 3.S3. Orientation and misorientation data on plastically-deformed zircon crystals from sample STG13. Columns as described for 3.S2. In (a), (c) and (e) EBSD misorientation map is superimposed on FSE image.

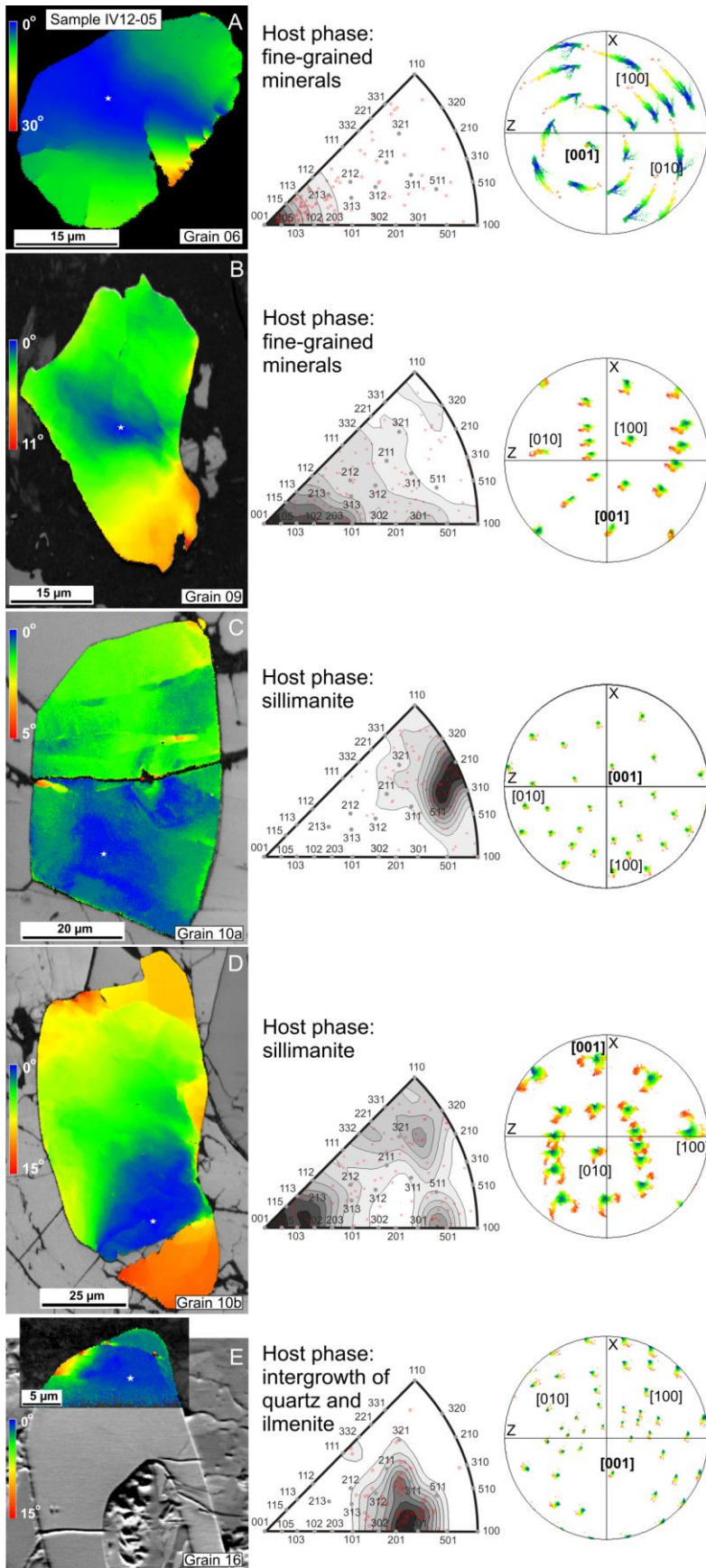


Figure 3.S4. Orientation and misorientation data of plastically-deformed zircon crystals from sample IV12-05. Columns as described for 3.S2. In **(e)** EBSD misorientation map is superimposed on FSE image.

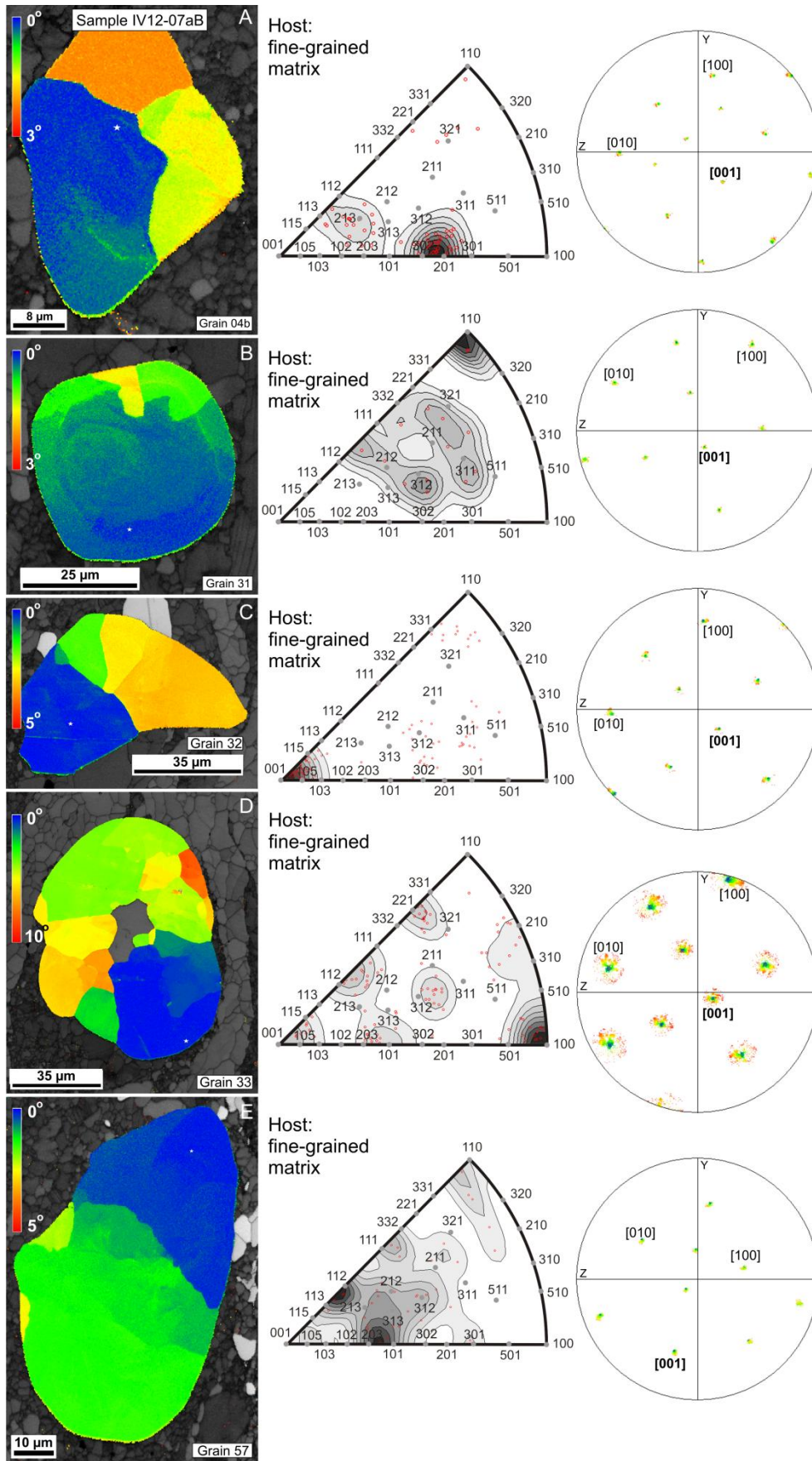


Figure 3.S5. Orientation and misorientation data of plastically-deformed zircon crystals from sample IV12-07aB. Columns as described for 3.S2.

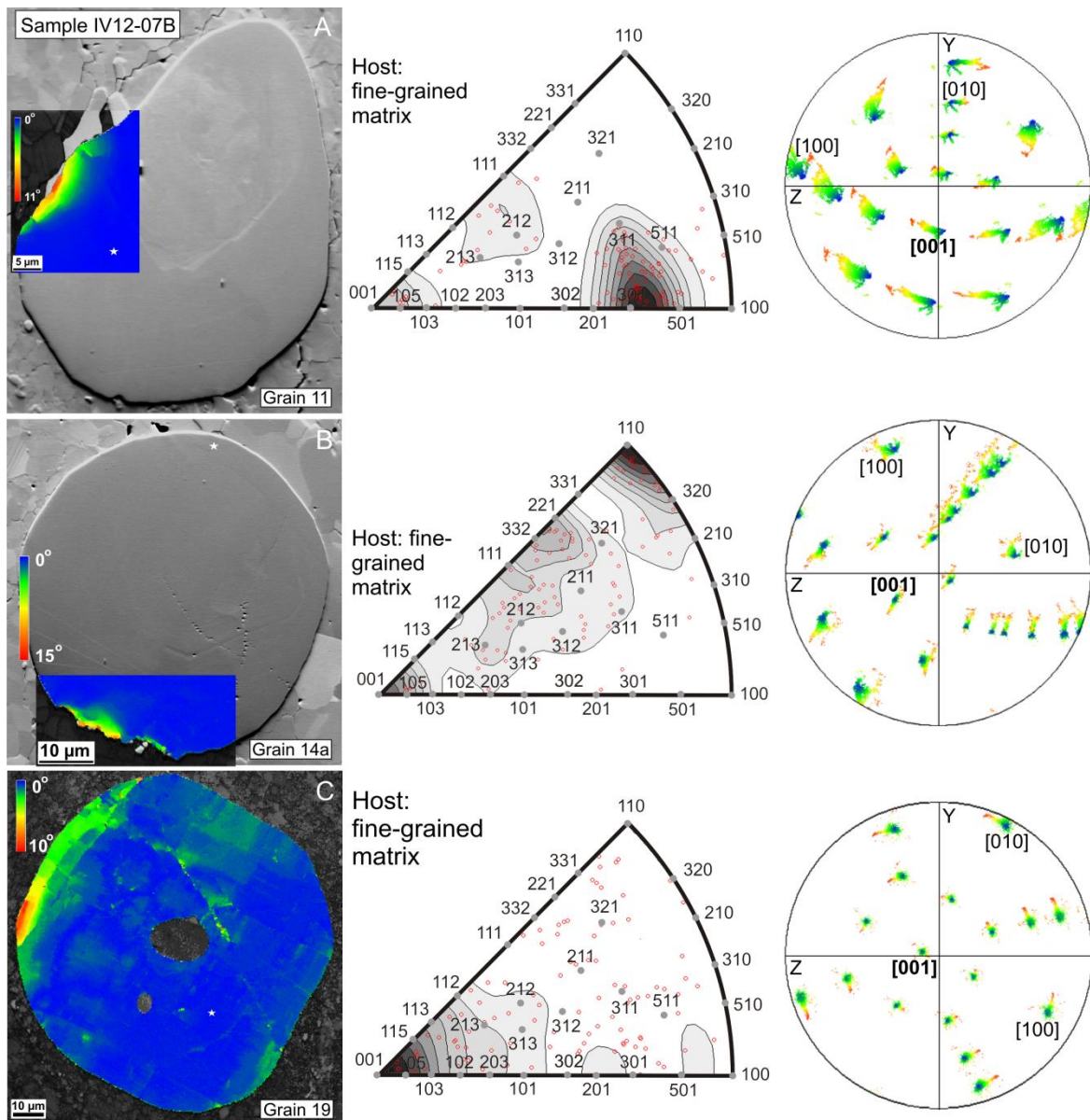


Figure 3.S6. Orientation and misorientation data of plastically-deformed zircon crystals from sample IV12-07B. Columns as described for 3.S2. (a) and (b) EBSD misorientation map is superimposed on FSE image.

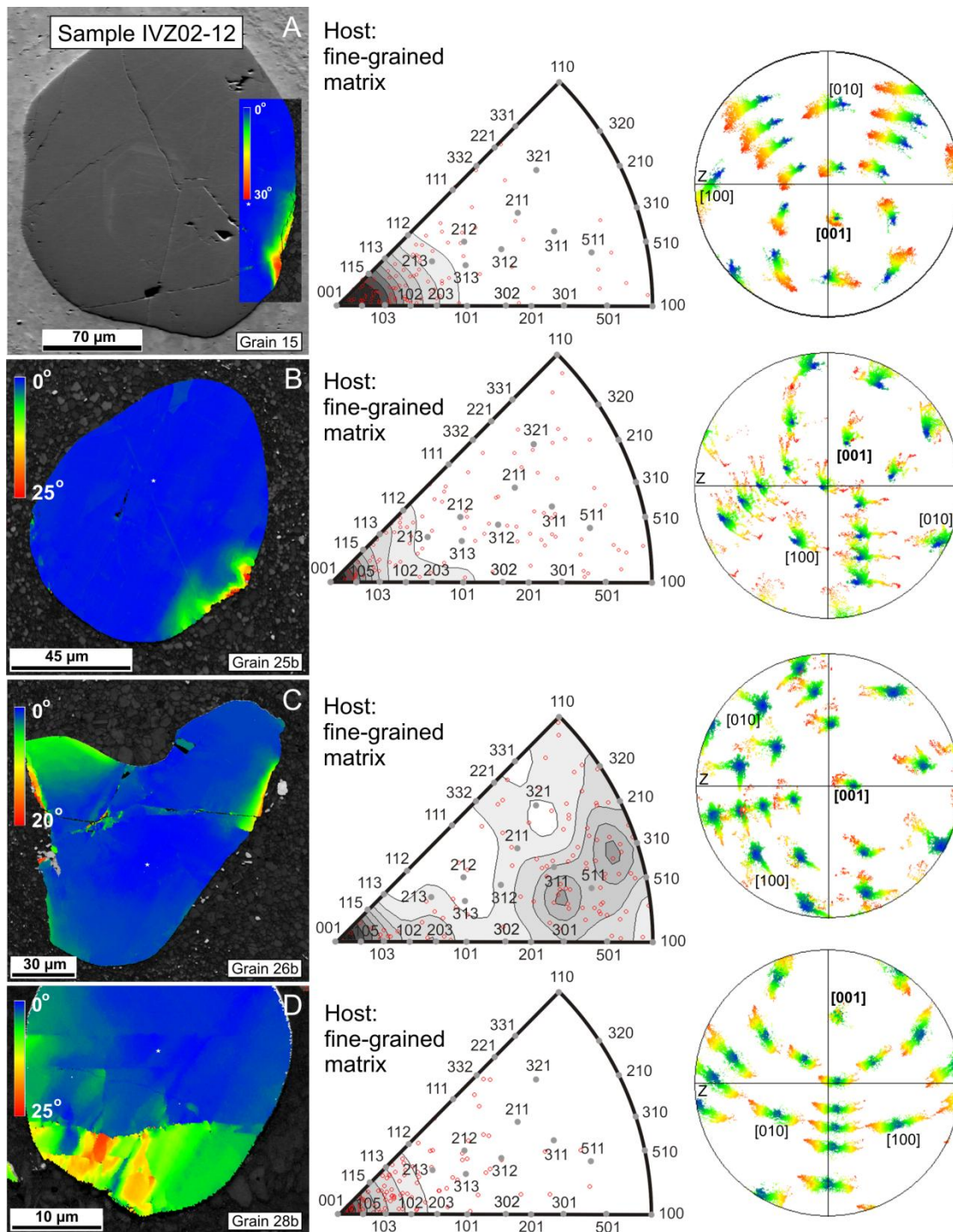


Figure 3.S7. Orientation and misorientation data of plastically-deformed zircon crystals from sample IVZ02-12. Columns as described for 3.S2. In (a) EBSD misorientation map is superimposed on FSE image.

4.0. The effect of crystal-plastic deformation on isotopes and trace element distribution in zircon

Elizaveta Kovaleva¹, Urs Klötzli¹, Benjamin Huet², Gerlinde Habler¹, Yunbin Guan³, Dieter Rhede⁴

¹ *Department of Lithospheric Research, Faculty of Earth Sciences, Geography and Astronomy, University of Vienna, Althanstrasse 14, A-1090 Vienna, Austria*

² *Department of Geodynamics and Sedimentology, Faculty of Earth Sciences, Geography and Astronomy, University of Vienna, Althanstrasse 14, A-1090 Vienna, Austria*

³ *Caltech Microanalysis Center, Division of Geological and Planetary Sciences, California Institute of Technology, Pasadena, CA 91125, USA*

⁴ *Helmholtz Centre Potsdam, German Research Centre for Geosciences, Telegrafenberg, 14473 Potsdam, Germany*

Article is in preparation for submission

Abstract

Plastically-deformed zircon grains from various ductile shear zones have been investigated for internal misorientation by electron backscatter diffraction (EBSD), for growth zoning by cathodoluminescence imaging (CL) and for trace elements and isotopes distribution by field emission gun electron microprobe analysis (FEG-EMPA) and nano-scale secondary ion mass spectrometry (NanoSIMS). Chemical maps and high-resolution profiles have shown that trace elements are redistributed in the zones that are affected by crystal-plastic deformation. Low angle boundaries and dislocations introduced to the crystal act as diffusion pathways for the trace cations. Such pathways allow the re-distribution of elements much faster than simple volume diffusion does.

Low angle boundaries and intensively-banded domains of crystal lattice show depletion in U, Y, Yb, Pb and enrichment in light rare earth elements (LREE) such as Ce and Nd. Elements such as Ti, P and Hf are either enriched, depleted, or remain unaffected. Y and Yb show simple compositional profiles across low angle boundaries with decreasing that corresponds to low angle boundary, and oscillations of profile across banded lattice. Change in trace element composition along low angle boundaries results in the distorted CL-signal that locally becomes brighter.

$^{207}\text{Pb}/^{206}\text{Pb}$ relative ages show significant rejuvenation or aging where crystal lattice is intensively banded. There is a positive correlation between dislocation density and the degree of isotopic ages distortion. Domains that contain fractures, pores and (sub)grain boundaries show significantly older $^{207}\text{Pb}/^{206}\text{Pb}$ relative ages than pristine domains. This is caused by contamination of damaged lattice by common lead from the matrix. Rejuvenation occurs in the deformed domains that are at a distance from the grain boundary and caused by out-diffusion of radiogenic lead.

Re-distribution of trace elements and re-equilibration of isotopic systems in plastically-deformed domains of zircon may have important implications for geochronology and geochemistry of zircon and should be taken into account. It can be used as a tool for mineral dating of deformation events.

4.1. Introduction

Zircon is one of the most robust, abundant and wide-spread accessory phase in many rock types. Due to its chemical stability and property to incorporate and preserve radioactive uranium and rare earth elements (REE) zircon is widely used for isotopic mineral dating (e.g. Davis et al., 2003; Kaczmarek et al., 2011; MacDonald et al., 2013; Klötzli et al., 2014), for the geochemical characterization of its formation environment (e.g. Hofmann et al., 2009; 2014; Nemchin et al., 2009; Erdmann et al., 2013; Storm et al., 2014), and for the estimation of (re)crystallization temperature (Watson et al., 2006; Kaczmarek et al., 2011; Hofmann et al., 2014).

Zircon is comparatively insoluble in melts and fluids; it can preserve resolvable overprints of multiple events within a single grain under a broad range of geological conditions. Thin (down to sub-micron scales) sharp compositional growth zoning is often observed in zircon and formed by variations of U, Th and REE concentrations (Corfu et al., 2003). Preserved sharp growth zoning, observed in crystals of various ages, presents a direct evidence for very slow, almost negligible, volume diffusion of important trace elements in this mineral. However with the help of high spatial resolution analyzing techniques it becomes possible to detect very slight changes in mineral chemistry and isotopic composition happening with time and under certain geological condition.

It would require extreme conditions, for example, temperatures of magmatic melt (Bea and Montero, 2013), to induce significant diffusional alteration of trace cations in zircon. For example, at 850 °C, a diffusion length of 5 µm by volume diffusion would require about 10 million years for Pb, one billion years for Dy, and tens of billions of years for Ti (Cherniak and Watson, 2007). However, other diffusion mechanisms at lower temperatures, especially so-called "Pb loss" (e.g. Compston et

al., 1986; Ashwal et al., 1999) have been well documented in natural samples which are not consistent with experimental predictions for volume diffusion (e.g. Geisler et al., 2002). In the past, the most common explanation for low temperature fast diffusion in zircon was the effect of self-irradiation that causes metamictization and inducing/enhancing volume diffusion (Cherniak et al., 1991; Cherniak and Watson, 2003). In the last few years, evidence for increased trace element diffusion in zircon due to plastic deformation has been found and described (Reddy et al., 2006, 2007, 2009; Timms et al., 2006, 2011, 2012; Timms and Reddy 2009; Reddy and Timms, 2010; Moser et al., 2009, 2011; Flowers et al., 2010; Piazzolo et al., 2012; MacDonald et al., 2013). These authors have shown that distortions in the crystal lattice can dramatically affect the content of trace elements and isotopes in zircon domains.

MacDonald et al. (2013) proposed that there are two general ways to alter the crystal chemistry by linear and planar defects:

(i) The most obvious mechanism suggests that planar and linear defects, such as dislocations and low angle boundaries, represent connections to the grain boundary, facilitating element exchange with the host rock. For example, Timms et al. (2006, 2011) observed variations of REE, U, Ti and Th contents in deformed zircon which are ~5 orders of magnitude greater than can be accounted for volume diffusion. Timms et al. unambiguously explained this by enhanced diffusion of U, Th and Ti along deformation-related fast-diffusion pathways. Introducing dislocation into crystal lattice also leads to radiogenic-Pb loss and, therefore, has dramatic consequences for interpretation of radiometric age data.

(ii) Another way to change local composition of trace elements in zircon is with re-equilibration exchange of trace elements between pristine crystal lattice and defect. Impurity atoms may have higher concentration along subgrain boundaries due to the defect's local stress field, which modifies the chemical potentials of elements. This effect is referred as "Cottrell atmosphere" because it was first discovered by Cottrell and Bilby (1949) and has been shown, for example, by Hofmann et al. (2009), who demonstrated with NanoSIMS mapping that the trace elements are enriched along the edges of fractures in zircon. Differential enrichment of REE as well as U and Th at low-angle boundaries was found by Timms et al. (2006, 2011). Therefore, dislocations incorporate higher amount of impurities, and the surrounding volume of the pristine crystal lattice becomes depleted with trace elements. However, re-equilibration exchange, acting alone, should not change the average composition of the domain and causes only re-distribution of trace elements within a small volume. Although, these impurities are removed easier from the grain, as far as low angle boundary also acts as a fast diffusion pathway, according to (i). Thus, two mechanisms, working

together, may change the trace element composition: re-equilibration exchange attracts ions from the surroundings to the defects, wherefrom ions are removed from the lattice.

Our study reveals evidence of trace elements and isotopes re-distribution in distorted zircon grains from various shear zones derived by high-resolution analytical techniques. We believe that accurate treatment of plastically-deformed zircons can open the possibility of direct dating of deformation events (e.g. Reddy and Timms, 2010; Timms et al., 2011), and thus input into expanding of knowledge and understanding of zircon deformation behaviors.

4.2. Geological settings and petrography

Samples were derived from ductile shear zones from two different localities.

4.2.1. Ivrea-Verbano Zone (IVZ), Southern Alps (Forno, Val Strona, Northern Italy)

The Ivrea-Verbano Zone (IVZ) consists of a NE-SW trending, steeply dipping sequence of meta-sedimentary and meta-igneous basic rocks, ultrabasic mantle tectonites and a large underplated igneous complex. The sequence consists of predominant metasedimentary rocks in the SE and prevailing metabasic rocks and strongly depleted metapelites in the NW. Metamorphism increases progressively from amphibolite facies in the SE to granulite facies in the NW. The Ivrea-Verbano Zone is supposed to represent a section through the lower continental crust that experienced regional metamorphism during the uppermost Palaeozoic (Rutter et al., 2007; Quick et al., 2009).

Within the Ivrea-Verbano Zone a network of high-temperature shear zones, which are subparallel to the NE-SW elongation direction of the IVZ are observed. The shear zone network extends from Anzola (Val d'Ossola) to Forno (Val Strona) and can be traced for more than 20 km in length (Brodie et al., 1992). Mylonites in the northern part of the Ivrea-Verbano zone are completely (re-) equilibrated under granulite-facies conditions prevailing during crustal attenuation/extension and contemporaneous magmatic underplating between 315 Ma and 270 Ma (Rutter et al., 2007; Quick et al., 2009; Sinigoi et al., 2011; Klötzli et al., 2014). In the Val d'Ossola section at Cuzzago peak *P-T* estimates are 0.6-1.0 GPa and > 800 °C, based on the peak *P-T* estimates from the neighboring Val Strona di Omegna (Redler et al., 2012).

Samples IV12-07aB and IVZ02-12 were collected from the outcrops at Premosello (N46°00'23.65"/E08°19'41.66" and N46°00'15.04"/E08°19'44.11" accordingly), where several tens of

meters thick layers of faulted, mylonitized and foliated felsic metasediments are cropping out. The mylonites represent strongly restitic, highly dehydrated rocks that contain garnet clasts ranging from 50 to 500 μm in size, which are surrounded by a fine-grained foliated matrix consisting of alternating plagioclase- and quartz-rich layers, with intercalated biotite-ilmenite layers. Accessory minerals are zircon and monazite. Zircon represents rounded clasts in the matrix and sometimes inclusions in garnet; zircons have the aspect ratio 1:1-1:2 and vary in size from 20 to 70 μm in length. Plastically-deformed grains make about 11% of all zircon population and show mostly lattice distortion types (II) and (III) (Piazolo et al., 2012; Kovaleva et al., 2014). Grains 04, 33 and 30 (Figs. 4.1a-d; 4.1e-h; 4.9e-g correspondingly) are derived from the sample IV12-07aB; grains 15, 25, 26 (Figs. 4.8a-c; 4.8d-g; 4.9a-d correspondingly) – from the sample IVZ02-12. The latter also contains pseudotachylytes and ultramylonites (Kovaleva et al., in press).

Sample IV12-06C (grains 05, 16b; Figs. 4.3c-e, 4.4) was collected at the village Cuzzago (N45°59'45.64"/E8°21'38.75"). It represents a weakly-foliated metasedimentary granulite-facies rock, locally known as stromalite (Kovaleva et al., 2014). Zircon forms inclusions within garnet but more often in the plagioclase-quartz matrix. Around 13% of grains of zircon population investigated by orientation contrast imaging are crystal-plastically deformed and have evidence of lattice distortion types (I) and (II) (Piazolo et al., 2012; Kovaleva et al., 2014).

Within the same outcrop stromalites are crosscut by a discordant layer of sillimanite-biotite-garnet gneiss (N45°59'46.46"/E8°21'38.65"), which is considered to be restitic material from the partial melting of a metapelitic precursor rock (Barboza et al., 1999). Sample IV12-05 was taken from this discordant layer. The foliation is formed by a fabric of elongated garnet and sillimanite crystals 0,5-1 mm in length that compose 90% of the sample. The lineation is formed by elongated biotite crystals. Fine-grained minerals, quartz and ilmenite-rutile-quartz intergrowths crystallize in fractures and between garnet and sillimanite crystals. Accessory minerals are zircon and monazite. When hosted by garnet, zircon forms euhedral elongated or roundish crystals with aspect ratio 1:1-1:3 and length from 30 to 100 μm . Sometimes crystals show irregular curved boundaries (Figs. 4.6a, 4.7e) when hosted by fine-grained mixed phases, or irregular shapes (Fig. 4.7a) when forming intergrowths with sillimanite or quartz and rutile. Plastically-deformed zircon crystals mostly show lattice distortion type (I) (Piazolo et al., 2012; Kovaleva et al., 2014). Grains 09, 10a, 10b, and 16a (Figs. 4.6 and 4.7) were derived from the sample IV12-05.

4.2.2. Western Tauern Window, Eastern Alps (Zillertal, Tyrol, Austria)

In the Tauern Window (Eastern Alps), continental and oceanic rocks of the Penninic and sub-Penninic nappe sequences are exposed, which represent the footwall of the Austroalpine nappe stack. Nappe stacking and predominant final metamorphism are related to the closure of the Alpine Neotethys and subsequent continental collision in late Cretaceous-Tertiary (Miller et al., 2007). Samples were collected from the "Zillertaler Kern" lobe of the "Zentralgneis" formation (Selverstone et al., 1991; Schmid et al., 2013).

The magmatic protholiths of the "Zentralgneis" formation are uppermost Devonian to lower Permian in age. Three magmatic "pulses" of potassium-rich and calc-alkaline granites, felsic and intermediate volcanites and tonalitic/granodioritic plutonites can be distinguished (Veselá et al., 2011). The granitoids intruded into pre-Carboniferous, partly poly-metamorphic basement rocks consisting of various schists, para- and orthogneisses, amphibolites and meta-ophiolites. In the Zillertal section Variscan amphibolite facies regional metamorphism has been overprinted at greenschist- to amphibolite-facies metamorphic conditions of 0.5-0.7 GPa and 550-600 °C at ca. 30 Ma (Selverstone, 1985; Pennacchioni and Mancktelow, 2007). Metamorphic (re)crystallization was accompanied by the formation of ductile extensional shear zones (Pennacchioni and Mancktelow, 2007).

Sample BH12-07 (grains 15a and 28, Figs. 4.2a-c and 4.3a-b; 4.2d-f accordingly) was taken from a ca. 1 m thick ductile shear zone (N47°01'18.129"/E11°50'26.709") that is exposed on the NE slope of the Zemmbach side valley. It is a high-strained mafic dyke (see detail description in Kovaleva et al., 2014). Zircon is present as small (10-30 µm) euhedral crystals. Plastically-deformed crystals show lattice distortion type (III) (Kovaleva et al., 2014); subgrains range from 1 to 10 µm in size.

4.3. Analytical methods

4.3.1. Sample preparation and scanning electron microscopy (SEM)

Zircon grains were examined in polished thin sections of rock chips and in grain separates embedded in epoxy resin. For the latter zircon grains were extracted from the host rock by the standard procedure involving rock crushing, sieving to the 300 µm size, density separation on a Wilfley table, in heavy liquids and with Frantz magnetic separator. All samples were mechanically polished with 0.25 µm diamond paste and subsequently chemically polished with alkaline colloidal

silica solution on an active rotary head polishing machine for 4 hours. Samples were cleaned in ethanol and distilled water before carbon coating that was applied to establish electrical conductivity.

All zircons were identified and characterized by cathodoluminescence (CL) imaging using a FEI Inspect S scanning electron microscope (SEM) equipped with a Gatan MonoCL system (Center of Earth Sciences, University of Vienna, Austria) or using a Jeol JSM 6490LV SEM coupled with Oxford Inca Energy EDS (Geologische Bundesanstalt of Austria (GBA), Vienna, Austria). Energy-dispersive X-ray spectrometry (EDS) was applied to identify the host phases. Imaging conditions were 10 kV accelerating voltage, CL-image resolution: 1500*1500 to 2500*2500 pixels using a dwell time of 80.0-150.0 ms and probe current/spot size 4.5-5.0.

4.3.2. Forward scattered electrons (FSE) imaging and electron backscatter diffraction (EBSD) mapping

Zircon grains were examined for potential crystal-plastic deformation structures using orientation contrast images. These were taken using a forward scatter detector (FSD) mounted on the EBSD-tube of an FEI Quanta 3D FEG instrument (Center of Earth Sciences, University of Vienna, Austria), which is equipped with a Schottky field emission electron source. Electron beam conditions were 15 kV accelerating voltage, 2.5-4 nA probe current using the analytic mode. Stage settings were at 70° tilt and 14-16 mm working distance. After identification of the potentially deformed grains, EBSD orientation mapping was applied to them. The FEI Quanta 3D FEG instrument is equipped with an EDAX Pegasus Apex 4 system consisting of a Digiview IV EBSD camera and an Apollo XV silicon drift detector for EDX analysis. EDX intensities and EBSD data were collected contemporaneously using the OIM v6.21 data collection software. Orientation maps were obtained from beam scanning in hexagonal grid mode at step sizes of 0.1 – 0.2 μm.

The raw indexing for the EBSD maps, including zircon and host phases varies from 70% to 99,7%, depending on the host phase; raw indexing for zircon grains is > 99,9%. In some cases, after EBSD data collecting the maps were recalculated based on chemical composition of phases with the OIM v6.21 software. The EBSD data are represented in the sample reference frame and plotted using the EDAX OIM v6.2.1 Analysis software and the MTEX toolbox for MATLAB (Bachmann et al., 2010; Bachman et al., 2011; Mainprice et al., 2011).

For several misorientation profiles we have estimated the density of geometrically necessary dislocations that are required to produce the corresponding lattice curvature. The density of dislocations is: $\rho = \Delta\theta/Lb$, where $\Delta\theta$ is the misorientation angle extracted from EBSD map, L – the

distance between two points and b is the length of burgers vector that is equal to the shortest interatomic distance in the lattice (Reddy et al., 2007). Because every individual microprobe point has a certain spatial resolution, misorientation varies along microprobe point. Thus, for every point a boxplot of dislocation densities was made.

4.3.3. Field emission gun electron microprobe analyzer (FEG-EMPA)

Electron beam techniques can reveal the internal microstructures at a spatial resolution down to 0.1 μm , and detects features of distribution of such trace elements as Y, Yb, Hf in zircon (Nasdala et al., 2010; Klemetti et al., 2011; Storm et al., 2014).

Back-scattered electron (BSE) images, wavelength dispersive X-ray analyses of chemical composition and element distribution maps were obtained at the Helmholtz Centre Potsdam, GFZ, on a JEOL JXA-8500F Hyperprobe electron probe micro-analyzer equipped with a thermal field emission gun. For point analyses an acceleration voltage of 20 kV, a beam current of 20 nA, and a focused beam were chosen. For more analytical and calibration details see Nasdala et al. (2010).

The chemical zoning of the zircons were investigated by X-ray element mapping in WDS mode moving the stage in steps of 0.1-0.3 μm (15 or 20 kV, 20 or 30 nA, focused beam, 1000-1200 ms per step) or in beam scanning mode with 0.03-0.04 μm steps (15 or 20 kV, 120 nA, focussed beam, 2 ms per step, 100 frame accumulations, probe tracking procedure were used to avoid the beam shift).

The following elements were mapped: K, Pb, Si, U, Y, Yb, Zr and Al.

4.3.4. Nano-scale secondary ion mass spectrometry (NanoSIMS)

Isotope-selective high-sensitive secondary ion mass spectrometry is able to detect low-content isotopes of trace elements at nm scales in zircon (Boehnke et al., 2013; Hofmann et al., 2009, 2014; Storm et al., 2014).

Samples were coated with 30 nm Au and analyzed with the Cameca NanoSIMS 50L at Caltech Microanalyses Center, Pasadena, USA. The analytical conditions were similar to those used in Hofmann et al. (2009, 2014). An O^- primary beam of -8 kV was used to sputter the samples and secondary ions of +8 kV were measured with electron multipliers under high mass resolution conditions. Mass spectrum scans were examined to make sure that any significant interference was well resolved from the masses of interest. For individual spot analyses and line profiles, samples were pre-sputtering for 210-360 sec with a rastering primary beam of $\sim 80\text{-}90$ pA across 1×1 μm or 2×2 μm areas. Data were collected in the "Combined Analysis" mode of the NanoSIMS for the

following masses: ^{31}P , ^{49}Ti , ^{89}Y , ^{90}Zr , ^{140}Ce , ^{174}Yb , ^{180}Hf , ^{206}Pb , ^{207}Pb and ^{208}Pb . Profiles were acquired with step sizes of 1.5 to 5 μm , depending on the grain sizes and profile lengths. Ion images of eight masses (^{31}P , ^{89}Y , ^{90}Zr , ^{174}Yb , ^{180}Hf , ^{206}Pb , ^{207}Pb and ^{208}Pb) were also collected in the “Combined Analysis” mode over areas of 10x10 μm to 20x20 μm . Ion image processing was done with the software Look@NanoSIMS (Polerecky et al., 2012). Ion images showed that ^{90}Zr and ^{180}Hf have fairly homogeneous distribution in zircon and thus were used as reference masses.

For correction of lead isotopes measurements, the standard measurements of zircons Plesovice and 91500 have been reevaluated. Those with good intensities and no correlation between Zr, Hf and Pb were chosen to calculate a correction factor for $^{207}\text{Pb}/^{206}\text{Pb}$ that is 1.016. $^{207}\text{Pb}/^{206}\text{Pb}$ relative ages were calculated using the toolbox Isoplot 4.15 for Microsoft Excel.

4.4. Results

4.4.1. Orientation, chemical and isotope mapping of plastically-deformed zircon grains

Mapping with FEG-EMPA vs orientation mapping

Concerning the mapped elements, Al and K showed low concentrations that are under the detection limit, and thus haven't yielded representable maps. Si and Zr showed fairly homogeneous distribution with some minor depletion along brittle fractures (grain 33). Pb was at the detection limit yielding at maximum from 12 to 47 counts for different maps, and showed very homogeneous distribution as well. U, Y and Yb yielded well defined features, in some cases connected with crystal-plastic deformation structures (grains 04 and 33).

Grain 04 reveals several subgrains separated by a set of subgrain boundaries with the maximum misorientation of ca. 2° (Fig. 4.1a). CL image demonstrates a dark core, crosscut by bright lines that spatially correspond to low angle boundaries, and bright rim around the core (Fig. 4.1b). The rim also reveals dark and blurred bright features corresponding to low angle boundaries (Fig. 4.1b, left side, marked by arrows). The BSE image shows a bright core that is crosscut by dark linear features corresponding to low angle boundaries (Fig. 4.1c). The darker BSE rim shows sharp transitions in color gradient between subgrains, which probably represents an orientation contrast. Chemical maps derived with FEG-EMPA show a Y- and U-rich core and linear features of Y and U depletion crosscutting this core, some of those features correspond to low angle boundaries. Maps

of Yb/Y and U/Y show slight enrichment along these features (Fig. 4.1d). There are no resolvable features in the Y- and U-depleted rim.

Grain 33 consists of multiple subgrains with the maximum misorientation ca. 9° (Fig. 4.1e). CL image reveals bright and, less frequently, dark features that correspond to low angle boundaries (Fig. 4.1f, arrows). The BSE image reveals a few dark features corresponding to low angle boundaries (Fig. 4.1g, lower part); in the upper right part sharp transitions in color gradient between subgrains probably represent orientation contrast. Chemical maps reveal Y-, U- and Yb-enriched core, crosscut by linear features of depletion that correspond to sub-horizontal fractures (thick dotted lines in Fig. 4.1a, black lines in Fig. 4.1g) and to low angle boundaries (Fig. 4.1h, white dotted lines). Depleted zones mostly correspond to those low angle boundaries, which misorientation exceeds 2° (red and black solid lines in Fig. 4.1e). These depleted linear zones, however, are thicker than corresponding low angle boundaries.

EBSD mapping of smaller grains 15a and 28 reveals several subgrains with a maximum misorientation of ca. $5\text{-}6^\circ$ (Fig. 4.2a, d). BSE images are not presented here because they do not reveal any visible contrast; although CL response documents bright linear features that spatially coincide with the positions of low angle boundaries (Fig. 4.2b, e, highlighted by arrows).

For the grain 15a the CL image also documents a bright core and an oscillatory-zoned rim. Chemical mapping shows an Y-enriched outer core and outer rim, an U-enriched core and outer rim. Yb is slightly depleted in the core; U/Y map shows depletion in the outer core; Pb does not reveal any resolvable features within this zircon. The only feature that spatially coincides with low angle boundaries is U/Y vague enrichment zones in the rim (Fig. 4.2c, arrows).

Grain 28 reveals a homogeneous distribution of Y, U and Yb, with some local spotty enrichment and depletion of Y and U in the core (Fig. 4.2f). There are no features corresponding to low angle boundaries in the trace element distribution maps of grain 28. But there are features in the matrix that indicate local enrichment in Y and U close to a low angle boundary in zircon (white arrows in Fig. 4.2f).

Mapping with NanoSIMS vs orientation mapping

Isotope mapping of the deformed zircon grains show that ^{31}P , ^{206}Pb , ^{207}Pb and ^{208}Pb have very low count rates, however for Pb some features connected with lattice distortion are resolvable whereas ^{89}Y and ^{174}Yb yielded well-defined features (Fig. 4.3).

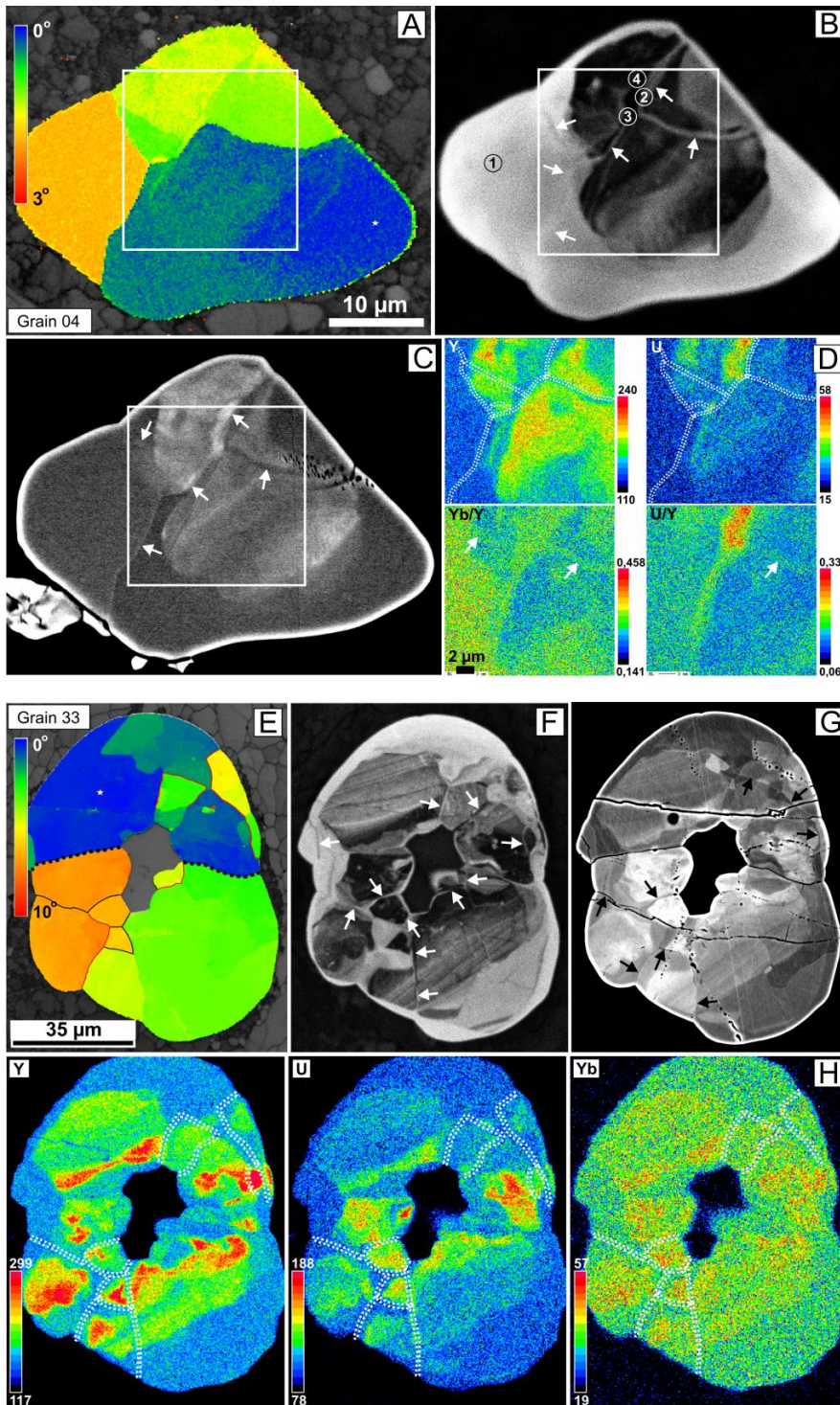


Figure 4.1. Various maps: (a)-(d) – grain 04, E-H – grain 33. **(a)** and **(e)** Cumulative EBSD maps, showing the orientation of every data point with respect to a reference point (white star marker); white frame in **(a)** indicates the location of chemical maps shown in **(d)**; red lines correspond to 2-5° misorientation between the subgrains, black solid lines correspond to 5-15° of misorientation, thick black dotted lines highlight fractures. **(b)** and **(f)** CL images, arrows show features that correspond to low angle boundaries, numbers in **(b)** indicate locations of point analyses derived by FEG-EMPA; **(c)** and **(g)** BSE image, arrows as in **(b)**; **(d)** and **(h)** chemical maps derived with FEG-EMPA, lines and arrows indicate features that correspond to low angle boundaries, numbers indicate lowest and highest counts for every map.

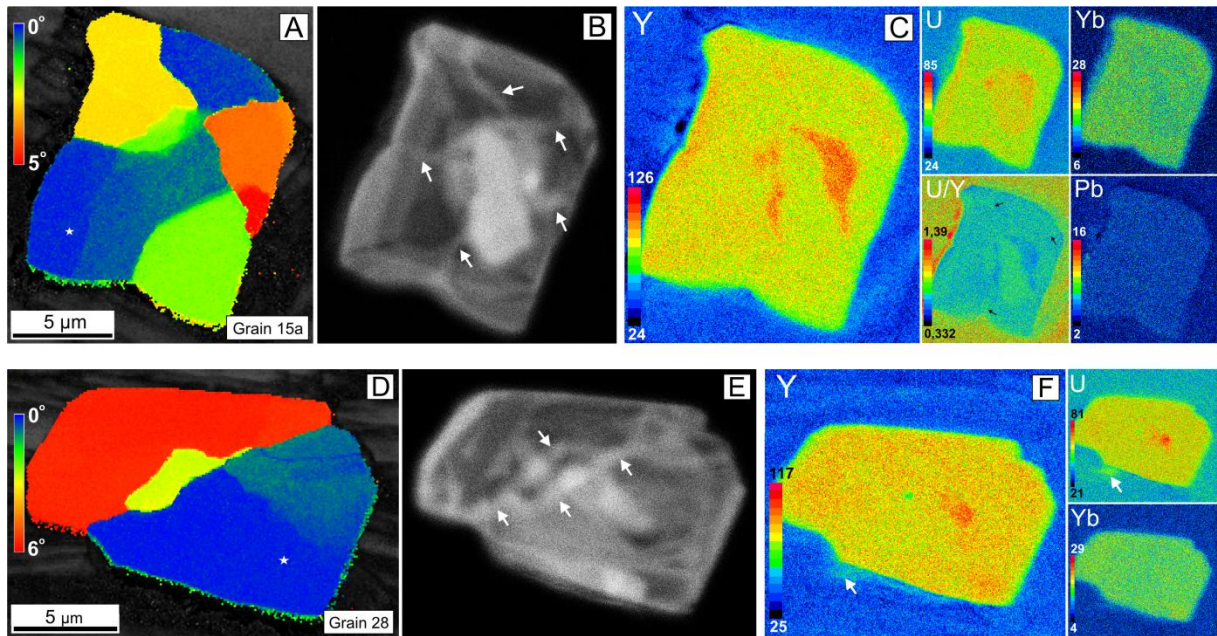


Figure 4.2. Various maps: (a)-(c) – grain 15a, (d)-(f) – grain 28. **(a)** and **(d)** are cumulative misorientation maps; **(b)** and **(e)** CL images, arrows show bright features that correspond to low angle boundaries; **(c)** and **(f)** chemical maps derived with FEG-EMPA, arrows in (c) highlight features corresponding to low angle boundaries. Arrows in (f) highlight spots of local enrichment of trace elements in matrix.

Isotope mapping of the grain 15a with NanoSIMS revealed more complicated internal features of this zircon crystal than by mapping with electron microprobe (Figs. 4.2c vs 4.3b). The local misorientation EBSD map shows a low angle boundary set with higher-angle boundaries in the upper right (Fig. 4.3a). Isotope mapping reveals an ^{89}Y -enriched outer core. In the rim, especially in the upper part depleted features are resolvable and corresponding to low angle boundaries (Fig. 4.3b, ^{89}Y). In the map of ^{174}Yb a depleted core and enriched rim and depletion features as in ^{89}Y map are resolvable. Depleted zones are even more pronounced in the summary map $^{89}\text{Y}+^{174}\text{Yb}$. The $^{90}\text{Zr}/(^{206}\text{Pb}+^{207}\text{Pb}+^{208}\text{Pb})$ ratio map shows enrichment in the core, as well as some indistinct enriched domains in the lower left and upper left part (arrows). These inhomogeneities are not linear; however they belong to domains that contain low angle boundaries. The $^{174}\text{Yb}/^{89}\text{Y}$ map shows depletion in the core and slightly depleted in the portions corresponding to low angle boundaries in the upper part (arrows).

The misorientation EBSD map of grain 05 shows intensive lattice distortion in the upper left part of the grain. The misorientation between data points reaches 20° in that domain (Fig. 4.3c). The CL image shows a distorted bright rim in this zone and isotope mapping shows patchy depletion of ^{89}Y , ^{174}Yb and $^{89}\text{Y}/^{174}\text{Yb}$ in this zone (Fig. 4.3d-e). Additionally, the inhomogeneity in

$\log((^{206}\text{Pb}+^{207}\text{Pb}+^{208}\text{Pb})/^{180}\text{Hf})$ map (enriched spot) belongs to distorted zone. This map also shows enrichment at the grain's upper border where it experiences marginal grain size reduction (arrows, for the detailed description of deformation microstructures in the grains 15a, 28 and 05 see Kovaleva et al., 2014).

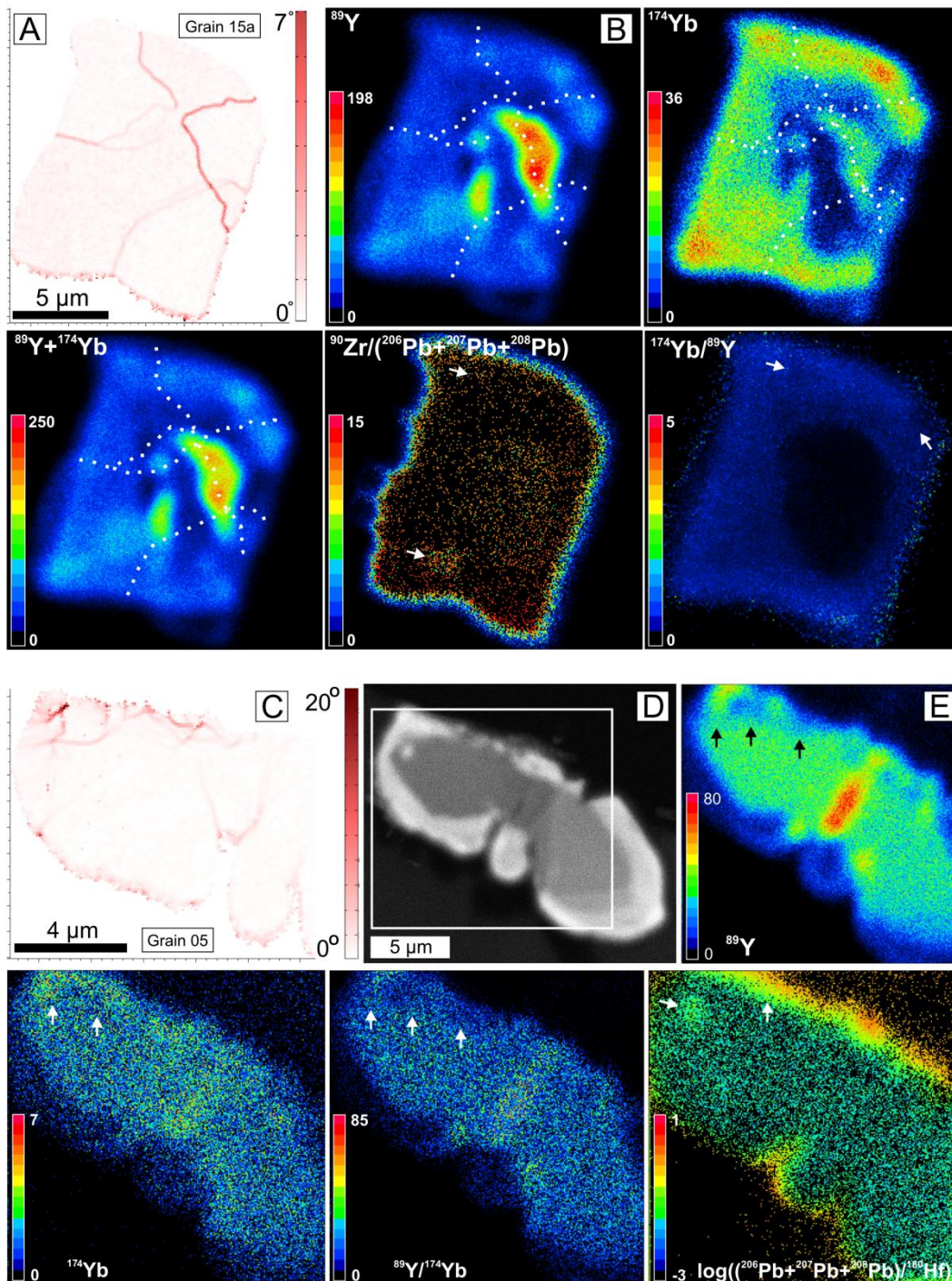


Figure 4.3. Various maps: (a)-(b) – grain 15a, (c)-(e) – grain 05. (a) and (c) are local misorientation EBSD maps, showing the misorientation of every data point compared with its neighbors; (b) and (e) isotopic maps derived with NanoSIMS, scales show amount of counts; arrows and dotted lines highlight the features related to lattice distortion; (d) CL image, frame highlights location of EBSD and NanoSIMS maps.

4.4.2. High-resolution profiles across plastically-deformed zircon grains

Profiling with FEG-EMPA

Electron beam analyses yielded inhomogeneous distribution of trace elements in zircon along the individual grains. Grain 16b shows intensive bending of the lattice that changes its orientation from $0,9^\circ$ to $1,8^\circ$ per μm (Kovaleva et al., 2014); and has maximum orientation gradient of 25° (Fig. 4.4a). Density of geometrically necessary dislocations along the profile A-B is oscillating on two levels: with periods $\sim 1 \mu\text{m}$ and $\sim 10\text{-}15 \mu\text{m}$ (Fig. 4.4e). The CL image shows a fairly homogeneous signal and there are no variations of intensity across the grain's elongation (Fig. 4.4b). However, the BSE image shows an inhomogeneous undulatory signal that may be either due to compositional variations or orientation contrast (Fig. 4.4c). High-resolution profiles and individual points along this grain were made with FEG-EMPA, locations are marked in Figure 4.4c. Points 1-25 were taken along the profile A-B (Fig. 4.4a, c) with the step-size of approximately $2 \mu\text{m}$. Microprobe element profiles show very consequent oscillation (Fig. 4.4d). Microprobe points 3-5, 10-13, 15-19, 24-26 belong to that parts of the misorientation profile that has elevated dislocation density (Fig. 4.4e).

Pb content varies in the grain from 0 to 930 ppm, Yb from 0 to 306 ppm, U from 0 to 577 ppm, Hf from 10 to 13 wt%, Ti from 100 to 853 ppm, Nb from 345 to 782, Ce from 0 to 608 ppm and Nd shows compositional fluctuations from 0 to 498 ppm. Pb, Yb and Nb profiles show complete or partial systematic depletion in points that correspond to intensively-deformed zones (Fig. 4.4d). U depletion in points 15-17 and 23-24 is also spatially attributed to high dislocation density; U content also decreases towards the grain boundary (point 1). Ti and Hf show no obvious correlation with deformed zones; Ce and Nd show local enrichment in zones with high dislocation density. However, it is hard to find the direct correlation because dislocation density is oscillating significantly across the entire grain and its small-scale oscillation period is smaller than analyses step size.

Four individual point analyses were made with FEG-EMPA over the grain 04; positions 1-4 are marked in Figure 4.1b. Thus, point 1 belongs to CL-bright rim, 2 and 3 were collected over the low angle boundaries and point 4 belongs to CL-dark core. Yb content varies in these data points from 154 to 520 ppm, U from 171 ppm to 4 wt%, Hf from 12,5 to 14,6 wt%, Ti from 0 to 48 ppm, Nb from 581 to 561, Ce from 0 to 786 ppm and Nd shows compositional fluctuations from 0 to 261 ppm. P and U show enrichment and Ti shows depletion towards the core. Yb indicates well-defined depletion in low angle boundaries, Hf shows no correlation, Nb is enriched in low angle boundaries whereas Ce and Nd show only partial enrichment that corresponds to low angle boundaries (Fig. 4.5).

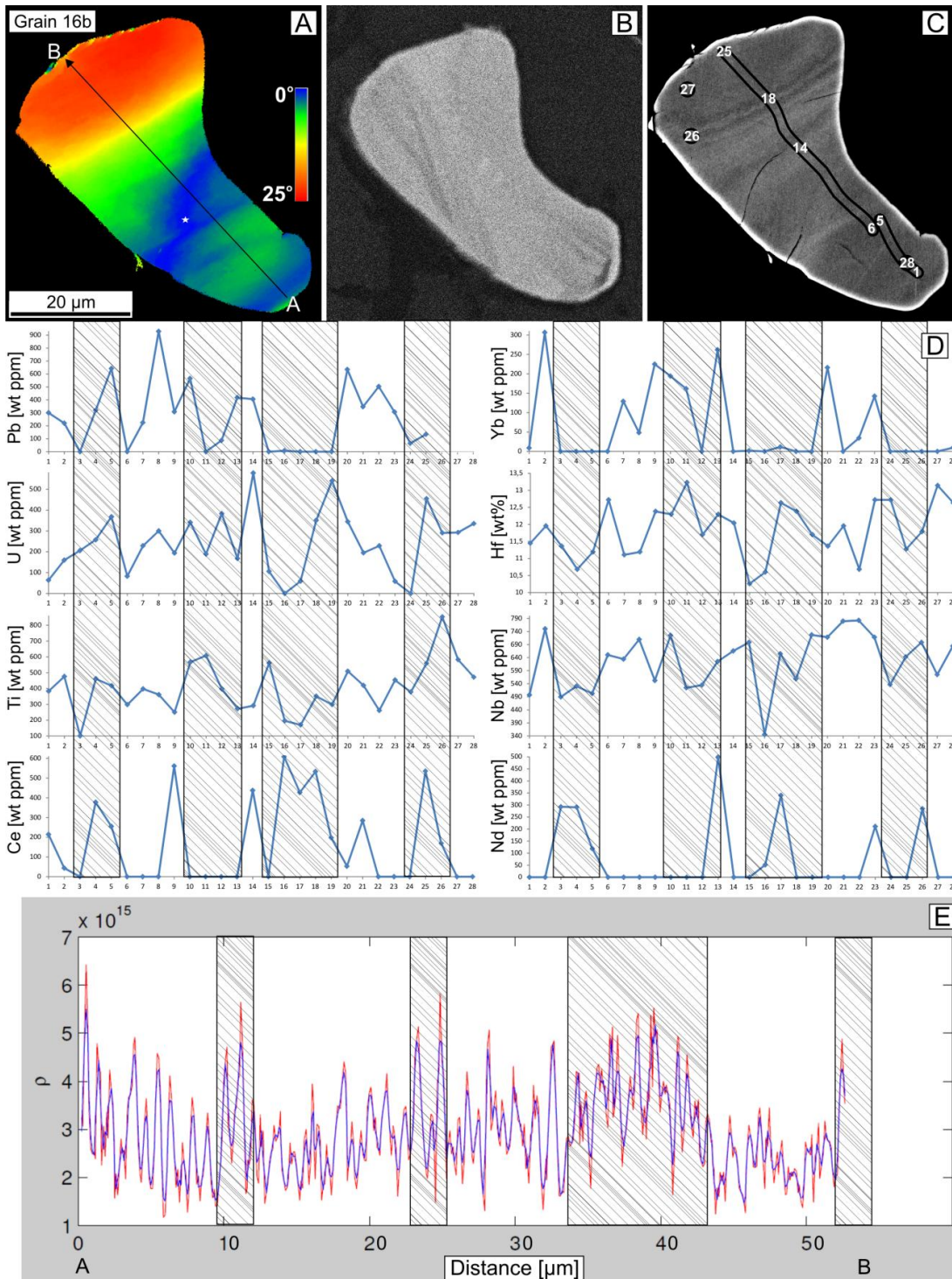


Figure 4.4. Grain 16b. **(a)** Cumulative EBSD map; arrow marks the position of misorientation profile A-B, shown in **(e)**. **(b)** CL image that is showing homogeneous signal. **(c)** BSE image, lines and numbers indicate positions of the profiles (1-5 and 6-25) and single point analyses (26-28) made with FEG-EMPA. **(d)** Chemical compositions corresponding to profiles and points indicated in **(c)**. Highlighted boxes indicate approximate areas of intense lattice rotation with high dislocation density. Pb, Yb and Nb are depleted in intensively-deformed zones; Ti and Hf perform no effect; U shows generally lower values; Ce and Nd show general enrichment. **(e)** Density of geometrically necessary dislocations along the profile A-B. Highlighted boxes are same as in **(d)**.

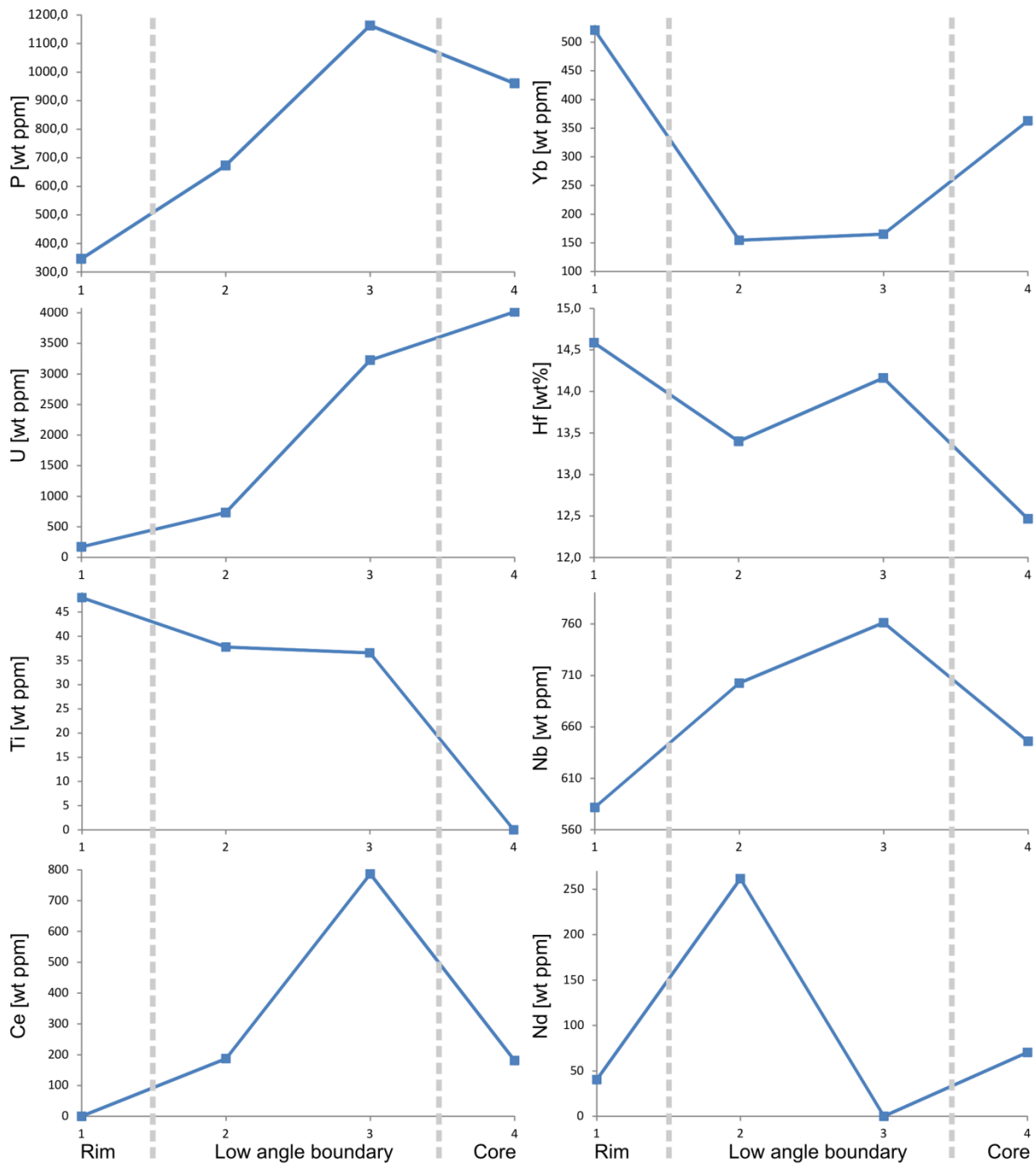


Figure 4.5. Chemical composition of the grain 04, numbers 1-4 are individual point analyses made with FEG-EMPA, location marked in Figure 1b. P and U show depletion towards the rim, Ti shows depletion towards the core, Yb is depleted in low angle boundaries, Hf and Nb perform no effect; Ce and Nd show general enrichment.

Profiling with NanoSIMS

High-resolution point analyses that were applied to eight grains with lattice distortion (09, 10a, 10b, 16a, 15, 25, 26 and 30). Locations of point analyses and profiles are marked over FSE maps and

CL images (Figs. 4.6a-b and e-f; 4.7a-b and e-f; 4.8a-b and d-e; 4.9a-b and e-f). The profiles with isotope intensities normalized to ^{90}Zr or ^{180}Hf intensities are shown in the Figures 4.6-4.9 (6d, g; 7d, g; 8c, g; 9d, g). $^{89}\text{Y}/^{90}\text{Zr}$ varies in the grains from $8 \cdot 10^{-4}$ to $1,9 \cdot 10^{-2}$; $^{174}\text{Yb}/^{90}\text{Zr}$ varies from $3 \cdot 10^{-5}$ to $1,9 \cdot 10^{-3}$; $^{208}\text{Pb}/^{90}\text{Zr}$, $^{207}\text{Pb}/^{90}\text{Zr}$ and $^{206}\text{Pb}/^{90}\text{Zr}$ vary from $2,5 \cdot 10^{-6}$ ($^{206}\text{Pb}/^{90}\text{Zr}$) to $6 \cdot 10^{-5}$ ($^{208}\text{Pb}/^{90}\text{Zr}$); $^{31}\text{P}/^{90}\text{Zr}$ varies from $8 \cdot 10^{-5}$ to $9 \cdot 10^{-4}$; $^{49}\text{Ti}/^{90}\text{Zr}$ from $1 \cdot 10^{-5}$ to $5 \cdot 10^{-4}$; $^{140}\text{Ce}/^{90}\text{Zr}$ from $4 \cdot 10^{-6}$ to $4 \cdot 10^{-4}$. For the grain 30, profile 2, isotopes are normalized to ^{180}Hf , so that $^{174}\text{Yb}/^{180}\text{Hf}$ value varies from $5,4 \cdot 10^{-2}$ to $7,4 \cdot 10^{-2}$; $^{208}\text{Pb}/^{180}\text{Hf}$, $^{207}\text{Pb}/^{180}\text{Hf}$ and $^{206}\text{Pb}/^{180}\text{Hf}$ vary from $4,8 \cdot 10^{-3}$ to $8,5 \cdot 10^{-3}$; $^{31}\text{P}/^{180}\text{Hf}$ from $1,17 \cdot 10^{-1}$ to $1,45 \cdot 10^{-1}$; $^{49}\text{Ti}/^{180}\text{Hf}$ from $1,2 \cdot 10^{-2}$ to $3 \cdot 10^{-2}$; $^{140}\text{Ce}/^{180}\text{Hf}$ from $1,6 \cdot 10^{-2}$ to $2,7 \cdot 10^{-2}$. The correspondence of isotope ratios with plastically deformed zones is sometimes not straight forward, because the latter are often conjugated with micro-pores and fractures that greatly influence analytical results. Initial growth zoning, revealed by CL imaging, can also influence isotopic composition and thus should be taken into account. However, an accurate picture of behavior of analyzed trace elements can be put together by statistically collecting data.

Grain 09 (Fig. 4.6a-d) reveals bending of the crystal lattice, misorientation along NanoSIMS profile reaches 9° with respect to the starting point and dislocation density is changing along (Fig. 4.6c). The CL image reveals homogeneously-bright signal with no zonation. Along the NanoSIMS profile the points 3-5 belong to the most damaged lattice, where the lattice rotation reaches $0,65^\circ/\mu\text{m}$. Points 3-6 show decreased value of $^{89}\text{Y}/^{90}\text{Zr}$ and $^{174}\text{Yb}/^{90}\text{Zr}$ ratios. $^{208}\text{Pb}/^{90}\text{Zr}$, $^{207}\text{Pb}/^{90}\text{Zr}$, $^{206}\text{Pb}/^{90}\text{Zr}$, $^{31}\text{P}/^{90}\text{Zr}$ and $^{140}\text{Ce}/^{90}\text{Zr}$ ratios are decreasing towards point 4. $^{49}\text{Ti}/^{90}\text{Zr}$ is decreased in points 1-4.

Grain 10a (Fig. 4.6e-g) shows very modest misorientation. In the corresponding CL image a dark oscillatory-zoned core and a bright rim are distinguishable; analyses were done within bright rim. Ratios for points 1, 2 and 4 are showing close values, except of the point 3 that was set close to the fracture. As a result, all isotope ratios are increased for the point 3.

Grain 10b (Fig. 4.7a-d) reveals intensive bending of the lattice, excluding the upper right tip that is undeformed, the misorientation profile shows a sharp step in orientation of 2° (low angle boundary) that corresponds to the transition from the non-deformed tip to the deformed middle part, where the lattice shows bending of $0,36^\circ/\mu\text{m}$ (Fig. 4.7c, inset). Box-and-whiskers plot for dislocation densities shows significant distortion in points 9, 10 and 2 (Fig. 4.7c). The CL image shows a dark oscillatory-zoned core, a bright rim, where the undeformed tip that is slightly darker than the rim. Profile was made starting with the undeformed tip (points 1, 6, 7, 8) towards the most deformed part (points 10, 2, 3). Points 9-10 were set on the low angle boundary. Individual points 4 and 5 were

also were set on the bright rim in the lower part of the deformed domain; point 4 close to the CL-dark core. $^{89}\text{Y}/^{90}\text{Zr}$ ratio is decreased near the low angle boundary; in points 4-5 $^{89}\text{Y}/^{90}\text{Zr}$ is relatively high (these points are close to CL-dark core). $^{174}\text{Yb}/^{90}\text{Zr}$ shows low values in the undeformed tip and increases in deformed part. $^{208}\text{Pb}/^{90}\text{Zr}$, $^{207}\text{Pb}/^{90}\text{Zr}$ and $^{206}\text{Pb}/^{90}\text{Zr}$ ratios are decreased in low angle boundary (points 9-10); $^{31}\text{P}/^{90}\text{Zr}$ is increased in the undeformed tip. $^{49}\text{Ti}/^{90}\text{Zr}$ has high value in the low angle boundary whereas $^{140}\text{Ce}/^{90}\text{Zr}$ is also slightly higher in low angle boundary and generally higher in deformed part than in the undeformed.

Grain 16a (Fig. 4.7e-g) is deformed at its upper tip. Analytical points 1-3 were set close to the deformed tip, points 4-5 were set in the undeformed domain and point 6 covers a fracture. The CL signal is fairly homogeneous within the analyzed area. $^{89}\text{Y}/^{90}\text{Zr}$ and $^{174}\text{Yb}/^{90}\text{Zr}$ ratios demonstrate decreasing in point 3 that is a transition between deformed and undeformed domain; whereas $^{208}\text{Pb}/^{90}\text{Zr}$, $^{207}\text{Pb}/^{90}\text{Zr}$, $^{206}\text{Pb}/^{90}\text{Zr}$ and $^{31}\text{P}/^{90}\text{Zr}$, $^{49}\text{Ti}/^{90}\text{Zr}$ and $^{140}\text{Ce}/^{90}\text{Zr}$ ratios are increased in the deformed tip. All ratios show high values in point 6 that is set on the fracture.

Grain 15 is deformed at its right rim (Fig. 4.8a). The CL signal documents a bright and oscillatory-zoned rim around a dark and oscillatory-zoned core. The analyses were made within the bright rim, points 1-4 were set on the outer bright rim, points 5-6 – in the inner rim that is slightly darker. Analysis point 1 is made in the undeformed part, points 2-4 in the highly deformed part, points 5 and 6 in the transition zone between deformed and undeformed domain. $^{89}\text{Y}/^{90}\text{Zr}$ and $^{174}\text{Yb}/^{90}\text{Zr}$ demonstrate relatively high values in point 1, lower values for the points 2-4 and are decreased in points 5-6. $^{208}\text{Pb}/^{90}\text{Zr}$, $^{207}\text{Pb}/^{90}\text{Zr}$ and $^{206}\text{Pb}/^{90}\text{Zr}$ values are very high in the point 2 and relatively high in the point 3. $^{31}\text{P}/^{90}\text{Zr}$ decreased in deformed rim; $^{49}\text{Ti}/^{90}\text{Zr}$ is increased in point 3 and otherwise is fairly even; $^{140}\text{Ce}/^{90}\text{Zr}$ shows no correlation with deformed rim.

Grain 25 is plastically-deformed at its rim (Fig. 4.8d). The CL signal shows a dark core and a bright homogeneous rim, where NanoSIMS points were set (Fig. 4.8e). The misorientation profile shows lattice rotation up to $6,5^\circ$ and oscillating dislocation density profile, most distorted domains with high dislocation density correspond to points 1-2, 5-6, 8, and 10, those are sections with high median and high mean values for dislocation density (Fig. 4.8f). Isotope ratio profiles show complicated oscillation across the deformed rim and don't reveal a straight forward correlation with distorted zones, however the period of oscillation is similar, for example, for $^{140}\text{Ce}/^{90}\text{Zr}$ (Fig. 4.8f-g).

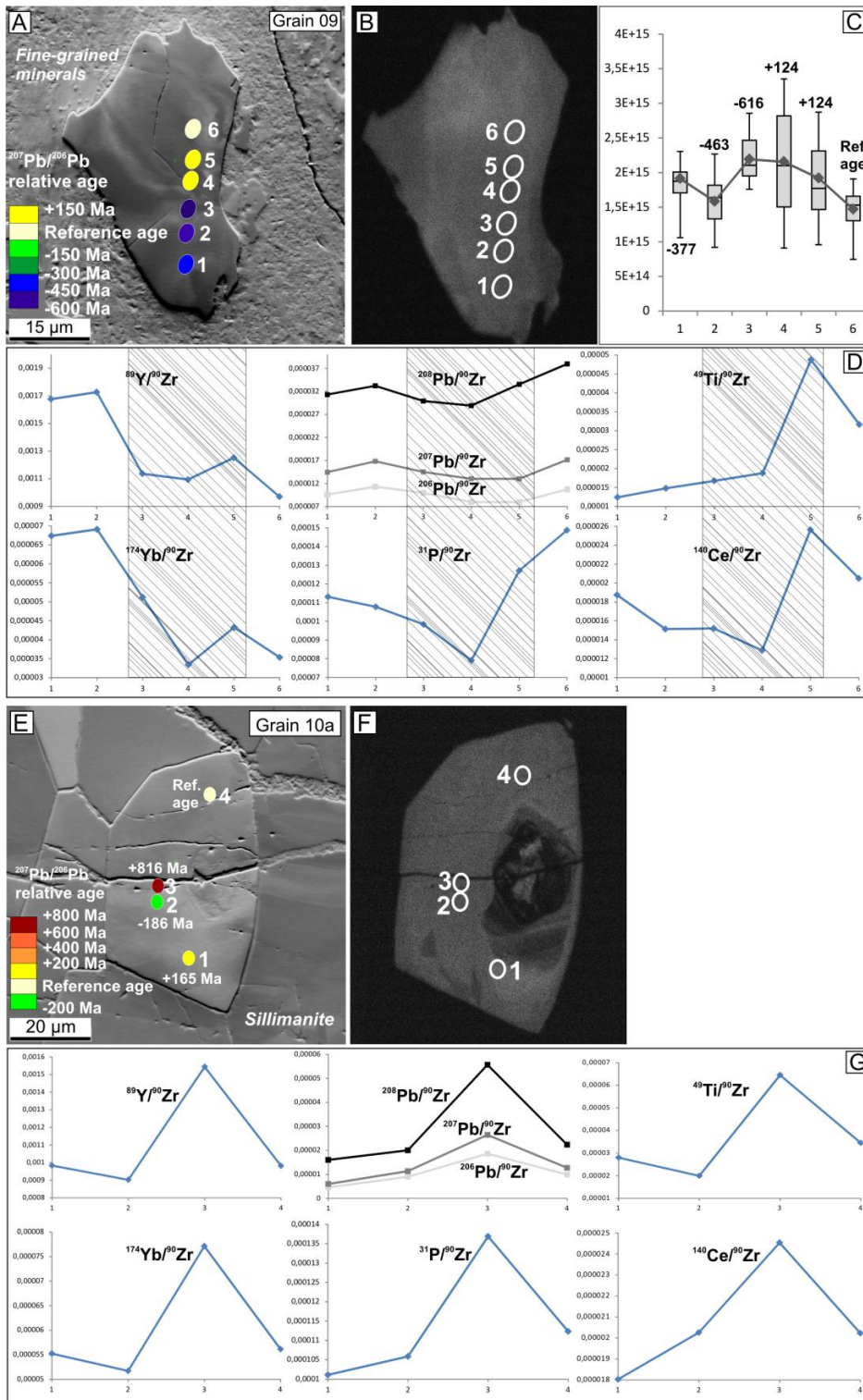


Figure 4.6. Grains from the sample IV12-05. **(a)** and **(e)** FSE images with locations of point analyses that are color-coded according to the $^{207}\text{Pb}/^{206}\text{Pb}$ relative ages; **(b)** and **(f)** CL images with locations of point analyses; **(c)** Box and whisker plot for dislocation density corresponding to each NanoSIMS point in grain 09. Upper and lower bars represent maximum and minimum, diamond symbols connected with line are mean dislocation density of each point. Numbers next to boxes are differences in $^{207}\text{Pb}/^{206}\text{Pb}$ relative age with respect to a reference age. **(d)** and **(g)** NanoSIMS profiles, each isotope normalized to ^{90}Zr . Highlighted boxes indicated points with high dislocation density.

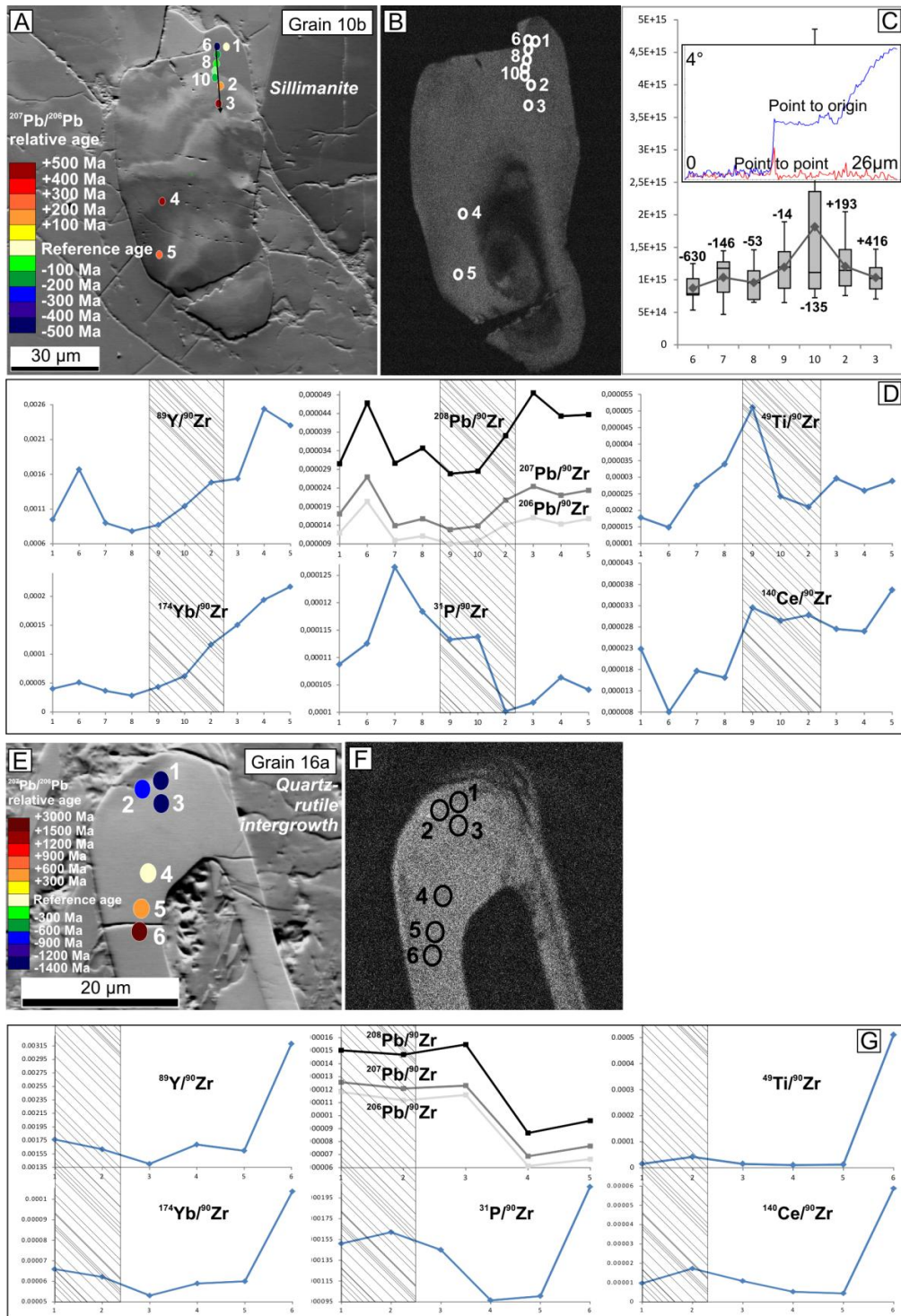


Figure 4.7. Grains from the sample IV12-05. **(a)** and **(e)** FSE images with locations of point analyses that are color-coded according to the $^{207}\text{Pb}/^{206}\text{Pb}$ relative ages; **(b)** and **(f)** CL images with locations of point analyses; **(c)** Box and whisker plot for dislocation density corresponding to each NanoSIMS point in grain 10b. Upper and lower bars represent maximum and minimum, diamond symbols connected with line are mean dislocation density of each point. Numbers next to boxes are differences in $^{207}\text{Pb}/^{206}\text{Pb}$ relative age with respect to a reference age. Inset shows misorientation profile along the NanoSIMS profile, location indicated in (a) by black arrow. **(d)** and **(g)** NanoSIMS profiles, each isotope normalized to ^{90}Zr . Highlighted boxes indicated points with high dislocation density.

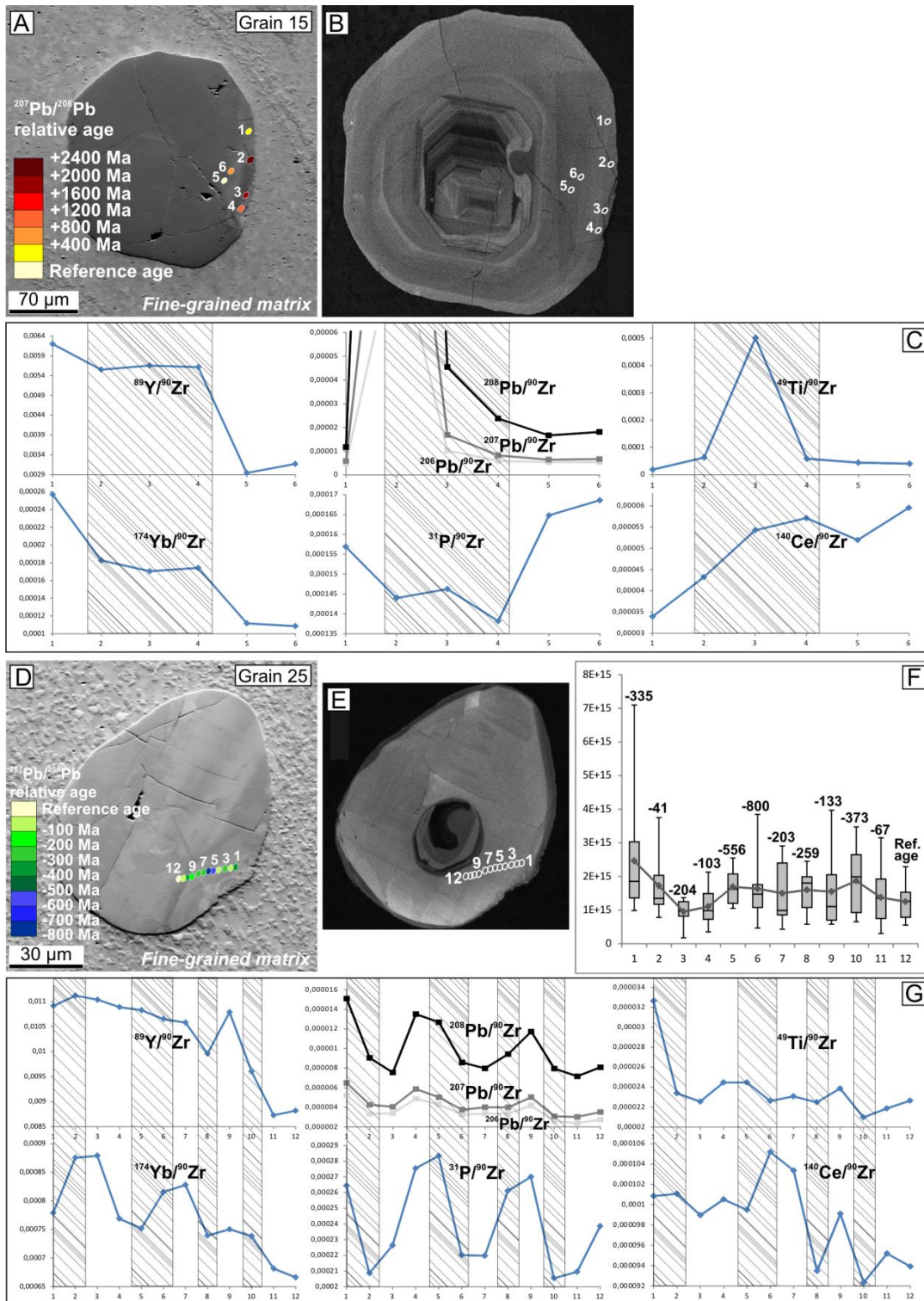


Figure 4.8. Grains from the sample IVZ02-12. (a) and (d) FSE images with locations of point analyses that are color-coded according to the $^{207}\text{Pb}/^{206}\text{Pb}$ relative ages; (b) and (e) CL images with locations of point analyses. (c) and (g) NanoSIMS profiles, each isotope normalized to ^{90}Zr . Highlighted boxes indicated points with high dislocation density. (f) Box and whisker plot for dislocation density corresponding to each NanoSIMS point in grain 25. Upper and lower bars represent maximum and minimum, diamond symbols connected with line are mean dislocation density of each point. Numbers next to boxes are differences in $^{207}\text{Pb}/^{206}\text{Pb}$ relative age with respect to a reference age.

Grain 26 (Fig. 4.9a-d) has deformed rims at the right (profile line 1) and at the left (profile line 2). The misorientation profile along line 1 shows gradual bending of the crystal (lattice distortion type I) and misorientation profile along line 2 shows high angle boundaries, connected with lattice distortion type (II) and marginal formation of new grains (Kovaleva et al., 2014; Kovaleva et al., in press). Along the profile line the most distorted domains correspond to points 1-2 and 4; along the profile 2 – to the points 2-4 (Fig. 4.9c). The CL image reveals a bright homogeneous rim, where the profile line 1 has been set; and darker zoned core, where profile line 2 belongs to (Fig. 4.9b). Isotope ratios from the zoned core (line 2) reveal much higher concentrations and higher magnitudes of fluctuation than from the rim (line 1). The enlarged profiles for the line 1 are therefore shown in the insets.

Profile line 1: $^{208}\text{Pb}/^{90}\text{Zr}$, $^{207}\text{Pb}/^{90}\text{Zr}$, $^{206}\text{Pb}/^{90}\text{Zr}$ and $^{140}\text{Ce}/^{90}\text{Zr}$ are generally increased in damaged zone; $^{49}\text{Ti}/^{90}\text{Zr}$ is decrease in damaged zone; $^{89}\text{Y}/^{90}\text{Zr}$, $^{174}\text{Yb}/^{90}\text{Zr}$ $^{31}\text{P}/^{90}\text{Zr}$ show no direct correspondence with damaged zones.

Profile line 2: point 1 was partially set in the matrix, so the isotope ratios are not reliable for the estimation of the zircon composition, and $^{208}\text{Pb}/^{90}\text{Zr}$, $^{207}\text{Pb}/^{90}\text{Zr}$, $^{206}\text{Pb}/^{90}\text{Zr}$, $^{49}\text{Ti}/^{90}\text{Zr}$, $^{31}\text{P}/^{90}\text{Zr}$ and $^{140}\text{Ce}/^{90}\text{Zr}$ show extremely high values in this point. Points 2-4 were made in the highly-deformed rim and points 6-7 in comparatively undamaged domain (Fig. 4.9c). $^{89}\text{Y}/^{90}\text{Zr}$ and $^{174}\text{Yb}/^{90}\text{Zr}$ are decreasing in damaged zone, with low value also in point 7. $^{208}\text{Pb}/^{90}\text{Zr}$, $^{207}\text{Pb}/^{90}\text{Zr}$, $^{206}\text{Pb}/^{90}\text{Zr}$, $^{49}\text{Ti}/^{90}\text{Zr}$ and $^{140}\text{Ce}/^{90}\text{Zr}$ are increasing in deformed rim. $^{31}\text{P}/^{90}\text{Zr}$ does not show significant fluctuations.

Grain 30 is embedded in epoxy resin; it shows lattice distortion at the upper left domain (Fig. 4.9e). CL imaging shows a bright core and a darker homogeneous rim (Fig. 4.9f). Profile line 1 was made across the boundary between the CL-dark and CL-bright zones, in an undistorted domain. Line 2 was set in a distorted domain, so that points 1-4 are located in undeformed zone and points 5-7 in distorted zone.

Analyses of the undistorted zone shows elevated $^{89}\text{Y}/^{90}\text{Zr}$ and $^{174}\text{Yb}/^{90}\text{Zr}$ ratios at the transition between the CL-dark and CL-bright zones with general higher values in bright zone. $^{208}\text{Pb}/^{90}\text{Zr}$, $^{207}\text{Pb}/^{90}\text{Zr}$, $^{206}\text{Pb}/^{90}\text{Zr}$ and $^{140}\text{Ce}/^{90}\text{Zr}$ show generally higher values in the CL-dark zone, $^{49}\text{Ti}/^{90}\text{Zr}$ decreases towards the grain boundary and $^{31}\text{P}/^{90}\text{Zr}$ demonstrates no correlation.

In line 2 $^{89}\text{Yb}/^{180}\text{Hf}$ demonstrates high values in the transition point between the deformed and undeformed lattice. $^{208}\text{Pb}/^{180}\text{Hf}$, $^{207}\text{Pb}/^{180}\text{Hf}$ and $^{206}\text{Pb}/^{180}\text{Hf}$ are slightly decreasing in the deformed zone, $^{31}\text{P}/^{180}\text{Hf}$ is oscillating, $^{49}\text{Ti}/^{180}\text{Hf}$ and $^{140}\text{Ce}/^{180}\text{Hf}$ demonstrate increased values in the deformed domain.

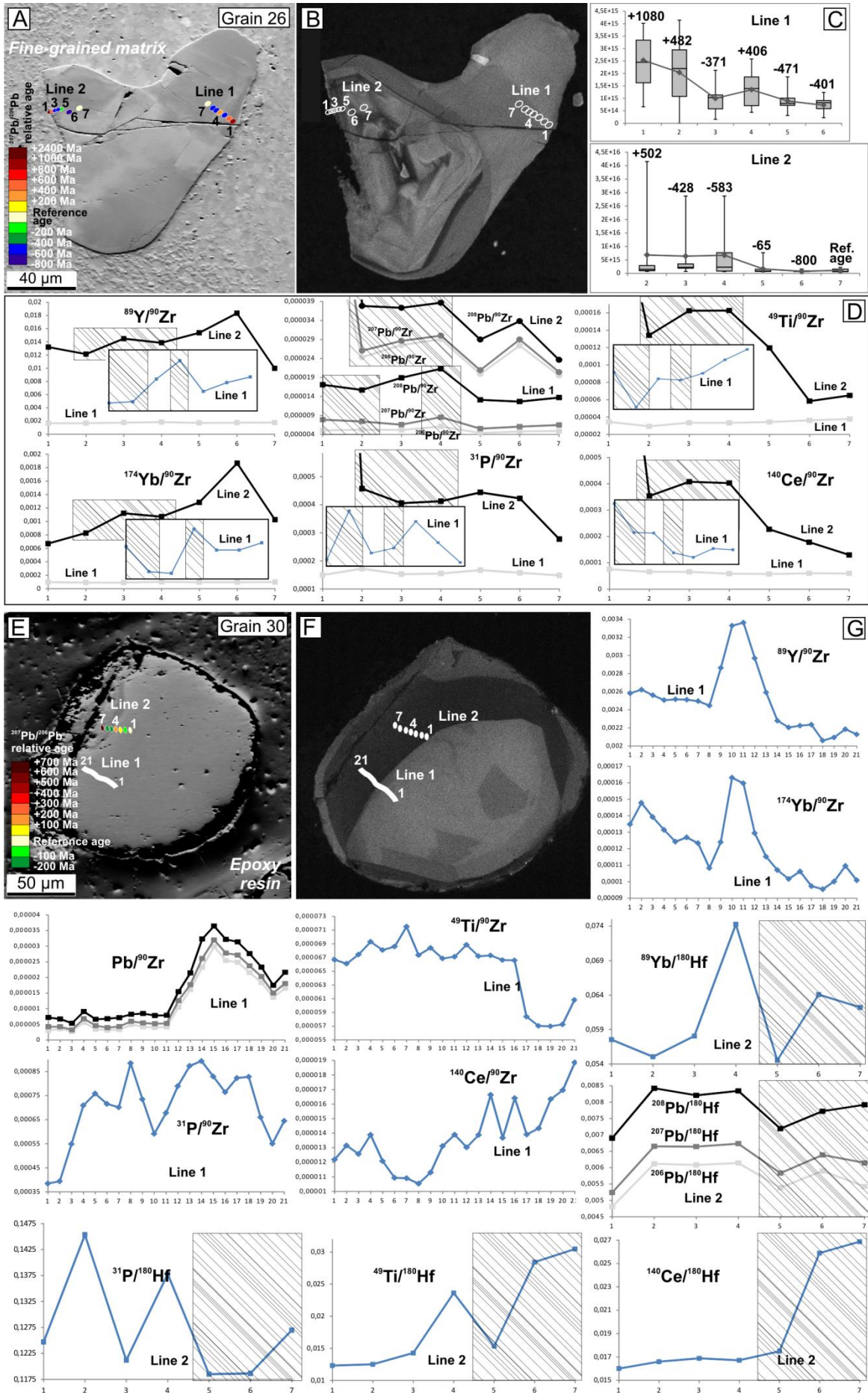


Figure 4.9. Grains from the sample IVZ02-12 and IV12-07. **(a)** and **(e)** FSE images with locations of point analyses that are color-coded according to the $^{207}\text{Pb}/^{206}\text{Pb}$ relative ages; **(b)** and **(f)** CL images with locations of point analyses; **(c)** Box and whisker plot for dislocation density corresponding to each NanoSIMS point in grain 26. Diamond symbols connected with line are mean dislocation density of each point. Numbers next to boxes are differences in $^{207}\text{Pb}/^{206}\text{Pb}$ relative age with respect to a reference age. **(d)** and **(g)** NanoSIMS profiles, each isotope normalized to ^{90}Zr or to ^{180}Hf (for line 2, grain 30). Highlighted boxes indicated points with high dislocation density.

4.5. Discussion

4.5.1. Efficiency of applied imaging techniques

High-resolution analytical techniques are able to analyze nano-scale features formed by trace elements distribution in minerals (e.g. Hofmann et al., 2009, 2014; Nasdala et al., 2010; Boehnke et al., 2013; Saunders et al., 2014; Storm et al., 2014). It is possible to resolve features genetically connected with lattice disturbances, which have only several hundreds of nm width.

We have demonstrated by chemical mapping (Figs. 4.1-4.2) that electron microprobe data can reflect inhomogeneities in trace elements concentrations in zircon, which are either connected with growth zoning (grains 04, 33, 15a), with fracturing (grain 33), and, most importantly, with crystal-plastic deformation (grains 04 and 33). Crystal-plastic deformation, resulting in the formation of low angle boundaries, affects the distribution of such trace elements as Y, Yb and U in zircon that are comparatively depleted along low angle boundaries. The strongest depletion of Y, Yb and U occurs along higher-angle boundaries (e.g. black solid lines in Fig. 4.1e) where the most prominent depletion along these zones is shown by Y (Fig. 4.1d). Depleted zones spatially correspond with linear features (dark and bright) as revealed by CL and BSE images. Changes in the CL intensity therefore occur due to compositional variations, and not due to the increased density of defects, as was suggested in Kovaleva et al. (2014). The BSE signal sometimes also documents orientation contrast, where the border between the subgrains is very sharp and represents gradient in color intensity (e.g. Fig. 4.1g, upper right). Orientation contrast is particularly visible where change in trace element composition is not so dramatic and does not influence the CL signal.

However, all these features are well-resolvable in large grains (> 40 μm in length), where CL-bright features have visible thickness up to 0,7 μm (e.g. grain 04). When it comes to smaller grains (10-15 μm in length, Fig. 4.2) with thinner CL-bright lines, corresponding to low angle boundaries,

EMPA mapping doesn't resolve any inhomogeneities in trace element distribution. It is only possible to resolve variations in Y, Yb and U connected with growth zonation and reflecting much larger features (grain 15a), but no smaller details are seen. Thus, electron beam analysis is a sufficient technique for resolving changes in trace element composition that: (i) result in changes of CL and BSE intensity, (ii) are thicker than 0,5 μm .

Ion beam techniques can achieve higher resolutions and documents not only growth zoning in more detail, but also the depletion in Y, Yb and re-distribution of Pb connected with low angle boundaries (grain 15a) and with distorted domains (grain 05, Fig. 4.3) in smaller grains. Thus the suggestion that inhomogeneities in CL intensity occur due to compositional variations (e.g. Timms et al., 2006; Kovaleva et al., 2014) is supported by ion beam mapping. Isotope mapping can resolve compositional features that are less than 0,5 μm thick, that otherwise could be clearly resolved by CL imaging only (e.g. Fig. 4.2b, e). The most pronounced features in trace elements depletion correspond to higher-angle boundaries. Thus, for fairly small zircons (< 30 μm in length) SIMS techniques are the most suitable.

4.5.2. Efficiency of chemical profiling

The interpretation of the results of chemical- and isotope profiling across plastically-deformed zones in zircon is not so straight forward. In most cases trace element variation occurs at different scales. This happens because the re-distribution of trace elements may be caused by various processes: metasomatism with fluid alteration or dissolution-reprecipitation (e.g. Geisler et al., 2001, 2003, 2007; Nasdala et al., 2010), dissolution, overgrowths or fracture healing (e.g. Corfu et al., 2003; Rimsa et al., 2007), presence of micro-inclusions and micro-fractures (e.g. Hofmann et al., 2009; Timms et al., 2012). Thus one cannot state with a high degree of confidence that fluctuations in trace elements and isotopes for each case occurred exclusively due to lattice distortion (see, for example, profile 1 in Fig. 4.9g). However, line 1 in grain 30 shows fluctuation of isotope ratios at a lower magnitude than in deformed zones, where isotope ratios often vary for orders of magnitude across deformed zones. Moreover we were trying to perform analyses over the CL- homogeneous areas, to avoid fractures and pores where possible, and thus minimize variety of trace elements that is not related to crystal-plastic deformation.

Variations in trace elements concentrations and isotope ratios across deformed zones show the range of 0,5-2 orders of magnitude. The trace element behavior is not consistent from grain to

grain and from one type of deformation pattern to another. However, in general, three types of distorted lattice (I)-(III) show rather pronounced change in trace element composition.

Often we see that dislocation density profile is oscillating with the period of 1-2 μm (grains 16 and 25), and in that case chemical and isotope profiling also demonstrate small-scale oscillation. We suggest that peaks in dislocation density (domains with high median and mean values of dislocation density) correspond to highly damaged bands of the lattice that serve as pathways for trace elements and radiogenic isotopes. Through such damaged bands elements are easily removed from these parts of lattice.

4.5.3. Trace elements behavior

The aggregated information about behavior of every trace element in plastically-deformed zones of different types in each analyzed grain is collected in Table 4.1. In order to make a conclusion for every individual trace element, the table contains information derived from both chemical mapping and profiling.

Y and Yb demonstrate similar behavior in plastically-deformed zones. They show depletion in low angle boundaries (deformation pattern (III), grains 04, 33, 15a, 10b) and in intensively bent zones (deformation patterns (I) and (II), grains 05, 16b, 09, 16a). Y experiences more intensive loss than Yb and U in low angle boundaries and distorted zones, which is visible from Yb/Y and U/Y maps. Close to sites where low angle boundaries pin the grain boundary, local enrichment of Y in matrix is observed (grains 15a and 28). This can indicate Y transport along low angle boundaries from the grain interiors into the matrix. Y and Yb often show oscillations along distorted domains where deformation patterns (I) and (II) are observed (e.g. grains 16b, 09, 15, 25, 26, 30). The oscillations could occur due to short-wave oscillations in dislocation density: elements are depleted in domains with high dislocation density. Oscillation across deformed rims is probably also connected with the chemical potential of these elements which is changing in the deformed zones. The frontal area of lattice bending attracts cations from the undistorted adjacent lattice by "Cottrell atmosphere" (Cottrell and Bilby, 1949) and then remove them from the grain via dislocations and (sub)grain boundaries. That is why the transition point between distorted and undistorted lattice is often enriched in Y and Yb, and sometimes in other trace elements. Schematic chemical profile for Y and Yb, reflecting potential distribution of Y and Yb across deformed zones in zircon is shown in Figure 4.10a-b.

Pb in ion beam analyses is presented as three distinct isotopes with masses 206, 207 and 208 that have similar behavior. Pb shows a mosaic pattern in deformed domains that provides some

evidence of Pb re-distribution. Pb is most often depleted in low angle boundaries and in intensively-bent zones and also can show oscillation across deformed zones (grain 25). It may behave similar to Y and Yb in distorted domains type (I) and (II) (grain 16 line 1; grain 30, line 2). However, Pb is often enriched in grain boundaries (grains 05, grain 26 line 2) and in micro-cracks in deformed zone close to grain boundaries open to the matrix (grains 15, 26 line 2). A possible process is Pb loss from deformed zones into the matrix and gain of common lead from the matrix. Such redistribution mostly occurs in lattice distortion type (II).

U shows depletion in low angle boundaries and intensively-bent zones and decreases towards grain boundaries.

Ti shows no strict consistency in its behavior with respect to plastically-deformed zones in zircon. In most cases (5 of 11) it is enriched, but also occur depleted or shows no resolvable correlation. This could be connected with the amount of Ti in the surrounding matrix, so it could move out of the grain along dislocations if the matrix is Ti-depleted, or inside the grain if matrix is Ti-enriched. Thus the effect of crystal-plastic deformation on Ti-content should be taken into account while constraining the formation temperature using the Ti-in-zircon thermometry. For example, Timms et al. (2011) and MacDonald et al. (2013) have documented decreased Ti-content from distorted grains.

The temperature estimations were made for grains 04 and 16b by Ti-in-zircon thermometry assuming TiO_2 activity of 1,0 (Watson et al., 2006). Ti concentration within zircon crystal 16b vary from 100 to 853 ppm, which correspond to crystallization temperatures of $995 - 1377 \pm 10$ °C, with average temperature of 1208 ± 10 °C. Ti-redistribution due to crystal-plastic deformation may cause the variety in temperature observed along the grain 16b. For the grain 04 Ti concentration vary from 0 to 48 ppm, yielding the temperature of $869 - 900 \pm 10$ °C with average of 881 ± 10 °C for non-zero concentration. However, in grain 04 Ti is apparently diffusing from Ti-rich rim towards the Ti-depleted core along low angle boundaries. Thus the temperature derived from Ti content in points 2 and 3 does not reflect formation temperature.

Hf behavior is not clearly correlated with plastically-deformed zircon domains. Usually, Hf variation is very moderate with respect to its high content that can reach up to 15 wt% in zircon. Hf shows 6 cases of no correlation, three cases of depletion, three cases of slight enrichment and one case of oscillation along the deformed zone.

Grain	Distortion type	Y	Yb	Pb	²⁰⁷ Pb/ ²⁰⁶ Pb ages	U	Ti	Hf	P	Nb	Ce	Nd
04	(III)	Depletion in low angle boundaries, enrichment of U/Y and Yb/Y in low angle boundaries	Depletion in low angle boundaries	-	-	Depletion in low angle boundaries; enrichment towards the core	Depletion towards the core	No correlation	Enrichment towards the core	Enrichment in low angle boundary	Partial enrichment in low angle boundary	Partial enrichment in low angle boundary
33	(III)	Depletion in low angle boundaries; enrichment of U/Y and Yb/Y in low angle boundaries	Depletion in low angle boundaries	-	-	Depletion in low angle boundaries	-	-	-	-	-	-
15a	(III)	Depletion in low angle boundaries	Same as Y	Depletion next to low angle boundaries	Aged or rejuvenated along low angle boundaries	U/Y is slightly increased in low angle boundaries	-	No correlation	No correlation	-	-	-
28	(III)	No correlation visible with EMPA	Same as Y	No correlation visible with EMPA	-	No correlation visible with EMPA	-	-	-	-	-	-
05	(II)	Depleted in deformed zone; depleted Y/Yb in deformed zone	Depleted in deformed zone	Re-distribution and enriched spot in deformed zone, enriched in the grain boundary next to deformed zone	Aged in intensively-deformed zone and rejuvenated around, at the deformation front	-	-	Slightly depleted in deformed tip	-	-	-	-
16b	(I)	-	Depleted in intensively banded zones	Depleted in intensively banded zones	-	Depleted in intensively banded zones; decreases towards grain	No correlation	No correlation	-	Depleted in banded zones	Partial enrichment in intensively banded	Partial enrichment in intensively banded

						boundary					zones	zones
09	(I)	Depleted in intensively bended zone	Same as Y	Depleted in intensively bended zone	Rejuvenated bended lattice domain	-	No correlation	No correlation	Depleted in highly bended zone	-	Slightly depleted in intensively bended zone	-
10a	No dist.	Enriched in fracture	Same as Y	Enriched in fracture	-	-	Enriched in fracture	No correlation	Enriched in fracture	-	Enriched in fracture	-
10b	(I), (III)	Depleted around low angle boundary	Same as Y	Decreased in low angle boundary	Aged in deformed domain	-	Enriched in low angle boundary	Depleted around low angle boundary	Enriched in un-deformed part	-	Enriched in deformed part	-
16a	(II)	Depleted close to deformed zone and slightly enriched at deformation front	Same as Y	Enriched in deformed zone	Rejuvenated in deformed domain	-	Enriched in deformed zone	Slightly depleted in deformed domain	Enriched in deformed zone	-	Enriched in deformed zone	-
15	(II)	Depleted in deformed zone	Same as Y	Enriched in deformed zone	Aged in deformed domain	-	No correlation	No correlation	Depleted in deformed zone	-	No correlation	-
25	(II)	Decreases in damaged lattice	Oscillating without correlation	Decreased in damaged lattice domains	Rejuvenated in bended lattice domain	-	Oscillating with no correlation	Slightly oscillating	Depleted in damaged domains	-	Mostly enriched in damaged domains	-
26, line 1	(I)	No direct correlation	Same as Y	Increased in damaged zone	Aged in most damaged zones and rejuvenated in less damaged domains	-	Depleted in deformed zone	No direct correlation	No correlation	-	Enriched in deformed zone	-
26, line 2	(II)	Decreased in deformed zone, increased in	Decreased in deformed zone,	Oscillation, generally increased in	Rejuvenated in bended lattice	-	Enriched in deformed zone	Enriched in deformed zone and	No correlation	-	Enriched in deformed zone	-

		transition point	increased in transition point	damaged zone	domain, aged at the boundary			depleted in transition point				
30, line 2	(II)	-	Increased in transition point	Decreased in deformed zone	Oscillation of aged and rejuvenated domains	-	Enriched in deformed zone	Enriched in deformed zone	No correlation	-	Enriched in deformed zone	-

Table 4.1. Behavior of trace elements in plastically-deformed zones. Types of lattice distortion were determined after Piazzolo et al. (2012) and Kovaleva et al. (2014).

P could be enriched, depleted or shows no correlation with deformed zones. Nb shows one case of enrichment in low angle boundary and in one case it is depleted in damaged zones. So far there is no possibility to make any statistically-supported conclusion on Hf, P and Nb behavior. Ce and Nd are usually enriched in low angle boundaries and bent zones.

Thus elemental depletion due crystal-plastic deformation is expected from HREE as Y, Yb; as well as from Pb and U. Enrichment is expected for LREE elements as Nd and Ce. Ti, P and Hf can behave either way or may even remain unaffected by crystal-plastic deformation. Difference in trace elements behavior is probably conditioned by their chemical potentials and atomic radii. For example, radii of Ce and Nd are much larger than the radii of the other elements discussed here, so they are harder to be removed from crystal defects and are enriched in deformed domains. Ti is a common rock- and mineral-forming element and can occur in large amounts in the matrix. Thus it can be enriched in deformed zones and low angle boundaries with respect to the pristine lattice, by moving from the matrix along fast diffusion pathways towards undeformed parts of zircon grains.

Enhanced diffusion of trace elements that resulted in strong geochemical modification of zircon is possible in crystal-plastically deformed domains. Deformation microstructures such as low-angle boundaries and dislocations act as pathways for fast migration of trace elements. Dislocation-connected so-called “pipe diffusion” (Ruoff, 1967) is estimated to be approximately five orders of magnitude greater than volume diffusion at the same conditions (Timms et al., 2006, 2011).

4.5.4. Relative $^{207}\text{Pb}/^{206}\text{Pb}$ age

The ages are represented as an absolute age difference between each data-point and a reference point that is selected in a least deformed analyzed portion of a corresponding zircon crystal. All points are color-coded accordingly and superimposed on top of FSE images.

In zircon 09 (Fig. 4.6a-d) point 6 was taken as a reference for $^{207}\text{Pb}/^{206}\text{Pb}$ relative age, because it belongs to the less deformed lattice domain (Fig. 4.6c). Other points are significantly distorted in $^{207}\text{Pb}/^{206}\text{Pb}$ age, points with large box-and-whisker plots are comparatively aged (4-5); points with smaller range are comparatively rejuvenated, where the smallest rejuvenation is attributed to the smallest box-and-whisker plot. Aging of points 4 and 5 could also be conditioned by a fracture that they may overlap.

In zircon 10a (Fig. 4.6e-g) point 1 is slightly aged relative to point 4, possibly because of the closeness to the dark magmatic core (Fig. 4.6f). Point 2 is rejuvenated possibly due to slight lattice distortion; and point 3 is heavily aged due to contamination of common lead from a fracture.

Zircon 10b shows comparatively younger $^{207}\text{Pb}/^{206}\text{Pb}$ ages in undeformed part and older ages in deformed part (Fig. 4.7a). It may evidence about gain of common lead from the external source (Timms et al., 2006) and increasing of $^{207}\text{Pb}/^{206}\text{Pb}$ ratio; but more likely happens due to post-deformation growth of the upper undeformed tip.

Zircon 16a (Fig. 4.7e-g) shows significant rejuvenation of deformed rim and heavily aged point 6 due to common lead from fracture.

In zircon 15 (Fig. 4.8a-c) deformed rim is heavily aged with respect to less deformed part (points 1 and 5) due to enrichment with common lead in fractures and high-angle boundaries (points 2-4) that is a result of pipe diffusion from external source.

In zircon 25 (Fig. 4.8d-g) rejuvenated lattice corresponds to deformed rim; the strongest rejuvenation corresponds to the strongest lattice distortion: points 1, 5-6, 8 and 10 show highest median and mean values for dislocation density and they are also the most rejuvenated ones.

In zircon 26 along the profile line 1 $^{207}\text{Pb}/^{206}\text{Pb}$ relative ages are heavily aged in the domains where the highest median and mean values for dislocation density are observed (points 1-2 and 4); the other distorted domains are rejuvenated. The data shows the opposite picture to the profile taken in grain 25 (Fig. 4.8c), but analyses in grain 26 were taken much closer to the grain's rim than in grain 25. Along the profile line 2 we observe strong aging of deformed rim close to grain boundary and rejuvenation in less deformed part. This effect can be explained by income diffusion of common lead with high $^{207}\text{Pb}/^{206}\text{Pb}$ ratio from the matrix to heavily deformed lattice via high angle boundaries, and, at the same time, outcome diffusion of radiogenic lead in the opposite direction from bended lattice.

Zircon 30 shows rejuvenated and aging of $^{207}\text{Pb}/^{206}\text{Pb}$ relative ages that are alternating (Fig. 4.9e). It can reflect out-diffusion of radiogenic lead from deformation front to the adjacent lattice domains and income diffusion of common lead at the rim.

$^{207}\text{Pb}/^{206}\text{Pb}$ relative ages were derived from the NanoSIMS maps of the grain 05. Color-coded points are superimposed on top of ^{89}Y isotope map (Fig. 4.10d). $^{207}\text{Pb}/^{206}\text{Pb}$ ages derived for grain 05 are aged in intensively-deformed zone with multiple subgrain boundaries; rejuvenated points are framing this zone. Aging occurs due to gain of common lead via (sub)grain boundaries, fractures and pores in deformed zone. Rejuvenation is likely in less reworked zones due to radiogenic lead loss.

Thus, $^{207}\text{Pb}/^{206}\text{Pb}$ relative ages demonstrate both – rejuvenation and aging of distorted zircon lattice, sometimes even within a single misorientation profile. Point analyses that overlap with fractures, low angle boundaries or pores and/or were set closer than 1 μm to grain boundaries give

heavily aged results (grains 10a, 16a, 15, 26, 30, 15a; Figs. 4.6e, 4.7e, 4.8a, 4.9a, 4.9e, 4.10d accordingly), mostly due to contamination with common lead. On the other hand, decrease in $^{207}\text{Pb}/^{206}\text{Pb}$ ratio and, therefore, decrease in $^{207}\text{Pb}/^{206}\text{Pb}$ relative age is caused by partial loss of radiogenic lead and isotopic system disturbance. Points that were made at a distance from grain boundaries and fractures in deformed lattice generally demonstrate rejuvenation (grains 09, 16a, 25, 26, 30, 15a; Figs. 4.6a, 4.7e, 4.8d, 4.9a, 4.9e, 4.10d). In a few cases $^{207}\text{Pb}/^{206}\text{Pb}$ relative age shows oscillation: zones of aging and rejuvenation are alternating across the misorientation profile (grains 26 line 1 and 2, 30, 15a; Figs. 4.9a, 4.9e, 4.10c). We suggest that radiogenic lead is diffusing from the front of lattice distortion in both directions: into already deformed rim and towards undeformed lattice domain, thus causing aging in adjacent lattice. Thus radiogenic lead along the deformation profiles of type (I) and (II) may behave similar to Y and Yb (Fig. 4.10a).

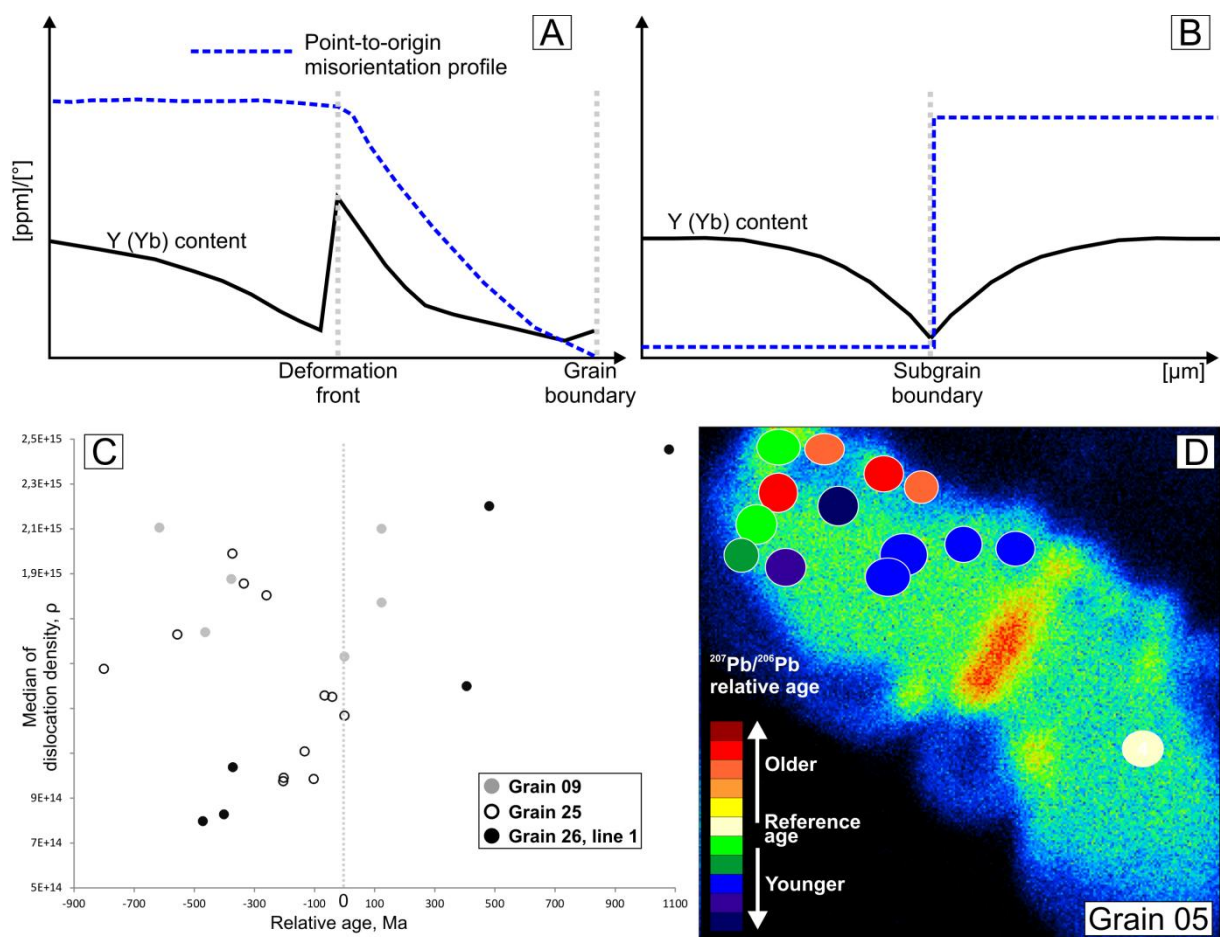


Figure 4.10. (a)-(b) Schematic diagrams picturing re-distribution of Y and Yb in zircon with respect to lattice distortion: (a) deformation pattern type (I); (b) deformation pattern type (III). (c) Differences with reference $^{207}\text{Pb}/^{206}\text{Pb}$ relative age plotted against median (quartile 2) of dislocation density in each data-point. (d) $^{207}\text{Pb}/^{206}\text{Pb}$ relative ages derived from the NanoSIMS maps of grain 05. Color-coded points are superimposed on top of ^{89}Y isotope map.

Lattice domains that are free of fractures, high-angle boundaries and pores should be selected in order to see rejuvenation of zircon isotopic system due to crystal-plastic deformation. Only intensively banded domains performing lattice distortion type (I) consistently demonstrate rejuvenation of zircon $^{207}\text{Pb}/^{206}\text{Pb}$ ages. Analyses also should be done at a distance of a few microns from a grain boundary.

There seem to be a correlation between dislocation density and relative $^{207}\text{Pb}/^{206}\text{Pb}$ ages. Age difference with a reference age plotted against the median of dislocation density show a positive correlation in case of aging, and negative correlation in case of rejuvenation (Fig. 4.10c). In other words, the more dislocations are introduced to the crystal lattice, the more disturbed are isotopic ages. At the distance from a grain boundary, remote from the source of common lead, we mostly observe rejuvenation of zircon lattice, which is increasing together with dislocation density. Close to grain boundary, increasing of dislocation density means aging of the crystal lattice.

The correlation between dislocation density and isotopic composition could be, however, not so straight forward. Dislocation density was calculated using 1D misorientation profiles, extracted from 2D EBSD maps; whereas microprobes analyzed certain 3D volume of crystal lattice. Thus, dislocation densities that are calculated in our study are only rough estimation of those dislocation densities that are present in crystal lattice in reality; and we don't provide estimation of dislocation densities in 3D volume, which could be different.

Relative $^{207}\text{Pb}/^{206}\text{Pb}$ ages are fairly inhomogeneous along high-resolution NanoSIMS profiles. This could be connected with micro- and nano-defects in crystal lattice and with inhomogeneous distribution of dislocations in such small volumes of lattice. Additionally, inhomogeneous distribution of lead isotopes at a very high resolution was shown by atom-probe tomography (Valley et al., 2014). This distribution however is not important at a lower resolution. In order to estimate the age of deformation event we suggest applying classical methods of isotopic dating that are not characterized by such a high spatial resolution. Before applying any mineral isotopic dating technique to deformed samples, they should be very carefully selected.

4.5.5. Comparing with existing data

Reddy et al. (2006), Timms et al. (2006, 2011) and Timms and Reddy (2009) demonstrate low-angle boundaries that mostly correspond to decreased CL-intensity zones. A dark CL signal attributed to low angle boundaries is interpreted to occur due to high defects density and enrichment of total

REE in distorted domains (Reddy et al., 2006). In other cases the dark CL-signal corresponds to low-angle boundaries due to high Pb, U and Th, derived from external source (Timms et al., 2006). Panchromatic and hyperspectral CL mapping revealed panchromatic reduction of CL-response and spectral shifts corresponding to deformation-related subgrain boundaries; reduced CL-signal is attributed to high defect density in crystal lattice and shifted spectrum – to re-distribution of REE elements in distorted domains, where REE are enriched along low angle boundaries, especially Tb, Er and LREE (Timms and Reddy, 2009). It has also been documented that the darker domains correspond to higher angle boundaries (Timms and Reddy, 2009).

In contrast with the previous studies, in our samples increased CL intensity corresponds to low angle boundaries and connected with trace elements content variations, specifically with Y, Yb and U depletion and increased Yb/Y and U/Y values. Our observations are consistent with regularities derived by Kaczmarek et al. (2008), where variations in CL intensity within zircon grains are interpreted to correspond with significant chemistry variation, for instance, U content. Hofmann et al. (2014) have shown that Y-poor domains correlate with bright CL bands and vice versa. Thus, in our samples the CL signal derived from low angle boundaries is not conditioned by high defect density but mainly by the described chemical variations.

Piazolo et al. (2012) have documented the largest chemical variations and the most severe isotopic system distortion and CL distortion that is attributed to lattice finite deformation type (III). It was considered to be due to the highest dislocation density and highest amount of low angle boundaries. Moser et al. (2011) consider crystal-plastic strain during heating and recovery with migration of defects into subgrain boundaries to be the major mechanisms for causing partial or complete resetting of U-Pb isotopic system in zircon. The lowest CL and isotopic system disturbance performed by distortion patterns type (I), where no migration of dislocations occurs and no low angle boundaries that could act as fast diffusion pathways are formed. According to our samples, the most prominent CL signal distortion corresponds to deformation type (III), but the distortion in chemical composition is comparable for all three types of lattice distortion. When lattice distortion type (III) is observed, it can only influence the closest surroundings of the lattice, whereas lattice distortion type (II) and, in particular type (I) affects larger volumes of the lattice and should cause trace element re-distribution at the larger scales.

Pb loss, localized resetting of the U-Pb system and rejuvenation connected with crystal-plastic deformation has been documented by number of authors, for example, Nemchin et al. (2009), Moser et al. (2009; 2011), Timms et al. (2011, 2012), Piazolo et al. (2012), Grange et al. (2013), MacDonald et al. (2013). Pb loss in deformed zircons was considered to be a result of lattice distortion, as well as high Th/U ratios, leading to younger isotopic ages (Timms et al., 2011; MacDonald et al., 2013).

Observed resetting of U-Pb system can potentially yield the timing of deformation (Nemchin et al., 2009; Moser et al., 2009). Moser et al. (2011) documented the domain of maximum misorientation spatially coincides with the area of maximum Pb-loss. Our observations on Pb behavior are consistent with the previous data and show rejuvenation of relative $^{207}\text{Pb}/^{206}\text{Pb}$ ages for zircon domains that are bent but free of pores, fractures and (sub)grain boundaries. In domains, where besides of crystal-plastic deformation fracturing is observed, Pb is enriched and relative $^{207}\text{Pb}/^{206}\text{Pb}$ ages are older.

Enrichment of U in distorted domains was documented by Timms et al. (2011). Our data show the opposite and U is depleted in highly-deformed domains, even though it's atomic radius is quite large and closer to that of Ce and Nd.

Some heterogeneity in Ti content that is restricted to distorted domains has been reported by MacDonald et al. (2013), and Ti depleted in low-angle boundaries has been found by Timms et al. (2011). Our data offers various possibilities of Ti behavior and generally does not contradict to the previously published data.

There is no information published on behavior of Hf, P or Nb that we are aware of. What concerns REE, Timms and Reddy (2009) and Timms et al. (2011) observed these elements to be enriched along low angle boundaries, especially Tb, Er and LREE (Timms and Reddy, 2009). MacDonald et al. (2013) reported about the REE profiles that are generally lying in the range of undistorted grains. Our data supports the observations of Timms and Reddy (2009), and LREE such as Ce and Nd are consistently enriched in distorted zones.

4.6. Conclusions

By two high-resolution techniques – FEG-EMPA and NanoSIMS – trace elements re-distribution related to crystal-plastic deformation has been documented in zircon:

1. Large (> 40 μm) and small (< 40 μm) zircon grains show similar behavior, even though they have to be analyzed with different techniques to document it.
2. Deformation-connected re-distribution of trace elements is equally observed for three types of lattice distortion pattern (I), (II) and (III).
3. Bright CL signal that spatially corresponds to low angle boundaries might be a result of variations in trace element composition along these zones.
4. The largest trace elements re-distribution is attributed to higher angle subgrain boundaries and to the domains with higher dislocation density. Dislocation density oscillation points to

the existence of damaged “bands” in the lattice, 1-2 μm thick, which serve as pathways to remove trace elements.

5. Low angle boundaries and intensively bended zones demonstrate depletion in the following trace elements: Y, Yb, U, Pb.
6. Y and Yb show complicated oscillation across the deformation profiles type (I) and (II), that is explained by changing in chemical potential by introducing of dislocations into the lattice.
7. Low angle boundaries and intensively bended zones demonstrate enrichment in the following rare earth trace elements: Ce, Nd.
8. Ti, P and Hf can be either enriched, depleted or show no correlation with plastically-deformed zones. Their behavior possibly reflects access of these elements in the surrounding matrix.
9. Difference in behavior of trace elements is conditioned by different chemical potentials and atomic radii, as well as by their content in the surrounding matrix.
10. Enhanced diffusion of trace elements in zircon is facilitated by dislocations and low angle boundaries that act as fast diffusion pathways and change chemical potential of the crystal lattice, thus removing or adding trace element cations to the distorted domains.
11. $^{207}\text{Pb}/^{206}\text{Pb}$ relative isotopic ages are distorted in intensively bent lattice domains; distortion in isotopic age has a positive correlation with dislocation density. Deformed lattice domains are aged if they are close to grain boundary and contain fractures, pores and (sub)grain boundaries. Deformed lattice domains are rejuvenated if they are at a distance from grain boundary.

Acknowledgments

This study was funded by the University of Vienna (doctoral school “DOGMA”, project IK 052) and the Austrian Science Foundation Fund (FWF): I471-N19, which is part of the DFG-FWF funded international research group FOR741-DACH.

The authors are grateful to Rainer Abart, Christian Auer, Claudia Beybel, Franz Biedermann, John Eiler, Bernhard Grasemann, Sigrid Hrabe, Matthew Huber, Hugh Rice, Arno Schintlmeister and all colleagues of the FOR741 research group for fruitful discussions and the Geologische Bundesanstalt (GBA) of Austria for access to the SEM; Helmholtz Centre Potsdam in Germany for access to FEG-EMPA; SIMS lab in Caltech, Pasadena, USA, for access to the NanoSIMS.

References

- Ashwal, L.D., Tucker, R.D., Zinner, E.K., 1999. Slow cooling of deep crustal granulites and Pb-loss in zircon. *Geochimica et Cosmochimica Acta*, 63, 2839–2851.
- Bachmann, F., Hielscher, R., Schaeben, H., 2010. Texture Analysis with MTEX – Free and Open Source Software Toolbox. *Solid State Phenomena*, 160, 63-68.
- Bachmann, F., Hielscher, R., Schaeben, H., 2011. Grain detection from 2d and 3d EBSD data-specification of the MTEX algorithm. *Ultramicroscopy*, 111, 1720-1733.
- Barboza, S.A., Bergantz, G.W., Brown, M., 1999. Regional granulite facies metamorphism in the Ivrea zone: is the Mafic Complex the smoking gun or a red herring? *Geology*, 27, 447–450.
- Bea, F., Montero, P., 2013. Diffusion-induced disturbances of the U-Pb isotope system in pre-magmatic zircon and their influence on SIMS dating. A numerical study. *Chemical Geology*. 349-350, 1-17. DOI: 10.1016/j.chemgeo.2013.04.014
- Boehnke, P., Watson, E. B., Trail, D., Harrison, T. M., Schmitt, A. K., 2013. Zircon saturation revisited. *Chemical Geology*, 351, 324–334. DOI: 10.1016/j.chemgeo.2013.05.028
- Brodie, K.H., Rutter, E.H., Evans, P., 1992. On the structure of the Ivrea-Verbano Zone (northern Italy) and its implications for present-day lower continental crust geometry. *Terra Nova*, 4, 34-39.
- Cherniak, D. J. and Watson E. B., 2003. Diffusion in Zircon. In: Hancher, J. M., Hoskin, P. W. O., eds. *Zircon*. Mineralogical Society of America and Geochemical Society, *Reviews in Mineralogy and Geochemistry*, 53, 113-143.
- Cherniak, D. J. and Watson, E. B., 2007. Ti diffusion in zircon. *Chemical Geology*, 242, 470–483.
- Cherniak, D.J., Lanford, W.A., Ryerson, F.J., 1991. Lead diffusion in apatite and zircon using ion implantation and Rutherford Backscattering techniques. *Geochimica et Cosmochimica Acta*, 55, 1663-1673.

- Compston, W., Kinny, P.D., Williams I.S., Foster J.J., 1986. The age and Pb loss behaviour of zircons from the Isua supracrustal belt as determined by ion microprobe. *Earth and Planetary Science Letters*, 80, 71-81.
- Corfu, F., Hanchar, J. M., Hoskin, P. W. O., Kinny, P., 2003. Atlas of zircon textures. In: Hanchar, J. M., Hoskin, P. W. O., eds. *Zircon*. Mineralogical Society of America and Geochemical Society, *Reviews in Mineralogy and Geochemistry*, 53, 469-500.
- Cottrell, A.H. and Bilby, B.A., 1949. Dislocation theory of yielding and strain ageing of iron. *Proceedings of the Physical Society London, Section A*, 62, 49–62.
- Davis, D.W., Williams, I.S., Krogh, T.E.: Historical development of zircon geochronology, 2003. In: *Zircon*, Hanchar, J. M., Hoskin, P. W. O., eds., Mineralogical Society of America and Geochemical Society, *Reviews in Mineralogy and Geochemistry*, Washington D.C., 53, 145-181.
- Erdmann, S., Wodicka, N., Jackson, S.E., Corrigan, D., 2013. Zircon textures and composition: refractory recorders of magmatic volatile evolution? *Contrib. Mineral. Petr.*, 165, 45–71.
- Flowers, R.M., Schmitt, A.K., Grove, M., 2010. Decoupling of U–Pb dates from chemical and crystallographic domains in granulite facies zircon. *Chemical Geology*, 270, 20–30.
- Geisler, T., Ulonska, M., Schleicher, H., Pidgeon, R. T., Van Bronswijk, W., 2001. Leaching and differential recrystallization of metamict zircon under experimental hydrothermal conditions. *Contributions to Mineralogy and Petrology*, 141, 53–65.
- Geisler, T., Pidgeon, R. T., Bronswijk, W., Kurtz, R., 2002. Transport of uranium, thorium, and lead in metamict zircon under low-temperature hydrothermal conditions. *Chemical Geology*, 191, 141–154.
- Geisler, T., Pidgeon, R. T., Kurtz, R., Bronswijk, W., Schleicher H., 2003. Experimental hydrothermal alteration of partially metamict zircon. *American Mineralogist*, V. 88, No. 10, 1496-1513
- Geisler, T., Schaltegger, U., Tomaschek, F., 2007. Re-equilibration of zircon in aqueous fluids and melts. *Elements*, V. 3, No. 1, 43-50.
- Grange, M.L., Pidgeon, R.T., Nemchin, A.A., Timms, N.E., Meyer, C., 2013. Interpreting U–Pb data from primary and secondary features in lunar zircon. *Geochimica et Cosmochimica Acta*, 101, 112–132.

- Hofmann, A. E., Valley, J. W., Watson, E. B., Cavosie, A. J., Eiler, J. M., 2009. Sub-micron scale distributions of trace elements in zircon. *Contributions to Mineralogy and Petrology*, 158, 317–335.
- Hofmann, A. E., Backer, B.M., Eiler, J. M., 2014. Sub-micron-scale trace-element distributions in natural zircons of known provenance: implications for Ti-in-zircon thermometry. *Contributions to Mineralogy and Petrology*, 168, 1057. DOI: 10.1007/s00410-014-1057-8.
- Kaczmarek, M.-A., Müntener, O., Rubatto, D., 2008. Trace element chemistry and U–Pb dating of zircons from oceanic gabbros and their relationship with whole rock composition (Lanzo, Italian Alps). *Contributions to Mineralogy and Petrology*, 155, 295–312.
- Kaczmarek, M. A., Reddy, S. M., Timms, N. E. 2011. Evolution of zircon deformation mechanisms in a shear zone (Lanzo massif, Western-Alps). *Lithos*, 127, 414-426.
- Klemetti, E. W., Deering, C. D., Cooper, K. M., Roeske, S. M., 2011. Magmatic perturbations in the Okataina Volcanic Complex, New Zealand at thousand-year timescales recorded in single zircon crystals. *Earth and Planetary Science Letters*, 305, 185–194.
- Klötzli, U.S., Sinigoi, S., Quick, J.E., Demarchi, G., Tassinari, C.C.G., Sato, K., Günes, Z., 2014. Duration of igneous activity in the Sesia Magmatic System and implications for high-temperature metamorphism in the Ivrea–Verbano deep crust, *Lithos*, 206–207, 19–33.
- Kovaleva, E., Klötzli, U., Habler, G., Libowitzky, E., 2014. Finite lattice distortion patterns in plastically deformed zircon grains. *Solid Earth*, 5, 1099-1122.
- Kovaleva, E., Klötzli, U., Habler, G., Wheeler, J., in press. Planar microstructures in zircon from paleo-seismic zones. *American Mineralogist*.
- MacDonald, J. M., Wheeler, J., Harley, S. L., Mariani, E., Goodenough, K. M., Crowley, Q., Tatham, D., 2013. Lattice distortion in a zircon population and its effects on trace element mobility and U–Th–Pb isotope systematics: examples from the Lewisian Gneiss Complex, northwest Scotland. *Contributions to Mineralogy and Petrology*, 166, 21–41.
- Mainprice, D., Hielscher, R., Schaeben, H., 2011. Calculating anisotropic physical properties from texture data using the MTEX open source package. In: Prior, D.J., Rutter, E.H., Tatham, D. J. (eds) *Deformation Mechanisms, Rheology and Tectonics: Microstructures, Mechanics and Anisotropy*. Geological Society, London, Special Publications, 360, 175-192.

- Miller, C., Konzett, J., Tiepolo, M., Armstrong, R.A., Thöni, M., 2007. Jadeite-gneiss from the eclogite zone, Tauern Window, Eastern Alps, Austria: metamorphic, geochemical and zircon record of a sedimentary protholith. *Lithos*, 93, 68-88.
- Moser, D.E., Davis, W.J., Reddy, S.M., Flemming, R.L., Hart, R.J., 2009. Zircon U–Pb strain chronometry reveals deep impact-triggered flow. *Earth and Planetary Science Letters* 277, 73–79.
- Moser, D. E., Cupelli, C.L., Barker, I.R., Flowers, R.M., Bowman, J.R., Wooden, J., Hart, J.R., 2011. New zircon shock phenomena and their use for dating and reconstruction of large impact structures revealed by electron nanobeam (EBSD, CL, EDS) and isotopic U–Pb and (U–Th)/He analysis of the Vredefort dome. *Canadian Journal of Earth Sciences*, 48, 117–139.
- Nasdala, L., Hanchar, J. M., Rhede, D., Kennedy, A. K., Vaczi, T., 2010. Retention of uranium in complexly altered zircon: an example from Bancroft, Ontario. *Chemical Geology*, 269, 290-300.
- Nemchin, A., Timms, N. E., Pidgeon, R., Geisler, T., Reddy, S. M., Meyer, C., 2009. Timing of crystallization of the lunar magma ocean constrained by the oldest zircon, *Nat. Geosci.*, 2, 133-136.
- Pennacchioni, G. and Mancktelow, N.S., 2007. Nucleation and initial growth of a shear zone network within compositionally and structurally heterogeneous granitoids under amphibolite facies conditions. *Journal of Structural Geology*, 29, 1757-1780.
- Piazolo, S., Austrheim, H., Whitehouse, M., 2012. Brittle-ductile microfabrics in naturally deformed zircon: Deformation mechanisms and consequences for U-Pb dating. *American Mineralogist*, 97, 1544–1563.
- Polerecky, L., Adam, B., Milucka, J., Musat, N., Vagner, T., Kuypers M.M.M., 2012. Look@NanoSIMS – a tool for the analysis of nanoSIMS data in environmental microbiology. *Environmental microbiology*, 14, 1009-1023. DOI:10.1111/j.1462-2920.2011.02681.x
- Quick, J.E., Sinigoi, S., Peressini, G., Demarchi, G., Wooden, J.L., Sbisà, A., 2009. Magmatic plumbing of a large Permian caldera exposed to a depth of 25 km. *Geology*, 37, 603-606.
- Reddy, S. M., Timms, N. E., 2010. Deformation of zircon and implications for geochemistry and geochronology. *Source Abstracts with Programs - Geological Society of America* 42, 634.

- Reddy, S.M., Timms, N.E., Trimby, P., Kinny, P.D., Buchan C., Blake K., 2006. Crystal-plastic deformation of zircon: a defect in the assumption of chemical robustness. *Geology*, 34, 257-260.
- Reddy, S.M., Timms, N.E., Pantleon, W., Trimby, P., 2007. Quantitative characterization of plastic deformation of zircon and geological implications. *Contributions to Mineralogy and Petrology* 153, 625–645.
- Reddy, S.M., Timms, N.E., Hamilton, P.J., Smyth, H.R., 2009. Deformation-related microstructures in magmatic zircon and implications for diffusion. *Contributions to Mineralogy and Petrology*, 157, 231–244.
- Redler, C., Johnson, T. E., White R. W., Kunz, B. E., 2012. Phase equilibrium constraints on a deep crustal metamorphic field gradient: metapelitic rocks from the Ivrea Zone (NW Italy). *Journal of Metamorphic Geology*, 30, 235–254.
- Rimsa, A., Whitehouse, M.J., Johansson, L., Piazzolo, S., 2007. Brittle fracturing and fracture healing of zircon: An integrated cathodoluminescence, EBSD, U-Th-Pb, and REE study. *American Mineralogist*, 92, 1213-1224.
- Ruoff, A.L., 1967. Enhanced diffusion during plastic deformation by mechanical diffusion. *Journal of Applied Physics*, 38, 3999-4003.
- Rutter E.H., Brodie K.H., James T., Burlini L., 2007. Large-scale folding in the upper part of the Ivrea-Verbano zone, NW Italy. *Journal of Structural Geology* 29, 1-17.
- Saunders, K., Buse, B., Kilburn, M.R., Kearns, S., Blundy, J., 2014. Nanoscale characterisation of crystal zoning. *Chemical Geology*, 364, 20–32.
- Schmid, S.M., Scharf, A., Handy, M.R., Rosenberg, C.L., 2013. The Tauern Window (Eastern Alps, Austria): a new tectonic map, with cross-sections and a tectonometamorphic synthesis. *Swiss Journal of Geosciences*, 106, 1-32.
- Silverstone, J., 1985. Petrologic constraints on imbrication, metamorphism, and uplift in the SW Tauern Window, Eastern Alps. *Tectonics*, 4, 687-704.

- Selverstone J., Morteani G., Staude J.-M., 1991. Fluid channelling during ductile shearing: transformation of granodiorite into aluminous schist in the Tauern Window, Eastern Alps. *Journal of Metamorphic Geology*, 9, 419–431.
- Sinigoi S., Quick, J.E., Demarchi, G., Klötzli, U., 2011. The role of crustal fertility in the generation of large silicic magmatic systems triggered by intrusion of mantle magma in the deep crust. *Contributions to Mineralogy and Petrology*, 162, 691-707.
- Storm, S., Schmitt, A.K., Shane, Ph., Lindsay, J.M., 2014. Zircon trace element chemistry at sub-micrometer resolution for Tarawera volcano, New Zealand, and implications for rhyolite magma evolution. *Contributions to Mineralogy and Petrology*, 167, 1000. DOI 10.1007/s00410-014-1000-z
- Timms, N.E. and Reddy, S.M., 2009. Response of cathodoluminescence to crystal-plastic deformation in zircon. *Chemical Geology* 261, 11–23.
- Timms, N.E., Kinny, P., Reddy, S.M., 2006. Enhanced diffusion of uranium and thorium linked to crystal plasticity in zircon. *Geochemical Transactions* 7, 10.
- Timms, N.E., Kinny, P., Reddy, S.M., Evans K., Clark C., Healy D., 2011. Relationship among titanium, rare earth elements, U–Pb ages and deformation microstructures in zircon: Implications for Ti-in-zircon thermometry. *Chemical Geology* 280, 33–46.
- Timms, N. E., Reddy, S. M., Gerald, F. J. D., Green, L., Muhling, J. R., 2012. Inclusion-localised crystal-plasticity, dynamic porosity, and fast-diffusion pathway generation in zircon, *Journal of Structural Geology*, 35, 78-89.
- Valley, J.W., Cavosie, A.J., Ushikubo, T., Reinhard, D.A., Lawrence, D.F., Larson, D.J., Clifton, P.H., Kelly, T.F., Wilde, S.A., Moser, D.E., Spicuzza, M.J., 2014. Hadean age for a post-magma-ocean zircon confirmed by atom-probe tomography. *Nature Geoscience*, 7, 219-223.
- Veselá, P., Söllner, F., Finger, F., Gerdes, A., 2011. Magmato-sedimentary Carboniferous to Jurassic evolution of the western Tauern window, Eastern Alps (constraints from U-Pb zircon dating and geochemistry). *International Journal of Earth Sciences*. 100, 993–1027.
- Watson, E. B., Wark, D. A., Thomas, J. B., 2006. Crystallization thermometers for zircon and rutile. *Contributions to Mineralogy and Petrology*, 151, 413–433.

5.0. Planar microstructures in zircon from paleo-seismic zones

Elizaveta Kovaleva^{1,*}, Urs Klötzli¹, Gerlinde Habler¹ and John Wheeler²

¹ Department of Lithospheric Research, Faculty of Geosciences, Geography and Astronomy, University of Vienna, Althanstrasse 14, A-1090 Vienna, Austria

² Department of Earth, Ocean and Ecological Sciences, School of Environmental Sciences, University of Liverpool, L69 3GP, Liverpool, United Kingdom

* Corresponding author. E-mail: elizaveta.kovaleva@univie.ac.at

Article is in press in *American Mineralogist*

Abstract

Pseudotachylytes resulted from frictional melts associated with ultramylonites in high-grade metapelitic rocks from the Ivrea-Verbano zone in the Southern Alps (Northern Italy) were studied with focus on the deformation microstructures in zircon. The aims were to investigate the characteristics of zircon deformation in seismic zones, and to recognize specific microstructures generated in zircon during earthquakes, which could be useful for mineral dating of paleo-seismic events; helps to understand how seismic energy is released at depth and interacts with metamorphic processes.

The interior of polished zircon grains ranging from 30 to 150 μm in length were investigated with optical microscope and scanning electron microscope (SEM) techniques, including secondary electron (SE), backscattered electron (BSE), forward scattered electron (FSE), cathodoluminescence (CL) imaging, and crystallographic orientation mapping by electron backscatter diffraction analysis (EBSD). Grains were studied in situ and as separated fractions embedded in epoxy discs. Among

different cataclastic and crystal-plastic deformation microstructures in zircon we identified characteristic planar deformation bands (PDBs), planar fractures (PFs) and curvilinear fractures (CFs).

Planar deformation bands in zircon are crystallographically controlled planar lattice volumes with misorientation from the host grain, which varies from 0.4° to 2.7°. PDBs are usually parallel to {100} crystallographic planes, have width from 0.3 to 1 µm and average spacing of 5 µm in 2D sections. Planar deformation bands appear as contrast lamellae in orientation contrast images and in EBSD maps, and in rare cases can be observed with the optical microscope. PDBs form in specifically oriented grains due to high differential stresses, high temperatures and high strain rates generated in seismically active environment and/or due to shearing in the vicinity of frictional melts. Discovered structures represent a result of crystal-plastic deformation of zircon grains with operating dislocations having $\langle 100 \rangle \{010\}$ glide system and $\langle 001 \rangle$ misorientation axis, therefore, they can be classified as a new type (IV) lattice distortion pattern, according to the existing classification for zircon (Piazolo et al. 2012; Kovaleva et al. 2014).

We have demonstrated that formation of planar fractures in zircon takes place not only during impacts, but also in seismically active zones. We observe at least two cases of formation of PFs with {100} orientation: a) as a result of evolution of PDBs in association with PFs; b) as micro-cleavage.

This study demonstrates that planar microstructures in terrestrial zircon do not exclusively form during impact events, but also as a result of seismic events at depth due to unusually high differential stress, strain rate and temperature. According to the new findings, PDBs in zircon from the deep-crust are supposed to represent newly recognized evidence of seismicity.

Keywords: Electron Backscatter Diffraction (EBSD), zircon, shear zone, pseudotachylytes, planar deformation bands, planar fractures, crystal-plastic deformation

5.1. Introduction

5.1.1. Pseudotachylytes in mylonites

Pseudotachylytes are quenched frictional melts formed along fault planes due to coseismic sliding and are described in many silicate rocks. Pseudotachylytes can convey information about depth, energy and mechanics of paleo-earthquakes (e.g. Pittarello et al. 2008). They are not only found in cataclastic rocks, but can also be associated with mylonites, pointing to deeper crustal levels of formation (Passchier 1982; Austrheim et al. 1996; Lund and Austrheim 2003; Austrheim and Corfu 2009; Pittarello et al. 2012). Mylonites represent zones of enhanced ductility within the lithosphere (Ranalli 1995); to nucleate and evolve, they generally require some structural heterogeneity (Pennacchioni and Mancktelow 2007). The mutual overprinting of pseudotachylytes and ultramylonites in metagabbro and felsic metapelites of Ivrea-Verbano zone (IVZ) was described in detail in Pittarello et al. (2012) who show that pseudotachylytes acted as precursor heterogeneities for strain localization and that ultramylonite formation immediately followed the post-seismic stress relaxation. Cycles of brittle/frictional and ductile/viscous shear zone formation could have repeatedly alternated.

So far the most reliable evidence of paleo-earthquakes was formation of pseudotachylytes (e.g. Sibson 1975; Austrheim et al. 1996; Pittarello et al. 2012). Planar and non-planar fractures and other microstructures have been previously described in garnet (Austrheim et al. 1996) and zircon (Austrheim and Corfu 2009) and interpreted to be the evidences of seismic activity. More recently Angiboust et al. (2012), Austrheim (2013), Yang et al. (2014a, 2014b) have interpreted breccia and specific metamorphic structures in eclogites as seismically-induced. In our study we investigate zircons from ultramylonites associated with pseudotachylyte veins, and provide microstructural evidence of paleo-seismic activity recorded in zircons from the deep crustal section of the IVZ.

5.1.2. Planar microstructures in zircon

In the current context the term “planar microstructures” comprises all groups of different planar features described for zircon, including planar deformation features (PDFs), planar fractures (PFs), microcleavage, shock twins, phase transition along the certain planes and planar deformation bands (PDBs).

Planar deformation features (PDFs) in zircon, as defined by Erickson et al. (2013a), are shock-induced planar lamellae that crosscut the zircon crystal lattice along specific crystallographic planes and are filled with amorphous material or so-called “diaplectic glass”; or represent lattice domains with a high defect density (Leroux et al., 1999; Timms et al., 2012b; Grange et al. 2013). Planar lamellae filled with amorphous material have not been yet documented in natural terrestrial zircon samples (Erickson et al. 2013a) and the phenomena defined as PDFs in natural terrestrial zircon are usually planar fractures (e.g. Bohor et al. 1993; Corfu et al. 2003). But Timms et al. (2012b, fig. 8) and Grange et al. (2013, fig. 12) describe true PDFs in lunar zircon. These are identified by optical microscopy, in EBSD maps representing planes of low EBSD pattern quality, and in rare cases as dark lines in CL images. The crystallographically-controlled thin (<200 nm) layers of amorphous material or “diaplectic glass” were produced experimentally by Leroux et al. (1999). PDFs occupy {320} and {110} (Leroux et al., 1999) and also {112} and {001} (Timms et al. 2012b) crystallographic planes in zircon and result from 40 GPa shock pressure (Leroux et al. 1999), being considered to be indicative of shock pressure.

Planar fractures (PFs) or parallel and closely-spaced open structures resembling cleavage, are well-known from terrestrial and lunar impactites (e.g. Bohor et al. 1993; Kamo et al. 1996; Kalleson et al. 2009; Cavosie et al. 2010; Moser et al. 2011; Erickson et al. 2013a, 2013b; Thomson et al. 2014). These shock-produced fractures are particularly noticeable in minerals such as quartz, garnet, monazite and zircon, which do not normally reveal any cleavage in most terrestrial tectonic settings (Timms et al. 2012b). PFs in zircon are usually detected by scanning electron microscopy (SEM) on etched surfaces (e.g. Bohor et al. 1993; Kamo et al. 1996; Erickson et al. 2013a, 2013b; Thomson et

al. 2014), and are often visible in the transmitted or reflected light microscope (Corfu et al. 2003; Thomson et al. 2014). Representing open structures, PFs can be filled with other material, and become noticeable in CL-images tracing as bright or dark patterns decorated by voids and pores. PFs can offset growth zonation (e.g. Kalleson et al. 2009; Cavosie et al. 2010; Moser et al. 2011; Erickson et al. 2013a, 2013b; Thomson et al. 2014); some PFs cause crystal lattice rotations from 1 to 10° (Erickson et al. 2013a). PFs in natural zircon are most frequently parallel to the {100}, {001}, {112} and {011} planes (Cavosie et al. 2010; Erickson et al. 2013a; Leroux et al. 1999). In experimental samples they also occupy (201), (211), (221) and (111) planes (Leroux et al. 1999).

Apart from planar fractures, sets of roughly parallel non-planar or curvilinear fractures (CFs) are also considered to be associated with impact events (Cavosie et al. 2010; Moser et al. 2011; Timms et al. 2012b; Erickson et al. 2013a). They may be crystallographically-controlled and may act as channels for impact melt (Moser et al. 2011; Erickson et al. 2013a).

Shock twins or microtwins are considered to be a characteristic feature of shock-deformed zircon grains (Leroux et al. 1999; Moser et al. 2011; Timms et al. 2012b; Erickson et al. 2013a, 2013b; Thomson et al. 2014). They were documented with EBSD mapping and TEM imaging and occupy {110} crystallographic planes with twin individuals rotated at 65° to the host lattice.

Reidite, the high-pressure shock induced polymorph of zircon with scheelite structure was documented with TEM occurring along {100} planes. Shock twins and reidite formation indicate shock pressure above 40 GPa (Leroux et al. 1999).

Planar deformation bands (PDBs) in zircon were described as planar portions of crystal lattice parallel to {100} planes, with few to hundreds of micrometers thickness showing misorientation up to 10° with respect to the host grain (Nemchin et al. 2009, Fig. 1; Timms et al. 2012b, Fig. 5). PDBs form two orthogonal sets crosscutting the initial growth zoning. They can be revealed only by orientation- and EBSD mapping. The most common misorientation axes for PDBs are $\langle 001 \rangle$, and the geometry of dislocation glide system, therefore, is considered to be $\langle 100 \rangle \{010\}$. This is characteristic not only for

impact-related dislocations (Leroux et al. 1999; Timms et al. 2012b), but also a dominant glide system in tectonically-deformed zircon grains (e.g. Reddy et al. 2007; Kaczmarek et al. 2011; Piazzolo et al. 2012; Kovelava et al. 2014).

Otherwise oriented planar microstructures in zircon were produced during shock recovery experiments by Leroux et al. (1999). At shock pressure of 20 GPa planar fractures or micro-cleavage along {100} and sometimes {310} planes were formed. Multiple dislocations indicate that shock-related intense crystal-plastic deformation occurs. Sometimes shock-related dislocations are aligned in narrow “*micro-bands*”, occupying glide planes {100}, which possibly could act as precursor for planar fractures.

However, shock-induced structures are not the only planar structures known in zircon. Some parallel parting has been observed in zircons from upper crustal xenoliths (Rudnick and Williams, 1987; Chen et al., 1994) and interpreted to form due to rapid decompression (Rudnick and Williams, 1987). Kresten et al. (1975) report on perfect partings or cleavages extending in several directions in kimberlitic zircon. Although such structures never appear to be perfectly parallel, as shock-induced structures do.

5.1.3. Motivation and challenge

After all, the classical definition of planar microstructures in zircon (especially for PDFs and PFs) exclusively ascribes their formation to shock metamorphism during impact events (Corfu et al. 2003; Timms et al. 2012b). However, planar microstructures in zircon that are not directly related to shock metamorphism were reported by Austrheim and Corfu (2009) in pseudotachylytes from the Svarthumlevatnet metagabbro, South-Central Norway. At few zircon grains presented in their study reveal sets of planar microstructures, which are visible in CL-images and considered to represent PDFs. These planar microstructures were assumed to have formed at very high strain rates during the

formation of pseudotachylytes. Among other seismic-related deformation structures in zircon the authors also describe fragmentation of zircon and subparallel faults decorated by inclusions.

Our study also reveals planar microstructures in zircon which are formed during a deep crustal seismic event in association with pseudotachylytes. Under extraordinarily high differential stress, temperature and strain rate, zircon grains with favorable crystallographic orientation can develop crystallographically-controlled parallel lamellae, or planar deformation bands. These have not been previously described for terrestrial rocks, thus enhancing our knowledge on zircon rheology in an uncommon geological environment.

5.2. Geological and field settings

Samples were collected from the Ivrea-Verbano zone (IVZ) at Premosello in the Val d'Ossola (Northern Italy). Geological map of the area and sampling location is presented in Pittarello et al. (2012), Fig. 1. IVZ forms a NE-SW trending, steeply dipping sequence of meta-pelitic to -psammitic and meta-igneous basic rocks in the SE, ultrabasic mantle tectonites and a large underplated igneous complex in the NW. Peak metamorphic grade increases progressively from amphibolite facies in the SE to granulite facies in the NW. The IVZ is supposed to represent a section through the lower continental crust that experienced regional metamorphism during the uppermost Palaeozoic (Rutter et al. 2007; Quick et al. 2009), tectonically uplifted and delimited by the Insubric line from the NW and by the Pogallo line from the SE.

Within the IVZ a network of high-temperature shear zones oriented subparallel to the NE-SW elongation of the IVZ is observed. The shear zone network extends from Anzola (Val d'Ossola) to Forno (Val Strona) and can be traced for more than 20 km in length (Brodie et al. 1992). Single shear zones range in width from a few centimeters to more than 10 meters, and are rarely up to 200 meters thick. Mylonites in the northern part of the IVZ consist of interlayered metagabbro and depleted metapelites. Both rock formations completely (re-)equilibrated under granulite- and

amphibolite-facies conditions during crustal attenuation/extension and contemporaneous magmatic underplating (Rutter et al. 2007) between 315 Ma and 270 Ma (Rutter et al. 2007; Quick et al. 2009; Sinigoi et al. 2011; Klötzli et al. 2014). In the Val d'Ossola section at Premosello peak *P-T* conditions are estimated at 0.6-1.0 GPa and > 800 °C, based on the data from neighboring Val Strona di Omegna (Redler et al. 2012).

Pseudotachylytes are found in mylonitic metagabbros and metapelites deformed under amphibolite to granulite facies metamorphism in the northern part of IVZ (Techmer et al. 1992; Pittarello et al. 2012). Pseudotachylytes are often overprinted by ultramylonites and interpreted to have formed coevally (Pittarello et al. 2012). The peak *P-T* estimates of pseudotachylyte formation yielded 550-650 °C and 0.4-0.6 GPa (Pittarello et al. 2012 and references therein).

Samples were taken from two outcrops at Premosello (N46°00'15.04"/E08°19'44.11" and N46°00'23.65"/E08°19'41.66"); each outcrop reveals several tens of meters thick layers of tectonically faulted, mylonitized and foliated felsic metasediments (Fig. 5.1a). At the hand specimen and thin section scale these mylonites contain dark shear zones that represent an association of ultramylonites and pseudotachylytes (Fig. 5.1b).

5.3. Analytical methods and data representation

5.3.1. Sample preparation

Zircon grains were examined in polished thin sections of rock chips and in grain separates embedded in epoxy resin. For the latter zircon grains were extracted from the host rock by the standard procedure involving rock crushing, sieving to the 300 µm size, density separation on a Wilfley table, in heavy liquids and with Frantz magnetic separator. All samples were mechanically polished with 0.25 µm diamond paste and subsequently chemically polished with alkaline colloidal silica solution on an active rotary head polishing machine for 4 hours. Samples were cleaned in

ethanol and distilled water before carbon coating that was applied to establish electrical conductivity.

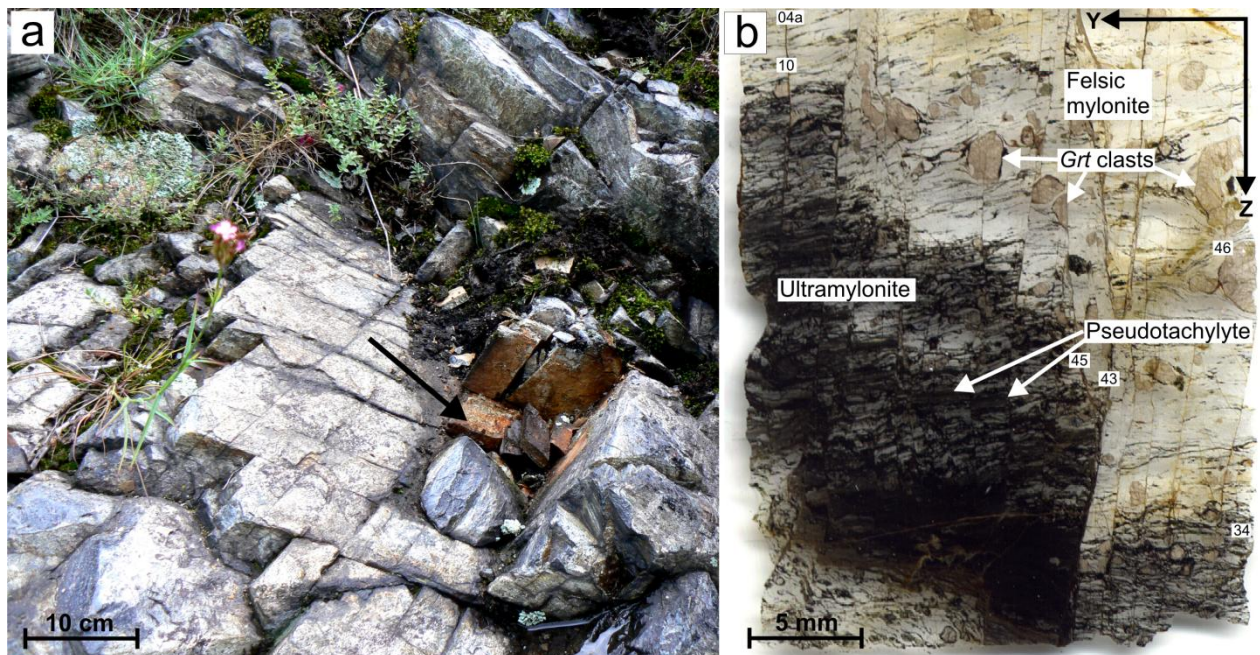


Figure 5.1. (a) Field photograph of the sampled outcrop, sampled site is indicated by arrow. (b) Plain polarized transmitted light photograph of the thin section with shear zone (dark area). *Grt* = garnet. Axes show orientation of thin section in the sample reference frame. Labels with numbers are locations of the analyzed zircon grains.

5.3.2. Scanning electron microscopy and cathodoluminescence (CL) imaging

All zircons were identified and characterized by backscattered-electron (BSE) and cathodoluminescence (CL) imaging in order to reveal the internal microstructures, using a FEI Inspect S scanning electron microscope equipped with a Gatan MonoCL system (Center of Earth Sciences, University of Vienna, Austria). Energy-dispersive X-ray spectrometry (EDS) was applied to identify the host phases. Imaging conditions were 10 kV accelerating voltage, CL-image resolution: 1500*1500 to 2500*2500 pixels using a dwell time of 80.0-150.0 ms and probe current/spot size 4.5-5.0.

5.3.3. Forward scattered electron (FSE) imaging and electron backscatter diffraction (EBSD) analysis

Zircon grains were examined for potential crystal-plastic deformation structures using orientation contrast images that were taken using a foreshattered-electron detector (FSD) mounted on the EBSD-tube of a FEI Quanta 3D FEG instrument (Faculty of Geosciences, Geography and Astronomy at the University of Vienna, Austria). For FSE imaging the EBSD tube has been retracted by c. 5 mm in order to obtain maximum signal intensity on the FSD. After identification of the potentially deformed grains, EBSD orientation mapping was applied to selected zircon grains or grain domains. The FEI Quanta 3D FEG instrument is equipped with an EDAX Pegasus Apex 4 system consisting of a Digiview IV EBSD camera and an Apollo XV silicon drift detector for EDX analysis. EDX intensities and EBSD data were collected contemporaneously using the OIM data collection software v6.2.1. FSD settings and EBSD orientation mapping settings applied are discussed in details in Kovaleva et al. (2014). Orientation maps were obtained from beam scanning in hexagonal grid mode at step sizes of 0.1 – 0.2 micrometer.

Raw indexing for zircon grains is more than 99.99%. In some cases, after EBSD data collecting the maps were recalculated based on chemical composition of phases with the OIM v6.21 software.

All EBSD data are presented in the sample reference frames X-Z or Y-Z. The EBSD data are presented as EBSD pattern quality images, and as false color-coded misorientation maps, with colors showing the relative angular misorientation of each data point with respect to a user-selected single reference point within the grain. The reference point is indicated by a red marker in each EBSD map. The orientations of the crystallographic axes are plotted as lower hemisphere equal area projections and are color-coded according to the corresponding EBSD map. The EBSD maps and pole figures were produced using the EDAX OIM Analysis software v6.2.1. All FSE and EBSD maps as well as the pole figures are oriented with X (Y) positive up and Z positive left.

We also gained insight into geometrically necessary dislocation densities using Weighted Burgers Vector (WBV) calculations (Wheeler et al. 2009). Rectangular areas with WBV components

were calculated over the EBSD maps with the MATLAB toolbox CrystalScape 1.3 based on the method described in Wheeler et al. (2009). For this goal the maps were transformed to a square grid and the Euler angles were recalculated accordingly with the Channel software. The actual algorithm used by Channel to import .ang files produces a square grid of data points and reduces the number of data points by approximately $(\sqrt{3})/2$, which should involve some kind of interpolation to create the square grid. This may introduce errors – but the key point here is that in using the integral method to determine WBV, in which an integration path passes through many pixels, the effects of local errors are reduced and thus not compromise our interpretations. The rectangular areas, presented in this publication, are superimposed on the EBSD pattern quality maps with hexagonal grid, derived with EDAX OIM Analysis software, where deformation structures are better visible.

5.4. Petrography

Felsic mylonites represent strongly restitic, highly dehydrated metasedimentary rocks. They contain garnet clasts ranging from 50 to 500 μm in size (Fig. 5.1b), which are surrounded by a fine-grained foliated matrix consisting of alternating plagioclase- and quartz-rich layers, with intercalated biotite-ilmenite layers. Accessory minerals are zircon and monazite.

Locally pseudotachylytes are visible macroscopically as concordant dark-gray 2-3 mm thick veins, fractured and offset by fractures. More often they are hosted by ultramylonites from which they are hard to distinguish. Ultramylonitic shear zones in the felsic mylonites appear as 1-2 cm thick dark rock portions extending parallel to the main foliation and limited by subvertical fractures (Fig. 5.1b). Shear zones contain pseudotachylyte veins concordant with the foliation, intensively folded and offset by fractures (Figs. 5.1b; 5.2a-b; 5.2f-g).

Both pseudotachylytes and ultramylonites mainly represent an ultra-fine-grained matrix composed of plagioclase, quartz, biotite and ilmenite, with minor amounts of garnet. Unlike the

mylonitic portions of the rock, the ultramylonite contains much less garnet clasts, and does not reveal monomineralic bands. The foliation in ultramylonite is represented by variations in the biotite-content. Pseudotachylytes can be occasionally distinguished from surrounding ultramylonites in optical microscope as homogeneously black layers in plane-polarized light (Fig. 5.2a), but more often as layers with bright rims in reflected light (Fig. 5.2f) and BSE images (Figs. 5.2b-c, 5.2g).

Pseudotachylytes are often rimmed by single garnets and garnet aggregates of second generation (Fig. 5.2), which is different from host rock garnets. These garnet grains have a dendritic morphology, range from 5 to 40 μm in size, and contain multiple inclusions, mostly ilmenite (Fig. 5.2d) as described by Austrheim et al. (1996), Austrheim and Corfu (2009) and Pittarello et al. (2012). Garnets rimming pseudotachylyte are supposed to form due to late low-temperature (about 550°) crystallization of garnet from the melt (Pittarello et al. 2012). Sometimes angular garnet fragments with dendritic overgrowths rim the injection veins. Such fragments form due to cataclasis of garnet porphyroclasts, dragging by melt and subsequent overgrowth by new dendritic rims (Pittarello et al. 2012).

Another feature characteristic for the pseudotachylytes is needle-shaped fine grains, ranging from 1 to 5 μm in length. Possibly these grains are locally preserved microlites, resulting from non-equilibrium crystallization of frictional melt (Figs. 5.2d and 5.2e).

In the sampled felsic mylonites, a fraction of 23-29% of all zircon grains are brittlely deformed, whereas 10-11% of all zircon grains show crystal-plastic deformation. These values are close to those for non-foliated metapelites sampled in the same area yielding about 24% brittlely and 11% crystal-plastically deformed grains, respectively. The content of deformed zircon grains in pseudotachylytes and in associated ultramylonites is much higher. There, 63-72% of grains are brittlely deformed (Fig. 5.3) and 19-28% show crystal-plastic deformation (Fig. 5.4), including grains with planar deformation bands (Figs. 5.5-5.8).

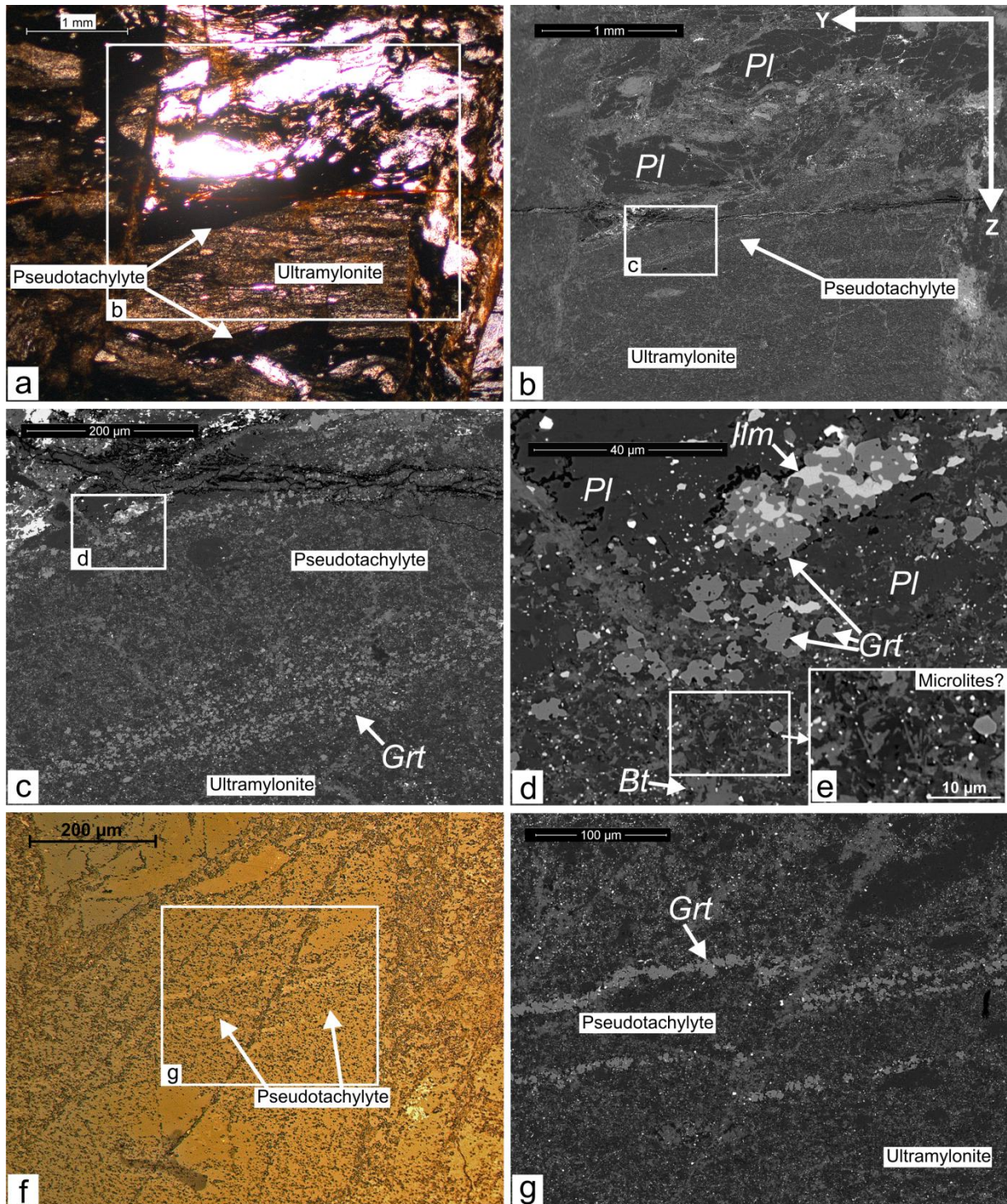


Figure 5.2. Pseudotachylyte veins (orientation as in Fig. 1b). *Pl* = plagioclase, *Grt* = garnet, *Ilm* = ilmenite, *Bt* = biotite. **(a)** Plane-polarized transmitted light photomicrograph, black veins are pseudotachylytes hosted by ultramylonite. **(b)** BSE image of the area marked in Figure 2a. Pseudotachylyte vein with bright rim due to garnet enrichment in contact with ultramylonite. **(c)** BSE image of pseudotachylyte vein in detail. **(d)** BSE image of the rim of pseudotachylyte vein. **(e)** Enlarged area from 2d with needle-shaped fine grains, resembling microlites. **(f)** Reflected light photomicrograph. The pseudotachylyte vein has a garnet rim (bright), separating it from the host ultramylonite. **(g)** BSE image of the pseudotachylyte vein shown in 2f, offset by a fracture zone.

5.5. Microstructural and crystallographic zircon data

5.5.1. Planar deformation bands

Planar deformation bands (PDBs) represent slightly misoriented (0.4° - 2.7°) planar grain portions crosscutting the zircon grains. PDBs in 2D sections trace in one or two directions and their amount varies from 2 (Fig. 5.5a) to several tens per grain (Fig. 5.6a) in each direction. The width of lamella traces in 2D sections varies from 0.3 to 1 μm , whereas at mutual intersections they show characteristic thickening (Figs. 5.5c and 5.5g, dashed circles). Misorientation from the host crystal may also slightly increase at the sites of mutual PDBs intersection. Spacing between PDBs ranges from 1 μm (Fig. 5.5a) to 25 μm , but most frequently is around 5 μm (Figs. 5.5e and 5.5i). These structures are oriented parallel to the $\{100\}$ plane (Figs. 5.5d, 5.5h, 5.5l and 5.6c). In one case they trace parallel to the $\{001\}$ (Fig. 5.6i).

PDBs can be identified in orientation contrast (FSE) images and EBSD pattern quality maps as dark or bright planar grain portions; in color-coded EBSD orientation deviation maps as lattice portions slightly misoriented with respect to the host. They are not visible in CL-images (Figs. 5.5-5.8) and some of the PDB sets are not visible in EBSD maps as well (Fig. 5.5g, NE-SW set; K, NE-SW set). Sometimes PDBs can be identified in the optical microscope as parallel lamellae (Fig. 5.6b, white arrows). Some PDB show steep misorientation profiles (e.g. Figs. 5.6d, 5.6h and 5.9), whereas some show blurred boundaries (Figs. 5.5c, 5.5k, 5.7c and 5.7f). In one case asymmetric PDBs are shown (Fig. 5.5g), which demonstrate abrupt misorientation change at left side and gradual orientation change towards the host grain orientation at the right side.

The true misorientation of the PDBs can be observed with misorientation profiles (Fig. 5.9) that are giving point-to-point and point-to-origin misorientation angles. The misorientation peaks clearly rise above the noise level, which usually does not exceed 0.3° . Peaks formed by point-to-origin misorientations (black line in Fig. 5.9) usually count one prominent peak for each PDB. They are a few

μm thick and have an asymmetric shape, with one steeper and one shallower slope (Fig. 5.9a: intersection 1, 2, 3a, 4; b: intersection 1, 3; c: intersection 1). In some cases maxima can form a plateau (Fig. 5.9c, int. 1: 1 μm -wide plateau, int. 2: 0.5 μm -wide plateau).

The documented intragranular distortion indicates the presence of geometrically necessary dislocations in the lattice. For a selected sample region in the EBSD map, the Weighted Burgers Vector (WBV) quantifies the total Burgers vector for all the dislocations passing through that region (the “integral form” according to Wheeler et al. 2009). This can be expressed in terms of lattice vectors and then divided by the sample region area to measure dislocation density including Burgers vector direction. Using rectangular sample regions, the WBV calculation has shown that in the domains of crystal lattice where PDBs are not observed the WBV is comparatively low (Fig. 5.10, rectangle areas with gray lines). In domains where two sets of PDBs intersect, the WBV is large and shows mixed directions (Fig. 5.10, rectangle areas with thin black lines). In domains, intersecting one set of PDBs, WBV usually has a large *b* component (dashed lines), whereas in rare cases the *c* component (Figs. 5.10a and 5.10d, white lines) and for grain 46 the *a* component is large (Fig. 5.10c, dotted lines).

PDBs can be pinned by structures causing misorientation of grain fragments (grain 46, Figs. 5.5i-k, black arrow) and by preexisting open fractures with offsets (grains 17, 03b; Fig. 5.6). However, structures that do not generate misorientations or offsets do not influence the geometry of PDBs (Figs. 5.5i-j, white arrow; Fig. 5.6a). For example, in grain 17 (Figs. 5.6a-e) a set of subvertical fractures crosscut the zircon grain at the left and at the right generating offsets. PDBs do not crosscut these fractures but terminate at the boundary of the central fragment. On the other hand, the subhorizontal fracture, which is decorated by pores and displaced by the crosscutting subvertical fracture at the right hand side, does not influence the geometry of the crosscutting PDBs.

Occasionally, PDBs occur together with other crystal-plastic and brittle deformation structures. Grain 14 (Fig. 5.7a-c) shows lattice distortion by crystal-plastic deformation, it is crosscut by multiple fractures and contains PDBs which mainly appear in the EBSD orientation deviation map (Fig. 5.7c),

crosscut the central part of the grain and intersect crystal-plastically deformed zones. PDBs seem to be slightly offset by a fracture (Fig. 5.7c, red dashed line). Grain 45 (Figs. 5.7d-f) also shows associated PDBs, fractures and lattice distortion (Fig. 5.7d, indicated by red arrow). PDBs cut across the fracture, but they seem to disappear in domains with lattice distortion (Figs. 5.7d and 5.7f, lower left).

Concerning the spatial distribution of the zircon grains revealing PDBs, these are observed at the contact between mylonites and ultramylonites, or in matrix within 1 cm from ultramylonites in 2D sections (Fig. 5.1b). Zircon grains hosted by central part of ultramylonites contain very indistinct PDBs that appear to be annealed. Approximately 3% of the separated large 100-300 μm crystals exhibit PDBs (e.g. grain 91, Figs. 5.8e and 5.8f).

5.5.2. Planar fractures

Planar fractures (PFs) occur less frequently than PDBs. Usually there are a maximum of 3-5 in one grain (Figs. 5.5e and 5.6a-b, black arrows; Fig. 5.8a and 5.8d, black arrows; Fig. 5.8e and 5.8f white arrows). They appear in BSE, SE and orientation contrast images as dark, straight, sometimes segmented lines (Figs. 5.5e, 5.6a, 5.8a and 5.8e). In rare cases, when PFs are thick enough and/or oriented normal to the thin section surface, can they be observed with transmitted light microscopy and in CL images as dark lamellae (Figs. 5.6b, 5.8b, 5.8d and 5.8f).

Sometimes PFs overprint PDBs (Figs. 5.5e, 5.6a and 5.8e) and in that case their trace consists of discontinuous fracture segments. However, they are not necessarily associated with PDBs (grain 21, Fig. 5.8a, black arrows), but in both cases they are oriented parallel to the $\{100\}$ planes and therefore are crystallographically controlled.

In grain 43 one PF is fragmented along the PDB and the fracture tips form a double-wing shape (Fig. 5.5e, inset). Wings initiate at the sites of intersection with the orthogonal set of PDBs.

5.5.3. Curvilinear fractures

Two sets of CFs are visible in FSE and CL images of grain 26 (Figs. 5.4c and 5.4d). A set of subparallel CFs crosscut the overgrowth rim (trace orientation indicated by white arrows); they are open and oriented roughly parallel to a {100} crystallographic plane. These CFs are terminated by another fracture set.

In this grain we also observe subparallel trails of pores, in CL image these traces appear as bright lines, therefore these inclusion trails are interpreted as healed CFs. (Figs. 5.4c and 5.4d, black arrows). They only crosscut the magmatic core and do not continue into the overgrowth.

Grain 03b (Fig. 5.6f) is fractured by two subvertical CFs that prevent PDBs penetration into the left fragment of the grain.

In grain 21 two CFs (Fig. 5.8a, white arrows) are terminated by a planar fracture (Fig. 5.8a, intersection sites are highlighted by gray arrows). CFs in this case have a crystallographic orientation roughly parallel to a {110} plane.

5.5.4. Cataclastic deformation structures in zircon

Cataclastic deformation of zircon is abundant in the pseudotachylyte-bearing rock (up to 72%). Some of the grains are strongly fragmented (Fig. 5.3), which does not occur in mylonites and non-foliated metamorphic rocks of the study area. The fragmented zircon grains occur in the vicinity of pseudotachylytes, within fractures that crosscut and offset pseudotachylytes and ultramylonites at a high angle (Fig. 5.1b).

Grain 12 is crosscut by several transgranular fractures with displacement of the fragments (Fig. 5.3a, subhorizontal fracture trace); the magnitude of the offset in the thin section plane is particularly well visible in the CL image revealing the initial growth zoning, yielding 50 μm apparent sinistral offset in Figure 5.3b. Fragments of grain 12 also preserve crystal-plastic deformation structures, visible in orientation contrast (fig. 5.3a). Grain 04a is crosscut by one transgranular

fracture (Fig. 5.3c, vertical), and fragmented by multiple sets of intragranular fractures. Grain 10 is embedded within an 80 μm -thick fracture zone and is strongly fragmented together with the surrounding phases (plagioclase, amphibole) (Figs. 5.3d and 5.3e). The fragments of zircon grain 10 and surrounding phases are mixed; they have similar size range and typical angular shapes. A set of open fractures crosscuts grain 26 (Fig. 5.4) but does not display significant offsets and neither causes rotation of the fragments. A fracture in grain 46 (Figs. 5.5i and 5.5k) cuts through PDBs and produces misorientation of the crystal lattice of about 1° (Fig. 5.5k). Fractures that have different chronological relationship with PDBs are also observed in grains 17 and 03b (Fig. 5.6), 14 and 45 (Fig. 5.7).

5.5.5. Crystal-plastic deformation structures

In rocks containing pseudotachylytes plastic deformation of zircon is reflected by gradual bending of the lattice, systematic rotation of crystallographic axes and formation of low-angle boundaries. Plastic deformation is also often associated with cataclastic deformation at the grain margins.

Grain 26 shows local lattice distortion in two domains (Fig. 5.4a). Domain i) belongs to a magmatic core that shows localized fragmentation at the left margin (Fig. 5.4d). The maximum misorientation of the lattice in domain i) is more than 20° with respect to a reference point in the undeformed part of the grain. The distorted edge shows bending from 1.5° to 10° per μm and the formation of low- and high-angle boundaries (with a threshold of 10° , as in Piazzolo et al., 2012) with radial semi-circular shapes. In Fig. 5.4b low-angle boundaries of the domain i) are highlighted with red and green lines; grain boundaries with misorientation of more than 15° are highlighted with blue lines. Fragments are detached from the parent grain and become involved in the fine-grained matrix (Figs. 5.4a, 5.4c and 5.4d). This lattice distortion pattern corresponds to type (II) according to the classification for zircon given by Piazzolo et al. (2012) and Kovaleva et al. (2014).

Domain ii) of grain 26 belongs to the overgrowth rim (Figs. 5.4a and 5.4d). The maximum misorientation in this domain reaches 15° and documents gradual bending at about 1° per μm around a rotation axis parallel to the [001] zircon direction (Fig. 5.4a, inset, in red circle) without low-angle boundary formation. This finite deformation pattern reveals the features of zircon lattice distortion type (I) (Piazolo et al. 2012; Kovaleva et al. 2014).

Grain 46 (Figs. 5.5i-l) reveals a low-angle boundary (Figs. 5.5j-l, black arrow) associated with a CL-bright $5\ \mu\text{m}$ -thick band (Fig. 5.5j, white arrow). The CL-bright band associated with low-angle boundary could be a result of hydrothermal alteration, facilitated by lattice distortion (Fig. 5.5j). The low-angle boundary appears as dark linear feature in the EBSD pattern quality map (Fig. 5.10c, top), and as a step in orientation of about 1° in the EBSD orientation deviation map (Fig. 5.5k, indicated by black arrow). The low-angle boundary traces approximately parallel to the {001} plane (Fig. 5.5l). Grain 46 contains strain-free subgrains that are separated by low-angle boundary (highlighted by black arrow), and thus has the characteristic type (III) zircon lattice distortion pattern (Piazolo et al. 2012; Kovaleva et al. 2014). The WBV of subareas across this boundary shows large a component and sometimes a large c component (Fig. 5.10c), indicating that dislocation lines with Burgers vectors [100] and [001] are dominant (MacDonald et al. 2013). The PDBs present in the grain crosscut the CL-bright band but terminate at low-angle boundary.

Crystal-plastic deformation overprinting PDBs occur in grains 14 and 45 (Fig. 5.7). Grain 14 shows grain internal lattice rotation of more than 20° with respect to a reference point and represents lattice distortion pattern type (I) (Piazolo et al. 2012; Kovaleva et al. 2014), which is offset by a set of subhorizontal fractures as apparent in orientation contrast image (Fig. 5.7a). Grain 45 is deformed locally at its margin (Fig. 5.7d, red arrow); PDBs become indistinct where crystal-plastic deformation takes place.

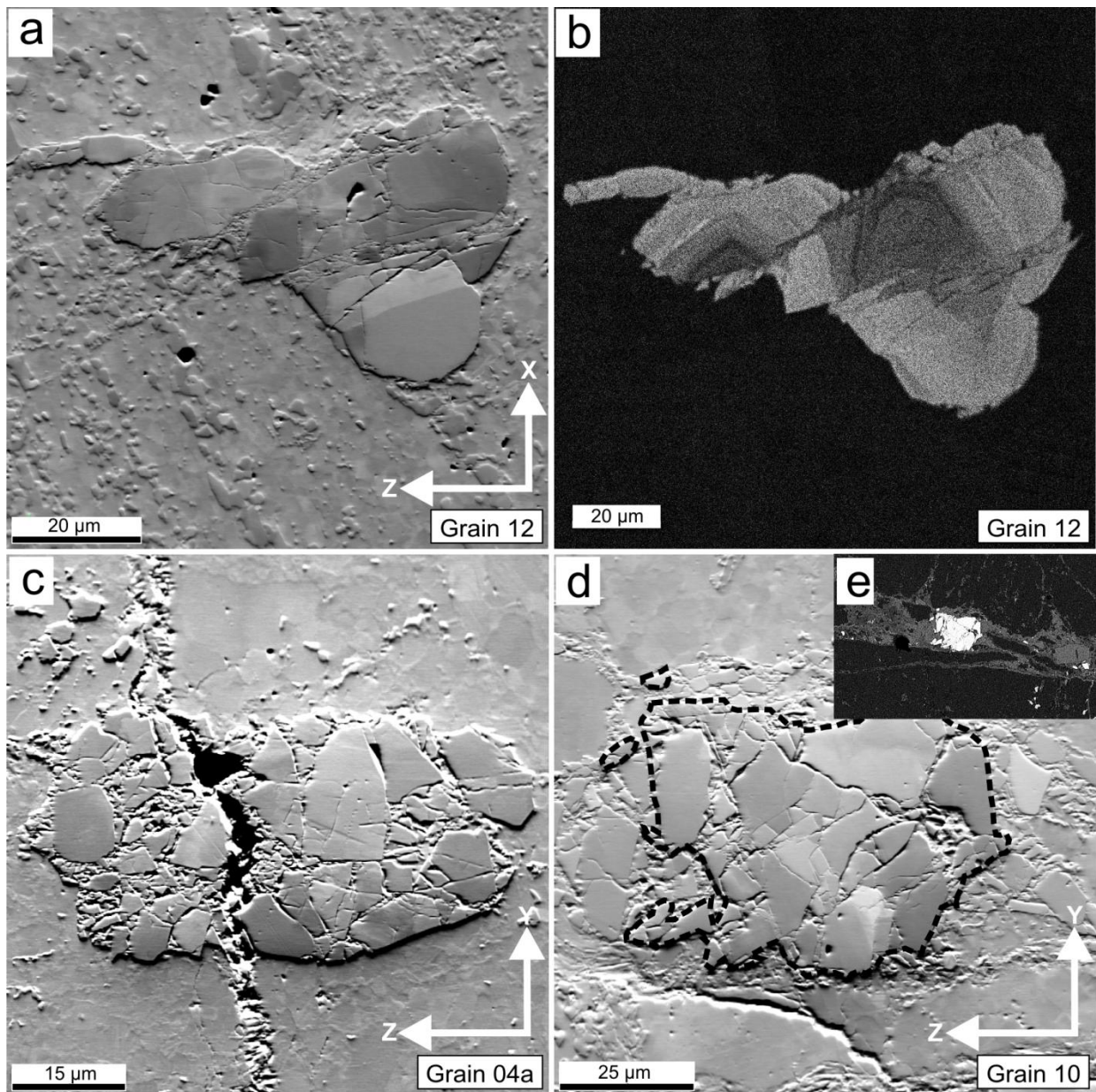


Figure 5.3. Fragmented zircon grains. Axes show the sample reference frame. **(a)** Orientation contrast (FSE) image of grain 12. **(b)** CL image of grain 12. **(c)** Orientation contrast image of grain 04a. **(d)** Orientation contrast image of grain 10, black dashed line contours the zircon grain. **(e)** BSE image of the grain 10.

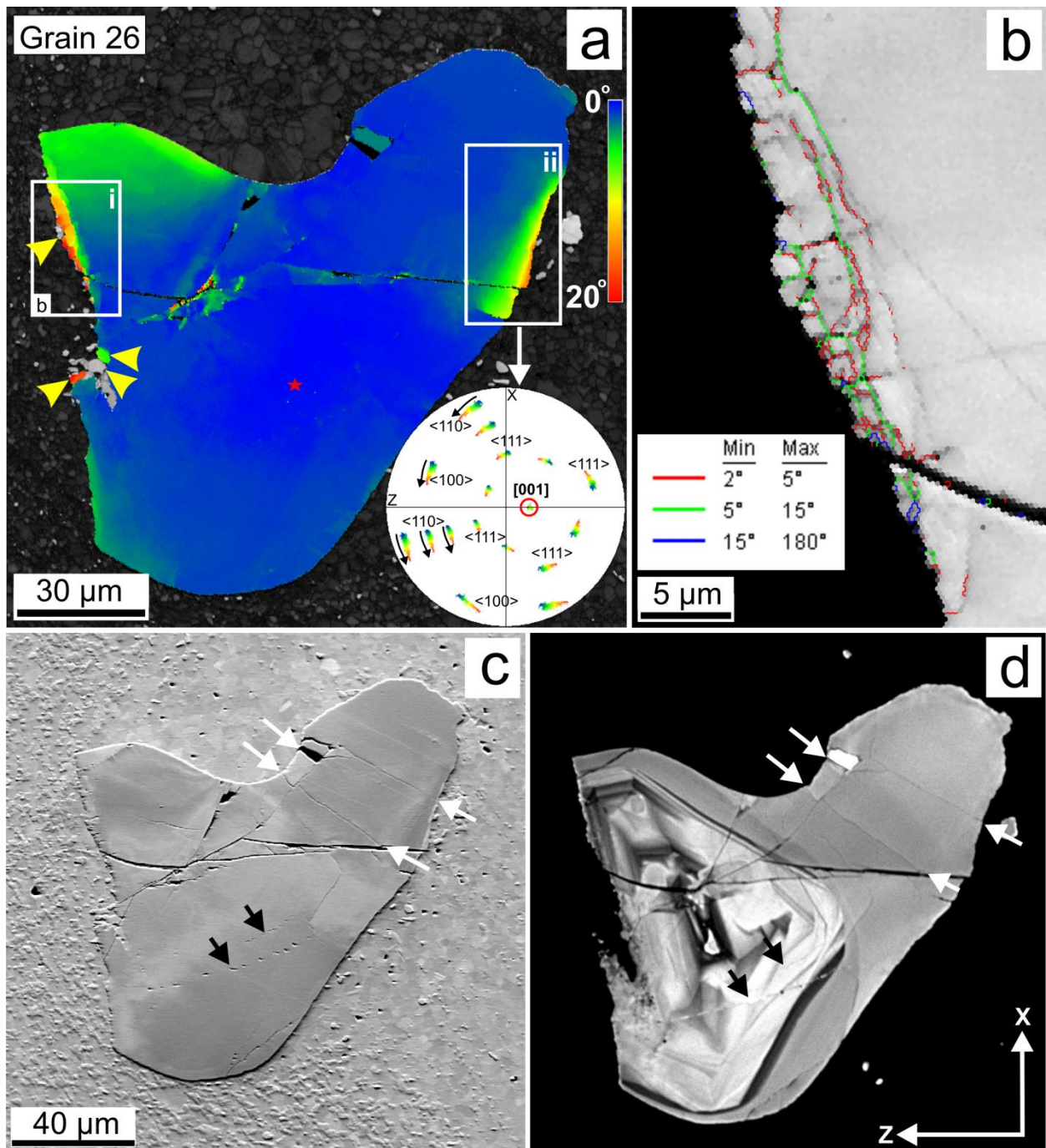


Figure 5.4. Grain 26 revealing evidence of crystal-plastic deformation. **(a)** EBSD map color coded for zircon misorientation with respect to a reference point (red star marker). Arrows indicate fragments detached from a parent grain. Inset: pole figure plot showing zircon crystal directions (lower hemisphere equal area projection) of the grain portion ii, color coded as in Figure 5.4a. Labels indicate the crystallographic directions. Plot shows scattering of axes due to rotation around $[001]$ (red circle), indicated by black arrows. **(b)** EBSD pattern quality map of zircon area i, showing boundaries colored for misorientation angles. **(c)** Orientation contrast image, arrows indicate curvilinear fractures (CFs), black – healed, white – open. **(d)** CL image, arrows as in 4c.

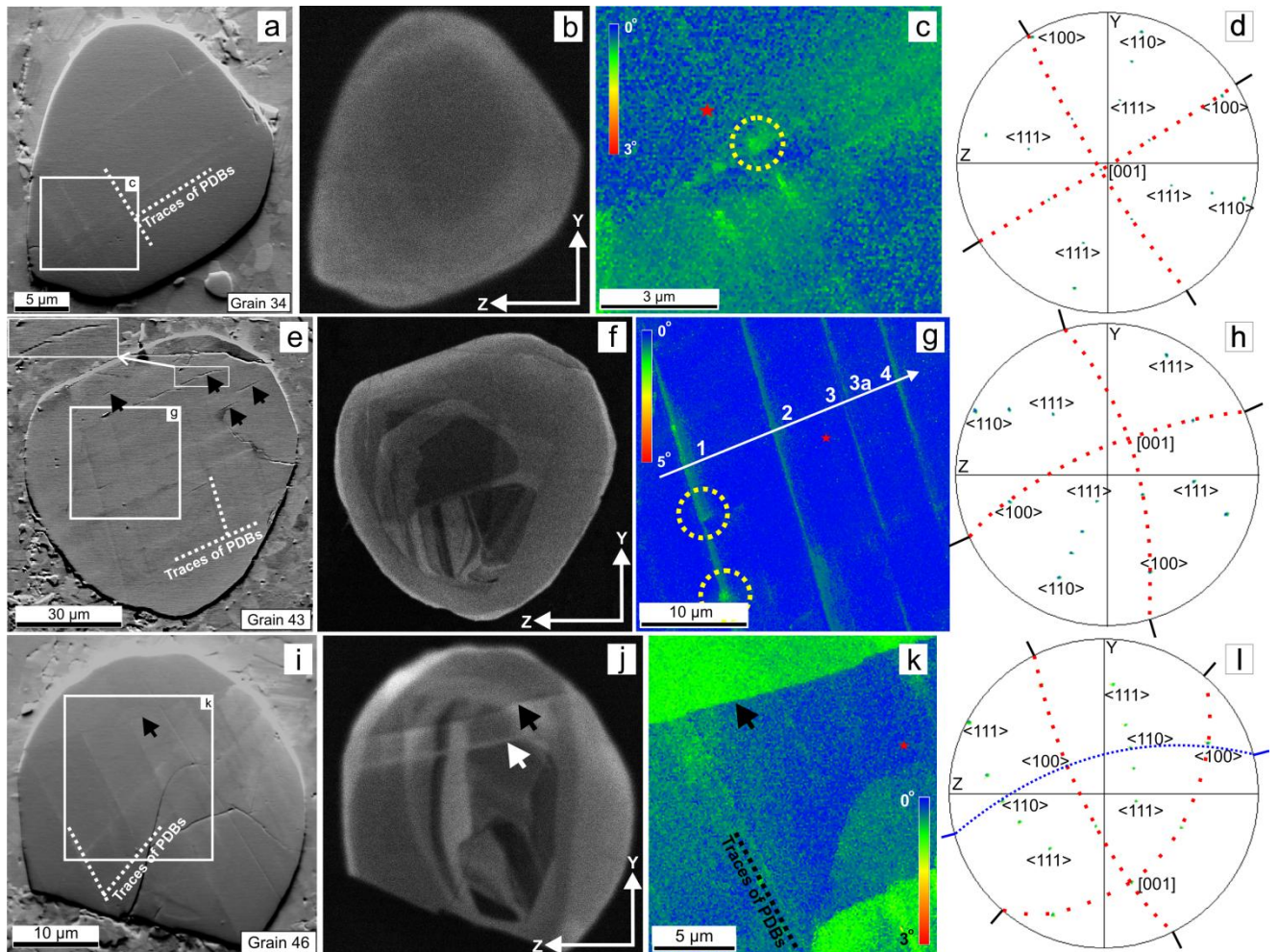


Figure 5.5. Grains with planar deformation bands (PDBs). **(a)** Orientation contrast image of grain 34. **(b)** CL image of grain 34. **(c)** EBSD orientation deviation map of grain portion highlighted in Figure 5.5a, color coded for zircon misorientation with respect to a reference point (red star marker). Dashed circle highlights thickening of the PDBs at intersection site. **(d)** Pole figure plot showing zircon crystal directions of the grain portion shown in 5.5c. Labels indicate the crystallographic directions. Black lines are orientations of PDBs traces, red dashed lines are the reconstruction of PDBs orientation. **(e)** Orientation contrast image of grain 43. Black arrows highlight planar fractures (PFs) aligned in array of segments with double-wings, enlarged in upper right inset. **(f)** CL image of grain 43. Dark rectangular area represents the position of the EBSD map. **(g)** EBSD orientation deviation map of grain portion highlighted in 5.5e, color coded for zircon misorientation with respect to a reference point. Dashed circles same as in 5.5c. White arrow indicates the position of misorientation profile, shown in Figure 5.9a, numbers are intersections with PDBs, shown in Figure 5.9a. **(h)** Pole figure plot showing zircon crystal directions of the grain portion shown in 5.5g, lines as in 5.5d. **(i)** Orientation contrast image of grain 46. Black arrow indicates low-angle boundary. **(j)** CL image of grain 46. Black arrow shows low-angle boundary, white arrow highlights bright CL-band. **(k)** EBSD orientation deviation map of the grain portion highlighted in 5.5i, black arrow as in 5.5i. **(l)** Pole figure plot showing zircon crystal directions of the grain portion shown in 5.5k, black and red lines as in 5.5d, blue line gives approximate orientation of low-angle boundary.

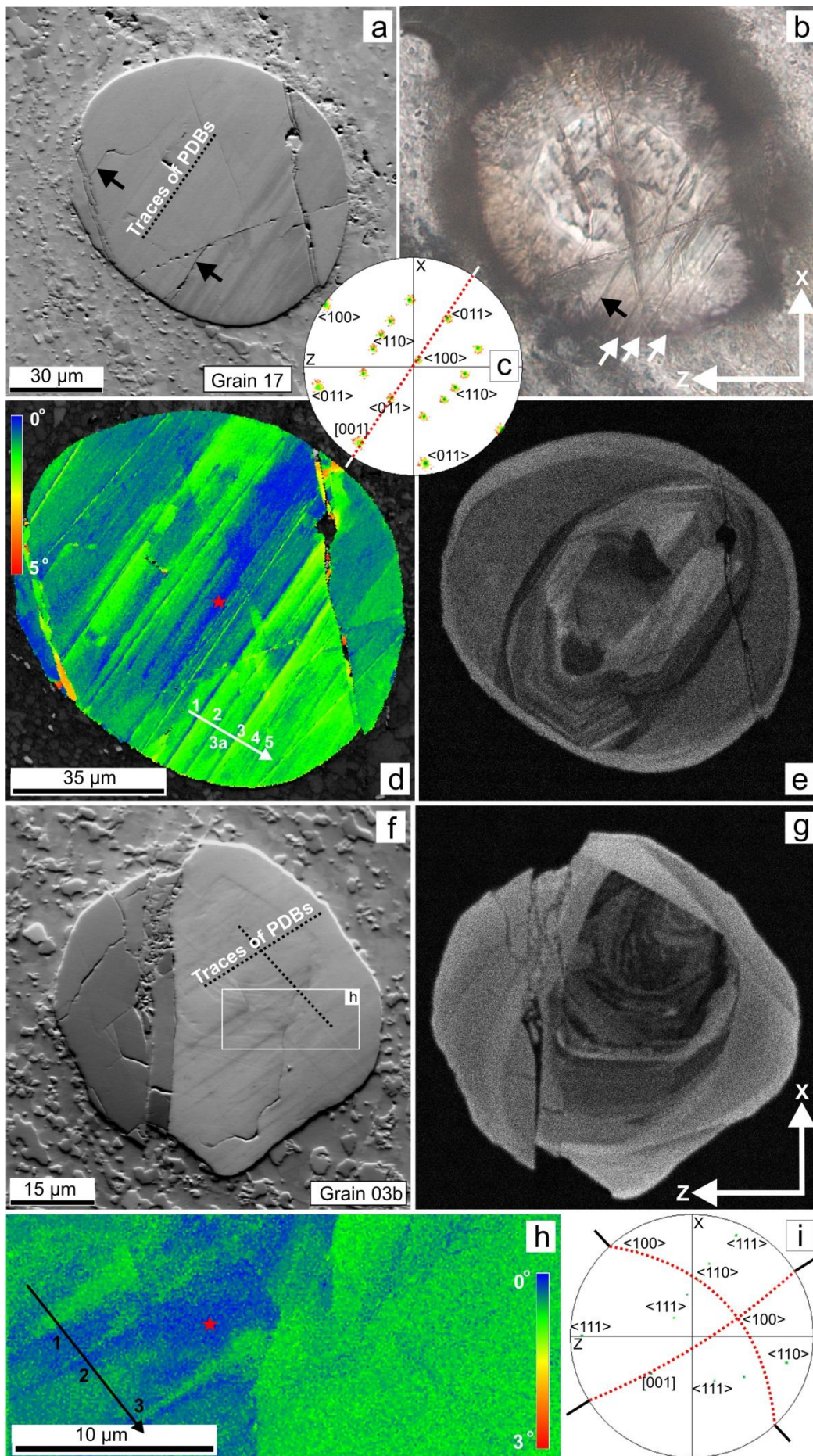


Figure 5.6. Grains with PDBs and brittle fractures. **(a)** Orientation contrast image of grain 17. Arrows indicate PFs. **(b)** Plain-polarized transmitted light photomicrograph of the grain 17, parallel lamellae are present in the lower right portion (direction indicated by white arrows), PF is indicated by black arrow. **(c)** Pole figure plot showing zircon crystallographic directions (labeled) of grain 17, color coding as in Figure 5.6d. PDBs trace orientations (white lines) and their reconstructed plane (red dashed line). **(d)** EBSD orientation deviation map of grain 17, color coded for zircon misorientation with respect to a reference point. White arrow indicates the position of misorientation profile, shown in Figure 5.9b, numbers are intersections with PDBs, shown in Figure 5.9b. **(e)** CL image of grain 17. **(f)** Orientation contrast image of grain 03b. **(g)** CL image of the grain 03b. **(h)** EBSD orientation deviation map of the domain highlighted in 5.6f, color coded for misorientation relative to a reference point. Black arrow indicates the position of the misorientation profile, shown in Figure 5.9c, numbers are intersections with PDBs, shown in 5.9c. **(i)** Pole figure plot showing zircon crystallographic directions (labeled) of the domain shown in Figure 5.6h. PDBs trace orientations are marked by black lines and their reconstructed planes by red dashed lines.

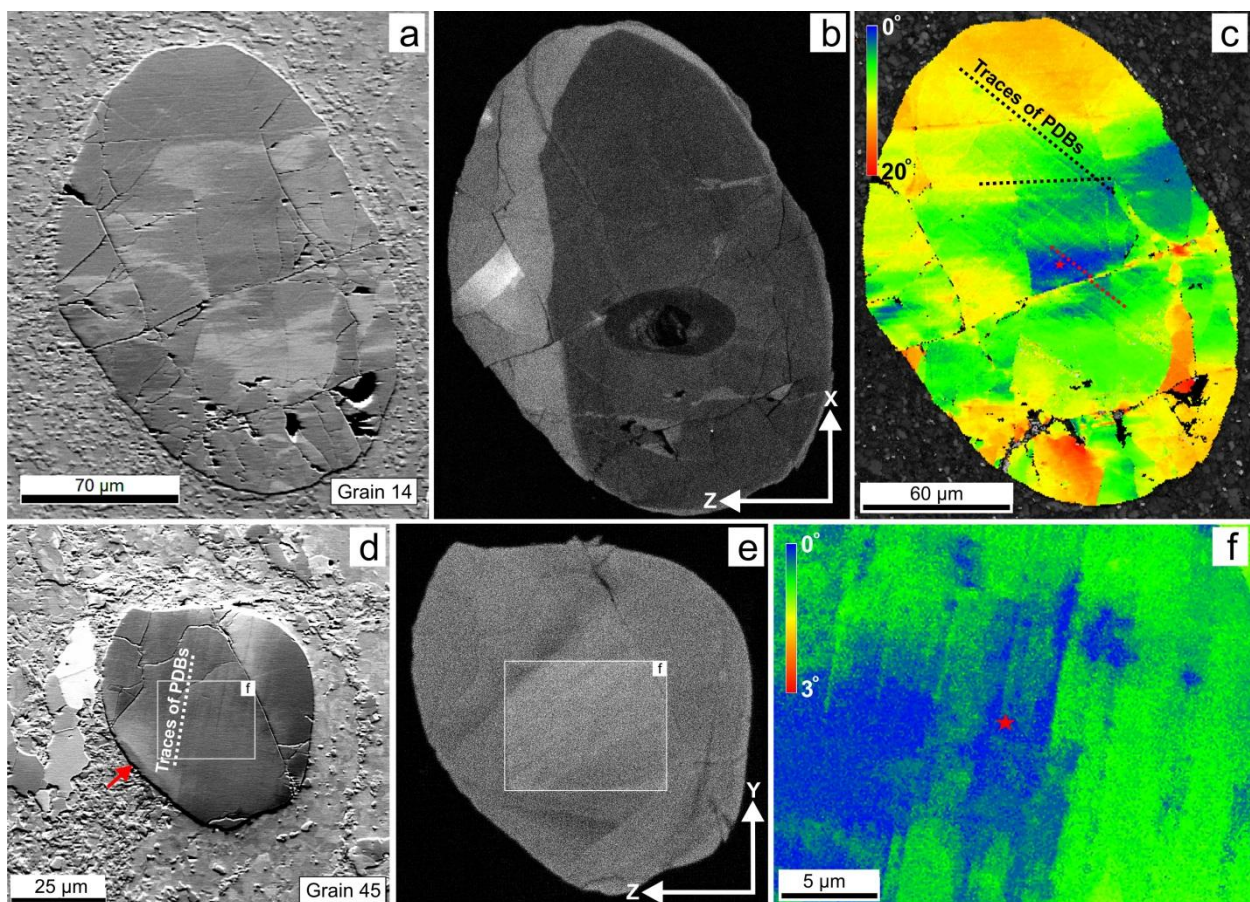


Figure 5.7. Grains showing crystal-plastic- and brittle deformation features and PDBs. **(a)** Orientation contrast image of grain 14. **(b)** CL image of grain 14. **(c)** EBSD orientation deviation map of grain 14 color coded for zircon misorientation with respect to a reference point (red star marker). Red dashed line shows offset of PDBs. **(d)** Orientation contrast image of grain 45. Red arrow indicates domain with crystal-plastic deformation. **(e)** CL image of grain 45. **(f)** EBSD orientation deviation map of grain 45 portion indicated in 5.7d and 5.7e, color coded for zircon misorientation with respect to a reference point.

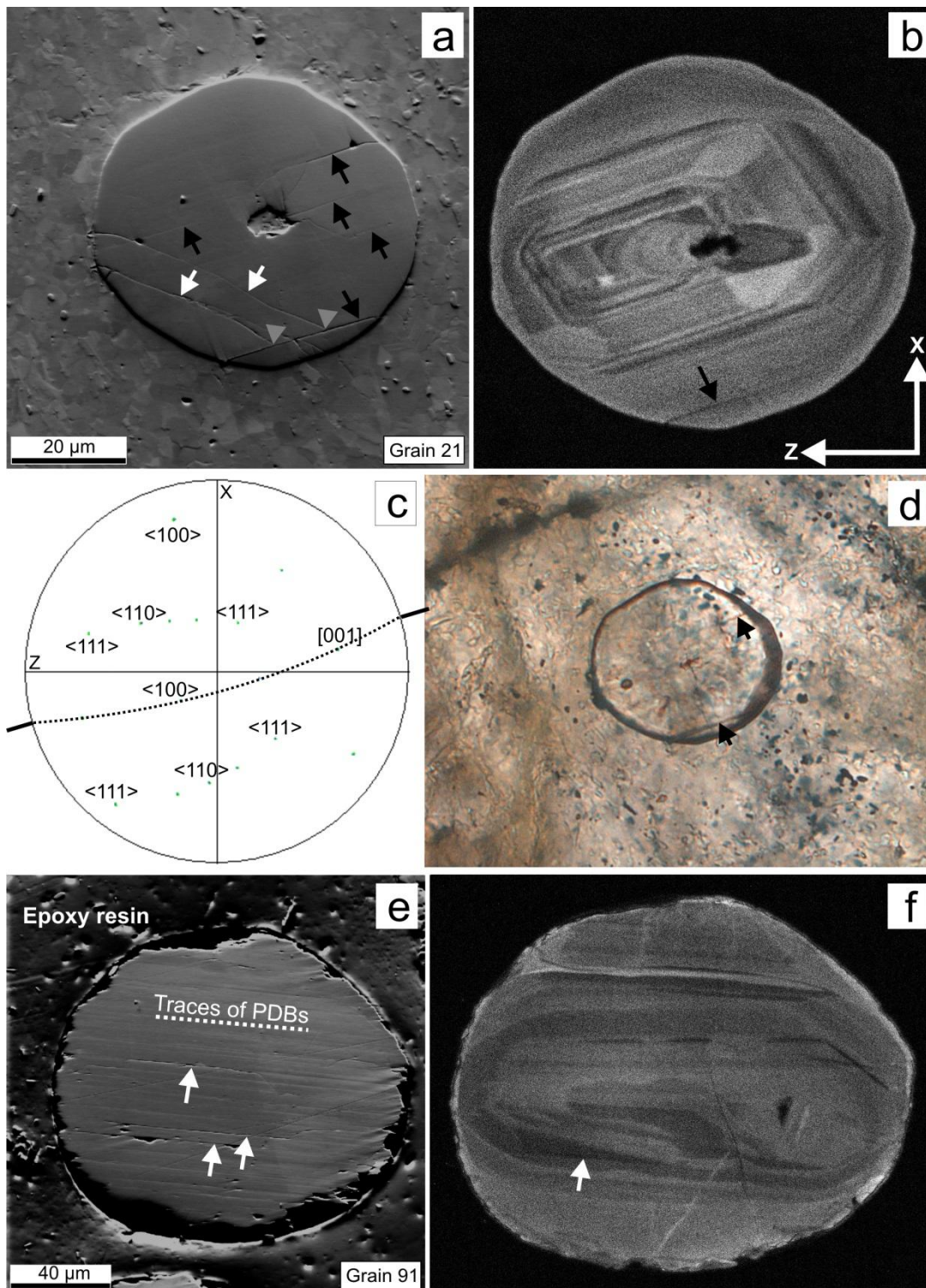


Figure 5.8. Grains with PFs. **(a)** Orientation contrast image of grain 21. black arrows indicate PFs, white arrows – CFs, grey arrows – spots, where the CFs are terminated by PFs. **(b)** CL image, black arrow highlights position of PF. **(c)** Pole figure plot showing zircon crystal directions of grain 21. PDBs trace orientation is marked by thick line and its reconstructed plane by dashed line. **(d)** Plane-polarized transmitted light photomicrograph of grain 21, dark parallel lamellae are highlighted by arrows and represent PFs. **(e)** Orientation contrast image of grain 91 embedded in epoxy resin. Arrows indicate PFs parallel to PDBs. **(f)** CL image of grain 91, arrow indicates PF.

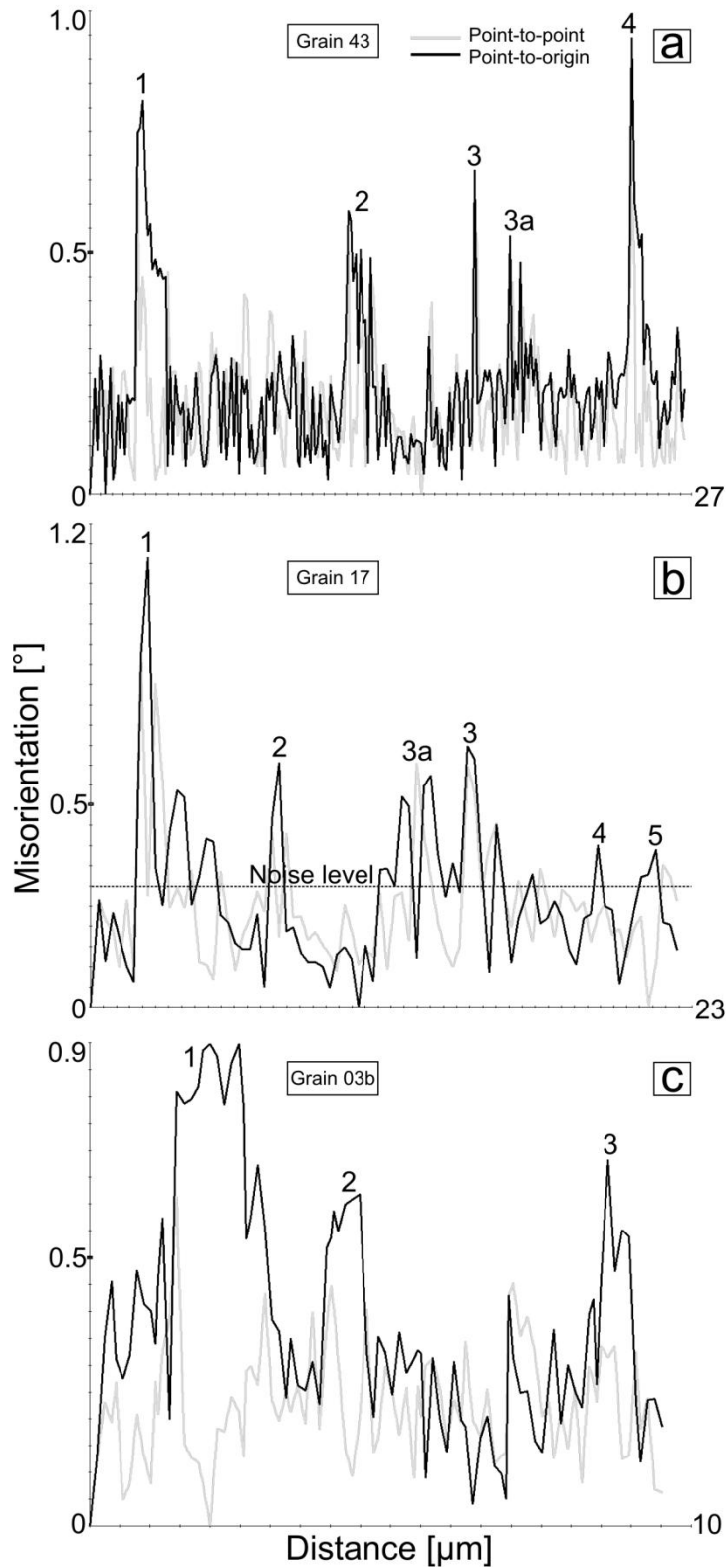


Figure 5.9. Misorientation profiles across zircon grains with PDBs. Gray line indicates misorientation between neighboring points; black line indicates misorientation relative to the starting point. Numbers mark misorientation peaks in the profiles that correspond to PDBs. **(a)** Grain 43, position of the profile is shown in Figure 5.5g. **(b)** Grain 17, position of the profile is shown in Figure 5.6d. **(c)** Grain 03b, position of the profile is shown in Figure 5.6h.

5.6. Discussion

5.6.1. Characterization of planar deformation bands

Properties of PDBs. PDBs yield high-quality EBSD patterns and therefore cannot be considered as open structures or amorphous material. Furthermore they cannot be regarded as domains with high dislocation density like “micro-bands” (Leroux et al. 1999) or domains with damaged crystal lattice, including, for example, metamictic zones or damaged during sample preparation. If so, EBSD quality maps should consistently reveal them as dark domains, but, contrastingly, many PDBs are bright (Fig. 5.10). Based on these observations we conclude that PDBs are crystalline portions of the zircon lattice. PDBs cannot be traced in CL-images, which is not only consistent with low defect density (Reddy et al. 2006), but also indicates the lack of variations in CL-active trace elements (Reddy et al. 2006; Timms et al. 2006; Timms and Reddy 2009). Misorientation profiles reveal PDBs as tabular misoriented domains of up to 2.7° from the host grain orientation (Fig. 5.9).

Another characteristic property of PDBs is their ability to cut through healed fractures, if adjacent crystal fragments have not changed their mutual orientation. When the fracture is open (grains 17, 03b), PDBs do not crosscut, but terminate at the fracture. Any other boundary, which causes relative rotation of the crystal lattice, represents a limit for the extent of PDBs (e.g. grain 46 with low-angle boundary). We conclude that PDBs in zircons are strictly crystallographically controlled structures and any pre-existing significant lattice distortion can stop their propagation.

Dislocations and slip associated with PDBs. PDBs are likely separated from the host lattice by low-angle boundaries that are associated with dislocations, indicated by high WBV values for the lattice portions that contain PDBs (Fig. 5.10). Most of the WBV measurements across PDBs show the large *b* (grains 34, 43, 03a) or large *a* (grain 46) component of the WBV, that are relevant for tetragonal symmetry and could imply high amount of dislocation lines with Burgers vector <100> (Wheeler et al. 2009; MacDonald et al. 2013). <100> is the energetically preferable orientation of the

Burgers vector as the shortest translation vector in the zircon structure (Leroux et al. 1999). Together with the geometry of PDBs that are parallel to {100} planes, this leads to a conclusion that the operating glide systems are $\langle 100 \rangle \{010\}$ with misorientation axis parallel to [001]. Those are the most frequently documented glide systems in naturally deformed zircon samples from different tectonic settings (e.g. Reddy et al. 2007; Kaczmarek et al. 2011; Piazzolo et al. 2012; Timms et al. 2012a, 2012b; Kovaleva et al. 2014).

Preferred orientation of Burger's vectors that increase towards the PDBs shows that PDBs contain deformation-related rather than growth-related dislocations. Considering deformation-related dislocations associated with PDBs, these are supposed to be a result of crystal-plastic deformation. Although similar features have been described previously (Timms et al. 2012b; Grange et al. 2013), they do not fit into the existing microstructural classification scheme of Piazzolo et al. (2012) and Kovaleva et al. (2014). Therefore, a new lattice distortion pattern classification, type (IV), is suggested for PDBs.

The glide directions $\langle 100 \rangle$ are activated under high differential stresses or ultrahigh shock pressure conditions (in case of impact-related microstructures) and at favorable orientation of the zircon lattice with respect to the local stress field. Indeed, there seems to be a specific orientation of zircon c-axes relative to the differential stress or shock wave that facilitates formation of c-axis parallel microstructures (Kaczmarek et al. 2011; Erickson et al. 2013a; Kovaleva et al. 2014).

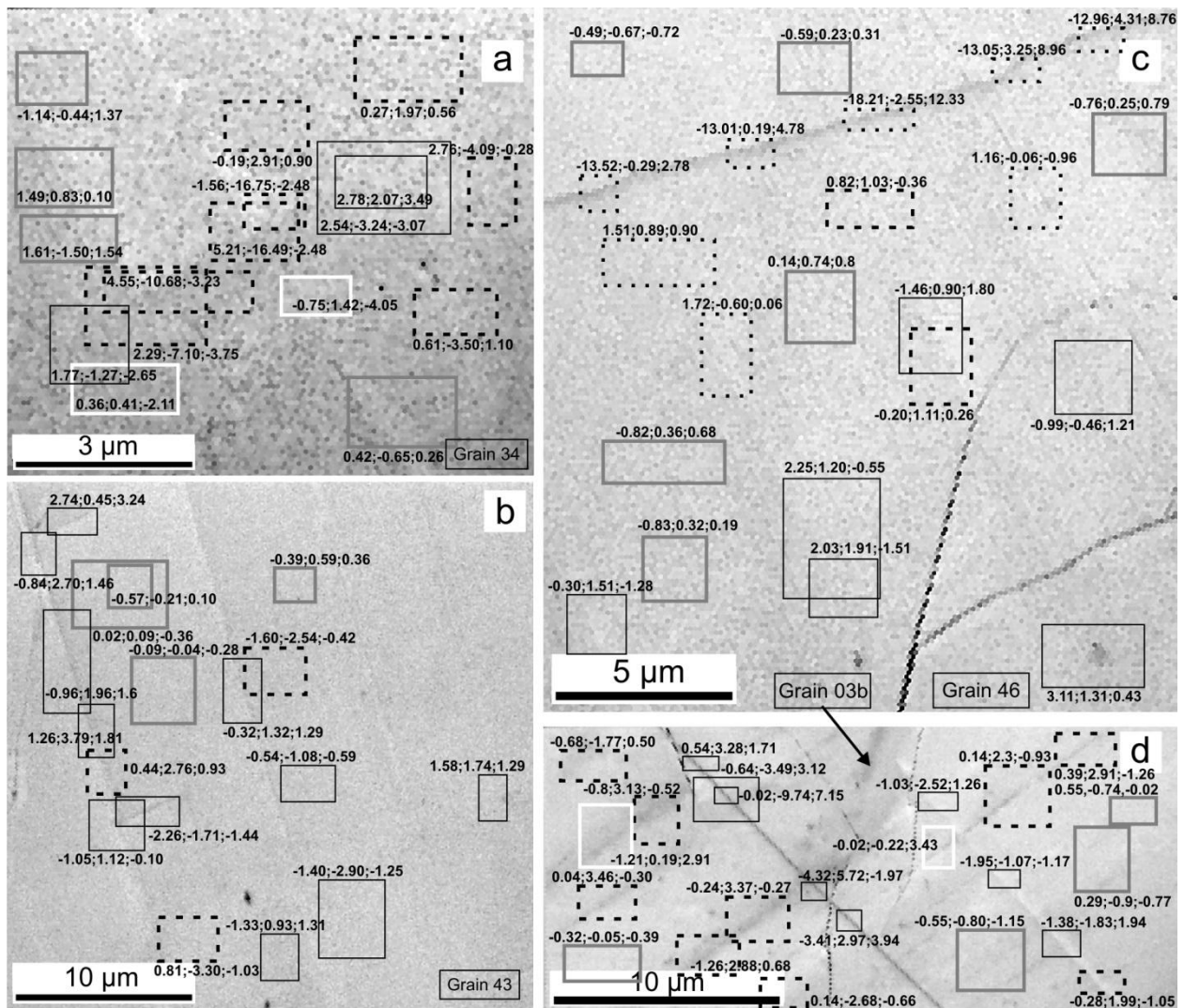


Figure 5.10. EBSD pattern quality maps with superimposed Weighted Burgers Vector (WBV) components for the highlighted rectangular subareas. The three numbers, listed for each subarea, are the a , b and c components of WBV, measured in $(\mu\text{m})^2$. Numbers were derived with the MATLAB toolbox CrystalScape 1.3 (Wheeler et al., 2009). Rectangles with grey lines show the areas with WBV that is comparatively low with respect to the rest of the mapped area. Dotted lines show rectangle areas with WBV dominated by a component, dashed lines – by b component, white lines – dominated by c component, black solid lines show areas with WBV with mixed components. **(a)** Grain 34. **(b)** Grain 43. **(c)** Grain 46. **(d)** Grain 03a.

Orientation of zircon crystals with PDBs. In Figure 5.11b we plotted crystallographic orientations of zircon grains with planar microstructures from the thin section shown in Figure 5.1b. Deformed grains show a strong $[001]$ alignment parallel to X axis of the shear flow, whereas $\langle 100 \rangle$ show no systematic orientation to the kinematic reference frame. Even though the orientation of

grains may have changed during the subsequent tectonic evolution of the rock, the clustering of the c-axes is still rather strong: 6 of 8 grains have c-axes oriented approximately parallel to the stretching lineation. Such a non-random distribution indicates that specific crystallographic orientation of grains in the sample is preferable for the formation of planar microstructures. This observation is not consistent with the theoretical model of crystal-plastic deformation in zircon by Kaczmarek et al. (2011), who suggested that zircons with c-axis parallel to the kinematic X form misorientation axes parallel to [100]. As we have shown above, dislocations associated with PDBs have misorientation axes [001].

Comparison of PDBs with PDFs. The structures that are described here as “planar deformation bands” or PDBs have strong similarity to so-called “planar deformation features” or PDFs that are well-known from zircon from impactites. Both types of structures are described as strictly parallel, crystallographically controlled portions of crystal lattice, with the visible width up to few micrometers and mean spacing of approximately 5-10 μm (Bohor et al. 1993; Corfu et al. 2003; Leroux et al. 1999; Erickson et al. 2013a; Timms et al. 2012b; Grange et al. 2013).

However, PDBs have principal differences from PDFs. PDFs described from impact-related zircon usually occupy the {001}, {110}, {112} and {320} crystallographic planes, and there are no reports of PDFs occupying {100} (Leroux et al. 1999; Timms et al. 2012b). Moreover, PDFs by definition should represent lamellae of amorphous material (Leroux et al. 1999; Erickson et al. 2013a). Therefore, PDFs are supposed to appear in CL images and show low EBSD pattern contrast. Unlike PDFs, PDBs described here do not appear in CL images and represent crystalline portions of the zircon lattice, because their EBSD quality pattern does not decrease relative to the host grain.

In addition, PDFs are often associated with shock twins (Leroux et al. 1999; Moser et al. 2011; Timms et al. 2012b; Erickson et al. 2013a, 2013b; Thomson et al. 2014) that form along the PDF planes. In our samples zircon twinning has not been observed.

PDBs presented here are similar to “planar deformation bands” described by Timms et al. (2012b) and Nemchin et al. (2009) and “planar features” described in Grange et al. (2013) in lunar zircon that was affected by shock metamorphism with partial metamictization (“oldest” zircon grain described multiple times in: Nemchin et al. 2009, Fig. 1; Timms et al. 2012b, Fig. 5; Grange et al. 2013, Figs. 10b, 12?). Those PDBs neither appear in BSE nor in CL images, but are clearly observed in the EBSD maps as planar portions with misorientation up to 10°. The misorientation profile looks similar to what is observed for PDBs presented here (Fig. 5.9). PDBs do not form a different phase and extend in two directions parallel to the {100} zircon planes (Timms et al. 2012b). Despite of the different formation environment and conditions, the PDBs reported by Timms et al. (2012b) and Grange et al. (2013) show strong similarities to the terrestrial PDBs described in our study.

Possible formation mechanisms of PDBs. The formation of PDBs in zircons from ultramylonites associated with pseudotachylytes can be explained as a result of:

- a) Shock deformation, similar to deformation due to impact events;
- b) High differential stress and strain rate during a compression stage of seismic wave propagation;
- c) High differential stress and strain rate during tectonic shearing.

Even though PDBs resemble shock-induced deformation structures like PDFs and PFs, they were formed under completely different environmental settings. Contrasting with ultrahigh shock pressure generated at the Earth’s surface during an impact event, earthquakes at depth generate significantly different stress fields and magnitudes. More specifically, peak pressure for seismic events in IVZ was estimated at 550 MPa (Khazanehdari et al. 2000). And, for example, transformation of quartz to coesite, which often happens during impacts, at a given temperature of 550° C would require pressure of about 2,7 GPa (Akaogi and Navrotsky, 1984). To compare, estimations for pressure generated by meteorite impacting the earth surface could vary from 100 to 4000 GPa (Öpik, 1958). Although ultrahigh pressure mineral associations have been previously reported to be coeval

for earthquakes (Yang et al. 2014a), but shock metamorphism have been not. On the other hand, deformation caused by an earthquake occurs in depth under lithostatic pressure, which may compensate shock pressure; lithostatic pressure is generally absent during impact-related shock deformation. We assume that scenario a) is unlikely for the PDBs formation.

Scenario b) is suggested in number of earlier studies: Leroux et al. (1999) do not explain the formation of micro-cleavage in 20-GPa experiment by shock waves, but rather due to shear stress during the compression stage. Consistently, Erickson et al. (2013a) reported initial development of {100} PFs in shocked zircon grains relative to other shock structures. This is explained by their formation during the shock loading stage (Erickson et al. 2013a), presumably induced by shear stress. Austrheim and Corfu (2009) explain formation of planar microstructures in zircon from pseudotachylytes by very high strain rates. Yang et al. (2014a) explain the formation of ultra-high pressure mineral assemblages in the dykes as a result of high stresses and friction-induced high temperatures that were coeval with the earthquake.

We suggest that high shear stresses and strain rates are responsible for PDBs formation in the studied sample material. Shear stresses, estimated by earthquakes can vary from 7 to 17 MPa at the depth of 2-10 km (estimation by Spudich et al. 1998). Even though impact shock pressure magnitudes are unlikely to be reached during seismic event, high strain rates are possible. This is indicated by intensively fragmented zircon grains in mylonites, broken and cleaved garnets in the host rock (Austrheim et al. 1996) and by presence of pseudotachylytes (Pittarello et al. 2008, 2012). Thus, newly found PDBs in zircon from the deep crust represent another evidence of paleo-seismicity.

Scenario c) suggests that the formation of PDBs is not directly related with the propagation of seismic waves, but with subsequent ductile shear zone formation accompanied by high stresses, strain rates and friction-induced high temperatures. This scenario is supported by the selective deformation of grains, which are parallel to kinematic X (Fig. 5.11b). Thus, PDBs in those grains and associated low-angle boundaries are also parallel to kinematic X. Usually, geometric control of macroscopic kinematic frame on deformation microstructures imply their genetic relationship (Reddy

and Buchan 2005; Kaczmarek et al. 2011). Therefore, PDBs could be a result of shearing at high differential stress and high strain rates that induced energetically-preferable slip in zircon; high temperatures in the vicinity of pseudotachylytes facilitated dislocation creep (e.g. Hobbs 1968; White 1973, 1976; Gerald et al. 1983; Ranalli 1995). Scenario c) implies formation of pseudotachylytes, followed by frictional heating of the surrounded rocks and by shearing that resulted in PDBs formation in zircon. However, differential stresses and strain rates operating in ductile shear zones are unlikely to be sufficient to form PDBs, even at elevated temperatures. Such structures have never been described in zircon from metamorphic rocks of deeper levels, derived, for example, from kimberlitic pipe (Timms et al. 2011).

Temperature regime of PDBs formation. To deform zircon crystal-plastically at high strain rates, very high temperature is required. Temperature conditions in the vicinity of frictional melts are supposed to be high, as the melt temperature has been estimated to > 1200 °C, and, according to estimations done for the fault segment, approximately 97–99% of the released energy was dissipated as heat during seismic slip (Pittarello et al. 2008). These conditions may enhance migration of dislocations (Timms et al. 2012b), their accumulation in {100} planes (Leroux et al. 1999; Reddy et al. 2007), and recovery in zircon grains. However, the grains from the core of the ultramylonite zones seem to be annealed, showing very indistinct degraded planar microstructures. The local temperature in the core of the ultramylonite zone supposedly did not allow PDBs to be preserved. This is consistent with the observation that well-defined PDBs are found at the contact of ultramylonite and mylonite or at a distance of 0.5-1 mm from the ultramylonite (Fig. 5.1b), where the local temperature was lower than in the pseudotachylyte core.

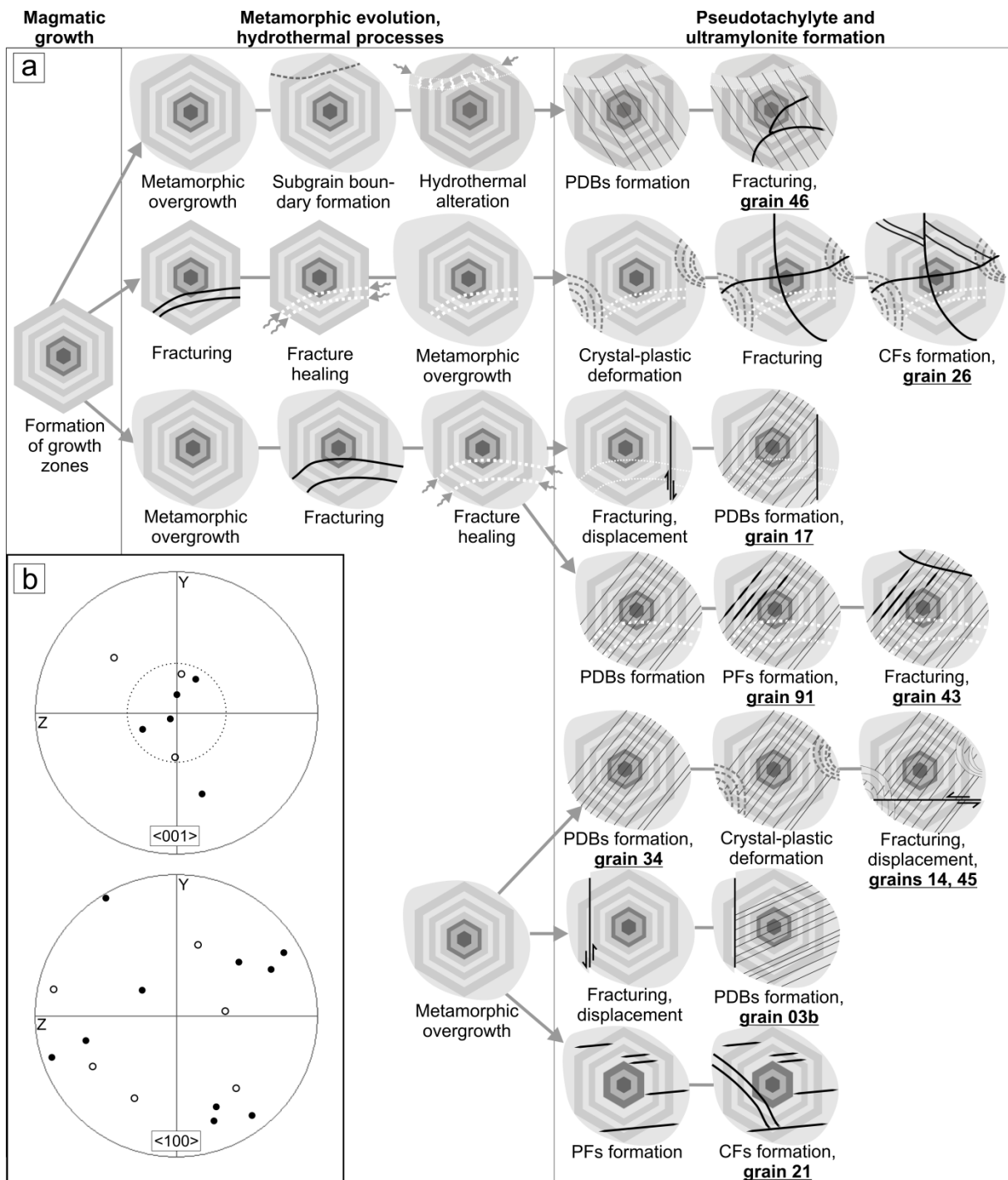


Figure 5.11. (a) Scenarios for zircon microstructural evolution in the IVZ (schematic sketch), summarizing microstructures observed in this study. Chronological sequence for microstructures reconstructed is based on crosscutting relationships. **(b)** Crystallographic orientations of the $\langle 001 \rangle$ and $\langle 100 \rangle$ axes of the zircon grains with PDBs from thin section shown in Figure 5.1b. Circles show data from grains with one (open) or two (filled) resolved sets of PDBs. 6 of 8 grains (75 %) have the c-axis approximately orientation normal to thin section plane (Y-Z plane).

5.6.2. Interrelation of PDBs with formation of other deformation structures (cataclastic and crystal-plastic)

Relative timing of multistage cataclastic deformation. The chronological sequence of the formation of microstructures in zircon is based on crosscutting relationships.

In grain 26 healed fractures do not extend into the deformed overgrowth rim (Figs. 5.4c and 5.4d, black arrows). Fractures therefore preceded rim overgrowth and crystal-plastic deformation. In grain 46 (Figs. 5.5i-l) the formation of a low-angle boundary together with an associated CL-bright alteration zone preceded the formation of PDBs, because the low-angle boundary limits the lateral extent of the PDBs. In grain 17 (Figs. 5.6a-e) healed subhorizontal fracture is offset by subvertical fractures, indicating that the latter postdated the formation of the healed fracture. Thus, healed fractures with pore traces and zones of hydrothermal alteration appearing as bright features in the CL images were formed in zircon before the formation of pseudotachylytes and ultramylonites.

On the other hand, none of the open fractures formed during the seismic activity and later on were healed or sealed. Traces of several different microstructures appear in FSE and CL images as dark lines which are not decorated by inclusions or pores and therefore are supposed to be open: i) fragmented grains (grains 03a, 10, 12, 14); ii) CFs that crosscut the metamorphic rim with crystallographic control of their spatial orientation (grain 26, upper right part); iii) fractures that limit PDBs (grains 03b and 17); iv) fractures that offset PDBs (grains 14, 45); v) CFs that are pinned by PFs (grain 21); vi) PFs (grains 43, 21, 91). We infer that healing of zircon did not occur during or after formation of pseudotachylytes, and therefore preceded PDBs formation. Formation of PDBs and cataclastic deformation, associated with seismicity and mylonitization, repeatedly alternated. For example, in grains 17 and 03b (Fig. 5.6) PDBs are terminated by fractures whereas in grain 14 and 45 (Fig. 5.7) fractures are crosscut by PDBs.

Planar fractures. So far PFs were only described from impact-related zircon grains. They are usually parallel to {001}, {100}, {111}, {201}, {211} and {221} planes in zircon crystal lattice (Leroux et al. 1999; Timms et al. 2012b; Erickson et al. 2013a). Erickson et al. (2013a) reported about frequent

occurrence of {100} orientation of PFs, and their relatively early development. PFs parallel to zircon {100} planes form at the first stage of shock deformation and are most easily annealed afterwards (Erickson et al. 2013a). That points to comparatively easy activation of these planes in the zircon crystal lattice. In our study we identified PFs tracing parallel to {100} planes, often overprinting PDBs. Their spatial relationships indicate that PDBs act as a structural precursor for PFs; both structures likely form as a result of one process and may represent different evolutionary stages of the same structure. We suggest that PFs can overprint PDBs in segments of high dislocation density. The possibility that low-angle boundaries could evolve to form PFs is suggested by Erickson et al. (2013a).

In grain 21 PFs are not associated with PDBs. In that case PFs could represent “micro-cleavage” in {100} planes, generated by high shear stresses as described with shock experiments of Leroux et al. (1999).

Curvilinear fractures. “Non-planar” or “Curvilinear fractures” are interpreted as impact- or seismic-related structures (Austrheim and Corfu 2009; Cavosie et al. 2010; Moser et al. 2011; Timms et al. 2012b; Erickson et al. 2013a). They represent “broadly parallel, spaced, and curved” fractures (Moser et al. 2011) and are supposed to result from shock deformation. The CFs in grains 03b, 17, 26 are not related to seismic activity and formed earlier than planar microstructures. CFs appear as regular fractures resulting from cataclastic deformation. They may or may not be healed and have broadly parallel orientation due to crystal internal heterogeneities (for example, growth zoning, crystallographic anisotropy), or due to specific grain shape- or crystallographic orientation in the local stress field. For example, open CFs described in grain 26 are roughly parallel to the crystallographic plane {100} and, moreover, parallel to the growth zoning; the healed CFs are roughly parallel to the plane {331} (Fig. 5.4c, white and black arrows correspondingly). In grain 21 CFs are parallel to {011}. In the study of Kaczmarek et al. (2011) CFs appear to be a result on deformation in a ductile shear zone.

We suggest that CFs cannot be used as a reliable indicator of seismic activity or shock deformation, as they can be easily formed during other deformation processes in the crust. An
Page | 174

argument for CFs formation during shock deformation could be the observation of impact melt filling CFs (Moser et al. 2011), but even then CFs might only represent reactivated preexisting fractures (Erickson et al. 2013a).

Crystal-plastic deformation (besides PDBs) and associated fragmentation at the margins.

Crystal-plastic deformation in zircon is characterized by lattice distortion due to formation and migration of geometrically necessary dislocations (Reddy et al. 2007) and has been documented for different geological settings: syn-magmatic deformation (Reddy et al. 2009; Timms and Reddy 2009; MacDonald et al. 2013), deformation in ductile shear zones (Kaczmarek et al. 2011; Piazzolo et al. 2012; Kovaleva et al. 2014), impact-related lattice distortion (Leroux et al. 1999; Moser et al. 2009; Nemchin et al. 2009; Timms et al. 2012b; Grange et al. 2013).

Lattice distortion, preserved by some fragments of grain 12 (Fig. 5.3a), indicates that crystal-plastic deformation preceded the fragmentation of this grain. Thus, fragmentation of zircon, together with rock faulting, should be a later and lower-temperature process. The lattice distortion pattern of grain 26 (Fig. 5.4) resembles that observed in zircon from ductile shear zones (e.g. Reddy et al. 2007; Piazzolo et al. 2012; Kovaleva et al. 2014). Marginal grain fragmentation observed in the domain (i) indicates that the differential stress increases towards the rim of the grain (Kenkmann 2000; Kovaleva et al. 2014). Deformation structures of the domain (i) are consistent with lattice distortion type (II), whereas domain (ii) can be classified as distortion pattern type (I) (Piazzolo et al. 2012; Kovaleva et al. 2014). The distortion patterns in zircon from the IVZ shear zone are similar those from other ductile shear zones in different tectonic settings (e.g. Reddy et al. 2007; Piazzolo et al. 2012; Kovaleva et al. 2014), where formation of pseudotachylytes has not been documented. However, the content of grains with lattice distortion in ultramylonites is 2-3 times higher than in host mylonites. Most likely, crystal-plastic deformation results from shearing and mylonitization of the host rocks during ultramylonite formation, and not necessarily related to seismic events.

Crystal-plastic deformation observed in grain 14 (Figs. 5.7a-c) likely overprinted PDBs, which were formed earlier; it looks like PDBs are slightly bending in plastically-deformed domains. In grain 45, the relative timing of crystal-plastic deformation and formation of PDBs is questionable.

5.6.3. Implications for the evolution of the IVZ

Multiple crosscutting relationships indicate that brittle and crystal-plastic deformation as well as formation of planar microstructures in zircon occurred coherently, but in different succession for each grain that is shown in the schematic sketch (Fig. 5.11a). Thus, our data support the scenario of IVZ tectono-metamorphic evolution suggested by Pittarello et al. (2012). Non-hydrous restitic rocks of the lower crustal granulite-facies section were supposed to be exhumed into the seismically active zone. Earthquakes caused frictional melting immediately followed by mylonitization localized at structural heterogeneities (Pennacchioni and Mancktelow 2007) under amphibolite facies conditions. Ultramylonite formation overprinted pseudotachylytes; cycle of fracturing, melting and mylonitization could be repeated several times in the same shear zone during a single tectono-metamorphic event (Pittarello et al. 2012).

Grain fragmentation and the formation of related transgranular faults likely occurred soon after the formation of pseudotachylytes and ultramylonites. The distribution of fragmented zircon grains frames ultramylonites (Fig. 5.1b, grains 04a and 10); and the faults hosting fragmented grains crosscut and offset ultramylonites and pseudotachylytes. Zircon grains within ultramylonites do not experience intensive fragmentation, presumably because the temperature in these zones remained higher.

5.7. Implications

This study demonstrates that planar microstructures in zircon are not restricted to shock-induced PDFs and PFs, are not exclusively evidence of shock metamorphism, but can also form in the

Earth's crust as a result of seismic activity. Furthermore, PDBs in zircon could be a newly identified indicator of seismic activity/earthquakes besides of pseudotachylytes.

Deformation microstructures as PDBs could change trace element composition in zircon and enhance partial- or complete resetting of zircon isotopic systems (e.g. Reddy et al. 2006; Timms et al. 2006, 2011, 2012b; Timms and Reddy 2009; Moser et al. 2009, 2011; Piazzolo et al. 2012; MacDonald et al. 2013), thus making possible to date paleo-seismic events directly.

On the other hand, new data provides the link between seismology, mineral physics and metamorphic petrology combined with structural geology; demonstrates how closely seismic and metamorphic processes were interacting in the IVZ rocks; and gives an example how in particular the released seismic energy at depth influences petrophysical properties of the deep crust.

Acknowledgments

This study was funded by the University of Vienna (doctoral school "DOGMA", project IK 052) and the Austrian Science Foundation Fund (FWF): I471-N19, which is part of the DFG-FWF funded international research group FOR741-DACH.

The authors are grateful to Christian Auer, Claudia Beybel, Franz Biedermann, Aaron Cavosie, Sigrid Hrabe, Matthew Huber, Lidia Pittarello, Claudia Trepmann, and all colleagues of the FOR741 research group for fruitful discussions and the Geologische Bundesanstalt (GBA) of Austria for access to the SEM.

References

- Akaogi, M. and Navrotsky, A. (1984) The quartz—coesite—stishovite transformations: new calorimetric measurements and calculation of phase diagrams. *Physics of the Earth and Planetary Interiors*, 36, 124-134.
- Angiboust, S., Agard, P., Yamato, P., Raimbourg, H. (2012) Eclogite breccias in a subducted ophiolite: a record of intermediate-depth earthquakes? *Geology*, 40, 707-710.
- Austrheim, H. (2013) Fluid and deformation induced metamorphic processes around Moho beneath continent collision zones: Examples from the exposed root zone of the Caledonian mountain belt, W-Norway. *Tectonophysics*, 609, 620-635.
- Austrheim, H. and Corfu, F. (2009) Formation of planar deformation features (PDFs) in zircon during coseismic faulting and an evaluation of potential effects on U—Pb systematics. *Chemical Geology*, 261, 25–31.
- Austrheim, H., Erambert, M., Boundy T.M. (1996) Garnet recording deep crustal earthquakes. *Earth and Planetary Science Letters*. 139, 223-238.
- Bohor, B.F., Betterton, W.J., and Krogh, T.E. (1993) Impact-shocked zircons: discovery of shock-induced textures reflecting increasing degrees of shock metamorphism. *Earth and Planetary Science Letters*, 119, 419-424.
- Brodie, K.H., Rutter, E.H., and Evans, P. (1992) On the structure of the Ivrea-Verbano Zone (northern Italy) and its implications for present-day lower continental crust geometry. *Terra Nova*, 4, 34-39.

- Cavosie, A.J., Quintero, R.R., Henri A. Radovan, H.A., and Moser, D.E. (2010) A record of ancient cataclysm in modern sand: Shock microstructures in detrital minerals from the Vaal River, Vredefort Dome, South Africa. *Geological Society of America Bulletin*, 122, 1968-1980.
- Chen, Y.D., O'Reilly, S.Y., Kinny, P.D., Griffin, W.L. (1994) Dating lower crust and upper mantle events: an ion microprobe study of xenoliths from kimberlitic pipes, South Australia. *Lithos* 32, 77–94.
- Corfu, F., Hanchar, J.M., Hoskin P.W.O., and Kinny, P. (2003) Atlas of zircon textures. In: J.M. Hanchar, P.W.O. Hoskin, Eds., *Zircon*, p. 468-500. Mineralogical Society of America and Geochemical Society, *Reviews in Mineralogy and Geochemistry*, 53, Washington D.C.
- Erickson, T.M., Cavosie, A.J., Moser, D.E., Barker, I.R., and Radovan, H.A. (2013a) Correlating planar microstructures in shocked zircon from the Vredefort Dome at multiple scales: Crystallographic modeling, external & internal imaging, and EBSD structural analysis. *American Mineralogist*, 98, 53-65.
- Erickson, T.M., Cavosie, A.J., Moser, D.E., Barker, I.R., Radovan, H.A., and Wooden, J. (2013b) Identification and provenance determination of distally transported, Vredefort-derived shocked minerals in the Vaal River, South Africa using SEM and SHRIMP-RG techniques. *Geochimica et Cosmochimica Acta*, 107, 170-188.
- Gerald, F.J.D., Etheridge, M.A., and Vernon, R.H. (1983) Dynamic recrystallization in a naturally deformed albite. *Textures and Microstructures*, 5, 219-237.
- Grange, M.L., Pidgeon, R.T., Nemchin, A.A., Timms, N.E., and Meyer, C. (2013) Interpreting U–Pb data from primary and secondary features in lunar zircon. *Geochimica et Cosmochimica Acta*, 101, 112–132.
- Hobbs, B.E. (1968) Recrystallization of single crystals of quartz. *Tectonophysics*, 6, 353-401.
- Kaczmarek, M.A., Reddy, S.M., and Timms, N.E. (2011) Evolution of zircon deformation mechanisms in a shear zone (Lanzo massif, Western-Alps). *Lithos*, 127, 414-426.

- Kallesen, E., Corfu, F., and Dypvik, H. (2009) U–Pb systematics of zircon and titanite from the Gardnos impact structure, Norway: Evidence for impact at 546 Ma? *Geochimica et Cosmochimica Acta*, 73, 3077–3092.
- Kamo, S.L., Reimold, W.U., Krogh, T.E., and Colliston, W.P. (1996) A 2.023 Ga age for the Vredefort impact event and a first report of shock metamorphosed zircons in pseudotachylitic breccias and granophyre. *Earth and Planetary Science Letters*, 144, 369–387.
- Khazanehdari, J., Rutter, E.H., Brodie K.H. (2000) High-pressure-high-temperature seismic velocity structure of the midcrustal and lower crustal rocks of the Ivrea-Verbano zone and Serie dei Laghi, NW Italy. *Journal of Geophysical Research*, 105, 13843-13858.
- Kenkmann, T. (2000) Processes controlling the shrinkage of porphyroclasts in gabbroic shear zones. *Journal of Structural Geology*, 22, 471-487.
- Klötzli, U.S., Sinigoi, S., Quick, J.E., Demarchi, G., Tassinari, C.C.G., Sato, K., and Günes, Z. (2014) Duration of igneous activity in the Sesia Magmatic System and implications for high-temperature metamorphism in the Ivrea–Verbano deep crust. *Lithos*, 206–207, 19–33.
- Kovaleva, E., Klötzli, U., Habler, G., and Libowitzky, E. (2014) Finite lattice distortion patterns in plastically deformed zircon grains. *Solid Earth*, 5, 1099-1122.
- Kresten, P., Fels, P., Berggren, G. (1975) Kimberlitic zircons — a possible aid in prospecting for kimberlites. *Mineralium Deposita*, 10, 47–56.
- Leroux, H., Reimold, W.U., Koeberl, C., Hornemann, U., and Doukhan, J.C. (1999) Experimental shock deformation in zircon: a transmission electron microscopic study. *Earth and Planetary Science Letters*, 169, 291–301.
- Lund, M.G. and Austrheim, H. (2003) High-pressure metamorphism and deep-crustal seismicity: evidence from contemporaneous formation of pseudotachylytes and eclogite facies coronas. *Tectonophysics*, 372, 59–83.

- MacDonald, J.M., Wheeler, J., Harley, S.L., Mariani, E., Goodenough, K.M., Crowley, Q., and Tatham, D. (2013) Lattice distortion in a zircon population and its effects on trace element mobility and U–Th–Pb isotope systematics: examples from the Lewisian Gneiss Complex, northwest Scotland. *Contributions to Mineralogy and Petrology*, 166, 21–41.
- Moser, D.E., Davis, W.J., Reddy, S.M., Flemming, R.L., and Hart, R.J. (2009) Zircon U–Pb strain chronometry reveals deep impact-triggered flow. *Earth and Planetary Science Letters*, 277, 73–79.
- Moser, D.E., Cupelli, C.L., Barker, I.R., Flowers, R.M., Bowman, J.R., Wooden, J., and Hart, J.R. (2011) New zircon shock phenomena and their use for dating and reconstruction of large impact structures revealed by electron nanobeam (EBSD, CL, EDS) and isotopic U–Pb and (U–Th)/He analysis of the Vredefort dome. *Canadian Journal of Earth Sciences*, 48, 117–139.
- Nemchin A., Timms N.E., Pidgeon R., Geisler T., Reddy S.M., and Meyer C. (2009) Timing of crystallization of the lunar magma ocean constrained by the oldest zircon. *Nature Geoscience*, 2, 133-136.
- Öpik, E.J., (1958) Meteor impact on solid surface. *Irish Astronomical Journal*, 5, 14-33.
- Passchier, C.W. (1982) Mylonitic deformation in the Saint-Barthélemy massif, French Pyrenees, with emphasis on the genetic relationship between ultramylonite and pseudotachylyte, 173 p. Ph.D. thesis, University of Amsterdam, Amsterdam.
- Pennacchioni, G. and Mancktelow, N.S. (2007) Nucleation and initial growth of a shear zone network within compositionally and structurally heterogeneous granitoids under amphibolite facies conditions. *Journal of Structural Geology*, 29, 1757-1780.
- Piazolo, S., Austrheim, H., and Whitehouse, M. (2012) Brittle-ductile microfabrics in naturally deformed zircon: Deformation mechanisms and consequences for U–Pb dating. *American Mineralogist*, 97, 1544–156.

- Pidgeon R., Nemchin A., and Kamo S.L. (2011) Comparison of structures in zircons from lunar and terrestrial impactites. *Canadian Journal of Earth Sciences*, 48, 107–116.
- Pittarello, L., Di Toro, G., Bizzarri, A., Pennacchioni, G., Hadizadeh, J., and Cocco, M. (2008) Energy partitioning during seismic slip in pseudotachylyte-bearing faults (Gole Larghe Fault, Adamello, Italy). *Earth and Planetary Science Letters*, 269, 131–139.
- Pittarello, L., Pennacchioni, G., and Di Toro, G. (2012) Amphibolite-facies pseudotachylytes in Premosello metagabbro and felsic mylonites (Ivrea Zone, Italy). *Tectonophysics*, 580, 43–57.
- Quick, J.E., Sinigoi, S., Peressini, G., Demarchi, G., Wooden, J.L., and Sbisà, A. (2009) Magmatic plumbing of a large Permian caldera exposed to a depth of 25 km. *Geology*, 37, 603-606.
- Ranalli, G. (1995) *Rheology of the Earth*, 2nd ed., 413 p. Chapman & Hall, London.
- Reddy, S.M. and Buchan, C. (2005) Constraining kinematic rotation axes in high-strain zones: a potential microstructural method? In: D. Gapais, J.P. Brun, P.R. Cobbold, Eds., *Deformation Mechanisms, Rheology and Tectonics: from Mineral to the Lithosphere*, 18, p. 1-10. Geological Society Special Publications, 243, London.
- Reddy, S.M., Timms, N.E., Trimby, P., Kinny, P.D., Buchan C., and Blake K. (2006) Crystal-plastic deformation of zircon: a defect in the assumption of chemical robustness. *Geology*, 34, 257-260.
- Reddy, S.M., Timms, N.E., Pantleon, W., and Trimby, P. (2007) Quantitative characterization of plastic deformation of zircon and geological implications. *Contributions to Mineralogy and Petrology*, 153, 625–645.
- Redler, C., Johnson, T.E., White R.W., and Kunz, B.E. (2012) Phase equilibrium constraints on a deep crustal metamorphic field gradient: metapelitic rocks from the Ivrea Zone (NW Italy). *Journal of Metamorphic Geology*, 30, 235–254.

- Rudnick, R.L. and Williams, I.S. (1987) Dating of lower crust by ion microprobe. *Earth and Planetary Science Letters* 85, 145–163.
- Rutter, E.H., Brodie K.H., James T., and Burlini L. (2007) Large-scale folding in the upper part of the Ivrea-Verbano zone, NW Italy. *Journal of Structural Geology*, 29, 1-17.
- Sibson, R.H. (1975) Generation of pseudotachylyte by ancient seismic faulting. *Geophysical Journal of the Royal Astronomical Society*, 43, 775–794.
- Sinigoï, S., Quick, J.E., Demarchi, G., and Klötzli, U. (2011) The role of crustal fertility in the generation of large silicic magmatic systems triggered by intrusion of mantle magma in the deep crust. *Contributions to Mineralogy and Petrology*, 162, 691-707.
- Spudich, P., Guatteri, M., Otsuki, K., Minagawa, J. (1998) Use of fault striations and dislocations models to infer tectonic shear stress during the 1995 Hyogo-ken (Kobe) earthquake. *Bulletin of the Seismological Society of America*, 88, 413–427.
- Techmer, K.S., Ahrendt, H., and Weber, K. (1992) The development of pseudotachylyte in the Ivrea-Verbano Zone of the Italian Alps. *Tectonophysics*, 204, 307–322.
- Timms, N.E. and Reddy, S.M. (2009) Response of cathodoluminescence to crystal-plastic deformation in zircon. *Chemical Geology*, 261, 11–23.
- Timms, N.E., Kinny, P., and Reddy, S.M. (2006) Enhanced diffusion of uranium and thorium linked to crystal plasticity in zircon. *Geochemical Transactions*, 7, 10.
- Timms, N.E., Kinny, P., Reddy, S.M., Evans K., Clark C., Healy D. (2011) Relationship among titanium, rare earth elements, U–Pb ages and deformation microstructures in zircon: Implications for Ti-in-zircon thermometry. *Chemical Geology* 280, 33–46.
- Timms, N.E., Reddy, S.M., Fitz Gerald, J.D., Green, L., Muhling, J.R. (2012a) Inclusion-localised crystal-plasticity, dynamic porosity, and fast-diffusion pathway generation in zircon, *Journal of Structural Geology*, 35, 78-89.

- Timms, N.E., Reddy, S.M., Healy, D., Nemchin, A.A., Grange, M.L., Pidgeon, R.T., and Hart, R. (2012b) Resolution of impact-related microstructures in lunar zircon: A shock-deformation mechanism map. *Meteoritics and Planetary Science*, 47, 120–141.
- Thomson, O.A., Cavosie, A. J., Moser, D.E., Barker, I., Radovan, H.A., and French, B.M. (2014) Preservation of detrital shocked minerals derived from the 1.85 Ga Sudbury impact structure in modern alluvium and Holocene glacial deposits. *Geological Society of America Bulletin*, 126, 720-737.
- Wheeler, J., Mariani, E., Piazzolo, S., Prior, D.J., Trimby, P., and Drury, M.R. (2009) The Weighted Burgers Vector: a new quantity for constraining dislocation densities and types using Electron Backscatter Diffraction on 2D sections through crystalline materials. *Journal of Microscopy*, 233, 482-494.
- White, S. (1973) Syntectonic recrystallization and texture development in quartz. *Nature*, 244, 276-278.
- White, S. (1976) The effects of strain and microstructure fabrics and deformation mechanisms in quartzite. *Philosophical Transactions of the Royal Society of London*, 283, 69-86.
- Yang, J.-J., Fan, Z.-F., Yu, C., Yan, R. (2014a) Coseismic formation of eclogite facies cataclasite dykes at Yangkou in Chinese Su-Lu UHP metamorphic belt. *Journal of Metamorphic Geology*, 32, 937-960.
- Yang, J.-J., Huang, M.-X., Wu, Q.-Y., Zhang, H.-R. (2014b). Coesite-bearing eclogite breccia: implications for coseismic ultrahigh-pressure metamorphism and the rate of the process. *Contributions to Mineralogy and Petrology*. 167, 1013-1030.

6.0. NanoSIMS study of planar deformation bands in zircon

Elizaveta Kovaleva¹, Urs Klötzli¹, Gerlinde Habler¹

¹Department of Lithospheric Research, Faculty of Earth Sciences, Geography and Astronomy, University of Vienna, Althanstrasse 14, A-1090 Vienna, Austria

Article is in preparation for submission

Abstract

Zircon is one of the most important minerals for geochronology where it is widely used for rock and mineral dating. However, various lattice defects cause trace elements re-distribution and disturbance of isotopic systems in zircon, which eventually may influence measured isotopic ages. This study investigates for the first time how do planar deformation bands in zircon from paleo-seismic zones influence trace elements and isotopes re-equilibration.

Samples of felsic mylonites with pseudotachylytes from Ivrea-Verbano zone were investigated for the presence of deformed zircons by electron backscatter diffraction (EBSD) and forward scatter detector (FSD) in situ and in embedded separates. CL images were made in order to see growth features and internal structure. For grains that reveal planar deformation bands (PDB) and planar fractures (PFs), nano-scale secondary ion mass spectrometry (NanoSIMS) mapping and profiling was applied.

NanoSIMS mapping show no influence of planar deformation bands on trace elements distribution. Re-distribution of lead isotopes was documented only for crystal-plastic deformation structures with misorientation not less than 3°. However, NanoSIMS high-resolution profiling demonstrated that Y and Yb are depleted in lattice portions with PDBs. Relative $^{207}\text{Pb}/^{206}\text{Pb}$ isotopic ages demonstrated rejuvenation in deformed domains. This study demonstrates that planar microstructures in zircon from terrestrial rocks can potentially yield Pb-loss and thus allow determining the timing of seismic event.

6.1. Introduction

6.1.1. Planar microstructures in zircon

Various planar microstructures are well-known in shock-deformed zircon and include planar deformation features (PDFs), planar fractures (PFs), micro-cleavage, shock twins and phase transition along certain planes, and planar deformation bands (PDBs).

Planar deformation features in zircon are shock-induced planar lamellae that crosscut the zircon crystal lattice along specific crystallographic planes and are filled with amorphous material or so-called “diaplectic glass” (Erickson et al., 2013a); or represent lattice domains with a high defect density (Grange et al., 2013). Planar fractures are parallel and closely-spaced open structures resembling cleavage and are well-known from terrestrial and lunar impactites (e.g. Bohor et al., 1993; Kamo et al., 1996; Kalleson et al., 2009; Cavosie et al., 2010; Moser et al., 2011; Erickson et al., 2013a, 2013b; Thomson et al., 2014). Shock twins or micro-twins are the characteristic feature of shock-deformed zircon grains (Leroux et al., 1999; Moser et al., 2011; Timms et al., 2012; Erickson et al., 2013a, 2013b; Thomson et al., 2014), as well as reidite, a high-pressure shock-induced polymorph of zircon with scheelite structure occurring along {100} planes (Wittmann et al., 2006). The formation of shock twins and reidite indicate shock pressure above 40 GPa (Leroux et al., 1999). Shocked lunar zircon with planar deformation bands has been described in detail and their misorientation of ca. 8-10° was documented (Timms et al., 2012).

However, shock-induced structures are not the only planar structures known in zircon. Some parallel parting has been observed in zircons from upper crustal xenoliths (Rudnick and Williams, 1987; Chen et al., 1994) and interpreted to form due to rapid decompression (Rudnick and Williams, 1987). Kresten et al. (1975) report on perfect partings or cleavages extending in several directions in kimberlitic zircon. Planar microstructures were reported by Austrheim and Corfu (2009) in zircon from pseudotachylytes from the Svarthumlevatnet metagabbro, South-Central Norway. Kovaleva et al. (in press) reported planar deformation bands (PDBs) coexisting with PFs in terrestrial zircons from paleo-seismic zones. These PDBs are crystallographically controlled lattice volumes revealing misorientation from the host grain, which varies from 0,4° to 2,7°. PDBs are usually parallel to {100} crystallographic planes, have width from 0,3 to 1 µm and average spacing of 5 µm. It was suggested that PDBs represent the result of crystal-plastic deformation and form due to high differential stress, temperature and strain rate generated in seismically active environment (Kovaleva et al., in press).

6.1.2. Trace element and isotopes distribution caused by planar microstructures in zircon

Re-distribution of trace elements and disturbance of isotopic systems in zircon due to crystal-plastic deformation is well-documented (Reddy et al., 2006, 2009; Timms et al., 2006, 2011; Timms and Reddy 2009; Reddy and Timms, 2010; Moser et al., 2009, 2011; Flowers et al., 2010; Piazzolo et al., 2012; MacDonald et al., 2013; Kovaleva et al., in preparation). These authors have described deformation-related Pb loss that dramatically affects the measured isotopic ages of zircon and explained by induced out-diffusion of radiogenic isotopes via dislocations and other lattice defects. For example, Moser et al. (2009) have reported strain-induced age disturbance and U-Pb age 100% resetting due to Pb loss in zircon that underwent shock-induced crystal-plastic deformation.

Pb loss in zircon is also associated with shock-induced planar microstructures. “Cold shock” microstructures in zircon attributed to grains that were affected by shock pressures but were not heated. The effect of such lattice distortion on isotopic system is negligible (Moser et al., 2011). However, intensive Pb loss due to “hot shock” deformation has been documented; thermally-driven intensive out-diffusion of Pb along planar and curvilinear microstructures was observed (Moser et al., 2011). Thus, deformation microstructures alone cannot cause significant age disturbance and some elevated temperatures are needed. Grange et al. (2013) report about deformation microstructures in zircon such as planar deformation features, crystal-plastic deformation and microfractures which provide channels for Pb diffusion. As a result, partial resetting of the U-Pb isotopic systems occurs. Shocked lunar zircon with PDBs (Timms et al., 2012) revealed the strongest U-Pb age rejuvenation that is attributed to the PDB lamella with highest misorientation (Nemchin et al., 2009). Decrease of $^{207}\text{Pb}/^{206}\text{Pb}$ ages was found to be correlating with increase of lattice misorientation, and it was considered to be a result of impact-related plastic deformation (Nemchin et al., 2009). Such precise dating could only be done with high-sensitive and high-resolution techniques as, for example, SHRIMP (Nemchin et al., 2009; Grange et al., 2013).

However, there were not many studies on trace elements and isotopes re-distribution associated with planar microstructures in zircon that are not shock-induced. Kresten et al. (1975) describe low abundances of U, Th, Y, P and REE in zircon grains with lattice distortion such as parallel partings. Austrheim and Corfu (2009) have not documented any U-Pb age disturbances connected with formation of seismically-induced planar microstructures in zircon.

In our study we are investigating the behavior of trace elements and lead isotopes in zircon grains with PDBs. These grains came from paleo-seismic zones and were found in mylonites close to pseudotachylytes. PDBs in this sample material however, most probably, are not the shock-induced features (Kovaleva et al., in press).

6.2. Sampling locality and samples

Samples were collected from the Ivrea-Verbano zone (IVZ) at Premosello in the Val d'Ossola (Northern Italy). The IVZ forms a NE-SW trending, steeply dipping sequence of meta-pelitic to meta-igneous basic rocks in the SE, ultrabasic mantle tectonites and a large underplated igneous complex in the NW. Peak metamorphic grade increases progressively from amphibolite facies in the SE to granulite facies in the NW. The IVZ represents a section through the lower continental crust that experienced regional metamorphism during the uppermost Palaeozoic (Rutter et al., 2007; Quick et al., 2009), subsequently tectonically uplifted to the present position.

Pseudotachylytes are found in mylonitic metagabbros and metapelites deformed under amphibolite to granulite facies metamorphism in the northern part of IVZ (Techmer et al., 1992; Pittarello et al., 2012). Pseudotachylytes are often overprinted by ultramylonites and interpreted to have formed coevally (Pittarello et al., 2012). The temperature-pressure estimates of pseudotachylyte formation yielded 550-650° C and 0,4-0,6 GPa (Pittarello et al., 2012 and references therein).

Samples were taken from two outcrops at Premosello (N46°00'15.04"/E08°19'44.11" and N46°00'23.65"/E08°19'41.66"); each outcrop reveals tectonically faulted, mylonitized and foliated felsic metasediments, containing ultramylonites and pseudotachylytes. Both pseudotachylytes and ultramylonites mainly represent an ultra-fine-grained matrix composed of plagioclase, quartz, biotite and ilmenite, with minor amounts of garnet. Zircon grains with PDBs are usually located in ultramylonites at the contact with pseudotachylytes. For more detail petrographic description see Kovaleva et al. (in press).

6.3. Analytical methods and data representation

6.3.1. Sample preparation and scanning electron microscopy (SEM)

Zircon grains were studied in polished thin sections of rock chips and in grain separates embedded in epoxy resin. For the latter zircon grains were extracted from the host rock by the standard procedure involving rock crushing, sieving to the 300 µm size, density separation on a Wilfley table, in heavy liquids and with Frantz magnetic separator. All samples were mechanically polished with 0.25 µm diamond paste and subsequently chemically polished with alkaline colloidal

silica solution on an active rotary head polishing machine for 4 hours. Samples were cleaned in ethanol and distilled water before carbon coating that was applied to establish electrical conductivity.

Zircons were identified and characterized by cathodoluminescence (CL) imaging using a FEI Inspect S scanning electron microscope (SEM) equipped with a Gatan MonoCL system (Center of Earth Sciences, University of Vienna, Austria) or using a Jeol JSM 6490LV SEM coupled with Oxford Inca Energy EDS (Geologische Bundesanstalt of Austria (GBA), Vienna, Austria). CL-imaging conditions were 10 kV accelerating voltage, CL-image resolution: 1500*1500 to 2500*2500 pixels using a dwell time of 80.0-150.0 ms and probe current/spot size 4.5-5.0.

6.3.2. Electron backscatter diffraction (EBSD)

Zircon grains were examined for potential crystal-plastic deformation structures using orientation contrast images that were taken using a forward scatter detector (FSD) mounted on the EBSD-tube of an FEI Quanta 3D FEG instrument (Center of Earth Sciences, University of Vienna, Austria), which is equipped with a Schottky field emission electron source. For more details on analytical settings see Kovaleva et al. (2014) and Kovaleva et al. (in press).

The raw indexing for the EBSD maps for zircon grains is > 99,9%. The EBSD data are represented in the sample reference frame and plotted using the EDAX OIM v6.2.1 Analysis software.

6.3.3. Nano-scale secondary ion mass spectrometry (NanoSIMS)

Isotope-selective high-sensitive secondary ion mass spectrometry is able to detect low-content isotopes of trace elements at nm scales in zircon (Boehnke et al., 2013; Hofmann et al., 2009, 2014; Storm et al., 2014).

Samples were coated with 30 nm Au and analyzed with the Cameca NanoSIMS 50L at Caltech Microanalyses Center, Pasadena, USA. The analytical conditions were similar to those used in Hofmann et al. (2009, 2014). An O⁻ primary beam of -8 kV was used to sputter the samples and secondary ions of +8 kV were measured with electron multipliers under high mass resolution conditions. Mass spectrum scans were examined to make sure that any significant interference was well resolved from the masses of interest. For individual spot analyses and line profiles, samples were pre-sputtered for 210-360 sec with a rastering primary beam of ~80-90 pA across 1x1 μm or

2x2 μm areas. Data were collected in the “Combined Analysis” mode of the NanoSIMS for the following masses: ^{31}P , ^{49}Ti , ^{89}Y , ^{90}Zr , ^{140}Ce , ^{174}Yb , ^{180}Hf , ^{206}Pb , ^{207}Pb and ^{208}Pb . Ion images of eight masses (^{31}P , ^{89}Y , ^{90}Zr , ^{174}Yb , ^{180}Hf , ^{206}Pb , ^{207}Pb and ^{208}Pb) were also collected in the “Combined Analysis” mode over areas of 10x10 μm to 20x20 μm . Ion image processing was done with the software Look@NanoSIMS (Polerecky et al., 2012). Ion images and ion beam point analyses showed that ^{90}Zr has fairly homogeneous distribution in zircon and thus was used as a reference mass.

6.4. Results

6.4.1. NanoSIMS mapping

In its central zircon 26 part reveals the evidence of crystal-plastic deformation, including formation of planar deformation bands (Fig. 6.1a, c) that are not indicated by CL signal (Fig. 6.1b). PDBs are discontinuous and locally reach maximum misorientation of 3° . Isotopic maps for ^{89}Y , ^{174}Yb and ^{31}P document depletion in upper right fracture (Fig. 6.1d). Three lead isotopes ^{206}Pb , ^{207}Pb and ^{208}Pb reveal enrichment in fracture accompanied by aging of relative $^{207}\text{Pb}/^{206}\text{Pb}$ model ages (Fig. 6.1e). Lead isotopes are re-distributed along the planar deformation bands: depleted within the PDBs and enriched in between, forming patchy distribution clusters (Fig. 6.1d). Model ages demonstrate unsystematic disturbance as well, mostly rejuvenation (Fig. 6.1e).

FSE image of the grain 43 reveals two sets of PDBs that reach maximum $\sim 1.5^\circ$ of misorientation in intersection sites (Fig. 6.2a, c). PDBs are not visible in CL image (Fig. 6.2b). Isotopic maps of ^{89}Y , ^{174}Yb , ^{31}P and ^{206}Pb demonstrate enrichment in CL-dark domain (Fig. 6.2d); ^{180}Hf reveals no distinguishable features; and counts for lead isotopes ^{206}Pb , ^{207}Pb and ^{208}Pb and for their sum are elevated in one spot between CL-dark core and CL-bright rim. No features dimensionally connected with PDBs were documented with NanoSIMS maps (Fig. 6.2d).

Grain 45 reveals one set of PDBs stretching in one direction (Fig. 6.3a, c) and not visible in CL image (Fig. 6.3b). NanoSIMS map of ^{89}Y isotope show enrichment coinciding with fracture at the left and enrichment corresponding to CL-dark feature (highlighted by arrow) that is subparallel to PDBs. ^{180}Hf is slightly depleted in fracture at the left. ^{174}Yb , ^{31}P , ^{206}Pb and ^{207}Pb isotopes do not reveal any features within the mapped area of zircon. ^{208}Pb isotope is slightly enriched in fracture (Fig. 6.3d).

Grain 91 reveals one set of PDBs that are occasionally overlapped by planar fractures (PFs). CL image shows concentric growth zoning and CL-bright healed fractures at high angle to PDBs and PFs.

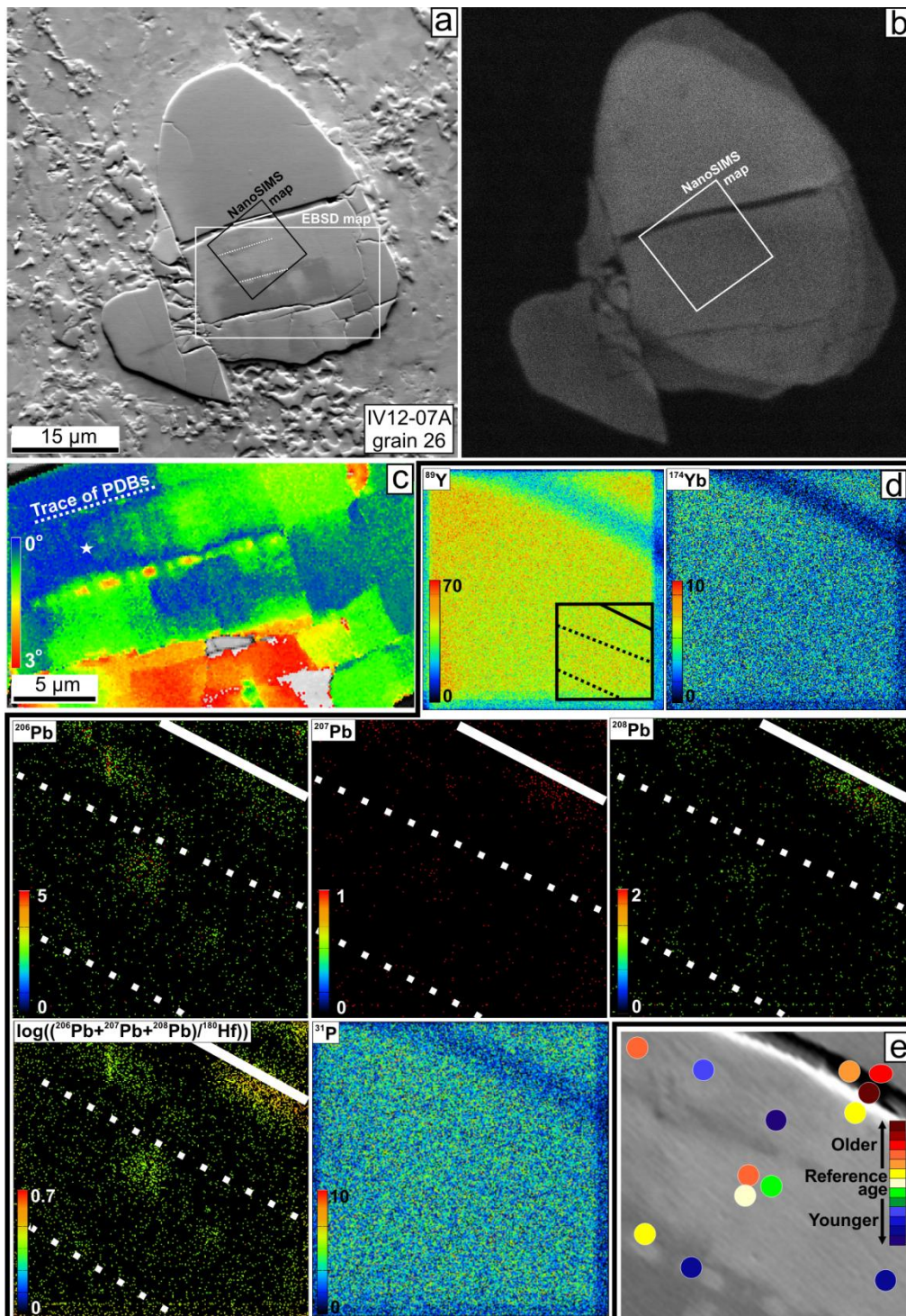


Figure 6.1. Grain 26: (a) forward scatter electron (FSE) image, (b) cathodoluminescence (CL) image, (c) EBSD cumulative misorientation map, location marked in a. (d) NanoSIMS isotopic maps, location marked in a and b. Intensity in counts. (e) $^{207}\text{Pb}/^{206}\text{Pb}$ relative ages derived from the NanoSIMS maps, color-coded points are superimposed on top of FSE image. Dotted lines indicate the positions of PDBs, solid line – position of fracture in isotopic maps.

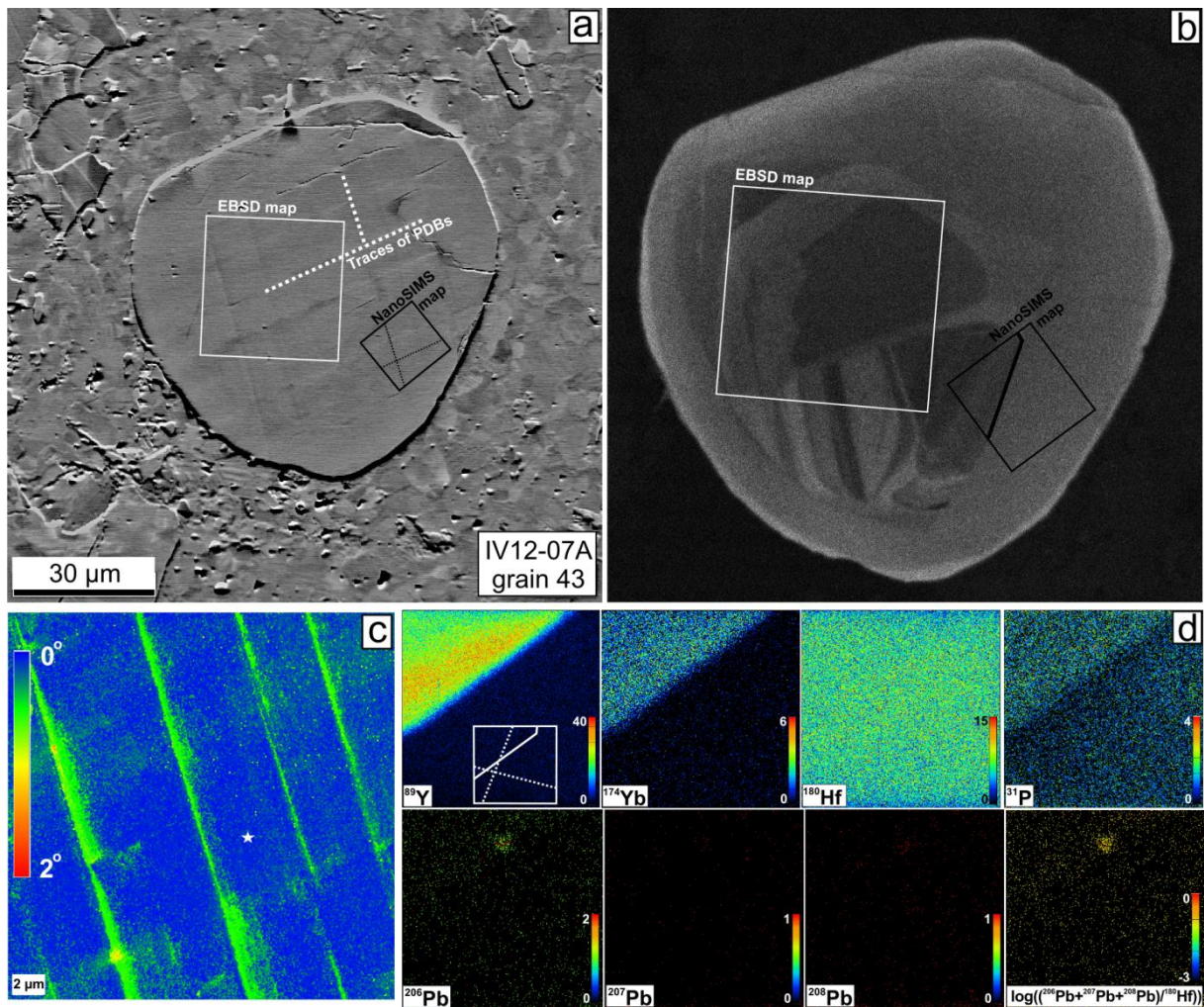


Figure 6.2. Grain 43: **(a)** forward scatter electron (FSE) image, **(b)** cathodoluminescence (CL) image, **(c)** EBSD cumulative misorientation map, location marked in a. **(d)** NanoSIMS isotopic maps, location marked in a and b. Intensity in counts. Dotted lines indicate directions of PDBs, solid line indicates position of the boundary between CL-bright core and CL-dark rim.

NanoSIMS maps of ^{31}P and ^{89}Y isotopes reveal features of CL zoning and healed fracture, while ^{174}Yb and ^{206}Pb show only CL zoning. No features that spatially coincide with PDBs or PFs are distinguishable in NanoSIMS maps (Fig. 6.4).

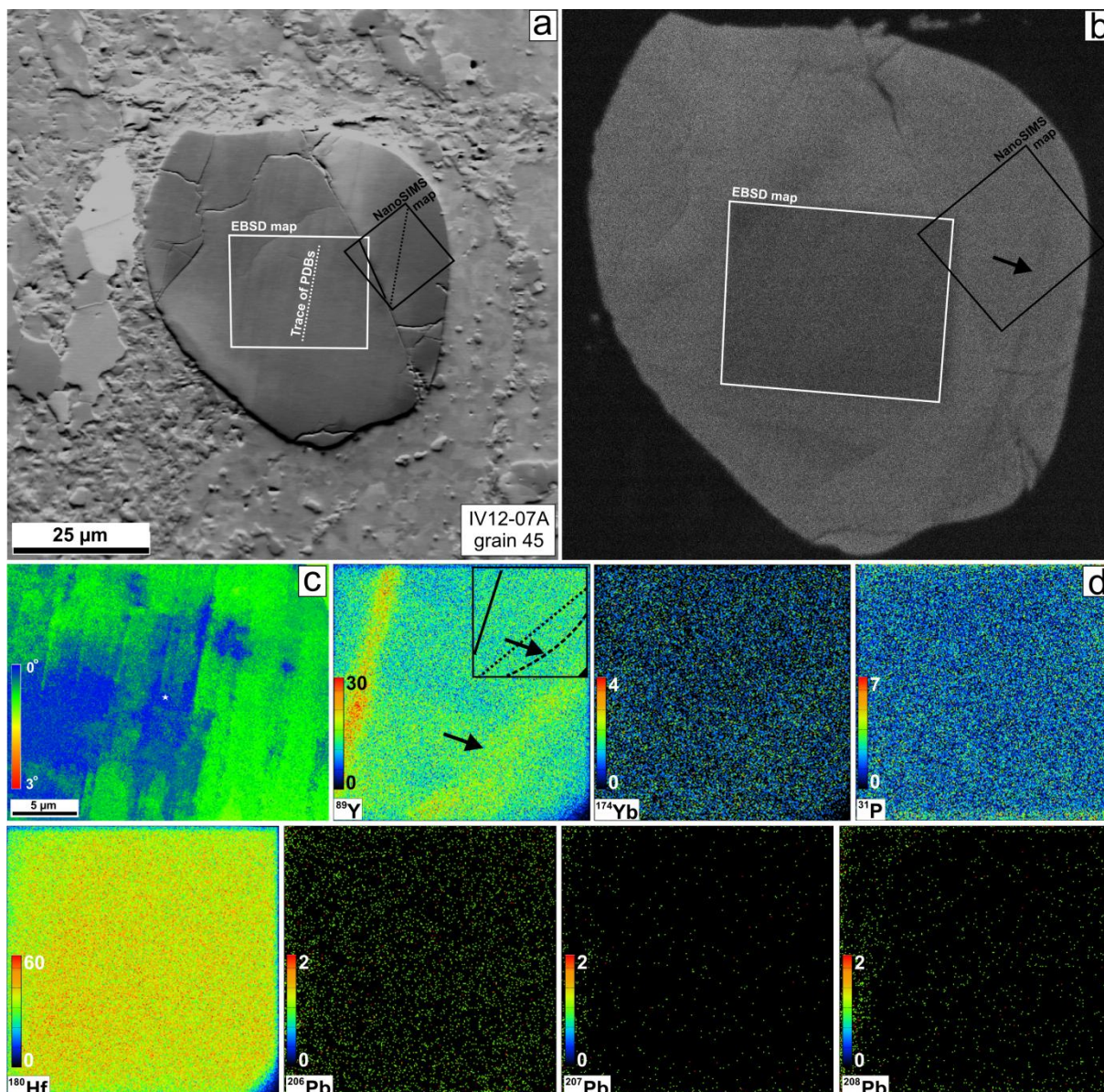


Figure 6.3. Grain 45: **(a)** forward scatter electron (FSE) image, **(b)** cathodoluminescence (CL) image, **(c)** EBSD cumulative misorientation map, location marked in a. **(d)** NanoSIMS isotopic maps, location marked in a and b. Intensity in counts. Dotted lines indicate directions of PDBs in this zircon, solid line indicates position of fracture, and dashed line – position of CL-dark band. Arrows indicate position of CL-dark band.

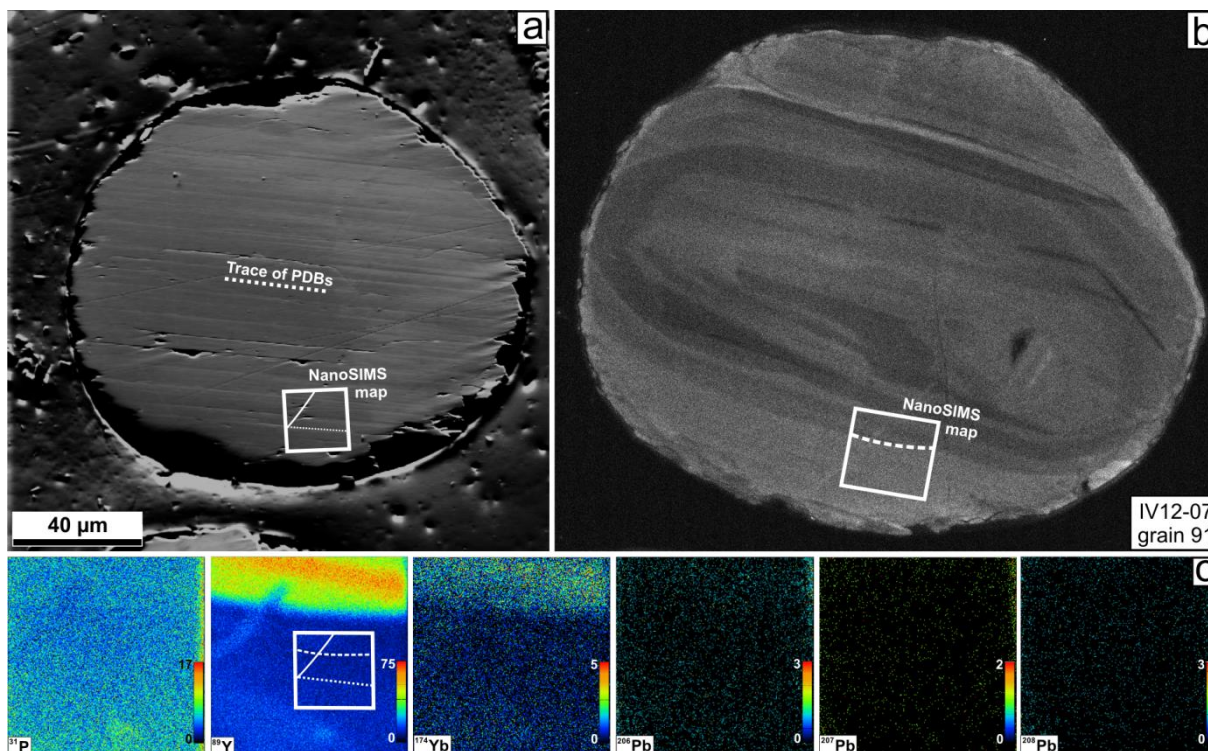


Figure 6.4. Grain 91: **(a)** forward scatter electron (FSE) image, **(b)** cathodoluminescence (CL) image, **(c)** NanoSIMS isotopic maps, location marked in (a) and (b). Intensity in counts. Dotted lines indicate directions of PDBs and PFs, solid line indicates position of healed fracture, and dashed line –boundary between CL-bright core and CL-dark rim.

6.4.2. NanoSIMS profiling

Grain 80 is embedded in epoxy resin and reveals a set of PDBs that are not visible in CL image (Fig. 6.5a). NanoSIMS profile is taken across two of PDBs presented in the inset in EBSD map (Fig. 6.5a). Profile was taken in almost homogeneous CL-bright rim. PDBs are measured by points 3 and 6-7 in profile. $^{89}\text{Y}/^{90}\text{Zr}$ and $^{174}\text{Yb}/^{90}\text{Zr}$ ratios are decreased in PDBs sites. $^{206}\text{Pb}/^{90}\text{Zr}$, $^{207}\text{Pb}/^{90}\text{Zr}$ and $^{208}\text{Pb}/^{90}\text{Zr}$ are distorted and do not show correlation with locations of PDBs. $^{31}\text{P}/^{90}\text{Zr}$ and $^{140}\text{Ce}/^{90}\text{Zr}$ ratios do not show correlation with PDBs, whereas $^{49}\text{Ti}/^{90}\text{Zr}$ ratio is relatively elevated in one PDB and decreased in the other one. Relative $^{207}\text{Pb}/^{206}\text{Pb}$ model ages show rejuvenation in the area of one PDB and aging in the other PDB with respect to the reference age.

Grain 03b (Fig. 6.5b) is broken in 2 parts by a large fracture, one of those parts has developed two sets of PDBs and the other does not contain these structures. NanoSIMS points were made in undeformed and deformed parts in CL-bright homogeneous rim. $^{89}\text{Y}/^{90}\text{Zr}$ and $^{174}\text{Yb}/^{90}\text{Zr}$ ratios as well as $^{31}\text{P}/^{90}\text{Zr}$ and $^{140}\text{Ce}/^{90}\text{Zr}$ are elevated in deformed part. $^{206}\text{Pb}/^{90}\text{Zr}$, $^{207}\text{Pb}/^{90}\text{Zr}$, $^{208}\text{Pb}/^{90}\text{Zr}$ and $^{49}\text{Ti}/^{90}\text{Zr}$ do not correlate with deformation and are elevated in the point 3 that is close to the fracture.

Relative $^{207}\text{Pb}/^{206}\text{Pb}$ model ages are strongly rejuvenated in deformed part with respect to undeformed; point 3 shows aging, being set on the fracture.

Grain 17 (Fig. 6.5c) is also broken in two parts where one of them is undeformed and the other deformed with formation of PDBs. As for the grain 03a, points were made in undeformed and deformed parts in CL-bright homogeneous rim. $^{89}\text{Y}/^{90}\text{Zr}$ and $^{174}\text{Yb}/^{90}\text{Zr}$ ratios are decreased in deformed part; $^{206}\text{Pb}/^{90}\text{Zr}$, $^{207}\text{Pb}/^{90}\text{Zr}$, $^{208}\text{Pb}/^{90}\text{Zr}$ and $^{31}\text{P}/^{90}\text{Zr}$ do not show any correlation; $^{49}\text{Ti}/^{90}\text{Zr}$ is slightly increased and $^{140}\text{Ce}/^{90}\text{Zr}$ is slightly decreased in deformed part. Relative $^{207}\text{Pb}/^{206}\text{Pb}$ model ages are generally rejuvenated in deformed part with respect to undeformed.

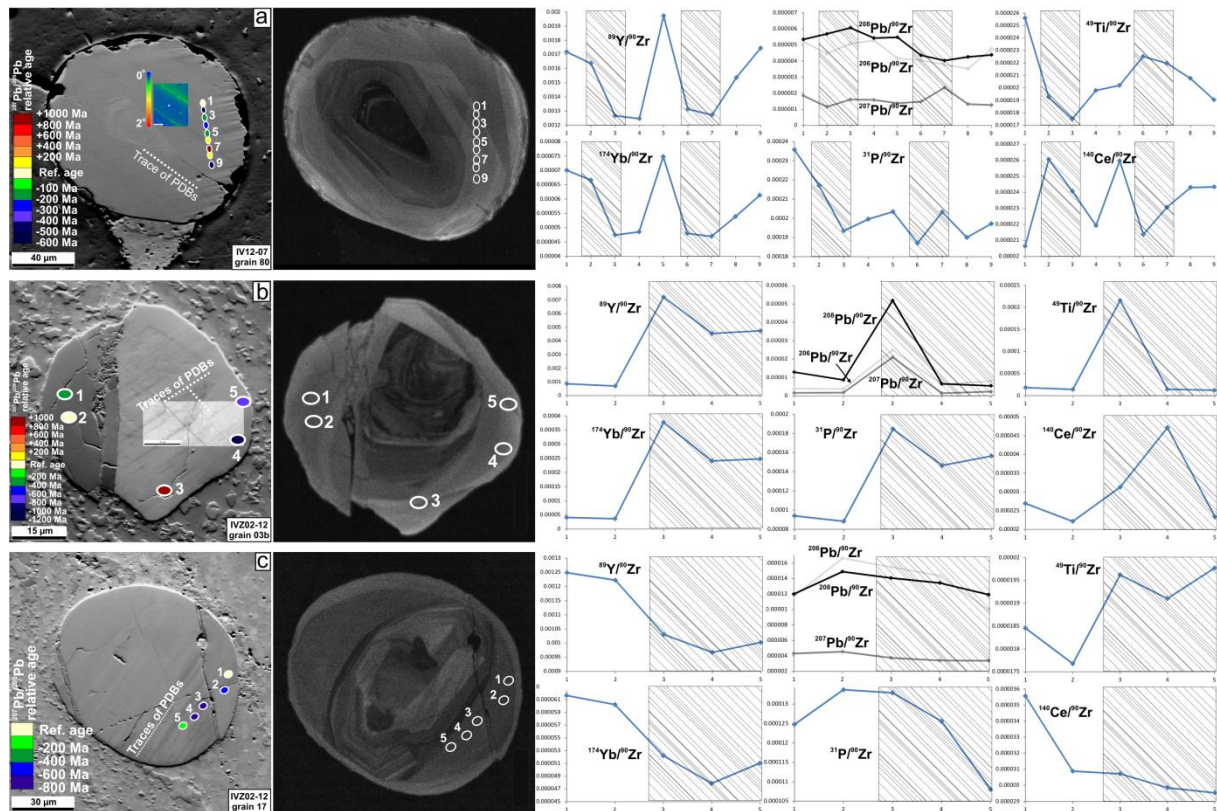


Figure 6.5. Grains from the sample IVZ02-12 and IV12-07. From left to right: FSE images with locations of point analyses that are color-coded according to the $^{207}\text{Pb}/^{206}\text{Pb}$ relative ages; CL images with locations of point analyses; isotope profiles made with NanoSIMS. In (a) and (b) EBSD maps are shown in inset. Highlighted boxes indicate zones with PDBs.

6.5. Discussion

The summary for behavior of each trace element in grains with PDBs is presented in Table 6.1.

Grain	Y	Yb	Pb isotopes	²⁰⁷ Pb/ ²⁰⁶ Pb age	Ti	Hf	P	Ce
26	No correlation with PDBs	No correlation with PDBs	Patchy distribution correlated with PDBs	Distorted ages, mostly rejuvenated	-	No correlation with PDBs	No correlation with PDBs	-
43	No correlation with PDBs	No correlation with PDBs	No correlation with PDBs	-	-	No correlation with PDBs	No correlation with PDBs	-
45	Enriched in CL-dark band	No correlation with PDBs	No correlation with PDBs	-	-	No correlation with PDBs	No correlation	-
91	No correlation with PDBs	No correlation with PDBs	No correlation with PDBs	-	-	No correlation with PDBs	-	-
80	Depleted in PDBs	Depleted in PDBs	Distorted distribution	One PDB is rejuvenated and the other one in aged	Depleted in one PDB and enriched in the other	No correlation	No correlation	No correlation
03b	Enriched in deformed part	Enriched in deformed part	No correlation	Strongly rejuvenated in deformed part	No correlation	Slightly enriched in deformed part	Enriched in deformed part	Partial enrichment in deformed part
17	Depleted in deformed part	Depleted in deformed part	Distorted distribution	Rejuvenated in deformed part	Enriched in deformed part	Partially depleted in deformed part	No correlation	Slightly depleted in deformed part

Table 6.1. Behavior of trace elements in zircon with PDBs (lattice distortion type IV).

6.5.1. Mapping and profiling

As it comes from the isotopes mapping, trace elements distribution is not affected by planar deformation bands. Clearly observed re-distribution is only observed for lead isotopes in zircon 26 (Fig. 6.1d), where they form enriched clusters ranging from 1 to 1,5 μm in diameter. Similar lead isotopes clusters, but having a diameter about 20 nm, were documented in zircon by atom-probe tomography (Valley et al., 2014). Micrometer-scale clusters observed in zircon 26 could be a result of re-distribution and accumulation of nanometer-scale clusters after crystal-plastic deformation. Misorientation of PDBs that yielded lead isotopes re-distribution in zircon 26, reaches maximum 3° with respect to a reference point (Fig. 6.1c); whereas smaller misorientations, observed in the other grains (maximum $1-1,5^\circ$, Figs. 6.2c, 6.3c), did not cause any disturbances in distribution of isotopes of trace elements. CL-dark feature in grain 45 (Fig. 6.3b, highlighted by arrow) represents the domain enriched in ^{89}Y and subparallel to PDBs. However, it is bending that is unusual for PDBs in grains that are not plastically-deformed (Kovaleva et al., in press). Moreover, it is not causing lead isotopes re-distribution and thus likely represents a growth feature.

Although we didn't see any significant re-distribution of trace elements in isotopic maps, some clear re-distribution is documented in NanoSIMS profiles, even for PDBs with low misorientation (Fig. 6.5a). It is apparently conditioned by:

- a. Focused beam is stronger and measuring is more precise than rastering over the large area;
- b. Re-distribution of trace elements facilitated by extensive PDBs affects larger areas of lattice than can be documented by NanoSIMS mapping. Maps are able to document trace elements distribution only locally.

As it was detected by profiling, the most sensitive elements to plastic deformation patterns type IV are Y and Yb. Mostly they show depletion spatially coinciding with PDBs (Fig. 6.5a, c), but in zircon 03b Y and Yb are increased in deformed domain (Fig. 6.5b). That possibly reflects outcome of these isotopes from distorted zircon interiors towards the rims, as point analyses were set in the outer rim of this grain. PDBs are extensive features that are often crosscutting through the whole grain, thus facilitating trace elements pipe diffusion at the grain scale.

Lead isotopes are strongly affected by deformation microstructures and their distribution is distorted. Other elements (Ti, Hf, P, Ce) show no correlation or no consistency in distribution in deformed domains (Table 6.1). There is no opportunity to conclude anything about their behavior, based on insignificant dataset.

6.5.2. $^{207}\text{Pb}/^{206}\text{Pb}$ relative ages

Relative $^{207}\text{Pb}/^{206}\text{Pb}$ model ages are clearly distorted in domains, containing PDBs, and mostly rejuvenated. It is particularly convenient to compare model ages in parts of zircons that were broken apart before formation of PDBs (grains 03a, 17; Fig. 6.5b-c). Due to specific property of PDBs not to penetrate through low angle boundaries and fractures (Kovaleva et al., in press), fragments of zircon grains remain unaffected by PDBs. These fragments show significantly older ages that is the evidence of undistorted isotopic systems, in contrast with deformed parts that are younger. Distortion of isotopic systems may have happened due to radiogenic Pb-loss and due to gain of common lead from matrix. Lead was diffusing out and in zircon lattice through PDBs using them as fast diffusion pathways, resulting in younger (grains 26, 80, 03b, 17) and older (grains 26 and 80) local isotopic ages correspondingly.

Such mechanism potentially has a very important implication for geochronology. When the isotopic ages of deformed zircons are rejuvenated, it becomes possible to date the timing of seismic event that resulted in PDBs formation.

6.6. Conclusions

Trace elements and isotopic systems study of zircon with PDBs resulted in new observations and allowed us to conclude the following:

1. In case of PDBs presence NanoSIMS profiling is more efficient than NanoSIMS mapping, because trace elements re-distribution is fairly extensive.
2. Mapping documents distortion in trace elements when misorientation is at least as high as $2-3^\circ$, point analyses document distortions connected with smaller misorientations of $0,5-1^\circ$.
3. Y and Yb are depleted in PDBs.
4. These trace elements can travel extensively within the grain and moving out of the grain's interiors via PDBs.
5. Other analyzed trace elements – Ti, Hf, P, Ce – are not so sensitive to PDBs and do not show consistency in behavior.
6. Relative isotopic ages are distorted and mostly rejuvenated in domains that contain PDBs.

Acknowledgments

This study was funded by the University of Vienna (doctoral school “DOGMA”, project IK 052) and the Austrian Science Foundation Fund (FWF): I471-N19, which is part of the DFG-FWF funded international research group FOR741-DACH.

The authors are grateful to Christian Auer, Claudia Beybel, Franz Biedermann, John Eiler, Yunbin Guan, Sigrid Hrabe, Matthew Huber, Arno Schintlmeister and all colleagues of the FOR741 research group for fruitful discussions and the Geologische Bundesanstalt (GBA) of Austria for access to the SEM; SIMS lab in Caltech, Pasadena, USA, for access to the NanoSIMS.

References

- Austrheim, H. and Corfu, F., 2009. Formation of planar deformation features (PDFs) in zircon during coseismic faulting and an evaluation of potential effects on U–Pb systematics. *Chemical Geology* 261, 25–31.
- Bohor, B.F., Betterton, W.J., Krogh, T.E., 1993. Impact-shocked zircons: discovery of shock-induced textures reflecting increasing degrees of shock metamorphism. *Earth and Planetary Science Letters*, 119, 419-424.
- Boehnke, P., Watson, E. B., Trail, D., Harrison, T. M., Schmitt, A. K., 2013. Zircon saturation re-revisited. *Chemical Geology*, 351, 324–334.
- Cavosie, A.J., Quintero, R.R., Henri A. Radovan, H.A., Desmond E. Moser, D.E., 2010. A record of ancient cataclysm in modern sand: Shock microstructures in detrital minerals from the Vaal River, Vredefort Dome, South Africa. *Geological Society of America Bulletin*, 122, 1968-1980.
- Chen, Y.D., O'Reilly, S.Y., Kinny, P.D., Griffin, W.L., 1994. Dating lower crust and upper mantle events: an ion microprobe study of xenoliths from kimberlitic pipes, South Australia. *Lithos*, 32, 77–94.
- Erickson, T.M., Cavosie, A. J., Moser, D.E., Barker, I.R., and Radovan, H.A., 2013a. Correlating planar microstructures in shocked zircon from the Vredefort Dome at multiple scales: Crystallographic modeling, external & internal imaging, and EBSD structural analysis. *American Mineralogist*, 98, 53-65.
- Erickson, T.M., Cavosie, A. J., Moser, D.E., Barker, I.R., and Radovan, H.A., Wooden, J., 2013b. Identification and provenance determination of distally transported, Vredefort-derived shocked minerals in the Vaal River, South Africa using SEM and SHRIMP-RG techniques. *Geochimica et Cosmochimica Acta*, 107, 170-188.
- Flowers, R.M., Schmitt, A.K., Grove, M., 2010. Decoupling of U–Pb dates from chemical and crystallographic domains in granulite facies zircon. *Chemical Geology*, 270, 20–30.
- Grange, M.L., Pidgeon, R.T., Nemchin, A.A., Timms, N.E., Meyer, C., 2013. Interpreting U–Pb data from primary and secondary features in lunar zircon. *Geochimica et Cosmochimica Acta*, 101, 112–132.

- Hofmann, A. E., Valley, J. W., Watson, E. B., Cavosie, A. J., Eiler, J. M., 2009. Sub-micron scale distributions of trace elements in zircon. *Contributions to Mineralogy and Petrology*, 158, 317–335.
- Hofmann, A. E., Backer, B.M., Eiler, J. M., 2014. Sub-micron-scale trace-element distributions in natural zircons of known provenance: implications for Ti-in-zircon thermometry. *Contributions to Mineralogy and Petrology*, 168, 1057.
- Kallesen, E., Corfu, F., Dypvik, H., 2009. U–Pb systematics of zircon and titanite from the Gardnos impact structure, Norway: Evidence for impact at 546 Ma? *Geochimica et Cosmochimica Acta*, 73, 3077–3092.
- Kamo, S. L., Reimold, W. U., Krogh, T. E., Colliston, W. P., 1996. A 2.023 Ga age for the Vredefort impact event and a first report of shock metamorphosed zircons in pseudotachylitic breccias and granophyre. *Earth and Planetary Science Letters*, 144, 369–387.
- Kovaleva, E., Klötzli, U., Habler, G., Libowitzky, E., 2014. Finite lattice distortion patterns in plastically deformed zircon grains. *Solid Earth*, 5, 1099–1122.
- Kovaleva, E., Klötzli, U., Habler, G., Wheeler, J., in press. Planar microstructures in zircon from paleo-seismic zones. *American Mineralogist*.
- Kovaleva, E., Klötzli, U., Habler, G., Guan, Y., Rhede, D., in preparation. The effect of crystal-plastic deformation on isotopes and trace element distribution in zircon
- Kresten, P., Fels, P., Berggren, G., 1975. Kimberlitic zircons – a possible aid in prospecting for kimberlites. *Mineralium Deposita*, 10, 47–56.
- Leroux, H., Reimold, W.U., Koeberl, C., Hornemann, U., Doukhan, J.C., 1999. Experimental shock deformation in zircon: a transmission electron microscopic study. *Earth and Planetary Science Letters*, 169, 291–301.
- MacDonald, J. M., Wheeler, J., Harley, S. L., Mariani, E., Goodenough, K. M., Crowley, Q., Tatham, D., 2013. Lattice distortion in a zircon population and its effects on trace element mobility and U–Th–Pb isotope systematics: examples from the Lewisian Gneiss Complex, northwest Scotland. *Contributions to Mineralogy and Petrology*, 166, 21–41.
- Moser, D.E., Davis, W.J., Reddy, S.M., Flemming, R.L., Hart, R.J., 2009. Zircon U–Pb strain chronometry reveals deep impact-triggered flow. *Earth and Planetary Science Letters* 277, 73–79.

- Moser, D. E., Cupelli, C.L., Barker, I.R., Flowers, R.M., Bowman, J.R., Wooden, J., Hart, J.R., 2011. New zircon shock phenomena and their use for dating and reconstruction of large impact structures revealed by electron nanobeam (EBSD, CL, EDS) and isotopic U–Pb and (U–Th)/He analysis of the Vredefort dome. *Canadian Journal of Earth Sciences*, 48, 117–139.
- Nemchin A., Timms N. E., Pidgeon R., Geisler T., Reddy S. M., Meyer C. 2009. Timing of crystallization of the lunar magma ocean constrained by the oldest zircon. *Nature Geoscience*, 2, 133-136.
- Piazolo, S., Austrheim, H., Whitehouse, M., 2012. Brittle-ductile microfabrics in naturally deformed zircon: Deformation mechanisms and consequences for U-Pb dating. *American Mineralogist*, 97, 1544–1563.
- Pittarello, L., Pennacchioni, G., Di Toro, G., 2012. Amphibolite-facies pseudotachylytes in Premosello metagabbro and felsic mylonites (Ivrea Zone, Italy). *Tectonophysics*, 580, 43–57.
- Polerecky, L., Adam, B., Milucka, J., Musat, N., Vagner, T., Kuypers, M.M., 2012. Look@NanoSIMS – a tool for the analysis of nanoSIMS data in environmental microbiology. *Environmental Microbiology*, 14 (4), 1009–1023.
- Quick, J.E., Sinigoi, S., Peressini, G., Demarchi, G., Wooden, J.L., Sbisà, A., 2009. Magmatic plumbing of a large Permian caldera exposed to a depth of 25 km. *Geology*, 37, 603-606.
- Reddy, S. M., Timms, N. E., 2010. Deformation of zircon and implications for geochemistry and geochronology. *Source Abstracts with Programs - Geological Society of America* 42 (5), 634.
- Reddy, S.M., Timms, N.E., Trimby, P., Kinny, P.D., Buchan C., Blake K., 2006. Crystal-plastic deformation of zircon: a defect in the assumption of chemical robustness. *Geology*, 34, 257-260.
- Reddy, S.M., Timms, N.E., Hamilton, P.J., Smyth, H.R., 2009. Deformation-related microstructures in magmatic zircon and implications for diffusion. *Contributions to Mineralogy and Petrology*, 157, 231–244.
- Rudnick, R.L., Williams, I.S., 1987. Dating of lower crust by ion microprobe. *Earth and Planetary Science Letters* 85, 145–163.
- Rutter, E.H., Brodie K.H., James T., Burlini L., 2007. Large-scale folding in the upper part of the Ivrea-Verbano zone, NW Italy. *Journal of Structural Geology* 29, 1-17.
- Storm, S., Schmitt, A.K., Shane, Ph., Lindsay, J.M., 2014. Zircon trace element chemistry at sub-micrometer resolution for Tarawera volcano, New Zealand, and implications for rhyolite magma evolution. *Contributions to Mineralogy and Petrology*, 167, 1000.

- Techmer, K.S., Ahrendt, H., Weber, K., 1992. The development of pseudotachylyte in the Ivrea-Verbano Zone of the Italian Alps. *Tectonophysics* 204, 307–322.
- Thomson, O.A., Cavosie, A. J., Moser, D.E., Barker, I., Radovan, H.A., French, B.M., 2014. Preservation of detrital shocked minerals derived from the 1.85 Ga Sudbury impact structure in modern alluvium and Holocene glacial deposits. *Geological Society of America Bulletin*, published online on 13 February 2014, doi:10.1130/B30958.1.
- Timms, N.E. and Reddy, S.M., 2009. Response of cathodoluminescence to crystal-plastic deformation in zircon. *Chemical Geology* 261, 11–23.
- Timms, N.E., Kinny, P., Reddy, S.M., 2006. Enhanced diffusion of uranium and thorium linked to crystal plasticity in zircon. *Geochemical Transactions* 7, 10.
- Timms, N.E., Kinny, P., Reddy, S.M., Evans K., Clark C., Healy D., 2011. Relationship among titanium, rare earth elements, U–Pb ages and deformation microstructures in zircon: Implications for Ti-in-zircon thermometry. *Chemical Geology* 280, 33–46.
- Timms, N.E., Reddy, S.M., Healy, D., Nemchin, A.A., Grange, M.L., Pidgeon, R.T., Hart, R., 2012. Resolution of impact-related microstructures in lunar zircon: A shock-deformation mechanism map. *Meteoritics and Planetary Science*, 47, 120–141.
- Valley, J.W., Cavosie, A.J., Ushikubo, T., Reinhard, D.A., Lawrence, D.F., Larson, D.J., Clifton, P.H., Kelly, T.F., Wilde, S.A., Moser, D.E., Spicuzza, M.J., 2014. Hadean age for a post-magma-ocean zircon confirmed by atom-probe tomography. *Nature Geoscience*, 7, 219–223.
- Wittmann, A., Kenkmann, R.T., Schmitt, R.T., Støffler, D., 2006. Shock-metamorphosed zircons in terrestrial impact craters. *Meteorites and Planetary Science* 41, 433–454.

7.0. Conclusions

During my three-year research project a significant input into the understanding of zircon physical and chemical properties has been made. I have described the specifics of its crystal-plastic behavior and the response of its trace element and isotopic composition on deformation microstructures. These findings have a significant effect on structural geology and on zircon rheology, geochronology and geochemistry investigations. Moreover, deformation-induced isotopic and trace element exchange of zircon with its environment can influence the chemical signature of the host rock.

Not only internal properties of this important accessory mineral were studied. Zircon deformation features were linked to the macroscopic kinematic frame of a shear zone. I have demonstrated how exactly the specific crystallographic orientation of zircon grains in a shear zone influence its deformation patterns. Thus I have checked and extended an existing theoretical model of zircon evolution in ductile shear zones. Also, this data provides important implications for the absolute dating of deformation events.

The zircon behavior in extreme conditions in a seismically-active environment under high differential stresses was described, which may provide a connection between seismology, metamorphic petrology and geophysics, helping to understand the effect of the released seismic energy in depth and the petrophysics at deep crustal levels.

7.1. Future research directions

I hope that our research would be continued and more intriguing findings related to crystal-plastic deformation of accessory minerals would be done. We believe that our study will inspire next generations of scientists to make further exciting discoveries. Information that is recorded and carried by accessory minerals through millions of years of Earth's history is extremely rich and multifaceted, even though the bulk volume of these minerals is rather insignificant for geological formations. All what we have to do now is to find various ways to extract and interpret this information, and the new prospects of geosciences would be wide opened in front of us.

8.0. CURRICULUM VITAE

Elizaveta Kovaleva (Moiseeva)

Date of birth: March 28, 1988

Citizenship: Russian

Gender: Female

Languages: Russian (native); English, French and German (fluent)

Current position: PhD student at the Department of Lithospheric Research, Faculty of Geosciences, Geography and Astronomy, University of Vienna

Address: UZA 2 B484, Althanstrasse 14, A-1090 Wien

Tel.: +43-(0)1-4277-53462

Mobile: +43-681-207-110-24; +7-916-181-87-24

E-mail: elizaveta.kovaleva@univie.ac.at; myzikant88@gmail.com

Computer skills: All basic Microsoft Office software, MatLab, CorelDraw, Photoshop, various special geological software; programming languages: HTML, C++

Driver's license: Category B from 2009



Education

1. March 2012 – February 2015: PhD student at the Doctoral School “DOGMA” (“Deformation of Geological Materials: Mechanical-chemical feedback and the coupling across scales”), Faculty of Geosciences, Geography and Astronomy, University of Vienna, Austria.

Research project: “Rejuvenation effects during plastic deformation; microchemistry, microstructure and texture of deformed zircon: geochronological implications.”

2. 2010 – 2011: Research engineer in the Institute of Experimental Mineralogy from the Russian Academy of Sciences, Chernogolovka.

Research project: “Fluid-induced dehydration and metasomatism in polymetamorphic gneisses of world’s high-grade complexes, experimental modeling.”

3. 2010: Graduated from Department of Petrology, Faculty of Geology, Lomonosov Moscow State University, Moscow, Russia with a specialization as Geochemist.

Diploma title: “Petrological and experimental study of charnockitization process of the Archaean gneisses in the Central Zone of the Limpopo granulite belt, South Africa.”

4. 2010: Graduated from Faculty of Education, Lomonosov Moscow State University, Moscow, Russia with a specialization as School Geography Teacher.

Diploma title: “Using gaming techniques in mineralogy lessons for senior schoolchild.”

Laboratory Work

1. General Laboratory Work

- Prepared thin sections, thick sections, and epoxy discs.
- Separated heavy mineral fraction.
- Prepared pressed powder discs for X-ray fluorescence.
- Dissolved samples for ICP-MS and other geological samples in various laboratories.

2. Scanning Electron Microscope

- Laboratory of Local Material Study, Moscow State University: Jeol JSM-6480LV equipped with X-Ray Spectrometer (WDS) INCA WAVE 500 Micro-Analysis System (Oxford Instrument Ltd.).
- Laboratory of the Geological Survey of Austria, Vienna: Jeol JSM 6490LV SEM coupled with Oxford Inca Energy EDS.
- Center of Earth Sciences, University of Vienna, Austria: FEI Inspect S scanning electron microscope equipped with a Gatan MonoCL system.

- Center of Earth Sciences, University of Vienna, Austria: FEI Quanta 3D FEG instrument equipped with a Schottky field emission electron source, an EDAX Pegasus Apex 4 system consisting of a Digiview IV EBSD camera and an Apollo XV silicon drift detector for EDX analysis.
3. Electron Microprobe
 - University of Vienna, Austria: Electron microprobe analyzer Cameca SX 100 instrument.
 - Hemholz Centre in Potsdam, Germany: JEOL Hyperprobe JXA-8500F field emission gun electron microprobe analyzer.
 4. Inductively Coupled Plasma Mass Spectrometry
 - Geochemistry Laboratory, Moscow State University, with ICP MS Element 2 Finnegan.
 5. Raman Spectrometry
 - University of Vienna, Austria: Renishaw RM1000 micro-Raman system.
 6. NanoSIMS
 - Caltech Microanalyses Center, Pasadena, CA, USA: Cameca NanoSIMS-50L.
 7. Experimental Work
 - Institute of Experimental Mineralogy RAS, Chernogolovka, Moscow
 - i. High-pressure experiments with piston cylinder.
 - ii. Laboratory study of fluid inclusions.

Work Experience

2012 – 2015: University of Vienna, Austria, researcher in the Department of Lithospheric Research.

2010 – 2011: Institute of Experimental Mineralogy from the Russian Academy of Sciences, Chernogolovka, Moscow region, research engineer in the Laboratory of Lithosphere.

2009 – 2011: Trade Company “Mineral Land”, Moscow, consulting geologists.

2006 – 2008: Faculty of Geology, Moscow State University, Moscow, teacher of mineralogy and geology for school students.

2006 – 2010: Danish travel agency “Academic Travel”, Moscow, guide for foreign student education travelers.

List of Publications

Papers

1. **Kovaleva E.**, Klötzli U., Habler G., Wheeler, J., in preparation for submission to *Geology*. On the relationship between deformation microstructures in zircon and the kinematic framework of the shear zone.
2. **Kovaleva E.**, Harlov, D., Klötzli, U., in preparation. Metamorphic textures in zircon from deformed granitic rocks.
3. **Kovaleva E.**, Klötzli U., Habler G., Rhede, D., Guan, Y., in preparation. The effect of crystal-plastic deformation on trace elements and isotopes re-distribution in zircon.
4. **Kovaleva E.**, Klötzli U., Habler G., in preparation. NanoSIMS study of planar deformation bands in zircon.
5. **Kovaleva E.**, Klötzli U., Habler G., Wheeler J., in press. Planar microstructures in zircon from paleoseismic zones. *American Mineralogist*.
6. **Kovaleva E.**, Klötzli U., Habler G., Libowitzky E., 2014. Finite lattice distortion patterns in plastically deformed zircon grains. *Solid Earth*, 5, 1099-1122.
7. Rajesh H.M., Belyanin G.A., Safonov O.G., **Kovaleva E.I.**, Golunova M.A., Van Reenen D.D., 2013. Fluid-induced dehydration of the paleoarchean Sand River biotite–hornblende gneiss, Central Zone, Limpopo Complex, South Africa. *Journal of Petrology*, 54, 41-74, doi: 10.1093/petrology/egs062.
8. Safonov O.G., **Kovaleva E.I.**, Kosova S.A., Rajesh H.M., Belyanin G.A., Golunova M.A., Van Reenen D.D., 2012. Experimental and petrological constraints on local-scale interaction of biotite-amphibole gneiss with H₂O-CO₂-(K, Na)Cl fluids at middle-crustal conditions: Example from the Limpopo Complex, South Africa. *Geoscience Frontiers*, 3 (6), 829-841.

9. Perchuk L.L., **Moiseeva E.I.**, Belyanin G.A., Van Reenen D.D., 2010. High-temperature polymetamorphism in the Central Zone of the Limpopo granulite complex (South Africa): structural and petrologic evidence. Transactions (Doklady) of the Russian Academy of Sciences, Earth Science Sections, 431 (6), 802-807.

Selected Abstracts from Conferences

1. **Kovaleva E.**, Habler G., Kloetzli U., Rhede D., Abart R., 2014. Rheological behavior of zircon in deformed rocks: crystal-plastic deformation and its consequences for trace element content. IMA 2014, abstract volume, 251.
2. Abart R., Griffiths T., Kuleci H., **Kovaleva E.**, Habler G., 2014. Mineral reactions and deformation of solid-phase inclusions and their host crystals. IMA 2014, abstract volume, 245.
3. **Kovaleva E.** and Klötzli U., 2014. Crystallographically controlled crystal-plastic deformation of zircon in shear zones. Geophysical Research Abstracts, 16, EGU2014-3678-4.
4. **Kovaleva E.**, Habler G., Klötzli U., 2014. Crystal-plastic deformation of zircon from strained natural rocks. Deutsche Gesellschaft für Kristallographie, 22 Jahrestagung, abstracts, 43-44.
5. Klötzli U. and **Kovaleva E.**, 2013. Plastic deformation of zircon: a high-T deformation dating tool? Mitteilungen der Österreichischen Mineralogischen Gesellschaft, 159, 73.
6. **Kovaleva E.** and Klötzli U., 2013. Zircon plastic deformation examples from the Tauern Window. Mitteilungen der Österreichischen Mineralogischen Gesellschaft, 159, 80.
7. **Kovaleva E.** and Klötzli U., 2013. Rejuvenation effects during plastic deformation of Zircon: geochronological implications. Geophysical Research Abstracts, 15, EGU2013-4181.
8. **Moiseeva E.I.**, Safonov O.G., Yapaskurt V.O., 2010. Experimental research of charnockitization of biotite-amphibole gneiss with H₂O-CO₂-KCl fluid affection under 750°C and 6.2 kbar. XVI Russian conference of experimental mineralogy. Theses of the speech, Chernogolovka, 103.
9. **Moiseeva E.I.** and Safonov O.G., 2010. Alkali activity during charnockitization of biotite-hornblende gneisses from the Limpopo Belt (South Africa): petrologic and experimental study. Geochemistry of magmatic rocks. Abstracts of XXVII International Conference School "Geochemistry of Alkaline rocks". Moscow-Koktebel', 120.
10. **Moiseeva E.**, 2009. Proterozoic granitization of the archaean gneisses in the Central Zone of the precambrian Limpopo high-grade terrain. Earth Science Frontiers, 16, 194.
11. **Moiseeva E.I.** and Safonov O.G., 2010. Petrological and experimental research of charnockitization process of Archaean gneisses from Limpopo Belt Central Zone, South Africa. Theses of the speech from VI Prof. Perchuk International School of Earth Sciences, Odessa, Ukraine, 90.
12. **Moiseeva E.**, Perchuk L., Safonov, O., 2010. Proterozoic granitization and charnockitization in the Central Zone of the Limpopo granulite belt, South Africa. Geophysical Research Abstracts, Vol. 12, EGU2010-516.
13. Zabrodskaaya T. A. and **Moiseeva E. I.**, 2009. A problem of high-grade polymetamorphism. Earth Science Frontiers, 16, 197.

Participation in Conferences

1. 21st General Meeting of the International Mineralogical Association 2014, Sandton, Johannesburg, South Africa, 01 – 05 September, 2014.
2. European Geosciences Union General Assembly 2014, Vienna, Austria, 27 April – 02 May, 2014.
3. 22nd Annual Conference of the German Crystallographic Society, Freie Universität Berlin, Germany, 17 - 20 March, 2014.
4. MinPet 2013, University of Graz, Graz, Austria, 19 – 23 September, 2013.
5. European Geosciences Union General Assembly 2013, Vienna, Austria, 07 – 12 April, 2013.
6. FOR741 Nanoscale Processes and Geomaterial Properties meeting, Freie Universität Berlin, Germany, 22 – 23 March, 2013.
7. XVI Russian session of experimental mineralogy, Chernogolovka, Russia, September, 2010.
8. XXVII International conference School "Geochemistry of Alkaline rocks", Moscow (Russia)-Koktebel' (Ukraine), September, 2010.

9. The 6th Professor L.L. Perchuk International School of Earth's Sciences (I.S.E.S.), Odessa, Ukraine, September, 2010.
10. European Geosciences Union General Assembly 2010, Vienna, Austria, 02 – 07 May, 2010.
11. 1st World - Y.E.S. (Young Earth Scientists for Society) Congress, Beijing, China, 25 – 28 October, 2009.
12. The 5th International School of Earth's Sciences, Odessa, Ukraine, September, 2009.
13. The 4th International School of Earth's Sciences, Odessa, Ukraine, September, 2008.
14. Workshop on Limpopo Belt Geology and Petrology, University of Johannesburg, South Africa, July, 2008.
15. Annual conference of students and young scientists at the Moscow State University, Russia, 2008-2010.

Courses, Doctoral Schools, and Seminars

1. Seminar “Academic Writing and how to spin it”, University of Vienna, Personal Entwicklung, Vienna, Austria, 10 – 11 April, 2014.
2. Seminar “BrainRead English” by “Immediate Effects”, University of Vienna, Personal Entwicklung, Vienna, Austria, 29 – 30 November, 2013.
3. Seminar “ProWrite English” by “Immediate Effects”, University of Vienna, Personal Entwicklung, Vienna, Austria, 27 – 28 November, 2013.
4. Summer School IK “DOGMA”, Greece, Serifos, organized by University of Vienna, 9 – 13 September, 2013.
5. Seminar on Presentation Techniques, University of Vienna, Personal Entwicklung, Vienna, Austria, 14 and 28 May, 2013.
6. Doctoral school “Texture Analysis with MTEX emphasizing EBSD Data Analysis”, Technical University Bergakademie Freiberg, Germany, 18 – 22 March, 2013.

Field Trips and Workshops

1. Field trip in Stubaital, Alps, mapping and sampling, July 2013.
2. Excursion on Regional Geology of the Calcareous Alps, July 2012.
3. Sampling in the Ivrea-Verbano Zone, Northern Italy, inner arc of the Alpine mountains, July 2012.
4. Structural geology and tectonics field excursion and sampling in the Eastern Alps, Western Tauern Window, Zillertal, June 2012.
5. Workshop on Limpopo Belt geology and petrology, University of Johannesburg, South Africa, July 2008.
6. Workshop in experimental petrology at the Institute of Experimental Mineralogy RAS, Chernogolovka, Moscow region, June 2008.
7. Workshop on magmatic and metamorphic petrology, Urals, Russia, July 2007.
8. Geological mapping and stratigraphy, Crimea, Ukraine, June-July 2007.
9. Field trip to Crimea, Ukraine, June 2006.
10. Field trips to Karelia, Solovetsky Islands, Khibini and Caucasus Mountains, Russia, summer 2006, 2007.

Non-Scientific Activities

- Publications in “Article of Faith”, parish journal of the Russian Orthodox Church of St. Nicholas in Vienna.
- Organization of charity events (fairs, concerts) in Vienna to support children’s hospitals, nursing homes and orphanages, as well as individual families with sick children.
- Organization of the Second Orthodox Meeting of Youth in Vienna (“Zweites Panorthodoxes Jugendtreffen in Wien”), Vienna, Austria, 28 September, 2013.